Kerr-Nonlinear Microresonators and Frequency Combs: Modelling, Design, and Applications

Zur Erlangung des akademischen Grades eines

DOKTORS DER INGENIEURWISSENSCHAFTEN (Dr.-Ing.)

von der KIT-Fakultät für
Elektrotechnik und Informationstechnik
des Karlsruher Instituts für Technologie (KIT)

angenommene

DISSERTATION

von

M.Sc. Philipp Trocha
geb. in Chemnitz

Tag der mündlichen Prüfung: 27.11.2020

Hauptreferent: Prof. Dr.-Ing. Christian Koos
Korreferenten: Prof. Dr.-Ing. Dr. h.c. Wolfgang Freude
Prof. Dr. Wolfgang Reichel

Table of contents

Abstract (German)

Ein optischer Frequenzkamm ist ein optisches Signal, dessen Spektrum aus einer Vielzahl streng äquidistanter, untereinander gekoppelter Spektrallinien besteht. Die Kopplung der Spektrallinien äußert sich in einer zeitlinearen Phasenbeziehung dieser optischen Töne, sowie im Zeitbereich in einer periodischen Signalform. In der Wissenschaft finden optische Frequenzkämme in unterschiedlichen Bereichen Anwendung, etwa als optisches "Zählwerk" bei der Entwicklung hochgenauer Uhren, bei der Entdeckung von Exoplaneten, oder in spektroskopischen Untersuchungen. Etablierte Frequenzkammquellen wie beispielsweise Titan:Saphir-Laser oder Erbium-Faserlaser werden inzwischen auch kommerziell eingesetzt, allerdings sind diese Kammquellen für bestimmte Anwendungen ungeeignet. Hierbei spielen, neben wirtschaftlichen Aspekten wie den Kosten der Kammquellen, physikalische Eigenschaften der emittierten Frequenzkämme eine Rolle. Dazu zählen beispielsweise der abgedeckte Spektralbereich der emittierten Spektrallinien, sowie deren spektraler Abstand zueinander. Dieser freie Spektralbereich skaliert invers mit der optischen Länge des Kammgenerators und ist bei den zuvor genannten Beispielen um mehrere Größenordnungen zu klein, um diese Kammquellen in Systemen wie etwa optischen Wellenlängenmultiplex-Telekommunikationsnetzen einzusetzen.

In jüngerer Vergangenheit wurden weitere Arten von Frequenzkammquellen entwickelt, die grundsätzlich als optische Mikrochipsysteme integriert werden können und die sich somit signifikant von existierenden, makroskopischen Varianten unter anderem hinsichtlich des freien Spektralbereiches der emittierten Frequenzkämme unterscheiden. Insbesondere eine Art von Kammquelle ist dabei in den Vordergrund gerückt: Kerr-Mikroresonatoren. Hierbei handelt es sich um millimetergroße optische Strukturen, in welche monochromatisches Licht von einer separaten Laserquelle eingekoppelt wird. Durch das Auftreten optischer Nichtlinearitäten dritter Ordnung im Mikroresonator werden neue Signale mit spektral äquidistanten Frequenzen erzeugt, die einen

Kerr-Frequenzkamm bilden. Die komplexe nichtlineare Dynamik, welche der Kammerzeugung hier zugrunde liegt, erlaubt in Verbindung mit der Variation der Leistung und der genauen Frequenz des eingekoppelten Lichtes eine große Vielfalt an möglichen Formen von Kerr-Frequenzkämmen. Von diesen besitzt der Einzel-Soliton-Frequenzkamm die größte technische Bedeutung aufgrund seines glatten Spektrums, seiner hohen optischen Bandbreite und der hohen Kohärenz zwischen allen Kammlinien.

In den letzten Jahren wurden erste Anwendungsfelder dieser Soliton-Frequenzkämme erschlossen, wie etwa massiv-parallele optische Datenübertragung mit Rekord-Übertragungsraten, optische Frequenzsynthese oder Mikrowellengeneration mit geringem Phasenrauschen. Es stellt sich im Anbetracht dieser ersten Ergebnisse die Frage, in welchen weiteren Anwendungen integrierte Kammquellen eingesetzt werden können. Hier kommen insbesondere optische Distanzmessungen (engl. Light detection and ranging, LiDAR) als weiteres, wichtiges Gebiet in Betracht, welches in der Vergangenheit bereits vom Einsatz makroskopischer Frequenzkammquellen profitierte. Die zunehmende Verwendung von LiDAR-Systemen, beispielsweise in der Überwachung von industriellen Fabrikationsprozessen oder in der Umgebungserfassung autonom navigierender Objekte, weckt den Bedarf nach hochperformanten und zugleich kompakten Distanzmesssystemen, was den Einsatz von miniaturisierten Frequenzkammgeneratoren als Lichtquellen motiviert. Dabei ist es naheliegend, neben systematischen Anwendungsdemonstrationen auch grundlegendere praxisbezogene Untersuchungen zu den Kammquellen mit theoretischen Ansätzen durchzuführen. Dies gilt insbesondere bei den bislang vorwiegend in ihren physikalischen Grundlagen erschlossenen Kerr-Mikroresonatoren, bei denen beispielsweise die Fragen nach der maximal erzielbaren Konversionseffizienz und der Eignung zur Massenproduktion mithilfe der weitverbreiteten Silizium-Photonik anstelle von exotischeren Materialplattformen nicht ausreichend beantwortet sind.

In der vorliegenden Arbeit werden Distanzmesssysteme basierend auf Soliton-Frequenzkämmen aus Kerr-Mikroresonatoren sowie basierend auf modengekoppelten Quanten-Strich-Laserdioden (engl. quantum-dash mode-locked laser diodes) entwickelt, systematisch charakterisiert und verglichen. Da insbesondere die maximale Leistung des emittierten Frequenzkamms in diesen Systemen ein limitierender Faktor ist, wird eine theoretische, universelle Untersuchung der Konversionseffizienz der nichtlinearen Prozesse in Kerr-

Mikroresonatoren durchgeführt. Dieser theoretischen Analyse schließt sich eine weitere theoretische Ausarbeitung an, die sich mit der Frage auseinandersetzt, ob Kerr-Mikroresonatoren aus Silizium als Frequenzkammgeneratoren bei Telekommunikationswellenlängen verwendet werden können. Dies beinhaltet die Untersuchung des Einflusses von Zwei-Photonen-Absorption und des Einflusses Freier-Ladungsträger-Absorption unter voller Berücksichtigung der Dynamik der freien Ladungsträger auf die Frequenzkammerzeugung. Einzelne Kapitel der vorliegenden Arbeit wurden in den internationalen Fachzeitschriften *Science*, *Physical Review A* und *Scientific Reports* veröffentlicht.

Kapitel 1 gibt eine kurze Einführung in die Frequenzkammerzeugung in Kerr-Mikroresonatoren, einen Überblick über den gegenwärtigen Stand der Technik und stellt offene Fragen, die sich im Zusammenhang mit der Praxistauglichkeit dieser Technologie ergeben.

In *Kapitel 2* werden grundlegende theoretische Konzepte zu optischen Frequenzkämmen, der Kammerzeugung in Kerr-Mikroresonatoren sowie zu frequenzkamm-basierten Distanzmessungen erläutert. Die Erzeugung von Kerr-Frequenzkämmen wird zunächst qualitativ beschrieben und im Anschluss ein mathematisches Modell zur quantitativen Beschreibung der zugrundeliegenden physikalischen Effekte eingeführt – die Lugiato-Lefever-Gleichung. Basierend auf diesem Modell werden Bedingungen für die Erzeugung von Frequenzkämmen in Kerr-Mikroresonatoren aufgestellt und die besonders relevanten Soliton-Frequenzkämme formell beschrieben. Im letzten Abschnitt des zweiten Kapitels werden verschiedene Methoden zur optischen Bestimmung von Distanzen vorgestellt. Dabei werden sowohl ein Verfahren mit Frequenzkämmen als auch solche ohne Frequenzkämme beschrieben.

Gegenstand von *Kapitel 3* ist die theoretische Analyse der in Kerr-Mikroresonatoren erzeugten Frequenzkämme hinsichtlich ihrer spektralen Bandbreite und der Leistungskonversionseffizienz, also dem Verhältnis von ausgehender optischer Kammleistung und eingehender optischer Pumpleistung. Beide Kenngrößen sind in Distanzmesssystemen von elementarer Bedeutung. Kapitel 3 bedient sich hierzu einer Bifurkationsanalyse der Lugiato-Lefever-Gleichung und der numerischen Bestimmung von Näherungslösungen, die Soliton-Frequenzkämmen entsprechen. Hiermit werden diese Frequenzkämme in einem dreidimensionalen Parameterraum sowohl für normal-dispersive als auch anomal-dispersive Kerr-Mikroresonatoren gefunden. Für den ersten

Fall werden mit diesem Ansatz erstmals universelle Aussagen über die erzielbare optische Bandbreite und die maximale Konversionseffizienz getroffen.

Kapitel 4 befasst sich mit der Möglichkeit der Erzeugung von Kerr-Frequenzkämmen bei Telekommunikationswellenlängen in silizium-photonischen Mikroresonatoren. Für kompakte LiDAR-Systeme wären solche Lichtquellen eine Revolution, da dann ein Großteil des Messsystems auf einem einzigen Mikrochip untergebracht werden könnte. In dem Spektralbereich um 1550 nm werden optische Felder bei der Propagation in Silizium allerdings durch die Erzeugung freier Ladungsträger über Zwei-Photonen-Absorption sowie durch freie Ladungsträger selbst gedämpft, was eine Frequenzkamm-Formierung erschwert. Zur Untersuchung dieses Prozesses führt Kapitel 4 ein neues Modell zur Beschreibung der räumlichen Verteilung der Dichte der freien Ladungsträger in Kerr-Mikroresonatoren ein und kombiniert dieses mit der Lugiato-Lefever-Gleichung. Basierend auf diesem Modell werden universelle Limits für die Zwei-Photonen-Absorption und die Absorption durch freie Ladungsträger gefunden, oberhalb derer keine Frequenzkammerzeugung mehr möglich ist. Darüber hinaus wird ein Design eines Silizium-Kerr-Mikroresonators vorgestellt, in dem die Erzeugung von Frequenzkämmen möglich sein sollte, sofern freie Ladungsträger mithilfe eines in Sperrrichtung vorgespannten *p*-*i*-*n*-Übergangs aus dem Mikroresonator entfernt werden. Mit Zeitintegrationen der Lugiato-Lefever-Gleichung werden diese theoretischen Erkenntnisse validiert und Unterschiede zwischen dem in Kapitel 4 vorgestellten Modell und existierenden Modellen herausgearbeitet.

In *Kapitel 5* wird, ungeachtet der offenen Fragestellungen zu dem optimierten Design und der Materialplattform von Kerr-Mikroresonatoren, die Anwendung von Soliton-Kerr-Kämmen in einem Distanzmessverfahren nach dem Prinzip der frequenzkamm-basierten Interferometrie mit synthetischer Wellenlänge beschrieben. Als Kammquellen kommen dabei Siliziumnitrid-Mikroresonatoren mit einer hohen Güte zum Einsatz, in denen Soliton-Kerr-Kämme erzeugt werden können. Es werden ultraschnelle optische Distanzmessungen mit Messraten bis zu 96 MHz bei einer gleichzeitigen Tiefenpräzision von 280 nm demonstriert. Exemplarisch wird das Profil einer fliegenden Luftgewehrkugel vermessen, welche sich mit einer Geschwindigkeit von 150 $\mathrm{m\,s^{-1}}$ fortbewegt.

Kapitel 6 behandelt die Messung von Distanzen mithilfe von modengekoppelten Quanten-Strich-Laserdioden, welche eine technisch einfach zu handhaben-

de und effiziente Alternative zu Kerr-Mikroresonatoren darstellen. Nach demselben Messprinzip wie zuvor werden noch höhere Messraten bis zu 500 MHz bei einer Tiefenpräzision von bis zu 1.7 μm gezeigt. Neben den Hochgeschwindigkeitsmessungen wird zudem noch der Einfluss optischer Verluste im Freistrahl auf die erzielte Genauigkeit, Präzision und auf den Anteil der als verlässlich eingestuften Distanzdatenpunkte untersucht. Dabei wird demonstriert, dass das Messsystem eine Signalminderung im Freistrahl von bis zu 71 dB, d.h. eine Abschwächung um mehr als sieben Größenordnungen noch tolerieren kann, bevor sich die zuvor genannten Kenngrößen überproportional verschlechtern. Für Anwendungen, bei denen nicht die allerhöchste Präzision im Mittelpunkt steht, sind Quanten-Strich-Laserdioden Kerr-Kämmen überlegen.

Schließlich wird die Arbeit in *Kapitel 7* zusammengefasst und die gewonnenen praktischen Erkenntnisse über den Einsatz von integrierten Kammquellen in LiDAR-Systemen interpretiert. Es werden Vorschläge gemacht, wie sich die Leistungsfähigkeit dieser frequenzkamm-basierten Systeme weiter steigern lässt, aber auch Möglichkeiten zur vollständigen Integration aufgezeigt, welche für einen weitverbreiteten Einsatz von maßgeblichem Vorteil ist. Im Rahmen von grundlegenderen Untersuchungen zu Kerr-Mikroresonatoren wird die experimentelle Kerr-Kamm-Erzeugung in silizium-photonischen Varianten basierend auf theoretischen Einsichten erörtert. Schließlich werden auf theoretischer Seite weitere Untersuchungen von praxisrelevanten Operationspunkten von Kerr-Mikroresonatoren vorgeschlagen.

Preface

As an optical frequency comb we denote an optical signal, whose spectrum consists of a multitude of strictly equidistant spectral lines that are locked to each other. Locking means that these spectral lines are in a time-linear phase relationship to each other, and in the time domain this results in a periodic waveform. In science, optical frequency combs are used in different areas, for examples as optical "clock counters" in the development of ultra-precise clocks, for the detection of exoplanets or in spectroscopy. Today, established frequency comb sources such as Ti:sapphire lasers or Er-doped fiber lasers are also used commercially, however, for some applications these comb sources are inappropriate. Besides economic aspects such as the costs of the comb sources, physical properties of the emitted frequency combs play a role. These include, for example, the covered spectral range of the emitted spectral lines, as well as their spectral distance from each other. This free spectral range scales inversely with the optical length of the comb generator and is several orders of magnitude too small to use the comb sources mentioned before in systems like optical telecommunication networks based on wavelength division multiplexing.

Recently, further types of frequency comb sources have been developed which can be integrated as optical microchip systems and which differ significantly from existing macroscopic sources, for instance with respect to the free spectral range of the emitted frequency combs. One type of comb source has become particular relevant: Kerr-nonlinear microresonators. These are millimeter-sized optical structures into which monochromatic light from a separate laser source is coupled. Due to third-order optical nonlinearities in the microresonator, new signals with spectrally equidistant frequencies are generated, which form a Kerr frequency comb. The complex nonlinear dynamics causing the comb formation and variations of the power and the exact frequency of the incoming light allow for a wide variety of possible forms of Kerr frequency combs. Amongst these, the single-soliton frequency comb has the greatest technical

importance due to its smooth spectrum, its large optical bandwidth and the high coherence among all comb lines.

Over the last couple of years, first implementations of these Kerr soliton frequency combs in various applications were shown, such as massively parallel optical data transmission with record transmission rates, optical frequency synthesis or microwave generation with low phase noise. In view of these first results, the question arises, which further applications might benefit from integrated comb sources. Here, optical ranging (Light detection and ranging, LiDAR) is another important field of interest, where the application potential of macroscopic comb generators has already been demonstrated. The increasing use of LiDAR systems, e.g., in the monitoring of industrial manufacturing processes or in the environmental detection of autonomously navigating objects, increases the demand for distance measurement systems with high-performance and a compact form factor. This motivates the use of miniaturized frequency comb generators as light sources in these systems. For a better understanding, such systematic application demonstrations should be accompanied by fundamental investigations of integrated comb sources based on theoretical analyses with focus on questions of practical relevance. This is especially true for Kerr-nonlinear microresonators, which have so far been mostly investigated in terms of their physical fundamentals. For these comb sources, questions such as the maximum achievable conversion efficiency and suitability for mass production using the widespread silicon-photonic platform instead of more exotic material platforms are not fully covered yet.

In this work, LiDAR systems based on soliton frequency combs emitted by Kerr-nonlinear microresonators and based on quantum-dash mode-locked laser diodes (QD-MLLDs) are developed, systematically characterized and compared with each other. Since the maximum power of the emitted frequency comb is a limiting factor in these ranging systems, a theoretical, universal investigation of the conversion efficiency of the nonlinear processes in Kerr-nonlinear microresonators is carried out. This theoretical analysis is followed by a second theoretical investigation, which deals with the question whether Kerr-nonlinear microresonators based on silicon photonics can be used as frequency comb generators at telecommunication wavelengths. This includes the analysis of the influence of two-photon absorption and the influence of free-carrier absorption, taking into account the full dynamics of free carriers and its impact on frequency comb generation. Chapters of this work have been pu-

blished in the peer-reviewed international academic journals *Science*, *Physical Review A*, and *Scientific Reports*.

Chapter 1 gives a brief introduction to frequency comb generation in Kerr-nonlinear microresonators, and a brief overview of the state of the art for this technology. Further, open questions are formulated, which arise in consideration of the suitability of Kerr-nonlinear microresonator frequency combs for large-spread use.

In *Chapter 2* basic theoretical concepts of optical frequency combs, comb generation in Kerr-nonlinear microresonators and frequency comb-based distance measurements are explained. The generation of Kerr frequency combs is described qualitatively in a first step. Then a mathematical model is introduced that allows to quantitatively describe the underlying physical effects – the Lugiato-Lefever equation. Based on this model, conditions for the generation of frequency combs in Kerr microresonators are formulated and the particularly relevant soliton frequency combs are formally described. In the last part of the second chapter, different methods for the optical determination of distances with and without optical frequency combs are explained.

Chapter 3 covers a theoretical analysis of Kerr-nonlinear microresonators with focus on the spectral bandwidth of Kerr frequency combs and the power conversion efficiency, i.e. the ratio of the optical comb power and optical input pump power. Both parameters are of fundamental importance in Kerr-comb-based distance measurement systems. Chapter 3 uses a bifurcation analysis of the Lugiato-Lefever equation and numerical methods to find approximate solutions corresponding to soliton frequency combs. These frequency combs are identified in a three-dimensional parameter space for both normal-dispersive and anomalous-dispersive Kerr-nonlinear microresonators. For the first case, this approach allows for the first time to make universal statements about the achievable optical bandwidth and the maximum power conversion efficiency.

Chapter 4 deals with the possibility of Kerr frequency comb generation at telecommunication wavelengths in silicon-photonic microresonators. For compact LiDAR systems, such light sources would be a revolution, since a large part of the measurement system could then be integrated on a single microchip. However, in the spectral regime around 1550 nm, optical fields are attenuated during propagation in silicon through the generation of free carriers via two-photon absorption as well as by free carriers themselves, which reduces the strength

of nonlinear effects leading to frequency comb formation. To study comb formation in presence of these absorption mechanisms, Chapter 4 introduces a new model that describes the spatial distribution of the free-carrier density in a Kerr-nonlinear microresonator and combines it with the Lugiato-Lefever equation. Based on this model, universal limits for the two-photon absorption and the free-carrier absorption are found, above which formation is not possible anymore. Furthermore, a design of a silicon-photonic Kerr-nonlinear microresonator is presented, that should enable comb formation, provided that free carriers are removed from the microresonator by a cointegrated, reverse-biased *p-i-n* junction. Time integrations of the Lugiato-Lefever equation validate these theoretical findings and demonstrate differences between the model presented in Chapter 4 and existing models.

Despite the open questions regarding the optimized design and material platform of Kerr-nonlinear microresonators, *Chapter 5* describes the application of soliton Kerr combs in a LiDAR system using the principle of frequency comb-based synthetic wavelength interferometry. Here, the comb sources are silicon nitride microresonators that feature a high quality factor and allow for the generation of soliton Kerr combs. Ultrafast optical distance measurements with measurement rates up to 96 MHz and a simultaneous depth precision of 280 nm are demonstrated. The in-flight determination of the profile of an air-gun pellet moving at a speed of 150 m s^{-1} is demonstrated with this system.

Chapter 6 discusses the measurement of distances using quantum-dash mode-locked laser diodes, which represent an easy to handle and power-efficient alternative to Kerr-nonlinear microresonators. Using the same measurement principle as before, even higher measurement rates of up to 500 MHz with a depth precision of 1.7 μm are shown. In addition to the high-speed measurements, the influence of optical losses in the free-space beam path on the achieved accuracy, precision and on the proportion of reliable distance data points is investigated. Here, it is demonstrated that the measurement system can tolerate a signal reduction of up to 71 dB, i.e. an attenuation of more than seven orders of magnitude, before the system performance deteriorates disproportionately in terms of the parameters mentioned before. For applications where highest precision is not the primary concern, quantum-dash mode-locked laser diodes are superior to Kerr combs.

Finally, *Chapter 7* summarizes this work and interprets the insights on the use of integrated comb sources in LiDAR systems. Suggestions are proposed on how

to further increase the performance of these frequency comb-based ranging systems, and possibilities for full integration are shown. In the context of more fundamental investigations on Kerr-nonlinear microresonators, the possibility of Kerr comb generation in silicon-photonic microresonators is discussed based on theoretical insights. Finally, on the theoretical side, further investigations of operating points of Kerr-nonlinear microresonators are proposed that are of practical relevance.

Achievements of the present work

Optical ranging using chip-scale comb generators is a novel concept that may lead to compact, high-performance distance measurement systems. Here, the application of Kerr-nonlinear microresonators as comb sources show great potential. An evaluation of LiDAR systems using Kerr combs requires not only experimental demonstrations and characterizations, but also an understanding of the comb generators. This refers to the question of the highest possible frequency comb power, which is determined by the power conversion efficiency of the nonlinear processes in Kerr-nonlinear microresonators. Furthermore, an understanding of Kerr comb sources requires an investigation whether these photonic structures can be implemented in the widespread silicon-photonic material platform, where two-photon absorption and free-carrier absorption impair comb formation at telecommunication wavelengths. Finally, the performance of a ranging system based on Kerr-nonlinear microresonators should be compared to a ranging system using other light sources. Here, quantum-dash mode-locked laser diodes are a suitable alternative, since they also show great potential as chip-scale frequency comb emitters.

This thesis focuses on these research aspects. In particular, the following main results were achieved:

Determination and description of soliton Kerr comb states in microresonators with normal and anomalous dispersion over a large space of technically accessible parameters: In Chapter 3, we find single-soliton Kerr comb states that can exist in Kerr-nonlinear microresonators based on a global bifurcation analysis of the Lugiato-Lefever equation for a large parameter space covering technically accessible parameters. This method allows to derive the temporal and spectral form of soliton Kerr combs both for normal and anomalous dispersion. Specifically, we identify the comb states with the largest optical bandwidth. We characterize these comb states in terms of power conversion efficiency and optical bandwidth. The associated publication has been published in *Physical Review A* [J1]. This work is a collaboration with

scientists of the Institute for Analysis (IANA) and of the Institute for Applied and Numerical Mathematics (IANM), Karlsruhe Institute of Technology (KIT) within the Collaborative Research Centre "Wave Phenomena" of the Deutsche Forschungsgemeinschaft (German research association).

Explanation of the impact of two-photon absorption and free-carrier absorption on Kerr comb formation in microresonators considering a spatially varying free-carrier density: By analyzing an extended Lugiato-Lefever equation including the generation of free-carriers through two-photon absorption, we show in Chapter 4 how two-photon absorption and free-carrier absorption influence the generation of frequency combs in Kerr-nonlinear microresonators. For this, we introduce a new model that allows to describe a spatially varying free-carrier density along with its interaction with the optical field. The model is general and can be applied to various waveguide platforms and spectral regimes, where these effects are pronounced. Based on this model, we derive fundamental limits for the two-photon absorption and free-carrier absorption, beyond which comb formation through modulation instability is not possible anymore. Time integrations of the Lugiato-Lefever equation confirm the theoretical findings. This work has been published in *Physical Review A* [J2].

Design of silicon microresonators for Kerr comb generation at telecommunication wavelengths: With knowledge about the impact of two-photon absorption and free-carrier absorption on comb formation in Kerr-nonlinear microresonators, we present in Chapter 4 the design of a silicon microresonator that may enable frequency comb formation at telecommunication wavelengths. This result is a part of the publication [J2] mentioned before.

Demonstration of optical ranging with record measurement speed using two soliton Kerr combs: In Chapter 5 we show the application of soliton Kerr combs in a ranging system based on multi-heterodyne synthetic-wavelength interferometry. We reach acquisition rates of up to 96 MHz while maintaining a sub-μm resolution. To the best of our knowledge, this was the highest acquisition rate achieved by any distance measurement system so far at the time of the demonstration. We highlight the ultra-fast acquisition capabilities by determining the profile of a flying air-gun projectile moving at a speed of $150\,\mathrm{m\,s^{-1}}$. The work has been published in *Science* [J3].

Demonstration of optical ranging at record measurement speed and high optical losses using two quantum-dash mode-locked laser diodes: In an experiment described in Chapter 6 we demonstrate the usage of frequency combs emitted by two quantum-dash mode-locked laser diodes in a ranging system with even higher sampling rates of up to 500 MHz. We show that at sampling rates of 50 MHz, such a system can still operate at free-space losses of up to 71 dB. The associated manuscript was published in *Scientific Reports* [J4].

1 Introduction

The first generation of optical frequency combs in 1999 [1] is a milestone in physics, which paved the way for major breakthroughs in many scientific disciplines over the past two decades. In timekeeping, frequency combs can be used for fast and extremely precise comparisons of atomic clocks [2], which in turn allows to verify the values of fundamental physical constants and confirm fundamental physical models [3]. In astronomy, frequency combs allow to detect exoplanets [4, 5], and may even enable to measure the expansion of the universe [6]. In consideration of the tremendous impact of frequency combs in the aforementioned and other disciplines, John L. Hall and Theodor W. Hänsch were awarded with the Nobel prize of physics in 2005 for their contributions to the development of frequency comb sources [7, 8]. Nowadays, frequency comb sources are commercially available mostly in form of mode-locked lasers [9] and mostly used in scientific areas. In principle, frequency combs could be deployed in many other fields, however established frequency comb sources such as Ti:sapphire lasers or Er-doped fiber lasers are inappropriate in some instances. Here, economic aspects such as the costs of the comb sources play a role, but also the physical properties of the emitted frequency combs. These include the spectral regime, where the frequency comb is emitted, and the spacing of the comb lines that is known as free spectral range (FSR). For example, optical telecommunication networks based on wavelength-division multiplexing (WDM) would strongly benefit from frequency combs with an FSR in the order of tens of Gigahertz, however such line separations can be difficult to achieve with the comb sources mentioned before.

About one decade ago, a new frequency comb source was developed that emits frequency combs with completely different comb properties and that has considerable potential for wide-spread use, both in scientific and commercial applications: High-Q microresonators with strong third-order (Kerr) nonlinearities, also known as Kerr-nonlinear microresonators [10]. These are chip-scale photonic structures, in which monochromatic light from a separate pump la-

ser can be converted into a multitude of frequencies with equidistant spectral separation through the Kerr-nonlinearity and the strong field enhancement in the microcavity [11]. Their small size results in a free spectral range that is orders of magnitudes larger than for frequency combs generated in conventional mode-locked solid-state lasers [11]. At the same time, Kerr combs can feature extreme optical bandwidths covering up to a full octave [12], which enables f/2f or 2f/3f self-referencing of the emitted light [13], and allows thus an absolute determination of the emitted frequencies. In scientific applications, this feature can be of great importance. When considering commercial applications, the large comb line spacing makes Kerr combs suitable for, e.g., optical communications, where they can be used as light sources in the transmitter and receiver of an optical fiber link based on wavelength-division-multiplexing [14]. Compared to, e.g., mode-locked lasers relying on free-space optics, the small size of Kerr comb generators is another advantage in such use cases. Over the last decade, the size could be reduced from a benchtop-format down to a few cm^3 [15]. In the same manner, the total power consumption was reduced, such that 100 mW of electric power supplied by an AAA-battery is sufficient for the comb generator operation [15]. This remarkable progress indicates the strong application potential of these comb sources.

So far, Kerr combs were used for, e.g., optical clocks [16], arbitrary waveform generation [17], and optical communications [14]. In optical metrology, a few applications have been investigated, for example spectroscopy [18], while others, in particular LiDAR are still open for research. In the past, ranging systems using optical frequency combs have shown strong performance [19, 20], however they were based on macroscopic comb sources prohibiting a full integration. In consideration of the strong performance of comb-based LiDAR systems and the unique properties of Kerr-nonlinear microresonator frequency combs, it seems natural to combine these two aspects and investigate the resulting ranging system. Here, dissipative Kerr soliton (DKS) frequency combs are the primary Kerr comb state of interest, since they feature a smooth spectrum, a large optical bandwidth and high coherence among all comb lines [21]. Yet it is evident that there are challenges which need to be addressed to increase the applicability of DKS frequency combs, in particular when considering optical ranging as an application scenario.

First, the achievable total power of DKS combs and the power per line need to be increased to match to application-specific requirements. In the past,

research efforts often focused on a reduction of the optical and electric powers necessary for operation, but not necessarily on achieving high comb powers and/or high powers per comb line. Kerr comb generators optimized for low power consumption reach comb line powers in the order of $1 \ldots 10\,\mu$W [15, 22, 23], which may not be enough in specific use cases. This holds especially true for LiDAR, where the optical signal received by a ranging system is orders of magnitude weaker than the emitted signal. Ideally, a Kerr comb generator should be designed with application-specific comb properties in mind, such as a certain comb power. This requires an understanding of the achievable pump-to-comb power conversion efficiency as well as the achievable bandwidth of DKS combs depending on the microresonator and pump laser parameters. A universal understanding of these comb properties is, however, only partially available today.

Second, it should be possible to manufacture Kerr-nonlinear microresonators on a large scale in commercial foundries and cointegrate these devices with other photonic components to build fully functional, integrated LiDAR systems suitable for a commercial use. Both of these challenges refer to the fact that most Kerr-nonlinear microresonators used for comb generation at the technical relevant telecommunication C- and L-band are made of silicon nitride [24] or silica [10], whose associated integration platforms offer a less developed component portfolio compared to, e.g., silicon photonics, in particular when considering active devices. As a result, these materials are less suited for the monolithic co-integration of Kerr-nonlinear microresonators in highly functional photonic circuits. Furthermore, mass production of silica Kerr-nonlinear microresonators may not be possible on the same scale as for established platforms for integrated photonic circuits. Ideally, Kerr comb generators would be made from silicon, which is the dominating material platform for photonic integrated circuits. At telecommunication wavelengths, however, two-photon absorption (TPA) and free-carrier absorption (FCA) in silicon impair the formation of Kerr combs, i.e., the occurrence of modulation instability (MI). It is subject to ongoing discussions [25–28], whether MI can occur in presence of TPA and FCA. It should be noted that the underlying models used so far might not accurately capture the dynamics of Kerr comb generation in presence of free carriers. Specifically, fast modulations of the free-carrier density along the microresonator circumference are not considered in theoretical investigations and only partially in simulations. Clearly, there is a need for further clarifica-

tion how TPA and FCA influence the formation of frequency combs, and this discussion would benefit from more refined models.

In this thesis, the potential of chip-scale Kerr-comb sources in distance metrology is verified by performing high-speed high-precision ranging experiments that rely on the concept of multi-heterodyne synthetic-wavelength interferometry. In a first set of experiments, we use soliton Kerr combs as light sources. At an acquisition rate of 96 MHz, a ranging precision of 280 nm is demonstrated that improves to 12 nm for a reduced acquisition rate of 74 kHz. The high-speed sampling capabilities are demonstrated by reconstructing the profile of an air-gun projectile, which crosses a measurement beam at a speed of $150\,\mathrm{m\,s^{-1}}$. Further tests yield an accuracy of 188 nm, and demonstrate the reproducibility of the measurement results as well as an agreement of this technique with other measurement methods.

While Kerr-comb generators offer vast potential in high-speed high-precision optical ranging, the underlying concept and the associated technical implementation are still rather complex. As a reference for evaluating the complexity-performance trade-offs, we also explore quantum-dash mode-locked laser diodes (QD-MLLDs) as an attractive alternative chip-scale comb generator with comb-line powers of approximately $400\,\mu$W compared to $10\,\mu$W for soliton Kerr combs. Though these devices have a smaller overall optical bandwidth and larger optical linewidths of the individual spectral lines compared to DKS combs, their operation is much simpler, since applying a direct current suffices. In a second LiDAR experiment using QD-MLLDs, we achieve a precision of $1.7\,\mu$m for a sampling rate of up to 500 MHz. In the manner as before, these high-speed measurement capabilities are demonstrated on flying air-gun projectiles. A direct comparison between the two sets of experiments shows that the ranging precision achieved with QD-MLLDs cannot compete with the precision of the DKS comb-based system. However, the simple operation of QD-MLLDs as well as their higher power per comb-line may compensate for this fact, if highest precision is not the primary concern. The investigation is accompanied by inspecting the tolerable free-space losses of the ranging system. Without using any optical amplifiers, a loss tolerance of 49 dB is reached that increases up to 71 dB when using an Er:fiber amplifier to boost the free-space beam power. These numbers indicate that QD-MLLD-based ranging systems can be used for targets located several meters away from the measurement system.

However, the fact that target distances of a few meters already lead to considerable round-trip losses clearly indicates that the achievable comb powers of DKS combs need to be understood and optimized. Otherwise, their low comb-line powers may limit their use in LiDAR systems. Using bifurcation analysis and numerical continuation, DKS combs states are found for arbitrary microresonator parameters and optimized pump field conditions in a technically relevant parameter space. This allows to derive the highest achievable pump-to-comb power conversion efficiency and Kerr comb bandwidth. The analysis is carried out in a universal manner both for normal and anomalous dispersive microresonators, i.e., both dark and bright soliton Kerr combs are investigated with the same methods. It is found that dark-soliton Kerr combs have a significantly larger power conversion efficiency than their bright-soliton counterparts, at the expense of a reduced optical bandwidth. These and other insights serve as guidelines, what pump lasers and microresonators need to be used to achieve application-specific Kerr combs with defined bandwidths and comb powers – crucial aspects for integrated, comb-based LiDAR systems.

To explore the potential of the versatile silicon-photonic platform for integrated ranging systems based on DKS combs, the impact of two-photon absorption and free-carrier absorption on Kerr comb generation in microresonators is investigated. For this purpose, a new model is introduced that allows describing the spatial distribution of free carriers along the microresonator waveguide as well as the impact of free carriers on frequency comb formation. This model, consisting of the Lugiato-Lefever equation as well as a modified rate-equation for the free carriers, is then analyzed theoretically to find the conditions for comb formation, i.e., for modulation instability. It is found that comb formation is possible, if the ratio of the imaginary part and the real part of the Kerr nonlinearity, i.e., the normalized two-photon absorption (TPA) coefficient, is smaller than $1/\sqrt{3}$. Below this threshold, a certain amount of free-carrier absorption is also tolerable. Considering specifically silicon-photonic microresonators, free carriers need to be removed by a reverse-biased *p*-*i*-*n*-junction [29] running in parallel to the microresonator waveguide with the aim to reach these tolerable levels. Based on this insight, a silicon Kerr-nonlinear microresonator is designed, which should support comb generation at telecommunication wavelengths. The theoretical predictions are validated by simulations of Kerr comb formation in a silicon microresonator, where the non-uniform distribution of free carriers in the microresonator causes further dynamics of the optical field.

The insights obtained from experiments on comb-based optical distance measurements provide crucial information for the design of integrated photonic systems, which include Kerr-nonlinear microresonators as frequency comb sources. In combination with the theoretical results, the findings of this work may be used to, e.g., develop fully integrated, Kerr comb-based optical ranging systems.

2 Optical frequency combs

This chapter introduces fundamental concepts, which are relevant for this work. In the first section, an introduction to frequency combs in general is given. Then, quantitative models describing Kerr-nonlinear microresonators and Kerr comb formation are introduced and soliton Kerr combs are described. Other chip-scale comb sources are also briefly discussed. In the last section of this chapter, an overview on optical distance metrology is presented, and different techniques are described. Specifically, a short description of comb-based multi-heterodyne synthetic wavelength interferometry is given, which is the working principle of the ranging systems presented in Chapters 5 and 6.

In this work, optical fields are represented mathematically by their electric fields. Unless specified otherwise, the electric field is assumed to be a scalar quantity for simplicity. In this representation, the measurable, real-valued electric field $E(t)$ with slowly varying complex field envelope $\underline{E}(t)$ and center frequency[1] ω_0 is given as

$$E(t) = \Re\left\{\underline{E}(t)\,\mathrm{e}^{\mathrm{j}\omega_0 t}\right\} = \frac{1}{2}\left(\underline{E}(t)\,\mathrm{e}^{\mathrm{j}\omega_0 t} + c.c.\right). \tag{2.1}$$

Here, $\Re\{\cdot\}$ denotes the real part, $\mathrm{j} = \sqrt{-1}$ is the imaginary unit, $c.c.$ the complex conjugate and t denotes time. Unless specified otherwise, a positive time dependence of the electric field is assumed. In particular, Chapters 3 and 4 and the associated Appendices B and C are formulated for a negative time dependence of the electric field, which is denoted as $E(t) = \Re\left\{\underline{E}^*(t)\,\mathrm{e}^{-\mathrm{j}\omega_0 t}\right\}$. This choice is the standard when describing frequency combs in Kerr-nonlinear microresonators via the Lugiato-Lefever-equation (LLE). Assuming a negative time dependence in the mentioned chapters simplifies a comparison of the presented work with literature.

[1] In this work, optical frequencies are denoted as angular frequencies.

2.1 Frequency combs in mode-locked lasers

A frequency comb is an optical signal consisting of narrow spectral tones ω_μ with a strictly equidistant spacing [30, 31]. The spectral separation ω_{FSR} of these optical tones is called the free spectral range (FSR) of the comb. In most instances, an optical tone ω_μ will not be an integer multiple of ω_{FSR}, but shifted by an offset that is defined as carrier-envelope offset frequency ω_{CEO}, which is smaller than the FSR. Given these two parameters, the spectral positions of the frequency comb lines with index μ are fully defined as

$$\omega_\mu = \omega_{\mathrm{CEO}} + \mu\,\omega_{\mathrm{FSR}}, \quad \mu \in \mathbb{N}. \tag{2.2}$$

Established frequency comb sources are mode-locked lasers (MLL), and well-known examples of solid-state MLLs are Ti:sapphire lasers [1, 32] and Er:fiber ring lasers [33, 34]. In such devices, the generated optical frequencies are in the order of 100 THz or more, and the FSR is in the order of 100 MHz. Therefore the comb line index μ is around 10^6 according to Eq. (2.2). Frequency combs only cover a finite range of μ that does not extend down to zero and therefore it is more practical to count the spectral tones from a center frequency ω_0 of the frequency comb. The spectrum is then defined by

$$\omega_\mu = \omega_0 + \mu\,\omega_{\mathrm{FSR}}, \quad \mu \in \mathbb{Z}, \tag{2.3}$$

such that $|\mu|$ is in the order of 10^5 to 10^6 for the comb sources mentioned before [1, 34].

In mode-locked lasers, a pulse train is generated and emitted [35]. This can be achieved through active or passive means. In Figure 2.1, a laser source using a passive mechanism for pulse generation is sketched: two mirrors and a pumped gain medium form a laser cavity [36]. A fraction of the circulating light in the cavity passes the semi-transparent mirror on the right. The mirror on the left includes a saturable absorber, e. g., a layer of a semiconductor material (semiconductor saturable absorber mirror, SESAM) [37]. Such a mirror absorbs photons through excitation of carriers from the valence band to the conduction band of the semiconductor. At high optical intensities, the free-carrier generation rate is larger than their recombination rate, thus the valence band will be depleted and the conduction band be filled, such that the material eventually becomes transparent. As a result, the net gain per round-trip of an

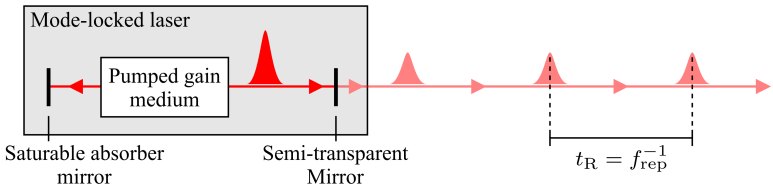

Figure 2.1: Passively mode-locked laser and emission of pulses. The mode-locked laser consists of two mirrors and a pumped gain medium. The right mirror is semi-transparent, such that a part of the light circulating in the cavity is coupled out of the laser. The other mirror on the left includes a saturable absorber, which leads to a pulsed state of the optical signal (red). If one pulse circulates in the cavity at a time, the cavity round-trip time t_R is the inverse of the pulse repetition rate f_{rep}^{-1}.

optical pulse with strong peak intensity is higher compared to the net gain of a continuous-wave (CW) field with weak peak intensity. In this configuration, the laser will favour a pulsed operation, indicated in red in Fig. 2.1. A fraction of the pulse circulating in the cavity will be emitted. The pulse repetition rate f_{rep} is the inverse of the time between two consecutive pulses. Assuming that only one pulse circulates in the cavity at a time, the time between two emitted pulses is equal to the round-trip time t_R in the MLL and therefore $f_{rep}^{-1} = t_R$. In a simple model, the emitted complex electric field $\underline{E}(t)$ is given as a pulse train and depends on the pulse envelope $\underline{E}_P(t)$, the round-trip time t_R and on the center frequency ω_0:

$$\underline{E}\,(t) = \sum_{\mu=-\infty}^{\infty} \underline{E}_P\,(t - \mu\, t_R)\, e^{j\omega_0 t}. \tag{2.4}$$

It should be noted that this is a strongly idealized model of the output of an MLL. In practice, the cavity round-trip time may not be perfectly stable and individual pulses may experience additional phase fluctuations. An analytic model considering these effects and their impact on the linewidth of individual lines of the frequency comb can be found in [38]. To obtain the spectrum

of the time domain signal $\underline{E}(t)$ defined in Eq. (2.4), the Fourier transform $\mathcal{F}\left\{\underline{E}(t)\right\}(\omega) = \hat{\underline{E}}(\omega)$ is determined[2]:

$$\begin{aligned}\hat{\underline{E}}(\omega) =& \mathcal{F}\left\{\underline{E}(t)\right\}(\omega) = \int_{-\infty}^{\infty} \underline{E}(t)\, \mathrm{e}^{-\mathrm{j}\omega t}\mathrm{d}t \\ =& \sum_{\mu=-\infty}^{\infty} \int_{-\infty}^{\infty} \underline{E}_{\mathrm{P}}(t-\mu\, t_{\mathrm{R}})\, \mathrm{e}^{-\mathrm{j}(\omega-\omega_0)t}\mathrm{d}t \\ =& \frac{1}{t_{\mathrm{R}}} \sum_{\mu=-\infty}^{\infty} \hat{\underline{E}}_{\mathrm{P}}(\omega-\omega_0)\, \delta\left(\frac{\omega}{2\pi} - \frac{\omega_0}{2\pi} - \mu\frac{1}{t_{\mathrm{R}}}\right) \\ =& f_{\mathrm{rep}} \sum_{\mu=-\infty}^{\infty} \hat{\underline{E}}_{\mathrm{P}}(\omega-\omega_0)\, \delta\left(\frac{\omega}{2\pi} - \frac{\omega_0}{2\pi} - \mu\, f_{\mathrm{rep}}\right). \end{aligned} \tag{2.5}$$

Here, $\hat{\underline{E}}_{\mathrm{P}}(\omega-\omega_0)$ is the Fourier transform of the pulse envelope $\underline{E}_{\mathrm{P}}(t)$ and $\delta(\omega/(2\pi))$ the Dirac delta function, defined as $\int_{-\infty}^{\infty} \delta(x)h(x)\mathrm{d}x = h(0)$ for a test function $h(x)$. We see that the Fourier transform of a pulse train is a frequency comb, whose FSR is defined by the pulse repetition rate $f_{\mathrm{rep}} = \omega_{\mathrm{FSR}}/(2\pi)$. The pulse envelope $\underline{E}_{\mathrm{P}}(t)$ defines the spectral envelope $\hat{\underline{E}}_{\mathrm{P}}(\omega-\omega_0)$ of the frequency comb. Both of these quantities are assumed to be constant along multiple pulse repetition periods. This requires that the various complex optical tones $\hat{\underline{E}}_{\mathrm{P}}(\omega-\omega_0)\,\delta((\omega-\omega_0-\mu\,\omega_{\mathrm{FSR}})/(2\pi))$ of the frequency comb, which are longitudinal modes of the laser cavity, remain locked to each other. More specifically, this means that the phases of the modes, given by $\arg\left\{\hat{\underline{E}}_{\mathrm{P}}(\omega-\omega_0)\,\delta((\omega-\omega_0-\mu\,\omega_{\mathrm{FSR}})/(2\pi))\right\}$, are in a time-linear phase relation to each other. At given points in time separated by f_{rep}^{-1}, the phases of these modes are equal, such that the superposition of the modes results in optical pulses, which, due to the saturable absorption of the SESAM experience highest intra-cavity gain. Between pulses, the phases of the modes are not equal, which leads to an absence of a measurable field intensity.

Besides using a SESAM, various other techniques allow for mode-locking in lasers. Another passive approach is Kerr lens mode locking, where a Kerr-nonlinear material is included into the laser cavity. The Kerr-nonlinear material changes its refractive index based on the intensity of the laser beam and thus

[2] The inverse Fourier transform is given by $\mathcal{F}^{-1}\left\{\hat{\underline{E}}(\omega)\right\}(t) = (2\pi)^{-1}\int_{-\infty}^{\infty}\hat{\underline{E}}(\omega)\,\mathrm{e}^{\mathrm{j}\omega t}\mathrm{d}\omega$.

leads to an intensity-dependent self-focusing [39,40]. By including an aperture after the Kerr lens in the laser cavity, the net gain of a self-focused laser beam becomes higher than the gain a non-focused beam such that a pulsed operation will be preferred. Active mode locking is performed by periodically changing the net gain in a laser cavity or the phase accumulated over one round-trip. This can be achieved , e. g., via pump current modulations of a semiconductor laser [41] or by including an electro-absorption modulator [42] in the cavity.

For many different frequency comb sources, both the carrier-envelope offset frequency ω_{CEO} and the free spectral range ω_{FSR} are in the order of $2\pi \times 100\,\mathrm{MHz}$. The FSR can easily be measured by guiding light of the frequency comb to a photodetector, which will produce an output current with an oscillation at a frequency $f = \omega_{\mathrm{FSR}}/(2\pi)$. A measurement of ω_{CEO} is more difficult, but possible via, e. g., $f/2f$-self referencing [43]. In this scheme, a frequency comb with frequencies $\omega_\mu = \omega_{\mathrm{CEO}} + \mu\omega_{\mathrm{FSR}}$ is superimposed with its second harmonic on a photodetector. The second harmonic is located at frequencies $\omega_{\mu'} = 2\omega_{\mathrm{CEO}} + 2\mu'\omega_{\mathrm{FSR}}$, which leads to beat signals at the difference frequencies $\left|\omega_{\mu'} - \omega_\mu\right| = \left|\omega_{\mathrm{CEO}} + (2\mu' - \mu)\,\omega_{\mathrm{FSR}}\right|$ in the photocurrent of the detector. Amongst these beat signals, there is one for which $2\mu' = \mu$ holds. It is located at lowest frequency $\left|\omega_{\mu'} - \omega_\mu\right| = \omega_{\mathrm{CEO}}$ of all difference frequencies and can therefore be used to determine the carrier-envelope offset frequency.

With these two measurements, the frequencies of all frequency comb lines can be precisely determined. This allows for extremely precise frequency metrology and spectral analysis of other optical signals, such as atomic lines [1] or exoplanet-induced doppler-shifts of the light of distant stars [5]. The precisely known frequencies of a frequency comb were also used to build an ultra-accurate clock [44]. Frequency combs showed also great potential in applications such as light detection and ranging (LiDAR) [19] that may be relevant not only in science, but also in commercial use cases. However mode-locked lasers with rather small free spectral ranges in the order of $2\pi \times 100\,\mathrm{MHz}$ are not suited for all kinds of applications[3]. Increasing the free spectral range

[3] This is reinforced by the fact that such small FSRs are associated with rather large optical round-trip lengths of several meters, such that the comb generator may have a substantial overall size, prohibiting its use in applications where the available space for a comb source is limited. For example, a pulse repetition rate of 100 MHz corresponds to an optical round-trip length of roughly 3 meters. The associated geometric length, which depends on the refractive indices of the materials along the optical path, is smaller, but in the same order of magnitude.

can be achieved by, e.g., harmonic mode-locking [45] which however requires additional active components compared to the scheme depicted in Fig. 2.1. Here, a significant reduction of the round-trip length of an MLL down to a few centimeters or less is a viable option, which motivates alternative concepts to, e.g., free-space MLLs or fiber-based MLLs.

Chip-scale frequency comb sources emit combs with the highest FSR. In the next section, frequency comb generation in Kerr-nonlinear microresonators is described, followed by Section 2.3 that discusses quantum-dash mode-locked laser diodes as an alternative to Kerr comb generators. These comb sources sources differ from Kerr comb generators in terms of comb parameters such as the overall optical bandwidth as well as in the complexity of their operation. While Kerr combs generally allow for a higher performance of comb-based systems in specific applications, they may more be difficult to use compared to QD-MLLDs, which can make these devices a viable alternative.

2.2 Kerr comb generators

Kerr-nonlinear microresonators are chip-scale photonic structures, in which monochromatic light is converted into a frequency comb through degenerate and non-degenerate four-wave mixing. After the initial demonstration of the comb formation principle [10], this technology rapidly evolved over the last years. The generation of frequency combs in Kerr-nonlinear microresonators was demonstrated based on various material platforms, including silicon nitride [24], silica [10], silicon [46], diamond [47], AlGaAs [48] and others [49–51]. With the discovery of dissipative Kerr soliton frequency combs [21], the generation of a special class of mode-locked frequency combs in Kerr-nonlinear microresonators was demonstrated. Improvements in the fabrication of Kerr-nonlinear microresonators lead to a continuous increase of their quality (Q)-factors, and consequently for a decrease of the required optical powers for parametric conversion, such that today Kerr comb generators can be operated using AAA batteries as power supplies [15]. The underlying nonlinear processes as well as the resulting frequency combs depend crucially on a number of microresonator properties, which are discussed in Section 2.2.1. In Section 2.2.2 the comb formation is described qualitatively and quantitatively. Section 2.2.3 gives an overview on dissipative Kerr solitons.

2.2.1 Properties of Kerr-nonlinear microresonators

The following description of Kerr-nonlinear microresonators refers to planar, integrated waveguide structures. Figure 2.2 shows a schematic of a ring-shaped microresonator waveguide that is coupled to a bus waveguide. Other variants, where the microresonator is, e. g., a microsphere [52] or a microtoroid [53], and light coupling is achieved using a prism [54] or a tapered optical fiber [55] can be described using the same formalism that is introduced in the following. For the moment, only linear optical properties of the microresonator are considered.

Light with angular frequency ω_0 propagates in a bus waveguide and is coupled to a microresonator at the coupling section through evanescent coupling [56], see Fig. 2.2. This process can be described by a matrix equation, that relates the incoming field $\underline{E}_{i_1}$ in the bus waveguide and the field $\underline{E}_{i_2}$ in the microresonator after one round-trip with the field $\underline{E}_{t_1}$ in the bus waveguide after the coupling section and with the field $\underline{E}_{t_2}$ in the microresonator after the coupling section [57]:

$$\begin{pmatrix} \underline{E}_{t_1} \\ \underline{E}_{t_2} \end{pmatrix} = \begin{pmatrix} \underline{t} & \underline{\kappa} \\ -\underline{\kappa}^* & \underline{t}^* \end{pmatrix} \begin{pmatrix} \underline{E}_{i_1} \\ \underline{E}_{i_2} \end{pmatrix}. \tag{2.6}$$

Here, $\underline{t}$ and $\underline{\kappa}$ are the complex transmission coefficient and the complex coupling coefficient of the coupler. In absence of losses in the coupling section, they are related by $\left|\underline{t}\right|^2 + \left|\underline{\kappa}\right|^2 = 1$. The coupling coefficient $\underline{\kappa}$ is linked to the power coupling coefficient θ_C via $\left|\underline{\kappa}\right|^2 = \theta_\mathrm{C}$.

During one round-trip in the microresonator, light experiences attenuation by a factor of $\exp\left(-\alpha_i L_\mathrm{MR}/2\right)$ and a phase accumulation of $\exp\left(-\mathrm{j}\beta(\omega_0)L_\mathrm{MR}\right)$. The attenuation is caused by material absorption, by scattering at the waveguide boundaries as well as by radiation due to waveguide bending [58]. It is characterized by the product of the power attenuation coefficient α_i (dimension m^{-1}) and the circumference of the microresonator L_MR. The accumulated phase depends on the propagation constant $\beta(\omega_0)$ and L_MR. Accordingly, the fields $\underline{E}_{i_2}$ and $\underline{E}_{t_2}$ are linked via $\underline{E}_{i_2} = \exp\left(-\alpha_i L_\mathrm{MR}/2 - \mathrm{j}\beta(\omega_0)L_\mathrm{MR}\right)\underline{E}_{t_2}$.

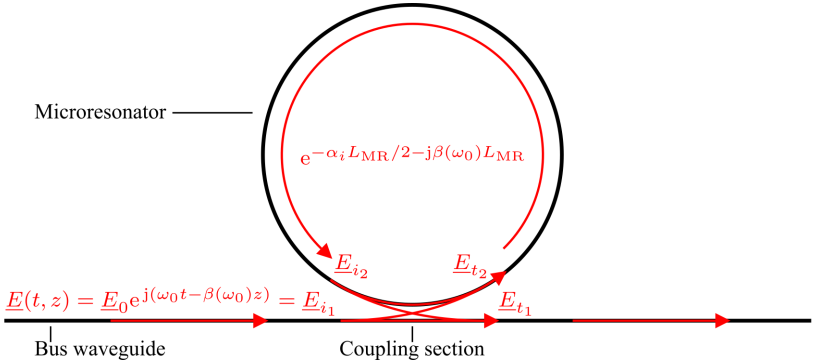

Figure 2.2: Sketch of light propagating in a coupled bus waveguide and microresonator. In this visualization, nonlinear properties of the microresonator are not considered. The electromagnetic field is defined by its complex amplitude $\underline{E}_0$ and angular frequency ω_0 as well as by the propagation constant $\beta(\omega_0)$. At the coupling section, the incoming optical field $\underline{E}_{i_1}$ is separated into a part $\underline{E}_{t_1}$ that continues to propagate in the bus waveguide, and a part $\underline{E}_{t_2}$ that is coupled in the microresonator. Over one round-trip inside the microresonator, the optical field experiences a phase accumulation $\exp(-j\beta(\omega_0)L_{MR})$ as well as a reduction of its amplitude by a factor of $\exp(-\alpha_i L_{MR}/2)$ depending on the waveguide attenuation coefficient α_i as well as on the circumference L_{MR} of the microresonator. The resulting field $\underline{E}_{i_2}$ inside the microresonator at the beginning of the coupling section is linked to $\underline{E}_{t_2}$ accordingly via $\underline{E}_{i_2} = \exp(-\alpha_i L_{MR}/2 - j\beta(\omega_0)L_{MR})\,\underline{E}_{t_2}$.

Using Eq. (2.6), one can derive the power transmission ratio $|\underline{E}_{t_1}|^2/|\underline{E}_{i_1}|^2$ of the combined waveguide and microresonator [57][4]:

$$\frac{|\underline{E}_{t_1}|^2}{|\underline{E}_{i_1}|^2} = \frac{|\underline{t}|^2 + e^{-\alpha_i L_{MR}} - 2|\underline{t}|e^{-\alpha_i L_{MR}/2}\cos\left(-\beta(\omega_0)L_{MR} + \arg\{\underline{t}\}\right)}{1 + |\underline{t}|^2 e^{-\alpha_i L_{MR}} - 2|\underline{t}|e^{-\alpha_i L_{MR}/2}\cos\left(-\beta(\omega_0)L_{MR} + \arg\{\underline{t}\}\right)}, \quad (2.7)$$

where $\arg\{\underline{t}\}$ corresponds to the phase accumulated by the optical field when passing the coupler through one of the two waveguides. In the following, this phase is incorporated into the phase that is accumulated during one round-trip in the microresonator for simplicity, $-\beta(\omega_0)L_{MR} + \arg\{\underline{t}\} \rightarrow -\beta(\omega_0)L_{MR}$.

[4] In [57], the loss coefficient α corresponds to $e^{-\alpha_i L_{MR}/2}$ and the incoming field is set to $\underline{E}_{i_1} = 1$. Furthermore, note that in [57] field amplitudes with a negative time-dependency are described, which leads to positive values $\beta L = \beta_0(\omega_0)L_{MR}$ for the accumulated phase during one round-trip in the microresonator, whereat in this work, for a positive time-dependency of the field amplitudes, these values are negative $-\beta_0(\omega_0)L_{MR}$.

In case of constructive interference, the accumulated phase $\beta(\omega_0)L_{\mathrm{MR}}$ corresponds to a multiple of 2π, such that Eq. (2.7) can be simplified to [57]

$$\frac{|\underline{E}_{t_1}|^2}{|\underline{E}_{i_1}|^2} = \frac{\left(|\underline{t}| - \mathrm{e}^{-\alpha_i L_{\mathrm{MR}}/2}\right)^2}{\left(1 - |\underline{t}|\mathrm{e}^{-\alpha_i L_{\mathrm{MR}}/2}\right)^2} = \frac{\left(\sqrt{1-\theta_{\mathrm{C}}} - \mathrm{e}^{-\alpha_i L_{\mathrm{MR}}/2}\right)^2}{\left(1 - \sqrt{1-\theta_{\mathrm{C}}}\mathrm{e}^{-\alpha_i L_{\mathrm{MR}}/2}\right)^2}. \tag{2.8}$$

Inspecting Eq. (2.8) shows that the transmitted field vanishes if the condition $\sqrt{1-\theta_{\mathrm{C}}} = \mathrm{e}^{-\alpha_i L_{\mathrm{MR}}/2}$ holds, a coupling state known as *critical coupling* [56][5]. Only critical coupling leads to a full power transfer of light from the bus waveguide to the microresonator on resonance, and therefore this state is of high practical relevance. If the power coupling coefficient θ_{C} has a smaller value, i.e., $\sqrt{1-\theta_{\mathrm{C}}} > \mathrm{e}^{-\alpha_i L_{\mathrm{MR}}/2}$, the microresonator is *undercoupled*, while for larger θ_{C}, i.e., $\sqrt{1-\theta_{\mathrm{C}}} < \mathrm{e}^{-\alpha_i L_{\mathrm{MR}}/2}$ it is *overcoupled*. In the limit of small coupling coefficients $\theta_{\mathrm{C}} \ll 1$ and small values for the product $\alpha_i L_{\mathrm{MR}} \ll 1$, these relations can be simplified. Then one may approximate $\sqrt{1-\theta_{\mathrm{C}}} \approx 1 - \theta_{\mathrm{C}}/2$ and $\mathrm{e}^{-\alpha_i L_{\mathrm{MR}}/2} \approx 1 - \alpha_i L_{\mathrm{MR}}/2$, which leads to the condition $\theta_{\mathrm{C}} = \alpha_i L_{\mathrm{MR}}$ for critical coupling, to $\theta_{\mathrm{C}} < \alpha_i L_{\mathrm{MR}}$ for undercoupled microresonators, and to $\theta_{\mathrm{C}} > \alpha_i L_{\mathrm{MR}}$ for overcoupled microresonators. In this limit, the total attenuation of an optical signal during one round-trip in the microresonator may also be approximated by a factor of $\sqrt{1-\theta_{\mathrm{C}}}\mathrm{e}^{-\alpha_i L_{\mathrm{MR}}/2} \approx \mathrm{e}^{-(\alpha_i L_{\mathrm{MR}} + \theta_{\mathrm{C}})/2}$.

An important measure of a microresonator related to the attenuation of the optical field is the dimensionless Q-factor, which represents the ratio of the stored energy in the microresonator and the dissipated energy per round-trip [57]. For critical coupling and $\alpha_i L_{\mathrm{MR}}, \theta_{\mathrm{C}} \ll 1$, the Q-factor of a specific resonance with index ν can be expressed in terms of the resonance frequency $\omega_{\mathrm{r},\nu}$, the waveguide loss coefficient α_i, the microresonator circumference L_{MR}

[5] See also [56], Eq. (1.2) with the condition that the round-trip phase $\beta(\omega)L_{\mathrm{MR}}$ is an integer multiple of 2π. Note that in [56], the authors consider the field loss denotes as α in their formalism, which has only half of the value of the power attenuation coefficient α_i used in this work, $\alpha \rightarrow \alpha_i/2$.

and the round-trip time t_R of an optical field envelope in the microresonator [56][6]

$$Q = \frac{\omega_{\mathrm{r},\nu} t_\mathrm{R}}{2\alpha_i L_\mathrm{MR}}. \tag{2.9}$$

The accumulated phase during one round-trip is determined by the circumference L_MR and the propagation constant $\beta(\omega_0)$, which is the product of the angular carrier frequency ω_0 of the optical field and the effective refractive index $n_\mathrm{e}(\omega_0)$ divided by the speed of light in vacuum c_0:

$$\beta(\omega_0) = \omega_0 \frac{n_\mathrm{e}(\omega_0)}{c_0}. \tag{2.10}$$

The effective refractive index depends on the waveguide materials, the waveguide geometry, and the vectorial field distribution $\underline{\mathbf{E}}(x,y), \underline{\mathbf{H}}(x,y)$ of the waveguide eigenmode, into which light is coupled from the bus waveguide. The value of $n_\mathrm{e}(\omega)$ can be obtained in finite-element simulations of the eigenmode field distribution [59]. It is common practice to express the propagation constant $\beta(\omega)$ as a Taylor series around the angular carrier frequency ω_0 of an optical field of interest,

$$\beta(\omega) = \sum_{n=0}^{\infty} \frac{1}{n!} \beta^{(n)}(\omega_0)\,(\omega-\omega_0)^n\,,\ \beta^{(n)}(\omega_0) = \left.\frac{\partial^n \beta(\omega)}{\partial \omega^n}\right|_{\omega=\omega_0}, \tag{2.11}$$

where we assume $0^0 = 1$ for $n = 0$ and $\omega = \omega_0$. Of particular importance are the first three Taylor coefficients $\beta^{(0)}$, $\beta^{(1)}$ and $\beta^{(2)}$, which read

$$\beta^{(0)}(\omega_0) = \omega_0 \frac{n_\mathrm{e}(\omega_0)}{c_0}, \tag{2.12}$$

[6] See Eq. (1.1) in [56] with the substitutions $\omega_0 \to \omega_{\mathrm{r},\nu}$, $\tau_\mathrm{R} \to t_\mathrm{R}$, $2\alpha \to \alpha_i$, and $L \to L_\mathrm{MR}$ for the Q-factor of a microresonator that is not coupled to a bus waveguide, i.e., the intrinsic Q-factor. If critical coupling is assumed, the round-trip losses increase by a factor of 2, and the expression for the Q-factor in [56] has therefore to be divided by 2, which leads to Eq. (2.9).

$$\beta^{(1)}(\omega_0) = \left.\frac{\partial\beta(\omega)}{\partial\omega}\right|_{\omega=\omega_0} = \left.\frac{1}{c_0}\left(n_\mathrm{e}(\omega) + \omega\frac{\partial n_\mathrm{e}(\omega)}{\partial\omega}\right)\right|_{\omega=\omega_0}$$
$$= \frac{n_\mathrm{eg}(\omega_0)}{c_0} = \frac{1}{v_\mathrm{g}(\omega_0)}, \tag{2.13}$$
$$\beta^{(2)}(\omega_0) = \left.\frac{\partial^2\beta(\omega)}{\partial\omega^2}\right|_{\omega=\omega_0} = \left.\frac{\partial\beta^{(1)}(\omega)}{\partial\omega}\right|_{\omega=\omega_0} = \left.\frac{1}{c_0}\frac{\partial n_\mathrm{eg}(\omega)}{\partial\omega}\right|_{\omega=\omega_0}. \tag{2.14}$$

In these definitions, the effective group refractive index $n_\mathrm{eg}(\omega_0)$ and the group velocity $v_\mathrm{g}(\omega_0) = c_0/n_\mathrm{eg}(\omega_0)$ were introduced to describe the speed, at which the envelope of an optical field with angular carrier frequency ω_0 propagates in a waveguide. The zeroth-order Taylor coefficient $\beta^{(0)}(\omega_0)$ is the ratio of the angular frequency ω_0 and the phase velocity $c_0/n_\mathrm{e}(\omega_0)$ of the optical field.

The first-order Taylor coefficient $\beta^{(1)}(\omega_0)$ is the inverse of the group velocity and dictates the angular free spectral range $\omega_\mathrm{r,FSR}$ (FSR) of the microresonator, which will be shown in the following. Resonance frequencies $\omega_{\mathrm{r},\nu}$ are determined by the condition that the accumulated phase in one round-trip must be a multiple of 2π:

$$\beta\left(\omega_{\mathrm{r},\nu}\right) L_\mathrm{MR} = \omega_{\mathrm{r},\nu}\frac{n_\mathrm{e}\left(\omega_{\mathrm{r},\nu}\right)}{c_0} L_\mathrm{MR} \stackrel{!}{=} \nu\, 2\pi, \quad \nu \in \mathbb{N}^*. \tag{2.15}$$

To find an expression for the free spectral range $\omega_\mathrm{FSR}(\omega_{\mathrm{r},\nu})$, we perform a first-order Taylor expansion of the propagation constant around $\omega_{\mathrm{r},\nu}$ and formulate the resonance condition Eq. (2.15) for the next resonance frequency, which is given by $\omega_{\mathrm{r},\nu+1} = \omega_{\mathrm{r},\nu} + \omega_\mathrm{FSR}(\omega_{\mathrm{r},\nu})$:

$$\beta\left(\omega_{\mathrm{r},\nu+1}\right) L_\mathrm{MR} \approx \beta^{(0)}\left(\omega_{\mathrm{r},\nu}\right) L_\mathrm{MR} + \beta^{(1)}\left(\omega_{\mathrm{r},\nu}\right) L_\mathrm{MR}\, \omega_\mathrm{FSR}(\omega_{\mathrm{r},\nu})$$
$$\stackrel{!}{=} (\nu+1)2\pi. \tag{2.16}$$

Subtracting Eq. (2.15) with $\beta\left(\omega_{\mathrm{r},\nu}\right) = \beta^{(0)}\left(\omega_{\mathrm{r},\nu}\right)$ from Eq. (2.16) allows to solve the resulting expression for the free spectral range $\omega_\mathrm{FSR}(\omega_{\mathrm{r},\nu})$,

$$\omega_\mathrm{r,FSR}(\omega_{\mathrm{r},\nu}) = \frac{2\pi}{\beta^{(1)}\left(\omega_{\mathrm{r},\nu}\right)} = \frac{2\pi c_0}{n_\mathrm{eg}\left(\omega_{\mathrm{r},\nu}\right) L_\mathrm{MR}}. \tag{2.17}$$

The FSR and the first-order Taylor coefficient of the propagation constant are linked to the round-trip time of the microresonator, which is given as

$$t_\mathrm{R} = \frac{2\pi}{\omega_{\mathrm{r,FSR}}(\omega_{\mathrm{r},\nu})} = \beta^{(1)}(\omega_{\mathrm{r},\nu}) L_\mathrm{MR} = n_\mathrm{eg}(\omega_{\mathrm{r},\nu}) L_\mathrm{MR}/c_0. \tag{2.18}$$

The second-order Taylor coefficient $\beta^{(2)}(\omega)$, also known as second-order dispersion coefficient or group-velocity dispersion (GVD), describes the frequency dependence of the effective group refractive index. This dispersive behaviour of the effective group refractive index $n_\mathrm{eg}(\omega)$ and the underlying effective refractive index $n_\mathrm{e}(\omega)$ are caused by chromatic material dispersion and waveguide dispersion[7] [60]. The sign of the second-order dispersion coefficient $\beta^{(2)}(\omega)$ determines whether a waveguide exhibits *normal* GVD ($\beta^{(2)}(\omega) > 0$), or *anomalous* GVD ($\beta^{(2)}(\omega) < 0$). Group-velocity dispersion can also be described as a dependence of the group refractive index on the wavelength $\lambda = 2\pi c_0/\omega$, $n_\mathrm{eg} = n_\mathrm{eg}(\lambda)$. In this case the second-order dispersion coefficient is given by the dispersion parameter $D_\lambda(\lambda) = -\frac{2\pi c_0}{\lambda^2}\beta^{(2)}(2\pi c_0/\lambda)$ [61]. For microresonators, it is also common practice to describe the dispersion as a change of the FSR per resonance mode index ν. For this, first the dependence of the FSR on the resonance frequencies is computed, see Eq. (2.17):

$$\begin{aligned}\frac{\partial \omega_{\mathrm{r,FSR}}(\omega_{\mathrm{r},\nu})}{\partial \omega_{\mathrm{r},\nu}} &= -\frac{2\pi}{L_\mathrm{MR}}\left(\frac{1}{\beta^{(1)}(\omega_{\mathrm{r},\nu})}\right)^2 \beta^{(2)}(\omega_{\mathrm{r},\nu}) \\ &= -\frac{L_\mathrm{MR}\omega^2_{\mathrm{r,FSR}}(\omega_{\mathrm{r},\nu})}{2\pi}\beta^{(2)}(\omega_{\mathrm{r},\nu}).\end{aligned} \tag{2.19}$$

The change of the FSR with the optical resonance frequency, $\partial\omega_{\mathrm{r,FSR}}/\partial\omega_{\mathrm{r},\nu}$, can also be expressed as a change of the FSR with respect to the resonance frequency index $\partial\omega_{\mathrm{r,FSR}}/\partial\nu$. These two derivatives are connected by the free spectral range $\omega_{\mathrm{r,FSR}}$, which can also be written as a change of the resonance

[7] Intermodal dispersion, i.e., differences of n_e of different waveguide eigenmodes, also contributes to the total dispersion, but is neglected in this work in most instances for simplicity.

frequency with the resonance index, $\omega_{\mathrm{r,FSR}}(\omega_{\mathrm{r},\nu}) = \partial\omega_{\mathrm{r},\nu}/\partial\nu$. Consequently, we can write $\partial/\partial\nu = \omega_{\mathrm{r,FSR}}\partial/\partial\omega_{\mathrm{r},\nu}$ and rephrase Eq. (2.19) as

$$\begin{aligned}\frac{\partial\omega_{\mathrm{r,FSR}}(\omega_{\mathrm{r},\nu})}{\partial\nu} &= \omega_{\mathrm{r,FSR}}(\omega_{\mathrm{r},\nu})\frac{\partial\omega_{\mathrm{r,FSR}}(\omega_{\mathrm{r},\nu})}{\partial\omega_{\mathrm{r},\nu}} = -\frac{L_{\mathrm{MR}}}{t_{\mathrm{R}}}\omega^2_{\mathrm{r,FSR}}(\omega_{\mathrm{r},\nu})\beta^{(2)}(\omega_{\mathrm{r},\nu}) \\ &= -\frac{c_0}{n_{\mathrm{eg}}}\omega^2_{\mathrm{r,FSR}}(\omega_{\mathrm{r},\nu})\beta^{(2)}(\omega_{\mathrm{r},\nu}). \end{aligned} \tag{2.20}$$

Anomalous dispersion, $\beta^{(2)}(\omega) < 0$, leads to an increase of the free spectral range with $\omega_{\mathrm{r},\nu}$ or ν, whereas normal dispersion, $\beta^{(2)}(\omega) > 0$, is associated with a decreasing microresonator FSR. In literature, the frequency-dependence of a microresonator's FSR is often also described by the term $D_2 = -\frac{c_0}{n_{\mathrm{eg}}}\beta^{(2)}(\omega)\,\omega^2_{\mathrm{r,FSR}}(\omega)$ [62][8], which has the same unit as the FSR. With this definition, the resonance frequencies around a center resonance frequency with index $\nu = 0$ can be approximated as

$$\begin{aligned}\omega_{\mathrm{r},\nu} &\approx \omega_{\mathrm{r},0} + \frac{\partial\omega_{\mathrm{r},\nu}}{\partial\nu}\nu + \frac{1}{2}\frac{\partial^2\omega_{\mathrm{r},\nu}}{\partial\nu^2}\nu^2 \\ &= \omega_{\mathrm{r},0} + \nu\,\omega_{\mathrm{r,FSR}} - \frac{c_0}{2n_{\mathrm{eg}}}\beta^{(2)}\left(\omega_{\mathrm{r},0}\right)\left(\nu\,\omega_{\mathrm{r,FSR}}\right)^2 \\ &= \omega_{\mathrm{r},0} + \nu\,\omega_{\mathrm{r,FSR}} + \frac{D_2}{2}\nu^2. \end{aligned} \tag{2.21}$$

In practice, light coupled into the microresonator will lead to a shift of these resonance frequencies. The shift is caused by the absorption of light which leads to an increased temperature and thereby an expansion of the microresonator as well as a change of the refractive index, which both alter the resonance condition, Eq. (2.15). Furthermore, in case of strong Kerr nonlinearities, a strong pump wave can lead to a resonance shift via cross-phase modulation (XPM). Therefore, Eq. (2.21) holds for a "cold" microresonator, where no light is present.

All quantities described so far are linear optical properties of waveguides and microresonators. For Kerr comb generation, however, the microresonator

[8] Note that in [62], the authors consider the effective refractive index n_{e} instead of the group refractive index n_{eg}. A discussion of this difference can be found in [57].

waveguide needs to feature a nonlinear susceptibility $\chi^{(3)}$ of third order[9]. In general, the susceptibility describes the relation of the vectorial polarization $\mathbf{P}$ in a material induced by a vectorial electric field $\mathbf{E}$ [65]. In appropriate materials, the susceptibility can be approximated as a scalar [66]. Furthermore, if the electric field $E(t)$ and the polarization can be approximated by scalars as well, the total polarization $P_\mathrm{t}(t)$ can be written as the following Volterra series[10]:

$$\begin{aligned} P_\mathrm{t}(t) =& \epsilon_0 \int_{-\infty}^{\infty} \chi_\mathrm{h}^{(1)}(t_1) E(t-t_1)\mathrm{d}t_1 \\ &+ \epsilon_0 \iint_{-\infty}^{\infty} \chi_\mathrm{h}^{(2)}(t_1,t_2) E(t-t_1)E(t-t_2)\mathrm{d}t_1\mathrm{d}t_2 \\ &+ \epsilon_0 \iiint_{-\infty}^{\infty} \chi_\mathrm{h}^{(3)}(t_1,t_2,t_3) E(t-t_1)E(t-t_2)E(t-t_3)\mathrm{d}t_1\mathrm{d}t_2\mathrm{d}t_3 + \ldots . \end{aligned} \tag{2.22}$$

Here, ϵ_0 is the vacuum permittivity and $\chi_\mathrm{h}^{(n)}$ is the nth-order impulse response function, i.e., the inverse Fourier transform of the nth-order susceptibility $\chi^{(n)}$. Further assuming that the impulse responses only depend on the current time, i.e., assuming $\chi_\mathrm{h}^{(1)}(t) = \chi^{(1)}\delta(t), \chi_\mathrm{h}^{(2)}(t,t') = \chi^{(2)}\delta(t)\delta(t'), \ldots$, the expression for the polarization can be simplified to

$$P_\mathrm{t}(t) = \underbrace{\epsilon_0\chi^{(1)}E(t)}_{=P_\mathrm{lin}(t)} + \underbrace{\epsilon_0\chi^{(2)}E^2(t) + \epsilon_0\chi^{(3)}E^3(t) + \ldots .}_{=P_\mathrm{nl}(t)} \tag{2.23}$$

In the following, only the third-order nonlinear susceptibility is assumed to contribute to the nonlinear polarization, i.e., $P_\mathrm{nl}(t) = \epsilon_0\chi^{(3)}E^3(t)$. In Kerr-nonlinear microresonators, self-phase modulation (SPM) is an important nonlinear process that allows to further investigate the nonlinear behaviour when only light of a single frequency ω_0 is present[11]. In this case, the non-

[9] Frequency comb formation in microresonators with a $\chi^{(2)}$ nonlinearity is also possible [63,64], but not discussed in this work.

[10] In Equation (2.22), the impulse response functions $\chi_\mathrm{h}^{(n)}$ are assumed be real-valued (i.e., a loss-less medium is assumed) and temporally constant. Potential spatial dependencies are not considered. For details, see, e.g., [67].

[11] Four-wave-mixing also plays an important role, and is considered in the coupled-mode equations, see Eq. (2.32).

linear polarization $P_{\mathrm{SPM}}(\omega_0, t) = \left(\underline{P}_{\mathrm{SPM}}(\omega_0)\exp(\,\mathrm{j}\omega_0 t) + c.c.\right)/2$ associated with SPM oscillates at the same frequency as the incoming electric field $E(\omega_0, t) = \left(\underline{E}(\omega_0)\exp(\,\mathrm{j}\omega_0 t) + c.c.\right)/2$. Only a subset of the terms occurring in the product $E^3(\omega_0, t)$ in Eq. (2.23) contributes to the nonlinear polarization, which reads in the frequency domain

$$\underline{P}_{\mathrm{SPM}}(\omega_0) = \epsilon_0 \chi^{(3)} \frac{3}{4} \left|\underline{E}(\omega_0)\right|^2 \underline{E}(\omega_0), \tag{2.24}$$

where $\chi^{(3)} = \chi^{(3)}\,(\omega_0 : \omega_0, -\omega_0, \omega_0)$ is the nonlinear susceptibility for SPM. The nonlinear polarization leads to a change of the total refractive index n_{tot} of the Kerr-nonlinear, non-magnetic medium depending on the field intensity, which, for the monochromatic electric field described above, is given by

$$I = n_0 \frac{\left|\underline{E}\,(\omega_0)\right|^2}{2Z_0}. \tag{2.25}$$

Here $n_0 = (1 + \chi^{(1)})^{1/2}$ is the linear refractive index of the non-magnetic medium [65] and Z_0 the impedance of free space. To find an expression for n_{tot}, the relative permittivity $\epsilon_{\mathrm{r}} = n_{\mathrm{tot}}^2$ is considered [65],

$$\epsilon_{\mathrm{r}} = n_{\mathrm{tot}}^2 = 1 + \chi^{(1)} + \chi^{(3)} \frac{3}{4} \left|\underline{E}(\omega_0)\right|^2 = n_0^2 + \chi^{(3)} \frac{3Z_0}{2n_0} I. \tag{2.26}$$

Further assuming that the nonlinear contribution to n_{tot} is small compared to the linear part, i.e., $n_0^2 \gg \epsilon_0 \chi^{(3)} \frac{3Z_0}{2n_0} I$, the total refractive index can be approximated as

$$\begin{aligned} n_{\mathrm{tot}} &= \sqrt{n_0^2 + \chi^{(3)} \frac{3Z_0}{2n_0} I} = n_0 \sqrt{1 + \chi^{(3)} \frac{3Z_0}{2n_0^3} I} \\ &\approx n_0 \left(1 + \chi^{(3)} \frac{3Z_0}{4n_0^3} I\right) = n_0 + n_2 I, \quad n_2 = \frac{3Z_0}{4n_0^2} \chi^{(3)}, \end{aligned} \tag{2.27}$$

where the nonlinear refractive index n_2 with unit $[n_2] = \mathrm{m}^2/\mathrm{V}$ was introduced. This material-specific quantity can be used to describe the Kerr nonlinearity in lossless media, where the third-order nonlinear susceptibility $\chi^{(3)}$ can be approximated as a scalar. Note that in other descriptions of the phase shift $n_2 I$

induced by the Kerr effect, the nonlinear refractive index may be defined with respect to the modulus squared of the electric field instead of the intensity. In this case, the nonlinear refractive index $\tilde{n}_2 = 3/(8n_0)\chi^{(3)}$ [65], related to n_2 via $n_2 I = \tilde{n}_2 \left|\underline{\hat{E}}(\omega_0)\right|^2$, has the unit $[\tilde{n}_2] = \mathrm{m}^2/\mathrm{V}^2$.

When describing the propagation of optical signals in nonlinear optical waveguides, it is common practice to describe the optical signal by complex electric field amplitudes $\underline{\mathcal{E}}$ normalized to the power of the field, i.e., with unit $\sqrt{\mathrm{W}}$. In this context, the effective mode field area A_{eff} is another important metric that describes how much of a certain field distribution of an optical field, represented by its electric field $\underline{\mathbf{E}}$ and magnetic field $\underline{\mathbf{H}}$, with carrier frequency ω_0 is located in a nonlinear waveguide. For a waveguide-orientation along the z-direction, i.e., with a waveguide cross-section located in the x-y-plane, the effective mode-field area reads [66]

$$A_{\mathrm{eff}} = Z_0^2 \frac{\left| \int\int_{\mathrm{Total}} \Re\left\{ \underline{\mathbf{E}}(x,y) \times \underline{\mathbf{H}}^*(x,y) \right\} \cdot \mathbf{e}_z \mathrm{d}x\mathrm{d}y \right|^2}{\int\int_{\mathrm{NL}} n_0^2 \left| \underline{\mathbf{E}}(x,y) \right|^4 \mathrm{d}x\mathrm{d}y}. \tag{2.28}$$

Here, $\mathbf{e}_z$ is the unit vector in the direction along the waveguide, i.e., only the third component of the product $\underline{\mathbf{E}} \times \underline{\mathbf{H}}^*$ is considered in the integrand of the upper integral. The integration of the upper integral has to be performed over the full x-y plane, such that the whole field distribution is considered. The denominator integral is performed only over the region, where the nonlinear (NL) material with refractive index n_0 is located. Given this expression for the effective mode field area A_{eff}, the Kerr-nonlinear response of a waveguide can be determined by computing the nonlinearity parameter γ, which reads

$$\gamma = \frac{\omega_0 n_2}{c_0 A_{\mathrm{eff}}} = \frac{3\omega_0 Z_0}{4 c_0 n_0^2 A_{\mathrm{eff}}} \chi^{(3)}. \tag{2.29}$$

An example of the determination of this nonlinearity parameter, where the effective mode field area is computed, can be found in Appendix C, Section C.4.

In this framework, the nonlinear phase shift for field amplitudes $\underline{\mathcal{E}}$ due to SPM amounts to $\gamma|\underline{\mathcal{E}}|^2$. Such nonlinear processes induced by a Kerr nonlinearity are commonly described by the nonlinear Schrödinger equation (NLSE) [65]. More precisely, the NLSE describes the evolution of the slowly varying amplitude $\underline{\mathcal{E}}_z(z,\tau)$ of an optical signal as a function of propagation distance z in a Kerr-

nonlinear medium and as a function of a retarded time frame τ. The index z of the electric field emphasizes its dependence on the spatial coordinate z. The retarded time frame τ propagates with the group velocity of the optical signal and is given as $\tau = t - \beta^{(1)} z = t - z/v_\mathrm{g}$. The NLSE reads[12]

$$\frac{\partial \underline{\mathcal{E}}_z(z,\tau)}{\partial z} = \mathrm{j}\frac{\beta^{(2)}(\omega)}{2}\frac{\partial^2 \underline{\mathcal{E}}_z(z,\tau)}{\partial \tau^2} - \mathrm{j}\gamma \left|\underline{\mathcal{E}}_z(z,\tau)\right|^2 \underline{\mathcal{E}}_z(z,\tau). \tag{2.30}$$

Note that Eq. (2.30) is valid for a *positive* time dependence $\exp(\mathrm{j}\omega t)$ of the electric field amplitude. To obtain the NLSE for an electric field with *negative* time dependence $\exp(-\mathrm{j}\omega t)$, Eq. (2.30) needs to be complex-conjugated. Such a version of the NLSE can be found, e.g., in [65]. Statements before equations or at the beginning of chapters clarify, whether they are formulated for a positive or negative time dependence of the electric field. Unless specified otherwise, this text uses a positive time dependence.

2.2.2 Theoretical description of Kerr frequency combs

Kerr-nonlinear microresonators rely on the parametric conversion of monochromatic light. In Figure 2.3(a), a basic scheme of a planar-waveguide microresonator with an optical pump laser is depicted. Continuous-wave (CW) light from a tunable laser source (TLS) is sent to a photonic chip, which comprises a Kerr-nonlinear microresonator[13]. The frequency $\omega = \omega_0$ of the light from the TLS is adjusted such that light is coupled into a microresonator resonance with center frequency $\omega_{\mathrm{r},0}$. Inside the microresonator, degenerate four-wave mixing (FWM) converts two photons of the pump light with frequency ω_0 into two

[12] A derivation of the NLSE from Maxwell's equations with a full description of the underlying assumptions is beyond the scope of this work and can be found, e. g., in [65, 68]. In short, the NLSE is valid in non-magnetic materials, where currents and charges are absent and where only electric susceptibilities of first ($\chi^{(1)}$) and third order ($\chi^{(3)}$) are present. These susceptibilities are assumed to be scalars, instantaneous and local in space. The nonlinear polarization P_nl arising from $\chi^{(3)}$ is assumed to be much weaker than the the linear polarization P_lin induced through $\chi^{(1)}$. Further the materials are assumed to be homogeneous, time-invariant and isotropic. The optical field described by the NLSE is assumed to be linearly polarized, and the field amplitude is assumed to vary much slower than the optical carrier. For more precise mathematical definitions of these assumptions, see, e. g., [65, 68].

[13] Other schemes without an external laser source exist [69, 70], but are not discussed in this work.

new photons at frequencies $\omega_{+|\mu|}$ and $\omega_{-|\mu|}$ [11], which are defined according to Eq. (2.3). This process is illustrated on the left-hand side of Fig. 2.3(b). Only frequencies ω_μ that are spectrally located within the resonances of the microresonator around frequencies $\omega_{\mathrm{r},\mu}$ can be generated. It should be noted though that the FSR ω_{FSR} of the frequency comb is not strictly bound to the FSR of the (cold) microresonator. For example, changes of the pump parameters can lead to minor changes of the comb FSR[14]. Still, this work only assumes the case $\omega_{\mathrm{FSR}} \approx \omega_{\mathrm{r,FSR}}(\omega_0)$ in the explanations of this chapter for simplicity. In a second step after the initial side-band formation, non-degenerate FWM will convert two photons with frequencies $\omega_{\mu'}$ and $\omega_{\mu''}$ into two different photons with frequencies $\omega_{\mu'''}$ and $\omega_{\mu'+\mu''-\mu'''}$ [11], as shown on the right-hand side of Fig. 2.3(b). In both FWM processes, the conservation of the total photon energy must be fulfilled, i.e., $\hbar\omega_{\mu'} + \hbar\omega_{\mu''} = \hbar\omega_{\mu'''} + \hbar\omega_{\mu'+\mu''-\mu'''}$, where $\hbar$ is the reduced Planck constant. According to the definition of the frequency comb frequencies, Eq. (2.3), this is true. The newly generated frequencies have an equidistant spacing, namely the FSR of the frequency comb. Furthermore, the conservation of momentum is another perquisite. The photon momenta are given as $\hbar\beta\left(\omega_{\mu'}\right), \hbar\beta\left(\omega_{\mu''}\right), \hbar\beta\left(\omega_{\mu'''}\right)$ and $\hbar\beta\left(\omega_{\mu'+\mu''-\mu'''}\right)$, respectively. Using the resonance condition of the microresonator, see Eq. (2.15), and assuming $\beta\left(\omega_{\mathrm{r},\mu}\right) \approx \beta\left(\omega_\mu\right) \forall\, \mu$, the conservation of momentum can be shown:

$$\begin{aligned} &\hbar\beta\left(\omega_{\mu'}\right) + \hbar\beta\left(\omega_{\mu''}\right) - \hbar\beta\left(\omega_{\mu'''}\right) - \hbar\beta\left(\omega_{\mu'+\mu''-\mu'''}\right) \\ &= \hbar\frac{2\pi}{L_{\mathrm{MR}}}\left(\mu' + \mu'' - \mu''' - (\mu' + \mu'' - \mu''')\right) = 0. \end{aligned} \tag{2.31}$$

The equidistant spacing of the frequency comb lines ω_μ and the dispersion-induced non-equidistant spacing of the microresonator frequencies[15] $\omega_{\mathrm{r},\mu}$ lead to an increasing mismatch between ω_μ and $\omega_{\mathrm{r},\mu}$ at the outer edges of the frequency comb, see Fig. 2.3(c). Here, the upper part depicts an optical transmission profile of a microresonator that can be obtained, e. g., by sweeping

[14] It should also be noted that it is possible to truly dictate the comb FSR by modulating the incoming pump with a modulation frequency that equals ω_{FSR}. However, this value still needs to be close to the FSR $\omega_{\mathrm{r,FSR}}$ of the microresonator, see, e.g., [71, 72].

[15] From here on, the comb line index μ and the resonance index ν are set equal, $\mu = \nu$, i.e., the pumped mode ω_0 of the frequency comb is located within the resonance at $\omega_{\mathrm{r},0}$ and every resonance $\omega_{\mathrm{r},\mu}$ contains a line of the frequency comb ω_μ. The latter is a simplifying assumption – in practice, the comb lines may be spaced by a multiple of the microresonator FSR, i.e., not each resonance of the microresonator may contain a Kerr frequency comb line.

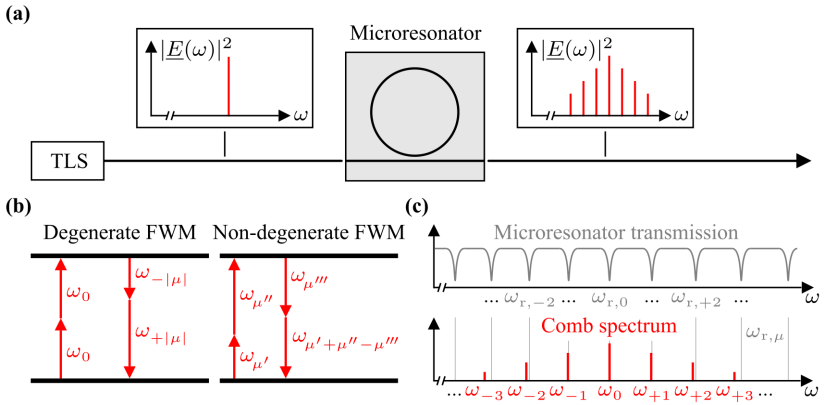

Figure 2.3: Kerr comb generation in a microresonator. (a) Schematic of the system. A tunable laser source (TLS) emits CW light with angular frequency ω_0 that is coupled into a Kerr-nonlinear microresonator. Inside the resonator, a frequency comb forms, which is partially coupled out again. (b) Underlying physical processes. Degenerate and non-degenerate four-wave mixing (FWM) causes the generation of new frequencies. (c) Bandwidth-limitation of the frequency comb. Resonance frequencies $\omega_{\mathrm{r},\nu}$ dictate the spectral positions of microresonator resonances, as indicated by the microresonator transmission profile (top, gray). In this example, anomalous dispersion causes an increase of the FSR $\omega_{\mathrm{r,FSR}}$ with increasing resonance index ν, see Eq. (2.20). The frequency comb (bottom, red) forms around the pumped mode ω_0. Four-wave mixing ensures that all comb lines have an equidistant spacing ω_{FSR} that is very similar to the microresonator FSR at the pumped resonance, $\omega_{\mathrm{FSR}} \approx \omega_{\mathrm{r,FSR}}$. As a result, a mismatch between the comb lines and the dispersion-dependent resonance frequencies of the microresonator arises that increases for comb lines further away from the pumped mode. This limits the bandwidth of the frequency comb generated in the microresonator. In the depicted scheme in (c), this mismatch is exaggerated.

the frequency of the light emitted by the TLS and recording the optical output power after the microresonator as a function of the TLS frequency[16]. Notches in the transmitted power indicate microresonator resonances. In the example depicted in Fig. 2.3(c), the microresonator exhibits anomalous GVD and therefore the FSR between the resonances increases with ω, see Eq.(2.20). The lower part of Fig. 2.3(c) shows the resonance frequencies $\omega_{\mathrm{r},\mu}$ as thin vertical gray lines as well as the spectral position of a frequency comb (red) generated in the microresonator. The increasing mismatch between the resonance

[16] The optical output power of the TLS has to be chosen weak enough such that nonlinear optical effects are not initiated.

frequencies and the frequency comb lines far off the pumped resonance leads to decreasing comb line amplitudes and a finite comb bandwidth. With this qualitative description in mind, two quantitative models for the description of Kerr frequency combs introduced in the following sections.

Coupled-mode equations

The formation of Kerr combs can be described by a set of coupled equations covering the evolution of optical modes with slowly varying amplitudes $\underline{\mathcal{E}}_{\mathrm{r},\mu}$ [73, 74]. Each mode corresponds to a continuous-wave electric field that circulates in a microresonator[17]. The frequencies of these fields are the resonance frequencies of the microresonator, defined in Eq. (2.21). Various effects alter the amplitudes $\underline{\mathcal{E}}_{\mathrm{r},\mu}$ over time t, such that $\underline{\mathcal{E}}_{\mathrm{r},\mu} = \underline{\mathcal{E}}_{\mathrm{r},\mu}(t)$. Over one round-trip in the microresonator, the modes experience an (amplitude) loss caused by the microresonator waveguide as well as by the coupling to the bus waveguide, and they experience a parametric gain through the Kerr nonlinearity. The resonator mode $\omega_{\mathrm{r},0}$ is pumped by an external laser source with pump frequency $\omega_\mathrm{p} = \omega_0$, which corresponds to the center line of the frequency comb. The coupled system of equations for the resonator modes $\underline{\mathcal{E}}_{\mathrm{r},\mu}(t)$ of the "cold" microresonator reads [74][18]:

$$\begin{aligned} t_\mathrm{R}\frac{\partial \underline{\mathcal{E}}_{\mathrm{r},\mu}(t)}{\partial t} = &-\frac{\alpha_i L_\mathrm{MR} + \theta_\mathrm{C}}{2}\underline{\mathcal{E}}_{\mathrm{r},\mu} + \delta_{\mu 0}\sqrt{\theta_\mathrm{C} P_\mathrm{in}}\mathrm{e}^{\mathrm{j}(\omega_\mathrm{p}-\omega_{\mathrm{r},0})t} \\ &- \mathrm{j}\gamma L_\mathrm{MR}\sum_{\mu',\mu''}\underline{\mathcal{E}}_{\mathrm{r},\mu'}\underline{\mathcal{E}}_{\mathrm{r},\mu''}\underline{\mathcal{E}}^*_{\mathrm{r},\mu'+\mu''-\mu} \\ &\times \mathrm{e}^{\mathrm{j}(\omega_{\mathrm{r},\mu'}+\omega_{\mathrm{r},\mu''}-\omega_{\mathrm{r},\mu'+\mu''-\mu}-\omega_{\mathrm{r},\mu})t}. \end{aligned} \tag{2.32}$$

[17] While the individual modes are constant along the microresonator circumference, the superposition of these modes, introduced in Eq. (2.37) will show spatial variations.

[18] In [74], field amplitudes are measured in units of photon numbers instead of $\sqrt{\mathrm{W}}$, and the underlying electric fields are considered with a negative time dependence $\exp(-\mathrm{j}\omega t)$. The Eqs. (2.32), described in the supplementary information of [74], have been adapted to be consistent with the notation used in this work. For this purpose the resonator mode amplitudes A_μ in [74] are rescaled and complex conjugated according to $A_\mu\sqrt{\hbar\omega_\mu} \rightarrow \sqrt{t_\mathrm{R}}\underline{\mathcal{E}}^*_{\mathrm{r},\mu}$. Accordingly, the phase shift induced by the Kerr nonlinearity changes its sign. Further, the internal decay rate κ_0 in [74] accounting for waveguide losses in the microresonator is replaced by $\alpha_i L_\mathrm{MR}/t_\mathrm{R}$ and the coupling rate κ_ext accounting for coupling to the bus waveguide is replaced by $\theta_\mathrm{C}/t_\mathrm{R}$.

In these equations, the first term on the r.h.s. $-(\alpha_i L_{\mathrm{MR}} + \theta_{\mathrm{C}})/2$ describes the aforementioned losses in the limit of small $\alpha_i L_{\mathrm{MR}} \ll 1$ and small $\theta_{\mathrm{C}} \ll 1$, see also the paragraph following Eq. (2.8) in Section 2.2.1. The second term on the r.h.s. describes the pump field coupled into the microresonator (input field power P_{in}). Here, $\delta_{\mu 0}$ is the Kronecker delta. The third term represents the Kerr nonlinearity, which causes a coupling of the equations. The time dependence of $\underline{\mathcal{E}}_{\mathrm{r},\mu}(t)$ on the r.h.s. of Eq. (2.32) has been omitted for improved readability. Since not the electric field amplitudes at the resonance frequencies $\omega_{\mathrm{r},\mu}$ are of interest, but the amplitudes at the spectral positions $\omega_\mu = \omega_{\mathrm{p}} + \mu\,\omega_{\mathrm{FSR}}$ of the frequency comb, a phase transformation is applied, that links the frequency comb amplitudes $\underline{\mathcal{E}}_{\mu}(t)$ with the resonator mode amplitudes $\underline{\mathcal{E}}_{\mathrm{r},\mu}(t)$:

$$\begin{aligned} \underline{\mathcal{E}}_{\mu}\,(t)\,\mathrm{e}^{\mathrm{j}\left(\omega_{\mathrm{p}}+\mu\,\omega_{\mathrm{FSR}}\right)t} &= \underline{\mathcal{E}}_{\mathrm{r},\mu}\,(t)\,\mathrm{e}^{\mathrm{j}\omega_{\mathrm{r},\mu}t}, \\ \underline{\mathcal{E}}_{\mu}\,(t) &= \underline{\mathcal{E}}_{\mathrm{r},\mu}\,(t)\,\mathrm{e}^{\mathrm{j}\left(\omega_{\mathrm{r},\mu}-\omega_{\mathrm{p}}-\mu\,\omega_{\mathrm{FSR}}\right)t}. \end{aligned} \tag{2.33}$$

Here, the spectral separation of the frequency comb modes $\underline{\mathcal{E}}_{\mu}(t)$, i.e., the FSR ω_{FSR} of the comb is assumed to be the FSR $\omega_{\mathrm{r,FSR}}$ of the microresonator at the pumped mode. The phase transformation allows to describe the dynamics of the field amplitudes of the frequency comb using the coupled mode equations, which are defined for fields at the resonance frequencies of the microresonator. Applying the transformation described in Eq. (2.33) to the field amplitudes $\underline{\mathcal{E}}_{\mathrm{r},\mu}\,(t)$ in Eq. (2.32) and multiplying the result with the expression $\mathrm{e}^{\mathrm{j}\left(\omega_{\mathrm{r},\mu}-\omega_{\mathrm{p}}-\mu\,\omega_{\mathrm{FSR}}\right)t}$ yields

$$\begin{aligned} t_{\mathrm{R}}\frac{\partial\underline{\mathcal{E}}_{\mu}\,(t)}{\partial t} = &-\frac{\alpha_i L_{\mathrm{MR}}+\theta_{\mathrm{C}}}{2}\underline{\mathcal{E}}_{\mu} + \mathrm{j}\left(\omega_{\mathrm{r},\mu}-\omega_{\mathrm{p}}-\mu\,\omega_{\mathrm{FSR}}\right)t_{\mathrm{R}}\underline{\mathcal{E}}_{\mu} \\ &+\delta_{\mu 0}\sqrt{\theta_{\mathrm{C}}P_{\mathrm{in}}} - \mathrm{j}\gamma L_{\mathrm{MR}}\sum_{\mu',\mu''}\underline{\mathcal{E}}_{\mu'}\underline{\mathcal{E}}_{\mu''}\underline{\mathcal{E}}^{*}_{\mu'+\mu''-\mu}. \end{aligned} \tag{2.34}$$

Note that these steps eliminate the explicit time dependence of the nonlinear terms. The Eqs. (2.34) can be further simplified by using the definition of

the resonance frequencies $\omega_{\mathrm{r},\mu}$, see Eq. (2.21). Additionally introducing the detuning $\delta_0 = \left(\omega_{\mathrm{r},0} - \omega_{\mathrm{p}}\right) t_{\mathrm{R}}$, the coupled-mode equations (CME) read

$$t_{\mathrm{R}} \frac{\partial \underline{\mathcal{E}}_\mu(t)}{\partial t} = -\left(\frac{\alpha_i L_{\mathrm{MR}} + \theta_{\mathrm{C}}}{2} - \mathrm{j}\delta_0\right) \underline{\mathcal{E}}_\mu - \mathrm{j}\frac{\beta^{(2)} L_{\mathrm{MR}}}{2} \left(\mu\, \omega_{\mathrm{FSR}}\right)^2 \underline{\mathcal{E}}_\mu + \delta_{\mu 0} \sqrt{\theta_{\mathrm{C}} P_{\mathrm{in}}} - \mathrm{j}\gamma L_{\mathrm{MR}} \sum_{\mu',\mu''} \underline{\mathcal{E}}_{\mu'} \underline{\mathcal{E}}_{\mu''} \underline{\mathcal{E}}^*_{\mu'+\mu''-\mu}. \tag{2.35}$$

Note that Eq (2.35) relies on a *positive* time dependence of the form $\exp(\mathrm{j}\omega t)$, which is commonly used in engineering. In contrast to this, most of the literature on the description of Kerr frequency combs uses a negative time dependence of the form $\exp(-\mathrm{j}\omega t)$. The corresponding coupled-mode equations for an optical signal with *negative* time dependence can be obtained by taking the complex conjugate of Eqs. (2.35):

$$t_{\mathrm{R}} \frac{\partial \underline{\mathcal{E}}^*_\mu(t)}{\partial t} = -\left(\frac{\alpha_i L_{\mathrm{MR}} + \theta_{\mathrm{C}}}{2} + \mathrm{j}\delta_0\right) \underline{\mathcal{E}}^*_\mu + \mathrm{j}\frac{\beta^{(2)} L_{\mathrm{MR}}}{2} \left(\mu\, \omega_{\mathrm{FSR}}\right)^2 \underline{\mathcal{E}}^*_\mu + \delta_{\mu 0} \sqrt{\theta_{\mathrm{C}} P_{\mathrm{in}}} + \mathrm{j}\gamma L_{\mathrm{MR}} \sum_{\mu',\mu''} \underline{\mathcal{E}}^*_{\mu'} \underline{\mathcal{E}}^*_{\mu''} \underline{\mathcal{E}}_{\mu'+\mu''-\mu}. \tag{2.36}$$

Both versions of the CME allow to compute the evolution of the modes of a frequency comb in a Kerr-nonlinear microresonator. However, the cubic nonlinearity becomes computational expensive for an increasing number of modes. For N sidebands and the pumped mode, the number of nonlinear elements in $N + 1$ equations amounts to $\approx N^3/3$ for large $N \approx 10^3$, see second page of the supplementary information in [21]. This results in increasing computational effort when increasing the number of considered modes [21,73], unless dedicated algorithms for the time integration of these equations are used [75].

Instead of considering the CME, it may be more convenient to consider the evolution of the superposition of the modes $\underline{\mathcal{E}}_\mu(t)$. Due to interference, the amplitude of this superposition will show spatial variations along the microresonator circumference, which are described using a spatial intracavity coordinate τ. In literature, this coordinate is also referred to as *fast time*, even though it is used as a spatial coordinate. Furthermore, the superposition will share the dependence on the physical time t with the individual modes, which is also known as *slow time* in this context. The differentiation of a *fast* and a *slow*

time refers to the fact that changes of the optical field along the fast-time axis, i.e., along the microresonator circumference, for at a given point in physical time, happen much more rapidly compared to changes of the overall optical field over multiple round-trips in the microresonator, i.e., along slow time[19]. For a *positive* (slow-)time dependence of the electrical fields, the intracavity field envelope $\underline{\mathcal{E}}(t,\tau)$, i.e., the superposition of the individual modes $\underline{\mathcal{E}}_\mu(t)$ described by Eq. (2.35), is given as [76][20]:

$$\underline{\mathcal{E}}(t,\tau) = \sum_\mu \underline{\mathcal{E}}_\mu(t)\,\mathrm{e}^{-\mathrm{j}2\pi\mu\tau/t_\mathrm{R}}. \tag{2.37}$$

When a *negative* (slow-)time dependence of the electric field is assumed, the field envelope $\underline{\mathcal{E}}^*(t,\tau)$ of the modes $\underline{\mathcal{E}}^*_\mu(t)$ as described by Eqs. (2.36) instead reads [77][21]

$$\underline{\mathcal{E}}^*(t,\tau) = \sum_\mu \underline{\mathcal{E}}^*_\mu(t)\,\mathrm{e}^{+\mathrm{j}2\pi\mu\tau/t_\mathrm{R}}. \tag{2.38}$$

In the next section, an equation equivalent to the coupled Eqs. (2.35) and (2.36) is presented that describes the evolution of $\underline{\mathcal{E}}(t,\tau)$.

Lugiato-Lefever equation

The Lugiato-Lefever equation (LLE) is a driven, damped nonlinear Schrödinger equation (NLSE) commonly used to describe the dynamics of an electric field circulating in a Kerr-nonlinear microresonator [77]. It was first introduced by L. Lugiato and R. Lefever to describe a passive nonlinear cavity driven

[19] For examples of simulated evolutions of an optical field in a microresonator, see Chapter 4, Section 4.5. Here, the total range of the fast time, i.e., the microresonator round-trip time, is set to 10 ps, whereas the slow time spans $72\,184 \times 626\,\mathrm{fs} \approx 45.2\,\mathrm{ns}$ to capture the dynamics of the optical field.

[20] See Eq. (4) in [76]. Note however that the formalism and definitions used by the authors [76] differ from the formalism in this work, and therefore this reference is only mentioned to highlight the sign of the dependence of $\underline{\mathcal{E}}(t,\tau)$ on the intracavity coordinate. In [76], the optical field envelope is denoted as $\mathcal{A}(\theta,t)$, where θ is the intracavity coordinate t the physical time. Compared to the theoretical description given in this work, θ corresponds to $2\pi\tau/t_\mathrm{R}$.

[21] See Chapter 3 and 4 in [77], in particular Equations (5) and (6), and the text before Eq. (6).

by a coherent stationary field [78]. While the authors do not give a direct derivation of their equation in [78], it can be obtained through several different approaches. One is to compute the slow-time temporal derivative $\partial \underline{\mathcal{E}}(t,\tau)/\partial t$ of Eq. (2.37) or (2.38) and then insert the evolution of the individual modes, Eqs. (2.35) or Eqs. (2.36) [76]. In another ansatz, the LLE can be derived from a more general framework known as Ikeda map [77].

In the present work, two aspects are considered to derive the LLE. First, the propagation of the slowly varying envelope $\underline{\mathcal{E}}_z(z,\tau)$ of an optical field in a straight Kerr-nonlinear waveguide with spatial coordinate z is considered via the NLSE [65]. The NLSE for an electric field with positive time dependence, see Eq. (2.30), including losses caused by the propagation in the waveguide reads

$$\frac{\partial}{\partial z}\underline{\mathcal{E}}_z(z,\tau) = -\frac{\alpha_i}{2}\underline{\mathcal{E}}_z(z,\tau) + \mathrm{j}\frac{\beta^{(2)}}{2}\frac{\partial^2}{\partial\tau^2}\underline{\mathcal{E}}_z(z,\tau) - \mathrm{j}\gamma\left|\underline{\mathcal{E}}_z(z,\tau)\right|^2\underline{\mathcal{E}}_z(z,\tau). \tag{2.39}$$

The second coordinate $\tau = t - z/v_\mathrm{g}$ of the field envelope $\underline{\mathcal{E}}_z(z,\tau)$ is a retarded time frame that describes the (fast) changes of the field envelope. For a given time t, it can also be considered as a re-scaled spatial coordinate of the localized electric field $\underline{\mathcal{E}}_z(z,\tau)$. In the context of Kerr microresonators, this means that τ is used to describe the variations of the field along the microresonator circumference, with values of τ being in the range $[0, t_\mathrm{R})$. The coordinate z generally describes the waveguide-position of the field envelope $\underline{\mathcal{E}}_z(z,\tau)$ moving with group velocity v_g. Therefore, this coordinate is directly linked to the natural time t via $z = v_\mathrm{g}t$. In the following, the z-dependence of the electric field $\underline{\mathcal{E}}_z(z,\tau)$ is replaced by a dependence on the natural time t by setting $\underline{\mathcal{E}}_z(z,\tau) = \underline{\mathcal{E}}(t,\tau)$. For this purpose, Eq. (2.39) is multiplied by $v_\mathrm{g}\,t_\mathrm{R} = L_\mathrm{MR}$ and z is replaced by $z = v_\mathrm{g}\,t$, which results in

$$t_\mathrm{R}\frac{\partial}{\partial t}\underline{\mathcal{E}}(t,\tau) = -\frac{\alpha_i L_\mathrm{MR}}{2}\underline{\mathcal{E}}(t,\tau) + \mathrm{j}\frac{\beta^{(2)}L_\mathrm{MR}}{2}\frac{\partial^2}{\partial\tau^2}\underline{\mathcal{E}}(t,\tau) - \mathrm{j}\gamma L_\mathrm{MR}\left|\underline{\mathcal{E}}(t,\tau)\right|^2\underline{\mathcal{E}}(t,\tau). \tag{2.40}$$

The switched roles of the spatial and the temporal coordinate can also be derived from the NLSE in the non-retarded time-frame[22]. The NLSE as represented in Eq. (2.40) considers linear losses, dispersive and nonlinear effects affecting the optical field during its propagation in the nonlinear medium, i.e., during its propagation along the microresonator with circumference L_{MR}.

The other aspect to consider in the derivation of the LLE is the boundary condition of the field envelope $\underline{\mathcal{E}}(t,\tau)$ at the coupling section. Here, a fraction $\sqrt{\theta_{\mathrm{C}}\,P_{\mathrm{in}}}$ of the pump light is coupled in the microresonator. Further, the field in the resonator is damped by a factor of $\sqrt{1-\theta_{\mathrm{C}}}$ in each round-trip, where $\theta_{\mathrm{C}} \ll 1$, and experiences a phase shift given by the detuning $\delta_0 = \left(\omega_{\mathrm{r},0} - \omega_{\mathrm{p}}\right) t_{\mathrm{R}}$, where $|\delta_0| \ll 1$. Thus, the field $\underline{\mathcal{E}}(t+t_{\mathrm{R}},\tau)$ after one round-trip in the microresonator is related to the previous field $\underline{\mathcal{E}}(t,\tau)$ by

$$\begin{aligned}\underline{\mathcal{E}}(t+t_{\mathrm{R}},\tau) =& \sqrt{\theta_{\mathrm{C}}\,P_{\mathrm{in}}} + \sqrt{1-\theta_{\mathrm{C}}}\,\mathrm{e}^{\mathrm{j}\delta_0}\underline{\mathcal{E}}(t,\tau)\\ \approx& \sqrt{\theta_{\mathrm{C}}\,P_{\mathrm{in}}} + (1-\theta_{\mathrm{C}}/2+\mathrm{j}\delta_0)\,\underline{\mathcal{E}}(t,\tau).\end{aligned} \tag{2.41}$$

Assuming the field does not change much over one round-trip, one may approximate $\underline{\mathcal{E}}(t+t_{\mathrm{R}},\tau) - \underline{\mathcal{E}}(t,\tau) = t_{\mathrm{R}}\,\partial\underline{\mathcal{E}}(t,\tau)/\partial t$ and obtain

$$t_{\mathrm{R}}\frac{\partial}{\partial t}\underline{\mathcal{E}}(t,\tau) = \sqrt{\theta_{\mathrm{C}}\,P_{\mathrm{in}}} - (\theta_{\mathrm{C}}/2-\mathrm{j}\delta_0)\,\underline{\mathcal{E}}(t,\tau). \tag{2.42}$$

In summary, Eq. (2.40) describes the temporal evolution of a field envelope in a nonlinear waveguide without the consideration of the boundary conditions of a microresonator, whereas Eq. (2.42) describes the temporal evolution of a field envelope caused by the boundary conditions in a microresonator neglecting changes due to the nonlinear waveguide. In reality, both aspects will determine the temporal evolution of the optical field envelope in parallel. Thus, the full

[22] See [68], Eq. (3.116) with $\beta_0^{(3)} = 0$ and $\beta_0^{(0)} = \beta_{\mathrm{ref}}$. Introducing a *retarded space frame*, which reads $Z = z - v_{\mathrm{g}}t$ for the notation given in [68] as well as a time variable $T = t$ in Eq. (3.116) in [68], leads to a set of terms $v_{\mathrm{g}}^2\frac{\partial^2}{\partial Z^2}A(T,Z)$, $-2v_{\mathrm{g}}\frac{\partial^2}{\partial T\,\partial Z}A(T,Z)$ and $\frac{\partial^2}{\partial T^2}A(T,Z)$. Of these terms, the first one is significantly larger than the others, therefore the second and the third term are neglected. Switching to the notation used in this dissertation via $T \to t$, $Z \to v_{\mathrm{g}}\tau$ and $A \to \underline{\mathcal{E}}$ and multiplying the result by L_{MR} yields Eq. (2.40).

description of the temporal field evolution is obtained by considering the physical effects on the r.h.s. of Eqs. (2.40) and (2.42) in a single equation:

$$t_\mathrm{R}\frac{\partial}{\partial t}\underline{\mathcal{E}}(t,\tau) = \sqrt{\theta_\mathrm{C}\,P_\mathrm{in}} - \left(\frac{\alpha_i L_\mathrm{MR} + \theta_\mathrm{C}}{2} - \mathrm{j}\delta_0\right)\underline{\mathcal{E}}(t,\tau) + \mathrm{j}\frac{\beta^{(2)} L_\mathrm{MR}}{2}\frac{\partial^2}{\partial\tau^2}\underline{\mathcal{E}}(t,\tau) - \mathrm{j}\gamma L_\mathrm{MR}\left|\underline{\mathcal{E}}(t,\tau)\right|^2\underline{\mathcal{E}}(t,\tau). \quad (2.43)$$

Equation (2.43) is valid for electric fields amplitudes with *positive* time dependence of the form $\exp(\mathrm{j}\omega t)$. The well-known Lugiato-Lefever equation (LLE) is the equivalent equation for electric fields amplitudes with *negative* time dependence of the form $\exp(-\mathrm{j}\omega t)$. The LLE can be obtained by taking the complex conjugate of all quantities in Eq. (2.43):

$$t_\mathrm{R}\frac{\partial}{\partial t}\underline{\mathcal{E}}^*(t,\tau) = \sqrt{\theta_\mathrm{C}\,P_\mathrm{in}} - \left(\frac{\alpha_i L_\mathrm{MR} + \theta_\mathrm{C}}{2} + \mathrm{j}\delta_0\right)\underline{\mathcal{E}}^*(t,\tau) - \mathrm{j}\frac{\beta^{(2)} L_\mathrm{MR}}{2}\frac{\partial^2}{\partial\tau^2}\underline{\mathcal{E}}^*(t,\tau) + \mathrm{j}\gamma L_\mathrm{MR}\left|\underline{\mathcal{E}}^*(t,\tau)\right|^2\underline{\mathcal{E}}^*(t,\tau). \quad (2.44)$$

Note that other, mathematically more rigorous procedures as, e. g., in [77] derive the same LLE. These results validate the assumptions of the simplified method, which was used to derive the LLE in this work.

Depending on the waveguide material and dimensions, it may be appropriate to include further effects in this model. Such extensions include higher-order dispersion terms, Raman-scattering, self-steepening, multi-photon absorption in conjunction with the generation of free-carriers, the interaction of different transverse mode families, and temperature effects [25, 77, 79, 80]. In Chapter 4 and Appendix C, the LLE including two-photon absorption and free-carrier absorption is analyzed in detail. In Section 4.6, the influence of the Raman effect is also briefly discussed. In absence of consideration of aforementioned effects, a normalization allows to reduce Eq. (2.44) to its relevant parameters, see Table 2.1. In this normalization, the natural time (slow time) is normalized to the photon lifetime of the microresonator. The intracavity coordinate (fast time) is normalized to the round-trip time of the optical signal in the microresonator, such that the FSR of the normalized field components is equal to 1. In these normalized units, the LLE reads

Table 2.1: Normalized quantities and substitutions.

Natural time (slow time)	t'	$=$	$t\,\frac{\alpha_i L_{\mathrm{MR}}+\theta_{\mathrm{C}}}{2t_{\mathrm{R}}}$
Intracavity coordinate (fast time)	τ'	$=$	$\tau\,\frac{2\pi}{t_{\mathrm{R}}}$
Optical field envelope	$\underline{a}\,(t',\tau')$	$=$	$\underline{\mathcal{E}}^{*}\,(t,\tau)\,\sqrt{\frac{2\gamma L_{\mathrm{MR}}}{\alpha_i L_{\mathrm{MR}}+\theta_{\mathrm{C}}}}$
Pump power (forcing)	F	$=$	$P_{\mathrm{in}}\,\frac{8\gamma L_{\mathrm{MR}}\,\theta_{\mathrm{C}}}{\left(\alpha_i L_{\mathrm{MR}}+\theta_{\mathrm{C}}\right)^3}$
Detuning	ζ	$=$	$\delta_0\,\frac{2}{\alpha_i L_{\mathrm{MR}}+\theta_{\mathrm{C}}} = \left(\omega_{\mathrm{r},0}-\omega_{\mathrm{p}}\right)\,\frac{2t_{\mathrm{R}}}{\alpha_i L_{\mathrm{MR}}+\theta_{\mathrm{C}}}$
Dispersion	β'	$=$	$-\beta^{(2)}\,\frac{4\pi^2 L_{\mathrm{MR}}}{\left(\alpha_i L_{\mathrm{MR}}+\theta_{\mathrm{C}}\right)t_{\mathrm{R}}^2}$

$$\frac{\partial\,\underline{a}\,(t',\tau')}{\partial t'} = \sqrt{F} - (1+\mathrm{j}\zeta)\,\underline{a}\,(t',\tau') + \mathrm{j}\beta'\frac{\partial^2}{\partial\tau'^2}\underline{a}\,(t',\tau') + \mathrm{j}\left|\underline{a}\,(t',\tau')\right|^2\underline{a}\,(t',\tau')\,. \tag{2.45}$$

In the same manner as for the electrical field envelope $\underline{\mathcal{E}}^{*}(t,\tau)$, the normalized field envelope in Eq. (2.45) can be written as a superposition of normalized field modes $\underline{a}_\mu(t)$, see also Eq. (2.38):

$$\underline{a}\,(t',\tau') = \sum_{\mu}\underline{a}_\mu(t')\mathrm{e}^{\mathrm{j}\mu\tau'}\,. \tag{2.46}$$

Equation (2.45) can be used to derive fundamental insights on Kerr comb generation. For example, the minimum optical pump power $P_{\mathrm{in}} = P_{\mathrm{th}}$ required for modulation instability (MI), i.e., for the first step of comb formation, is an important quantity. In the next section, this onset of comb generation is discussed using the normalized quantities defined in Table 2.1. An expression for the normalized threshold pump power $F = F_{\mathrm{th}}$ to achieve MI is derived, which is then converted back into a physical power P_{th}.

Modulation instability

In materials with suitable nonlinear and dispersive properties, parametric amplification can lead to the growth of optical signals due to the presence of a strong field. In a pumped Kerr-nonlinear microresonator, this parametric gain may lead to the growth of certain modes $\underline{a}_\mu(t')$ from quantum noise, if the power of the (normalized) pumped mode $|\underline{a}_0|^2$ is high enough and the resulting parametric gain is larger than the losses of the microresonator. This process, which is known as modulation instability (MI) [65], is associated with the degenerate four-wave mixing mentioned at the beginning of Section 2.2.2 and is the first step of frequency comb formation in microresonators. To find the conditions for MI, the field envelope is modelled as a superposition of the pumped mode $\underline{a}_0$ and two sidebands $\underline{a}_{\pm M}$, $M = 1, 2, 3\ldots$, which may grow over time t' [81]:

$$\begin{aligned}\underline{a}\,(t',\tau') =& \underline{a}_0 + \underline{a}_{+M}\,(t',\tau') + \underline{a}_{-M}\,(t',\tau') \\ =& \underline{a}_0 + \hat{\underline{a}}_{+M} \mathrm{e}^{\underline{g} t'} \mathrm{e}^{\mathrm{j}M\tau'} + \hat{\underline{a}}_{-M} \mathrm{e}^{\underline{g}^* t'} \mathrm{e}^{-\mathrm{j}M\tau'}\end{aligned} \tag{2.47}$$

The sidebands may grow exponentially over time, if the real part g of the complex gain parameter $\underline{g} = g + \mathrm{j}g_\mathrm{j}$ is positive. The imaginary part g_j describes a potential movement of the optical field along the fast time scale, for an example see, e.g., Section 4.5, Figure 4.4. The ansatz described in Eq. (2.47) can be inserted in Eq. (2.45). Neglecting terms of order 2 or more in $\hat{\underline{a}}_{\pm M}$ and sorting terms by their fast time oscillation $\mathrm{e}^{\mathrm{j}M\tau'}$, $\mathrm{e}^{\mathrm{j}0}$ or $\mathrm{e}^{-\mathrm{j}M\tau'}$ yields three equations:

$$0 = \sqrt{F} - (1 + \mathrm{j}\zeta)\,\underline{a}_0 + \mathrm{j}\left|\underline{a}_0\right|^2 \underline{a}_0, \tag{2.48}$$

$$\underline{g}\underline{a}_{+M} = \left[-(1 + \mathrm{j}\zeta) - \mathrm{j}\beta' M^2 + \mathrm{j}2\left|\underline{a}_0\right|^2\right] \underline{a}_{+M} + \underline{a}_0^2\, \underline{a}_{-M}^*, \tag{2.49}$$

$$\underline{g}^*\underline{a}_{-M} = \left[-(1 + \mathrm{j}\zeta) - \mathrm{j}\beta' M^2 + \mathrm{j}2\left|\underline{a}_0\right|^2\right] \underline{a}_{-M} + \underline{a}_0^2\, \underline{a}_{+M}^*. \tag{2.50}$$

Equation (2.48) can be used to find an implicit expression for the intracavity (IC) power $A = \left|\underline{a}_0\right|^2$ of the normalized field $\underline{a}_0$ for a given normalized pump power (forcing) F and detuning ζ:

$$F = \left(1 + (A - \zeta)^2\right) A. \tag{2.51}$$

It should be noted that it is possible to derive an explicit expression for the (real-valued, non-negative) IC power A by solving the cubic Eq. (2.51) [82], however, for the scope of this work, these extensive expressions for A are not required. In order to find an expression for the gain parameter $\underline{g}$, Eqs. (2.49) and (2.50) are considered. Taking the complex conjugate of Eq. (2.50) and combining it with Eq. (2.49) leads to an eigenvalue problem for $\underline{g}$:

$$\begin{pmatrix} -1 - \mathrm{j}\zeta - \mathrm{j}\beta' M^2 + \mathrm{j}2A & \underline{a}_0^2 \\ \left(\underline{a}_0^*\right)^2 & -1 + \mathrm{j}\zeta + \mathrm{j}\beta' M^2 - \mathrm{j}2A \end{pmatrix} \begin{pmatrix} \underline{a}_{+M} \\ \underline{a}_{-M}^* \end{pmatrix} = \underline{g} \begin{pmatrix} \underline{a}_{+M} \\ \underline{a}_{-M}^* \end{pmatrix}. \tag{2.52}$$

Solving Eq. (2.52) for the gain parameter $\underline{g}$ yields

$$\underline{g}\,(M) = -1 \pm \sqrt{A^2 - \left(\zeta + \beta' M^2 - 2A\right)^2}. \tag{2.53}$$

Sideband growth is determined by the condition, that the real part of $\underline{g}$ needs to be positive. Therefore, the solution of $\underline{g}$ with a negative sign in front of the square root is not relevant and the expression for the real part of the gain parameter reads

$$\Re\{\underline{g}\,(M)\} = g(M) = -1 + \Re\left\{\sqrt{A^2 - \left(\zeta + \beta' M^2 - 2A\right)^2}\right\}. \tag{2.54}$$

The sidebands separated by $\pm M_{\mathrm{max}}$ from the pumped mode that experience the highest gain $g(M_{\mathrm{max}})$ are determined by

$$\beta' M_{\mathrm{max}}^2 = 2A - \zeta, \tag{2.55}$$

$$g\,(M_{\mathrm{max}}) = -1 + A. \tag{2.56}$$

For the modes located at a separation of $\pm M_{\mathrm{max}}$ with respect to the pumped modes, the IC power has to reach at least $A = 1$ for a non-negative gain, see Eq. (2.56). This requires a minimum threshold forcing $F_{\mathrm{th}} = 1$ for an optimized detuning $\zeta = A$ according to Eq. (2.51). The condition $F_{\mathrm{th}} = 1$

allows to compute the physical threshold pump power by back-transforming F_{th} into a physical power P_{th}, see Table 2.1, leading to

$$P_{\mathrm{th}} = \frac{(\alpha_i L_{\mathrm{MR}} + \theta_{\mathrm{C}})^3}{8\gamma L_{\mathrm{MR}} \theta_{\mathrm{C}}}. \tag{2.57}$$

Assuming critical coupling of the microresonator, i.e., $\alpha_i L_{\mathrm{MR}} = \theta_{\mathrm{C}}$, the expression for the physical threshold pump power P_{th} simplifies to

$$P_{\mathrm{th}} = \frac{\alpha_i^2 L_{\mathrm{MR}}}{\gamma}. \tag{2.58}$$

The threshold pump power depends on the waveguide power loss α_i, the waveguide nonlinearity parameter γ, and on the circumference L_{MR} of the microresonator. If the power of an external laser source coupled to a microresonator surpasses P_{th}, MI may occur and a frequency comb forms. When designing Kerr comb generators according to the scheme depicted in Fig. 2.3(a), the available power of a (tunable) pump laser as well as a waveguide technology defining α_i and γ may be predetermined. Then, Eq. (2.58) defines an upper limit for the microresonator circumference L_{MR}, since the power of the pump laser needs to be at least equal to the threshold pump power P_{th}. Here, additional losses that may occur between the laser output and the microresonator need to be taken into account. The maximum value for the circumference will determine the minimum free spectral range of the Kerr comb. Kerr frequency combs with an FSR of less than 100 GHz at moderate pump powers were demonstrated [22, 83, 84].

Besides this estimation of the lower required pump power for modulation instability, the previous formalism also allows to derive conclusions on the necessary dispersion, if the power transfer from the pump to the pumped mode, Eq. (2.51), should be optimum, i.e., $\zeta = A$. The modes with the highest gain are then defined by $\beta' M_{\mathrm{max}}^2 = A$, see Eq. (2.55). Since M_{max} and A are both positive numbers, the dispersion parameter β' also has to be positive, which corresponds to anomalous dispersion. In principle, the real part of the gain parameter can also become positive for normal dispersion $\beta' < 0$ according to Eq. (2.54), if the detuning ζ and the forcing F are chosen properly. However in practice, this is usually not possible due to temperature effects [61], for details see Appendix A. Fabricating waveguides with anomalous dispersion $\beta' > 0$, small waveguide losses α_i and high waveguide nonlinearities γ is instrumental for

the development of Kerr comb generators and the development of fabrication processes of such waveguides has become a research topic on its own [85].

2.2.3 Dissipative Kerr solitons

In Kerr-nonlinear microresonators, different kinds of stationary frequency combs can be generated[23]. These combs differ, e. g., in their free spectral range, which may not only be equivalent to a single FSR $\omega_{\mathrm{r,FSR}}$ of the microresonator around the pumped resonance, but also to an integer multiple thereof [86]. Further, the combs can differ in their mutual comb line coherence [86], and they can differ in their comb envelopes.

A particular important class of Kerr combs are dissipative Kerr solitons (DKS) [21]. In the time domain, these combs correspond to strongly localized optical pulses circulating in the microresonator[24]. Very similar to optical solitons propagating, e. g., in an optical fiber, these pulses do not change their shape, spectral composition and time-linear phase relation between the individual modes over time due to a balance of dispersion and Kerr nonlinearity. However, the relatively high losses in a microresonator due to waveguide losses and the coupling between the resonator and the bus waveguide require a constant CW background that "refreshes" the DKS. This distinguishes DKS from regular solitons, which may propagate without the need of a CW background signal, assuming that no relevant loss mechanisms are present. A DKS comb state can be identified, e. g., by sending the frequency comb out of the microresonator to a frequency-resolved optical gating (FROG) setup [21], which allows to reconstruct the temporal shape of ultra-short optical pulses. Another indicator is the linewidth of an RF-signal that is obtained by detecting the Kerr frequency comb with a high-speed photodiode. The width of this beat note, which is spectrally located at a frequency corresponding to the FSR of the comb, may vary between tens of MHz for non-soliton Kerr combs [21,74] and significantly less than 1 MHz for soliton comb states [21].

[23] Dynamic pump parameters F and ζ can also lead to different, non-stationary frequency combs states. For more information, see Chapter 5.

[24] See also Chapter 4, Figs. 4.4(d), 4.5(d) and 4.6(d) for examples of field distributions of soliton and non-soliton comb states.

Microresonators support the existence of several DKS circulating in the microresonator at the same time [21]. These comb states are known as multi-soliton comb states. They can be distinguished and identified by the comb envelope that depends on the amount of circulating solitons and their distribution to each other along the microresonator waveguide [21]. A specific class of multi-soliton states are soliton crystals [87]. In these comb states, multiple solitons are propagating with a defined spatial separation to each other in the microresonator. The distribution of soliton pulses in soliton crystals is linked to the spectrum of the overall circulating field. The spectrum depends, amongst other parameters, on the dispersion of the microresonator. In microresonators, where the waveguide supports the propagation of multiple waveguide (transversal) eigenmodes, a coupling of different eigenmodes at certain resonance frequencies will alter the spectral position of these resonances, which locally alters the dispersion of the microresonator. This in turn affects the spectrum of the frequency comb and thereby the distribution of solitons in the microresonator [87].

For many applications, the (bright) single-soliton state is of particular interest, which features a smooth broadband spectral envelope. In this comb state, only a single pulse circulates in a microresonator with anomalous dispersion $\beta' > 0$ ($\beta^{(2)} < 0$). Experimentally, the single soliton state can be obtained by applying a constant forcing F and sweeping the detuning ζ from a blue-detuned value ($\zeta < 0$, $\omega_\mathrm{p} > \omega_{\mathrm{r},0}$) to a final red-detuned value[25] ($\zeta > 0$, $\omega_\mathrm{p} < \omega_{\mathrm{r},0}$). In the formalism of the normalized LLE, see Eq. (2.45), the single soliton comb state $\underline{a}_\mathrm{soliton}(\tau')$ with a soliton center position τ_0' can be approximated as [21]

$$\underline{a}_\mathrm{soliton}(\tau') \approx \underline{a}_0 + \sqrt{2\zeta}\mathrm{e}^{\mathrm{j}\arccos\left(\frac{\sqrt{8\zeta}}{\pi\sqrt{F}}\right)}\operatorname{sech}\left(\sqrt{\zeta/\beta'}\left(\tau' - \tau_0'\right)\right). \tag{2.59}$$

Here, the CW background $\underline{a}_0$ is determined by the detuning ζ and forcing F, see Eq. (2.48). The arccos function in the exponent on the r.h.s. of Eq. (2.59) implies an upper limit for the detuning ζ that still allows for a soliton in the Kerr-nonlinear microresonator. Specifically, the expression $\sqrt{8\zeta}/(\pi\sqrt{F})$ must not be larger than 1, which leads to a maximum value of the detuning of $\zeta_\mathrm{max} = \pi^2 F/8$ [21].

[25] For a simulated example, see Chapter 4, Section 4.5. For a description of an experimental realization, see Chapter 5 Section 5.2

The spectrum of a soliton pulse form consists of a strong peak associated with the first term on the r.h.s. of Eq. (2.59). The second term on the r.h.s of Eq. (2.59) determines the remaining part of the comb spectrum, whose smoothly decaying comb envelope can be computed by a Fourier transform[26]:

$$\begin{aligned}\left|\mathcal{F}\left\{\underline{\hat{a}}_{\text{soliton}}(\tau') - \underline{a}_0\right\}(\mu)\right|^2 &= 2\zeta\left|\mathcal{F}\left\{\operatorname{sech}\left(\sqrt{\zeta/\beta'}\,(\tau'-\tau_0')\right)\right\}\right|^2 \\ &\propto \operatorname{sech}^2\left(\frac{\pi}{2}\sqrt{\beta'/\zeta}\,\mu\right). \end{aligned} \tag{2.60}$$

Single solitons can also be obtained for normal dispersion, i.e., $\beta' < 0$ [61]. In this case, a so-called "dark" soliton forms, which can be thought of as a a localized drop of the intensity of the field circulating in the microresonator[27]. In both dispersion cases, a strong localization of the DKS will lead to a large comb bandwidth, which is a key advantage of DKS combs for numerous comb-based applications. These include optical communications based on wavelength-division multiplexing (WDM) [C1, C2] [J5], frequency synthesis [88], frequency metrology [89], spectroscopy [18], and optical distance metrology [90] [C3, C4] [J3].

In a laboratory environment, DKS frequency combs can remain stable for several hours or even weeks [91]. Spontaneous breakdown can be caused, e.g., by a drift of the pump light power coupled into the bus waveguide, or by a drift of the pump laser frequency. It was observed that such a breakdown may be accompanied by a short, strong increase of the frequency comb power. Such power spikes can potentially be harmful for optical components when being amplified by an optical amplifier. While these power spikes occurring during the breakdown of a soliton are not directly relevant for the results of this work, a more detailed discussion of them is given in Appendix A, Section A.2.

[26] For a numerically computed spectrum, see Chapter 4, Section 4.5. For an experimentally obtained spectrum with a suppressed mode $\underline{a}_0$, see Chapter 5, Section 5.2

[27] A detailed discussion of the difference between the two kinds of DKS with emphasis on practically relevant properties is given in Chapter 3.

2.3 Quantum-dash mode-locked laser diodes

Following the descriptions of Kerr comb generators in the previous section, another comb source is introduced in this section: quantum-dash mode-locked laser diodes (QD-MLLDs). In this work, these comb sources are used for comb-based distance measurements. Details on the experiment and the MLLDs in use can be found in Chapter 6.

Quantum-dash mode-locked laser diodes (QD-MLLDs) are chip-scale frequency comb emitters based on an electrically pumped InAs/InGaAsP quantum-dash gain medium [92, 93]. They emit frequency combs when a DC (direct current) is applied, see Fig. 2.4 for a schematic. The active medium, a stack of InAs quantum-dash layers separated by InGaAsP layers, is indicated as bright and dark red stripes the MLLD cross-section schematic. Charge carriers of the applied DC enter the active medium vertically through p-doped InP and n-doped InP and recombine in the quantum dashes. The current is confined to the center region of the device by proton implantation (H^+) of the surrounding InP. Varying geometric properties of the QD lead to an inhomogeneous broadening of the gain medium, such that multiple longitudinal mode can oscillate simultaneously. A combination of a Kerr-nonlinear interaction and cross-gain modulation leads to strongly correlated phases of the optical tones, similar to mode-locking, and thereby to the emission of a pulse train, i.e., a frequency comb [94, 95].

The free spectral range of these devices depends on the cavity length. Values between 10 GHz [96, 97] and 300 GHz [98] have been reported [99]. The mean band-gap of the QD is in the order of 0.8 eV, which results in frequency comb center frequencies around 1550 nm. The 3-dB gain bandwidth is approximately 10 nm ($\approx$ 1 THz). The small size and the simple operation of QD-MLLDs make them interesting light sources, e. g., in optical communication links based on coherent wavelength-division multiplexing (WDM) [C5–C7]. Using MLLDs as transmitter and the receiver light sources, data transmission rates between 3 and 10 TBit s^{-1} were demonstrated [J6, J7].

This concludes the introduction on integrated frequency comb sources in this work. In the next section, different techniques for optical ranging are discussed, which is an important application field for optical frequency combs.

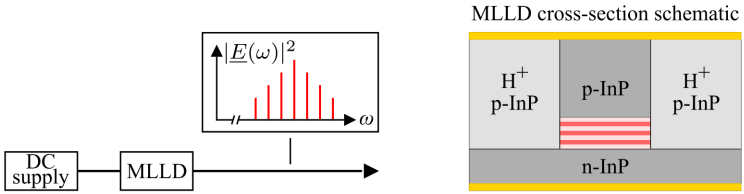

Figure 2.4: Schematic of quantum-dash mode-locked laser diodes (QD-MLLDs). QD-MLLDs emit frequency combs by applying a DC. The DC crosses the device vertically through a top- and a bottom contact, indicated as orange bars in the MLLD cross-section schematic. Proton (H^+) implantation in InP restricts the current flow to the center region. There, radiative recombination occurs in the gain-medium, indicated as a stack of horizontal red lines (QD-InAs / InGaAsP).

2.4 Application of frequency combs in optical ranging

An important application for optical frequency combs is optical distance metrology, generally known as light detection and ranging (LiDAR). Optical ranging systems (ORS) emit light towards a target, which is then reflected back from the target surface to the ORS. Typical application scenarios comprise environment detection by autonomously navigating vehicles [100], terrestrial laser scanning of the earth surface [101], as well as 3D object scanning [102]. Depending on the type of ORS, further information on the target can be retrieved in addition to the distance, such as the reflectivity [103] or its speed relative to the ORS [104].
In this work, the determination of distances using integrated frequency comb sources is investigated. In particular, a measurement scheme known as dual-comb synthetic wavelength interferometry is used. It is described in the next section along with other LiDAR measurement techniques.

2.4.1 Optical ranging techniques

Optical ranging can be performed using many different techniques [105]. This section discusses most basic variants as well as the one used in this work. For other methods using for example intensity-based, confocal or triangulation sensors see, e. g., [105]. A noteworthy method, though not relevant for this

work, is frequency-modulated continuous-wave (FMCW) LiDAR [104], where the integration of subsystems into photonic integrated circuits has already been demonstrated [106].

Time-of-flight techniques

Time-of-flight (ToF) techniques are some of the most common distance measurement schemes [105]. In most instances, a ranging system based on ToF emits short laser pulses. These pulses are reflected and/or scattered by the target, and a small fraction of the returning light is detected by a photodetector at the ORS. The time delay Δt between the emission of a specific pulse and the detection of the reflected light is related to the target distance d via

$$2d = \Delta t \, c_0 / n_{\mathrm{g,air}}. \tag{2.61}$$

The refractive index of air n_{air} has almost no dispersion[28], such that one can approximate the group refractive index as $n_{\mathrm{g,air}} \approx n_{\mathrm{air}}$ and therefore $d = \Delta t \, c_0/(2n_{\mathrm{air}})$. Today, time of flight sensors are well established, and commercially available as ToF cameras using different versions of the underlying approach. Flash LiDAR systems [108] emit light to all points of an area to be scanned in parallel and detect the returning light with a CCD camera chip, which reduces or eliminates the need for mechanically moving components. Such systems can be then improved by making use of shuttered sensors [109].

Interferometry

The most basic interferometric ORS is the Michelson interferometer, see Figure 2.5 for a fiber-based schematic. Here, light of a CW laser with frequency ω_0 (vacuum wavelength $\lambda = 2\pi c_0/\omega_0$) is split in two parts at a 50/50 coupler. One part is sent to the upper collimator (COL) and reaches a reference target after traversing a distance d_{ref}. The other part is sent towards the target of interest located at a distance d via a second collimator. The light reflected from both the target and the reference is superimposed again at the 50/50 coupler and guided

[28] In a wavelength range of 400 nm to 1600 nm, the GVD parameter of air has a value of less than $0.05\,\mathrm{ps}^2/\mathrm{km}$ [107].

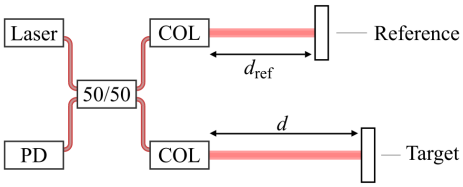

Figure 2.5: Schematic of a fiber-based Michelson interferometer. A laser emits monochromatic light, which is split into two parts at 50/50 coupler. One part is guided towards the upper collimator (COL) and sent towards a reference mirror, while the other part reaches the target through the lower collimator. Both parts are reflected and combined again at the 50/50 coupler before reaching a photodetector (PD). The path length difference between the reference path length d_{ref} and the distance d of the target determine the signal reaching the PD.

to a photodetector (PD). On the two free-space paths, light will accumulate a phase of

$$\Phi_{\omega_0,\mathrm{meas}} = 2d\,\frac{\omega_0 n_{\mathrm{air}}}{c_0} = 2\pi\frac{2dn_{\mathrm{air}}}{\lambda}, \text{ and} \tag{2.62}$$

$$\Phi_{\omega_0,\mathrm{ref}} = 2d_{\mathrm{ref}}\,\frac{\omega_0 n_{\mathrm{air}}}{c_0} = 2\pi\frac{2d_{\mathrm{ref}}n_{\mathrm{air}}}{\lambda}. \tag{2.63}$$

Note that this description neglects phase accumulated by the optical signals in optical fibers as well as when passing the 50/50 coupler for simplicity. Assuming that the optical losses on both signal propagation paths are the same, the power $P(d, d_{\mathrm{ref}})$ of the optical field on the photodetector is given by the phase difference $\delta\Phi_{\omega_0}$ according to

$$P(d, d_{\mathrm{ref}}) = P_{\max}\cos^2\left(\delta\Phi_{\omega_0}/2\right), \tag{2.64}$$

$$\begin{aligned}\delta\Phi_{\omega_0} &= \Phi_{\omega_0,\mathrm{meas}} - \Phi_{\omega_0,\mathrm{ref}} \\ &= 2(d - d_{\mathrm{ref}})\,\frac{\omega_0 n_{\mathrm{air}}}{c_0} = 2\pi\frac{2(d - d_{\mathrm{ref}})n_{\mathrm{air}}}{\lambda},\end{aligned} \tag{2.65}$$

$$d - d_{\mathrm{ref}} = \frac{\lambda}{2n_{\mathrm{air}}}\frac{\delta\Phi_{\omega_0}}{2\pi}. \tag{2.66}$$

Here, $P_{\max}$ is the maximum power. Relative changes of d with respect to d_{ref} can be detected by monitoring the photodetector current that is proportional to $P(d, d_{\mathrm{ref}})$.

This basic configuration comes with a couple of drawbacks. First, changes of the target distance can only be determined unambiguously within the unambiguity distance d_{ua} of the interferometric ORS. The measurement range is limited by the fact that the phase difference $\delta\Phi\omega_0$, see Eq. (2.65), can only be determined up to a multiple of 2π by monitoring changes of the power $P(d, d_{\mathrm{ref}})$. As a result, the unambiguity distance is given by

$$d_{\mathrm{ua}} = \frac{\lambda}{2n_{\mathrm{air}}}. \tag{2.67}$$

Here, λ is the vacuum wavelength. For ORS operated at wavelengths around 1550 nm, this translates into unambiguity distances of less than 1 μm, which limits the use of such an ORS in many applications.

Another drawback is the dependence of the sensitivity $\mathrm{d}P/\mathrm{d}d$ of the ORS on the distance difference $d - d_{\mathrm{ref}}$. The sensitivity will be low at points near constructive or destructive interference. The measurement sensitivity also depends on the difference of losses along the two light paths. If the signals returning from the reference and the target have different power, they cannot interfere completely in a constructive or destructive manner. Formally this can be expressed as an additional constant term on the r.h.s. of Eq. (2.64). Since there is an upper limit for the detectable power, this constant offset will reduce the effectively available power measurement range and thereby the measurement sensitivity. Furthermore, even if these phase changes can be determined precisely, the determination of $d - d_{\mathrm{ref}}$ requires a precise knowledge of the optical frequency ω_0 that is usually not available. Finally, the measurable length difference $2(d - d_{\mathrm{ref}})$ is limited by the coherence time of the laser[29].

While these aspects limit the performance of such an ORS, very small changes of the target position can still be determined. For example, a mirror setup can be implemented, such that the measurement beam is reflected between the target mirror and a mirror belonging to the ORS multiple times before reentering the ORS, see Fig. 1 in [111]. Changes of the target position will then lead to a change of the measured displacement, that is roughly proportional to the number of reflections[30]. Dividing the measured distance change by the number of reflections yields the actual target displacement, of which changes on a pm-

[29] It should be noted though that fiber lasers can achieve coherence lengths of several km [110].
[30] In [111], 100 reflections between a target mirror and a static mirror were used.

scale can be determined. Achieving such a resolution with a ToF techniques as described in the previous subsection is not possible.

Heterodyne synthetic wavelength interferometry

Synthetic wavelength interferometry (SWI) [112] allows to overcome some of the drawbacks of basic interferometry as described above. In such a scheme, instead of one CW laser, multiple lasers with different optical frequencies are used. In the following, SWI using two lasers [113] is explained.

Figure 2.6 depicts a fiber-optic SWI setup scheme relying on heterodyne detection to recover the phase information required for the distance determination of the target. In this configuration, light of two signal (SI) lasers with frequencies ω_0 and $\omega_0 + \Delta\omega$ is superimposed and split again at a 50/50 coupler. The light emitted at one output of the 50/50 coupler is directly guided to a balanced photodetector ($\mathrm{BD_{ref}}$). The traversed distance is associated with $2d_{\mathrm{ref}}$. The light at the second output of the 50/50 coupler is sent to the target through a collimator (COL), reflected and received by a second balanced photodetector ($\mathrm{BD_{meas}}$). Here, the total covered distance amounts to $2d$. On the two photodetectors, the optical signals of the signal lasers are superimposed with light of two other lasers acting as local oscillators (LO) with frequencies $\omega_{\mathrm{LO},0}$ and $\omega_{\mathrm{LO},0} + \Delta\omega_{\mathrm{LO}}$, respectively. The detection of the superimposed optical signals by the photodetectors generates mixing products at RF frequencies $\left|\omega_0 - \omega_{\mathrm{LO},0}\right|$ and $\left|\omega_0 + \Delta\omega - (\omega_{\mathrm{LO},0} + \Delta\omega_{\mathrm{LO}})\right|$ [31]. The phases of these RF signals on the respective photodetector contain the phases $\Phi_{\omega_0,\mathrm{ref}}$, $\Phi_{\omega_0+\Delta\omega,\mathrm{ref}}$, $\Phi_{\omega_0,\mathrm{meas}}$ and $\Phi_{\omega_0+\Delta\omega,\mathrm{meas}}$ as defined in Eqs. (2.62) and (2.63), which can be used to compute the phase differences $\delta\Phi_{\omega_0}$ and $\delta\Phi_{\omega_0+\Delta\omega}$, see Eq. (2.65)[32]. The phase differences $\delta\Phi_{\omega_0}$ and $\delta\Phi_{\omega_0+\Delta\omega}$ are linked to the distance difference $d - d_{\mathrm{ref}}$ according to

[31] Other mixing products are neglected here for simplicity.

[32] This description does not consider the impact of the LO laser phases on the measured phases at the photodetectors for simplicity. A full description can be found in Appendix D, Section D.1

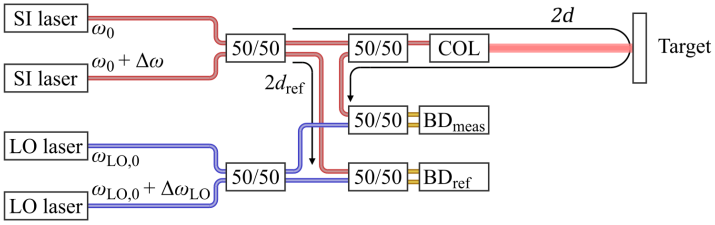

Figure 2.6: Schematic of a fiber-based ORS with synthetic wavelength and heterodyne detection. Light of two signal (SI) lasers with frequencies ω_0 and $\omega_0 + \Delta\omega$ is combined and split at a 50/50 coupler. The light of one output of the 50/50 coupler is guided to a reference balanced photodetector (BD_{ref}) over a distance corresponding to $2d_{ref}$. The light at the other output passes a second coupler, is then sent to the target by a collimator, reflected at the target and guided to a second balanced photodetector (BD_{meas}). On the photodetectors, the optical signals of the two SI lasers are superimposed with two lasers acting as local oscillators (LO) that allow for heterodyne coherent detection of the accumulated phases $\Phi_{\omega_0,ref}$, $\Phi_{\omega_0+\Delta\omega,ref}$, $\Phi_{\omega_0,meas}$ and $\Phi_{\omega_0+\Delta\omega,meas}$.

$$d - d_{ref} = \frac{1}{2}\frac{\delta\Phi_{\omega_0}}{\omega_0}\frac{c_0}{n_{air}}, \tag{2.68}$$

$$d - d_{ref} = \frac{1}{2}\frac{\delta\Phi_{\omega_0+\Delta\omega}}{\omega_0 + \Delta\omega}\frac{c_0}{n_{air}}. \tag{2.69}$$

These two equations can be combined into a single expression for the distance difference $d - d_{ref}$, which reads

$$d - d_{ref} = \frac{1}{2}\frac{\delta\Phi_{\omega_0+\Delta\omega} - \delta\Phi_{\omega_0}}{\Delta\omega}\frac{c_0}{n_{air}} = \frac{\Lambda_S}{2n_{air}}\frac{\delta\Phi_{\omega_0+\Delta\omega} - \delta\Phi_{\omega_0}}{2\pi}, \tag{2.70}$$

$$\Lambda_S = \frac{2\pi c_0}{\Delta\omega}. \tag{2.71}$$

Here the synthetic wavelength Λ_S was introduced. Comparing Eqs. (2.66) and (2.70), one can see that the synthetic wavelength of an SWI ranging system corresponds to the optical wavelength in a single-wavelength interferometric ranging system. Using two lasers for interference-based distance measurements offers several advantages. First, the synthetic wavelength and thereby the unambiguity distance $d_{ua} = \Lambda_S/(2n_{air})$, see Eq. (2.67), is usually orders of magnitude larger compared to single-color interferometry. Second, the frequency difference $\Delta\omega$, i.e., Λ_S can be measured with high precision relatively easy by using high-speed electronics, if $\Delta\omega$ is in the range of up to tens of

gigahertz. However, the increased measurement range also implies that uncertainties of measured phase differences $\delta\Phi_{\omega_0+\Delta\omega} - \delta\Phi_{\omega_0}$ will result in larger absolute distance errors.

2.4.2 Comb-based synthetic wavelength interferometry

The dual-color measurement principle described in the previous section can be extended to $N_\mathrm{b} = 10 \ldots 100$ comb lines of an optical frequency comb, see also Appendix D, Section D.1 for a more rigorous description. In this case, the SI lasers as well as the LO lasers in the setup depicted in Fig. 2.6 are each replaced by an optical frequency comb source [20, 114]. The frequencies of the signal comb reaching the target are given by $\omega_{\mathrm{SI},\mu} = \omega_{\mathrm{SI},0} + \mu\omega_{\mathrm{SI,FSR}}$, see also Eq. (2.3). The frequencies of the LO comb should be chosen such that the RF signals generated at the photodetectors BD_ref and $\mathrm{BD}_\mathrm{meas}$, see Fig. 2.6, are located at detectable frequencies. Furthermore, the FSR of the LO comb needs to differ from the FSR of the SI comb, since otherwise the corresponding RF signals spectrally overlap and a phase readout of the individual phase differences $\delta\Phi$ is not possible, for details see Appendix D, Section D.1. In the following, the phase difference of the μth comb line is denoted as $\delta\Phi_\mu$. It is related to the distance difference $d - d_\mathrm{ref}$, as described in Eqs. (2.68) and (2.69), via

$$\begin{aligned} d - d_\mathrm{ref} &= \frac{1}{2}\frac{\delta\Phi_\mu}{\omega_0 + \mu\omega_{\mathrm{SI,FSR}}}\frac{c_0}{n_\mathrm{air}}, \\ \delta\Phi_\mu &= \mu\omega_{\mathrm{SI,FSR}}\frac{n_\mathrm{air}}{c_0}2\,(d - d_\mathrm{ref}) + \omega_0\frac{n_\mathrm{air}}{c_0}2\,(d - d_\mathrm{ref}) \\ &= D\,(d, d_\mathrm{ref})\,\mu + \omega_0\frac{n_\mathrm{air}}{c_0}2\,(d - d_\mathrm{ref})\,. \end{aligned} \tag{2.72}$$

The distance difference $d - d_\mathrm{ref}$ can be determined by fitting a straight line to a set of measured phase differences $\delta\Phi_\mu$ over the comb line index μ. The slope parameter $D\,(d, d_\mathrm{ref}) = \omega_{\mathrm{SI,FSR}}\frac{n_\mathrm{air}}{c_0}2\,(d - d_\mathrm{ref})$ of the fit contains the

distance information. The unambiguity range is given by the fact that the slope $D\left(d, d_{\mathrm{ref}}\right)$ can only be determined up to a multiple of 2π, which results in

$$d_{\mathrm{ua}} = \frac{1}{2}\frac{2\pi}{\omega_{\mathrm{SI,FSR}}}\frac{c_0}{n_{\mathrm{air}}} = \frac{\Lambda_{\mathrm{S}}}{2n_{\mathrm{air}}}, \tag{2.73}$$

$$\Lambda_{\mathrm{S}} = \frac{2\pi c_0}{\omega_{\mathrm{SI,FSR}}}. \tag{2.74}$$

Dispersion in the setup-internal optical paths induces additional phase contributions to the phases on the measurement detector $\Phi_{\mu,\mathrm{meas}}$ and the reference detector $\Phi_{\mu,\mathrm{ref}}$, which may not necessarily be equal. As a result, the phase differences $\delta\Phi_\mu$ may be impaired by the dispersion in the ranging system, which results in a nonlinear relation of the phase differences $\delta\Phi_\mu$ and the comb line index μ, see Appendix D, Section D.4 for details. This will disturb a linear fit used to retrieve the distance information. By performing an additional calibration measurement, these dispersion effects can be mitigated, see Section D.1, Eq. (D.13). This may become necessary, when the optical frequency combs cover large optical bandwidths and setup-internal (fiber) path-lengths are not matched perfectly. While this adds additional effort to the ranging method, the usage of optical frequency combs in synthetic wavelength interferometry is still extremely promising, since the achievable precision can be improved greatly. By determining the slope parameter $D\left(d, d_{\mathrm{ref}}\right)$ not only for two, but for 100 phase differences $\delta\Phi_\mu$, the associated distance information becomes much more resilient against, e.g., electronic noise in the receiver circuits.

3 Bandwidth and conversion efficiency analysis of dissipative Kerr soliton frequency combs based on bifurcation theory

In this chapter, an analysis of the bandwidth and power conversion efficiency of dissipative Kerr soliton combs based on bifurcation theory and numerical continuation is described. The content of this chapter has been published in *Physical Review A* [J1] and was adapted to fit the layout, structure and notation of this dissertation. Supplementary information can be found in Appendix B and further mathematical details in [115]. This chapter assumes a negative time dependence of the optical signal of the form $\exp(-\mathrm{j}\omega t)$.

J. Gärtner and R. Mandel developed the bifurcation analysis for the Lugiato-Lefever equation and investigated soliton frequency comb states along bifurcation branches, see Sections 3.2, 3.3 and Appendices B.1, B.2 and B.5. The author of this dissertation developed the idea of exploiting these tools for studying conversion efficiency of Kerr-soliton comb generators and developed the associated metrics such as bandwidth and conversion efficiency, see Section 3.4. Based on these metrics, J. Gärtner characterized the soliton frequency combs quantitatively, see Section 3.4. The author of this dissertation then translated the results into physical quantities, see Appendices B.3 and B.4. The author wrote Appendices B.3 and B.4 and contributed substantial parts of Sections 3.4, and 3.5. The work was jointly supervised by T. Jahnke, W. Reichel, and C. Koos.

[Start of publication [J1]]

Bandwidth and Conversion Efficiency Analysis of Dissipative Kerr Soliton Frequency Combs Based on Bifurcation Theory

Physical Review A, **100**(3), 033819 (2019)

J. Gärtner,[1] **P. Trocha**,[2] R. Mandel,[1] C. Koos,[2,3] T. Jahnke,[4] W. Reichel[1]

[1] Institute for Analysis (IANA), Karlsruhe Institute of Technology (KIT), Karlsruhe, Germany

[2] Institute of Photonics and Quantum Electronics (IPQ), Karlsruhe Institute of Technology (KIT), Karlsruhe, Germany

[3] Institute of Microstructure Technology (IMT), Karlsruhe Institute of Technology (KIT), Karlsruhe, Germany

[4] Institute for Applied and Numberical Mathematics (IANM), Karlsruhe Institute of Technology (KIT), Karlsruhe, Germany

Dissipative Kerr soliton frequency combs generated in high-Q microresonators may unlock novel perspectives in a variety of applications and crucially rely on quantitative models for systematic device design. Here, we present a global bifurcation study of the Lugiato-Lefever equation which describes Kerr comb formation. Our study allows systematic investigation of stationary comb states over a wide range of technically relevant parameters. Quantifying key performance parameters of bright and dark-soliton combs, our findings may serve as a design guideline for Kerr comb generators.

3.1 Introduction and main results

Kerr frequency combs have the potential to revolutionize a variety of applications such as high-speed data transmission [14, 116] [J5], high-precision optical ranging [90] [J3] and spectroscopy, [18] as well as highly accurate optical frequency synthesis [88]. Kerr frequency combs stand out due to their high optical bandwidth that may exceed an octave of frequencies, narrow linewidths down to 1 kHz, and large line spacings of tens of GHz [12, 23, 117]. Moreover, Kerr comb generators feature a small footprint and are amenable to efficient wafer-level mass production, thereby paving the path to large-scale industrial deployment. On a physical level, Kerr comb generators rely on third-order nonlinear interaction in high-Q microresonators that are pumped by a

continuous-wave (CW) laser [11]. Under appropriate pump conditions, cascaded degenerate and non-degenerate four-wave mixing can lead to a soliton waveform that circulates in the cavity, balancing self-phase modulation and dispersion, as well as cavity loss and parametric gain [21]. These dissipative Kerr soliton combs consist of strictly equidistant phase-locked optical tones and stand out due to smooth spectral envelopes and extraordinary robustness with respect to variations of the pump conditions.

Mathematically, Kerr frequency comb generators are represented by nonlinear systems with rather complex dynamics. Systematic design and theory-guided improvement of Kerr comb sources therefore require reliable mathematical models that cover practically relevant parameter spaces and that combine intuitive qualitative understanding with quantitatively correct predictions of the behavior of the nonlinear system. Kerr comb dynamics are described by the Lugiato-Lefever equation (LLE), a damped, driven and detuned nonlinear Schrödinger equation [78, 118, 119]. The LLE has been extensively studied, using, e.g., numerical simulations of the temporal comb formation dynamics, which have reached remarkable accuracy in predicting and explaining experimental results [120, 121]. However, time-domain integration of the LLE only allows to access specific comb states that strongly depend on the individual device parameters as well as on the complex interplay of the initial conditions and the time-dependent tuning of the pump. Specifically, time-integration techniques do not permit us to globally study the variety of different stationary Kerr comb states that can be accessed by exploiting the full range of technically accessible device and operation parameters. This gap can be closed by bifurcation analysis, which allows us to investigate the structure of stationary solutions and to obtain qualitative as well as quantitative insights. So far, stationary states of the LLE have been mainly investigated by local bifurcation analysis [118, 119, 122–128], focusing on states in the vicinity of the trivial LLE solution that consists of a single CW tone at the pumped resonance. Global aspects, in particular, concerning the snaking behavior of solution branches are discussed in Refs. [119, 123, 124] and, recently, a rigorous stability analysis of stationary states closing the gap between linearized stability and nonlinear stability was achieved in Ref. [129]. These methods revealed a large variety of comb states, and were partially extended via numerical continuation methods to regions further away from the trivial state where solitons occur. However, a global study that identifies pronounced soliton states and favorable operation regimes across the full range of technical accessible device and operation parameters has not been presented so far.

In this chapter, we present a global bifurcation study of the LLE, covering a large space of technically accessible parameters. Our analysis comprises both bright-soliton (BSO) states in resonators with anomalous group-velocity dispersion (GVD) [21] as well as dark-soliton (DSO) states that form in the presence of normal GVD [130]. For both types of combs, we classify branches associated with single and multi-soliton states and characterize single-soliton states by their optical bandwidth as well as by the pump-to-comb power transfer efficiency. Our bifurcation analysis hence allows determining and systematically optimizing the performance of Kerr comb generators in integrated photonic systems, which is of significant importance for industrial adoption of these devices. This chapter is organized as follows: In Sec. 3.2, we introduce the LLE and derive sufficient conditions for bifurcations from the trivial state. In Sec. 3.3, we identify bifurcation branches leading to single-soliton states and investigate the behavior of the soliton and its characteristics along these branches. Section 3.4 is dedicated to a quantitative characterization of single-soliton frequency combs using the bandwidth and the power conversion efficiency as performance metrics. Mathematical details and derivations can be found in Appendices B.1– B.5.

3.2 Bifurcation analysis for the Lugiato-Lefever equation

We start our our analysis from the LLE,

$$\mathrm{j}\frac{\partial}{\partial t'}\underline{a} = -\beta'\frac{\partial^2}{\partial \tau'^2}\underline{a} - (\mathrm{j}-\zeta)\underline{a} - |\underline{a}|^2\underline{a} + \mathrm{j}\sqrt{F} \tag{3.1}$$

and its stationary version,

$$-\beta'\frac{\partial^2}{\partial \tau'^2}\underline{a} - (\mathrm{j}-\zeta)\underline{a} - |\underline{a}|^2\underline{a} + \mathrm{j}\sqrt{F} = 0. \tag{3.2}$$

Here, $\underline{a}(t', \tau')$ represents the optical intracavity field as a function of normalized time t' and angular position $\tau' \in [0, 2\pi]$ within the cavity. Hence $\underline{a}$ is 2π-periodic with respect to τ'. Moreover, β' is the GVD parameter, and ζ the detuning of the input pump laser as a free real-valued parameter. The forcing $\sqrt{F}$ corresponds to the amplitude of the optical driving field. Relations that

connect the normalized quantities β', ζ, $\sqrt{F}$ to their physical counterparts can be found in Appendix B.4. In the following, we consider 2π-periodic solutions $\underline{a}$ of Eq. (3.2), which feature even symmetry about $\tau' = \pi$ and therefore fulfill the Neumann boundary conditions:

$$\frac{\partial \underline{a}}{\partial \tau'}(0) = \frac{\partial \underline{a}}{\partial \tau'}(\pi) = 0. \tag{3.3}$$

Thus, from now on we restrict our attention to functions $\underline{a} : [0, 2\pi] \to \mathbb{C}$, which satisfy Eq. (3.2) on $[0, \pi]$ together with Eq. (3.3) and are evenly reflected around $\tau' = \pi$. In Fourier modes, the solution is represented as $\underline{a}(\tau') = \sum_{\mu \in \mathbb{Z}} \underline{a}_\mu \mathrm{e}^{\mathrm{j}\mu\tau'}$ with $\underline{a}_{-\mu} = \underline{a}_\mu$. The intracavity power of the field is given by the square of the L^2-norm $\|\underline{a}\|_2^2 := \sum_{\mu \in \mathbb{Z}} |\underline{a}_\mu|^2$. There are trivial solutions $\underline{a}_0$ of Eqs. (3.2) and (3.3) which are complex constants. Let us assume that the trivial solution $\underline{a}_0$ can be parametrized (locally) as $\underline{a}_0 = \underline{a}_0(\zeta)$.[1] As an example, the curve $(\zeta, \underline{a}_0(\zeta))$ of constant solutions is shown in black for $\sqrt{F} = 2$ in Fig. 3.1(a) in the case of anomalous dispersion ($\beta' = 0.1$) and in Fig. 3.2(a) in the case of normal dispersion ($\beta' = -0.1$). For each ζ, the squared L^2-norm of $\underline{a}_0(\zeta)$ is plotted.[2] Note that three different constant solutions exist for certain values of ζ. Nontrivial solutions associated with frequency combs may arise from the curve of trivial solutions at bifurcation points, which can be defined in the simplest form applicable for our purposes as follows: *A point $P = (\zeta_0, \underline{a}_0(\zeta_0)) \in \mathbb{R} \times \mathbb{C}$ on the trivial curve is called a bifurcation point for Eqs. (3.2) and (3.3) if there exists a second curve $(\zeta_p, \underline{a}_p)$ of solutions of Eqs. (3.2) and (3.3), which is parameterized by p in some interval and crosses transversally the trivial curve at P.*

[1] This assumption is for simplicity of the presentation. It fails only at the turning points of the trivial curve, which does not lead to any undesirable effect. Other parametrizations $\zeta_0 = \zeta_0(p_1) = F(1 - p_1^2) + p_1/(1 - p_1^2)^{1/2}$, $\underline{a}_0 = \underline{a}_0(p_1) = \sqrt{F}(1 - p_1^2) - \mathrm{j}\sqrt{F} p_1 (1 - p_1^2)^{1/2}$ with $p_1 \in (-1, 1)$ are also possible, cf. Ref. [125].

[2] In all figures, units on axes are dimensionless.

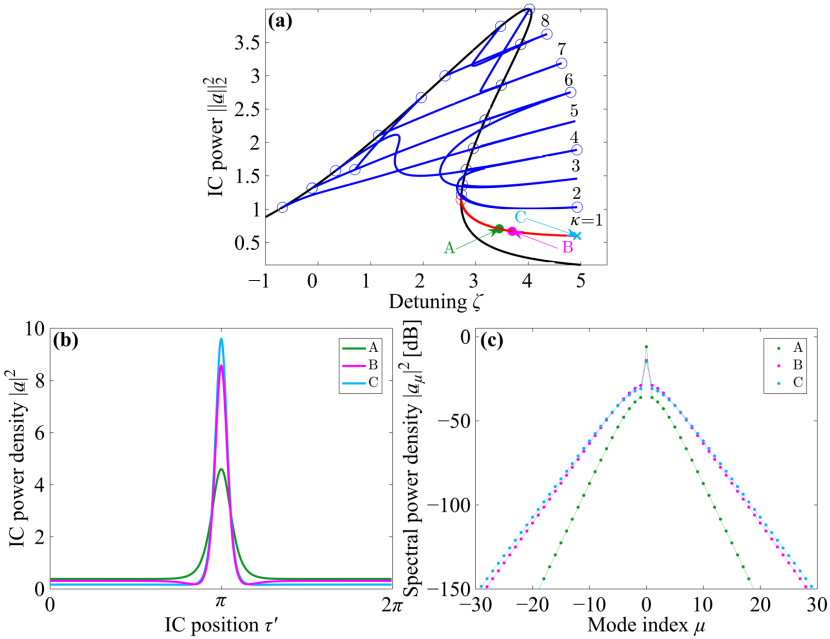

Figure 3.1: Bifurcation maps and nontrivial comb states for bright solitons in anomalous-dispersion ($\beta' > 0$) microresonators. Quantities on axes are dimensionless. (a) Bifurcation map of the LLE for $\sqrt{F} = 2$ and $\beta' = 0.1$, indicating the normalized intracavity power $\|\underline{a}\|_2^2$ vs. the normalized detuning ζ. The constant solution is indicated in black, the single soliton state bifurcation branch ($\kappa = 1$) in red, while blue corresponds to other bifurcation branches of multisoliton states with $\kappa = 2, \ldots, 8$ pulses circulating in the cavity. Circles indicate bifurcation points. (b) Spatial power distribution as a function of normalized intracavity position τ' of single-soliton states corresponding to points A, B, and to the turning point C indicated in (a). (c) Spectral power distribution of single-soliton states corresponding to points A, B, and to the turning point C indicated in (a). Note that for illustrative purposes, a relatively low forcing $\sqrt{F} = 2$ was chosen, resulting in a quick drop of the power of spectral modes further away from the pump. Here the bifurcation-and-continuation method is sufficiently precise to correctly predict spectral components which are more than 150 dB below the pump, hence safely covering technical relevant power ranges.

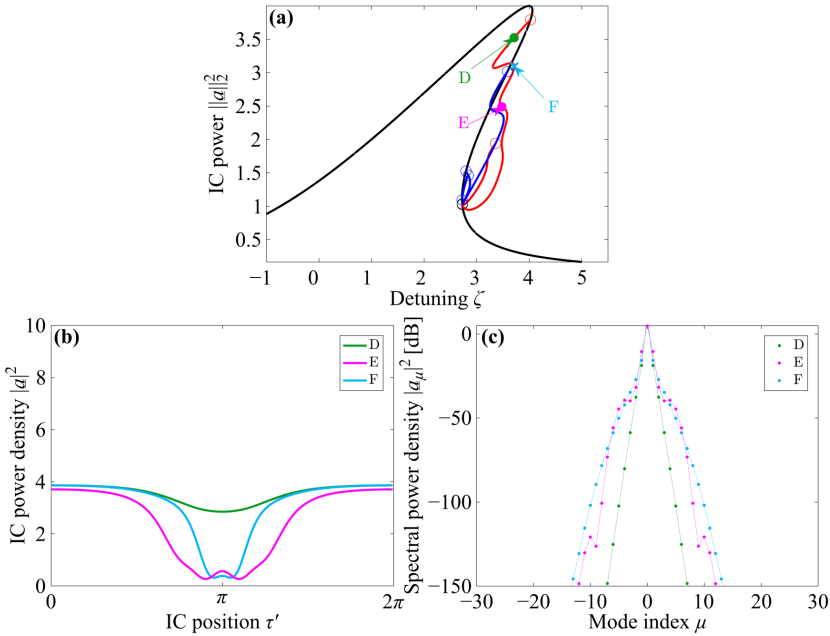

Figure 3.2: Bifurcation maps and nontrivial comb states for dark solitons in normal-dispersion microresonators ($\beta' < 0$). Quantities on axes are dimensionless. (a) Bifurcation map of the LLE for $\sqrt{F} = 2$ and $\beta' = -0.1$, indicating the normalized intracavity power $\|\underline{a}\|_2^2$ vs. the normalized detuning ζ. The constant solution is indicated in black, the single soliton state bifurcation branch in red, while blue corresponds to other bifurcation branches. Circles indicate bifurcation points. (b) Spatial power distribution as a function of normalized intracavity position τ' of single-soliton states corresponding to points D, E, and to the turning point F indicated in (a). (c) Spectral power distribution of single-soliton states corresponding to points D, E, and to the turning point F indicated in (a).

The structure of the solution set near $(\zeta_0, \underline{a}_0(\zeta_0))$ depends on the properties of the linearized operator $\hat{L}$, defined by

$$\hat{L}\underline{a}_\phi := -\beta' \frac{\partial^2}{\partial \tau'^2}\underline{a}_\phi - (\mathrm{j} - \zeta_0)\underline{a}_\phi - 2|\underline{a}_0|^2\underline{a}_\phi - \underline{a}_0^2\bar{\underline{a}}_\phi, \tag{3.4a}$$

$$\frac{\partial \underline{a}_\phi}{\partial \tau'}(0) = \frac{\partial \underline{a}_\phi}{\partial \tau'}(\pi) = 0, \tag{3.4b}$$

where we write $\underline{a}_0$ instead of $\underline{a}_0(\zeta_0)$. The spectrum of $\hat{L}$ consists of countably many complex eigenvalues whose real parts tend to $+\infty$ in the case $\beta' > 0$ and to $-\infty$ in the case $\beta' < 0$. This can be shown via Fourier series expansion as in Ref. [125], Proposition 4.3. Because of the implicit function theorem, cf. Ref. [131], Theorem I.1.1, nontrivial solutions can only bifurcate from the trivial branch at $(\zeta_0, \underline{a}_0(\zeta_0))$ if the kernel $\operatorname{Ker}\hat{L} = \{\underline{a}_\phi : \hat{L}\underline{a}_\phi = 0, \partial\underline{a}_\phi(0)/\partial\tau' = \partial\underline{a}_\phi(\pi)/\partial\tau' = 0\}$ is at least one-dimensional. This is the case provided that there is an integer $\mu \in \mathbb{N}$ such that

$$(\zeta_0 + \beta'\mu^2)^2 - 4|\underline{a}_0(\zeta_0)|^2(\zeta_0 + \beta'\mu^2) + 1 + 3|\underline{a}_0(\zeta_0)|^4 = 0. \tag{3.5}$$

Solving Eq. (3.5) yields

$$\mu_{1,2} := \sqrt{\frac{2|\underline{a}_0(\zeta_0)|^2 - \zeta_0 \pm \sqrt{|\underline{a}_0(\zeta_0)|^4 - 1}}{\beta'}}. \tag{3.6}$$

For details on the derivation of Eqs. (3.5) and (3.6), see Appendix B.1. The wave number $\mu_{1,2}$ obtained by evaluating the expression on the right side of Eq. (3.6) defines the angular periodicity $2\pi/\mu_{1,2}$, after which the nontrivial comb state in the vicinity of the bifurcation point repeats itself, i.e., $\underline{a}(\tau') = \underline{a}(\tau' + 2\pi/\mu_{1,2})$. Equations (3.5) and (3.6) naturally occur in bifurcation studies of Eq. (3.2). In Refs. [118, 119, 123, 128], for instance, bifurcations are considered from the point of view of spatial dynamics both for normal and anomalous dispersion, and parameter regimes are determined where Turing patterns as well as 1-soliton states bifurcate from trivial solutions. In Ref. [124], a similar approach is taken to study bifurcation of DSOs from trivial solutions in the normal-dispersion regime. In most of these works, local bifurcations from the trivial solution family are determined analytically and a numerical global bifurcation analysis is performed for periodic solutions (cf. Refs. [119, 123, 124, 128]). Typically, the forcing parameter $\sqrt{F}$ is taken as the bifurcation parameter. In contrast, we study global bifurcations of 2π-periodic solutions with respect to the detuning ζ, whose physically accessible parameter space is usually larger than the parameter space for $\sqrt{F}$. Our central goal is the localization of the most pronounced 1-solitons in the global bifurcation picture. With the help of Eq. (3.6), we can formulate the following bifurcation result, which explains under what conditions bifurcations from the line of trivial solutions occur:

For a point $P = (\zeta_0, \underline{a}_0(\zeta_0))$ on the curve of trivial solutions, the following is true:

(i) If exactly one of the two numbers $\mu_{1,2}$ from Eq. (3.6) is an integer and if the transversality condition

$$2|\underline{a}_0(\zeta_0)|^4(|\underline{a}_0(\zeta_0)|^2 - \zeta_0) \mp (1 + \zeta_0^2 - |\underline{a}_0(\zeta_0)|^4)\sqrt{|\underline{a}_0(\zeta_0)|^4 - 1} \neq 0 \tag{3.7}$$

holds with "−" if $\mu_1 \in \mathbb{N}$ and "+" if $\mu_2 \in \mathbb{N}$, then P is a bifurcation point for Eqs. (3.2) and (3.3).

(ii) If neither μ_1 nor μ_2 is an integer, then P is not a bifurcation point for Eqs. (3.2) and (3.3), and near P only trivial solutions of Eqs. (3.2) and (3.3) exist.

In the remaining cases, where either the condition from Eq. (3.7) fails or both μ_1 and μ_2 are integers, no statement can be made. Let us add that Eq. (3.7) is in general not implied by Eq. (3.6) and therefore has to be checked separately. The above result mainly goes back to Theorem 4 in [125]. Compared to Ref. [125], its present formulation as well as its proof allow substantial simplifications as we will show in Appendix B.2. Computations reveal that our bifurcation points on the trivial solution family are either of center or of saddle center type in the language of spatial dynamics as used, e.g., in Ref. [124], Table 3.1. To see this, notice that for the bifurcation of periodic solutions from a constant solution $\underline{c}_0$ of $\partial\underline{c}/\partial\tau' = F_{\tau'}(\underline{c})$, $\underline{c} = (\Re\{\underline{a}\}, \Im\{\underline{a}\}, \Re\{\partial\underline{a}/\partial\tau'\}, \Im\{\partial\underline{a}/\partial\tau'\})$ at least one pair of purely imaginary eigenvalues of $\partial F_{\tau'}/\partial\tau'(\underline{c}_0)$ is necessary. The eigenvalues Λ of $\partial F_{\tau'}/\partial\tau'(\underline{c}_0)$ solve Eq. (3.5) with μ replaced by $\pm\mathrm{j}\Lambda$, and the solutions $\mathrm{e}^{\Lambda\tau'}(v_1, v_2, v_3, v_4)$ of the linearized spatial dynamics system correspond to solutions $\cos(\mu\tau')(v_1 + \mathrm{j}v_2)$ in the kernel of $\hat{L}$ as defined in Eqs. (3.4).

For the cases $\sqrt{F} = 2$ and $\beta' = \pm 0.1$, we numerically computed the bifurcation points determined by Eq. (3.5). We also checked, for all bifurcation points, which of the numbers $\mu_{1,2}$ in Eq. (3.6) is an integer, and whether the transversality condition from Eq. (3.7) holds, cf. Table 3.1. The computed bifurcation points on the trivial branch are marked by circles in Figs. 3.1(a) and 3.2(a) for $\beta' = 0.1$ and $\beta' = -0.1$, respectively. In case (i) of the above result, we may

Table 3.1: Bifurcation points on the trivial branch for anomalous dispersion $\beta' = 0.1$, $\sqrt{F} = 2$. The coordinates $(\zeta_0, \underline{a}_0(\zeta_0))$ shown in the first two columns are determined so at least one of the values $\mu_{1,2}$ (third and fourth columns) from Eq. (3.6) is an integer. The integer value of either μ_1 or μ_2 determines the periodicity of the field in the vicinity of the corresponding bifurcation point. The last column lists the values obtained from evaluating the left side of Eq. (3.7) to determine whether the transversality condition is fulfilled.

ζ_0	$\mathbf{a_0}(\zeta_0)$	μ_1	μ_2	**Transv.**
−0.6770	0.51 + 0.87j	5.44	5	3.67
−0.1117	0.66 + 0.94j	6	4.35	5.56
0.3325	0.79 + 0.98j	6.35	4	4.49
1.1508	1.05 + 1.00j	7	3.47	12.26
1.9646	1.34 + 0.94j	7.65	3	4.44
2.4179	1.50 + 0.87j	8	2.74	16.42
3.4759	1.87 + 0.49j	8.72	2	4.12
4.0242	2.00 − 0.05j	8.85	1	3.85
3.8603	1.73 − 0.68j	8	1.56j	−22.26
3.4893	1.43 + 0.90j	7	2.13j	−23.74
3.1793	1.17 − 0.99j	6	2.49j	−21.14
2.9576	0.96 − 1.00j	5	2.76j	−17.57
2.8218	0.80 − 0.98j	4	2.96j	−14.19
2.7541	0.68 − 0.95j	3	3.09j	−11.41
2.7293	0.61 − 0.92j	2	3.14j	−9.32
2.7239	0.57 − 0.90j	1	3.15j	−8.00

apply Rabinowitz's global bifurcation theorem from Ref. [132]. As a result, we obtain that a branch bifurcating from the trivial curve at $(\zeta_0, \underline{a}_0(\zeta_0))$ either returns to the trivial curve at some other bifurcation point or joins another branch of nontrivial solutions, since unbounded branches are excluded due to Theorems 1 and 2 in Ref. [125].

In Fig. 3.1(a), a complete picture of all branches bifurcating from the trivial branch is shown for anomalous dispersion with $\beta' = 0.1$. For clarity of the figures, we did not include any secondary bifurcation branches, i.e., branches not directly coming off the trivial branch. A discussion of secondary bifurcation points is given in Appendix B.5. The analytical and numerical description of secondary bifurcations coming with the effect of period-doubling, -tripling

etc. is provided in Ref. [133]. Let us mention that this phenomenon was discovered in earlier bifurcation analyses, cf. Refs. [128], Fig. 5, and [119], Fig. 10 for BSOs and [124], Fig. 12 for DSOs. We recall that in these studies the detuning was fixed and the forcing parameter was considered as a bifurcation parameter. The bifurcation branches in Fig. 3.1 and 3.2 were computed by the software `pde2path` (cf. Refs. [134, 135]) which is designed to numerically treat continuation and bifurcation of PDE systems. Given a starting point on the trivial branch together with a tangent direction, `pde2path` starts a continuation algorithm to compute the trivial branch. Whenever a simple eigenvalue of the linearization crosses zero, a bifurcation point is detected and the bifurcating branch can be followed.

For the example given in Fig. 3.1(a), all calculated bifurcation points in Table I were reproduced by `pde2path`. Bifurcation branches determined by `pde2path` are shown in Fig. 3.1(a) as colored lines. Here, the single-soliton branch ($\kappa = 1$) is highlighted in red. Blue branches are related to higher-order soliton frequency combs ($\kappa = 2, \ldots, 8$). Note that the bifurcation branches seem to stop at the points where a maximal value of ζ is reached. But, in fact, these points are turning points, and each branch continues in opposite directions on nearly the same path. A finer resolution of the turning of the branches reveals a snaking behavior shown in Fig. B.1(b) in Appendix B.5. In Fig. 3.2(a), the same analysis is performed for normal dispersion ($\beta' = -0.1$). The single dark-soliton branch is again marked in red, higher-order soliton branches are marked in blue. Note that `pde2path` does not only generate the bifurcation map, but also allows us to calculate the stationary solutions of the LLE along the various branches.

Our choice of resonator length equals 2π in contrast to 100 in Ref. [128] and 160 in Refs. [119, 124]. Rescaling the solutions from larger periodicities to 2π changes the dispersion from $|\beta'| = 1$ in Refs. [119, 124, 128] to values of $|\beta'| \approx 10^{-3}$, which is much smaller than our choice of $|\beta'| = 0.1$. Notice that smaller dispersion parameters $|d|$ lead to a larger number of bifurcation points, cf. Ref. [125], Theorems 1.4 and 1.5, so it is to be expected that the diagrams in Refs. [119, 124, 128] show more bifurcation branches than shown here. Our choice of $\sqrt{F} = 2$ is for illustrative purposes, so global features in Fig. 3.1 and 3.2 can be visualized more easily.

Complementing Figures 3.1 and 3.2, we give further information on the connectedness of the branches as well as stability properties of solutions including

those with multiple peaks in Appendix B.5. In the following, we will study the properties of the 1-solitons.

3.3 Solitons along bifurcation branches

For a global study, we use `pde2path` to explore a much more extensive parameter space aiming at the detection of 1-soliton states on bifurcating branches. Based on a large number of numerical experiments, we developed heuristics that allow us to identify branches with single-soliton states and to find the solitons with the strongest spatial localization. Let us number the bifurcation points and bifurcating branches along $(\zeta, \underline{a}_0(\zeta))$, starting from the left end of the trivial branch.

(i) For anomalous dispersion ($\beta' > 0$), bright 1-solitons occur on the last bifurcating branch. The most localized 1-solitons occur near the first turning point of this branch (locally maximizing ζ). In Fig. 3.1(a), the corresponding branch is labeled $\kappa = 1$. It contains the solutions A,B,C that are illustrated with regard to the spatial and spectral power distribution in Figs. 3.1(b) and 3.1(c), respectively. The first turning point is indicated by C.

(ii) For normal dispersion ($\beta' < 0$), dark 1-solitons occur on the first bifurcating branch. The most localized 1-solitons occur near the second turning point of this branch (locally maximizing ζ). In Fig. 3.2(a), the corresponding branch contains the solutions D,E,F that are illustrated with regard to the spatial and spectral power distribution in Figs. 3.2(b) and 3.2(c), respectively. The second turning point is indicated by F.

These heuristics are illustrated in Fig. 3.3, where the full width at half maximum (FWHM_a) in case of BSOs as well as the full width at half minimum (FWHM_i) in the case of DSOs are plotted for the spatial field distribution along the bifurcating branch starting from the initial bifurcation point. Note that the bright 1-soliton at point C in Fig. 3.1(a) has slightly smaller $\mathrm{FWHM}_a = 0.3330$ than the bright 1-soliton at point B ($\mathrm{FWHM}_a = 0.3393$). Both for normal and anomalous dispersion, the common feature of the most localized 1-solitons is their occurrence at maximal detuning values within all turning points of the bifurcating branch. These heuristics are illustrated in Fig. 3.1 and 3.2. For

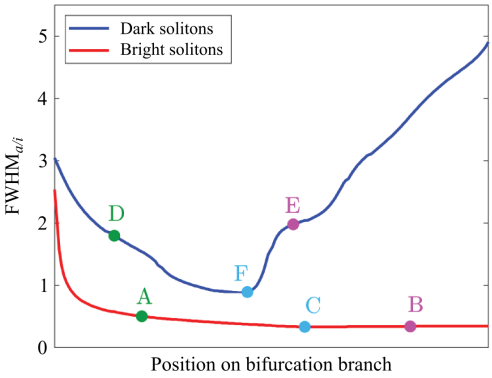

Figure 3.3: Full width at half maximum (FWHM$_a$) of bright solitons along the bifurcating branch for anomalous dispersion (red, $\beta' = 0.1$) and full width at half minimum (FWHM$_i$) of dark solitons for normal dispersion (blue, $\beta' = -0.1$) for $\sqrt{F} = 2$. Horizontal axis shows normalized arc length along bifurcation branches. Quantities on both axes are dimensionless.

different points A, B, C along the bright-single-soliton branch and D, E, F along the dark-single-soliton branch, respectively, comb states are depicted in the spatial and frequency domain in Figs. 3.1(b), 3.1(c), 3.2(b), and 3.2(c). As expected, the comb states with the smallest FWHM$_{a/i}$ identified in points C and F by using the aforementioned heuristics show the strongest localization in the spatial domain. Furthermore, we can see that in the case of anomalous dispersion, there is no other state on the branch $\kappa = 1$ for the same value of ζ. However, in the case of normal dispersion, we find another DSO state with equal detuning marked by point D in Fig. 3.2(a), cf. Ref. [118]. Yet point F in Fig. 3.2(a) shows a stronger spatial localization, cf. Fig. 3.3, and has a broader frequency comb than D.

In this example, the soliton character of the solutions, i.e., their strong localization in the spatial domain at the turning point is visible but not yet very pronounced due to the moderate value of $\sqrt{F}$. With increasing $\sqrt{F}$, the soliton localization as well as the comb power and comb bandwidth will be much enhanced. At the same time, the graphs of the bifurcation branches will be less illustrative due to a steeply increasing number and density of bifurcation points. Therefore, $\sqrt{F} = 2$ is chosen merely for illustrative reasons, and much larger ranges of $\sqrt{F}$ are covered in Sec. 3.4.

3.4 Quantitative characterization of soliton frequency combs

Using the heuristics from the previous section, we are able to identify single-soliton states with the strongest spatial localization for any fixed forcing both in the normal as well as anomalous-dispersion regime. Based on this approach, we now characterize these comb states $\underline{a}(\tau') = \sum_{\mu\in\mathbb{Z}} \underline{a}_\mu \mathrm{e}^{\mathrm{j}\mu\tau'}$ by their comb bandwidth $\mu^\star$ and their power conversion efficiency (PCE) η. The comb bandwidth is quantified by the 3dB point, i.e., by the minimal integer $\mu^\star$ that fulfills $|\underline{a}_{\mu^\star}|^2 \leq \frac{1}{2}|\underline{a}_1|^2$. Note that the 3dB comb bandwidth is defined with respect to the power $|\underline{a}_1|^2$ of the mode directly adjacent to the pumped mode rather than the power $|\underline{a}_0|^2$ of the pumped mode itself, which is usually much stronger than all other modes of the comb. The PCE is the ratio between the intracavity comb power

$$P_{\mathrm{FC}} = \sum_{\mu\in\mathbb{Z}\setminus\{0\}} |\underline{a}_\mu|^2 \tag{3.8}$$

and the pump power F. Note that the intracavity comb power does not contain the zero mode, since $|\underline{a}_0|^2$ mostly stems from the pump and is therefore nonzero even if no comb is formed in the microresonator. For BSOs, under the assumption of small damping and small forcing, approximation formulas for the comb bandwidth as well as the PCE exist, cf. Refs. [21, 136–139]. Assuming a detuning set to the maximum value that permits a single soliton $\zeta_{\mathrm{BSO,max}} = \pi^2 F/8$ [21, 137], they read as follows:

$$2\mu^\star_{\mathrm{BSO,max}} \approx \sqrt{2}\ln(1+\sqrt{2})\sqrt{F/\beta'}, \tag{3.9a}$$

$$\eta_{\mathrm{BSO,max}} \approx \sqrt{\beta'/(2F)}. \tag{3.9b}$$

More details on these equations can be found in Appendix B.3. Expressions for the approximation of DSOs resembling a flipped sech function on top of a cw background are given in Ref. [124]; compare the green curve in Fig. 3.2(b). They are valid near the bifurcation point and are obtained using multiple scale asymptotics. As mentioned before, this kind of solitons, indicated in Fig. 3.2(a) by point D, is of less interest due to its weaker localization, reduced comb bandwidth, and power compared to the DSO at point F. For DSOs of the latter type,

no formula for the comb bandwidth or PCE is available, to the best of our knowledge.

For dispersion parameters $\beta' = \pm 0.1, \pm 0.15, \pm 0.2, \pm 0.25$ and $\sqrt{F} > 1$, we have carried out a large parameter study. For $\beta' > 0$, we computed the last bifurcation point and its corresponding bifurcating branch. Based on the heuristics in Sec. 3.3, we stopped the computation as soon as we reached the first turning point, i.e., point C in Fig. 3.1(a), where the most localized BSO is found. In the same manner, the strongest localized DSO in the case $\beta' < 0$ is at the second turning point of the first bifurcating branch, i.e., point F in Fig. 3.2(a). For all of the above values of the dispersion β' and the pump power $\sqrt{F}$, the corresponding solitons at the turning point were investigated and their comb bandwidth as well as their PCE were evaluated.

The results are plotted in Fig. 3.4. For BSOs, gray lines corresponding to the approximate expressions in Eqs. (3.9a) and (3.9b) are also shown in Figs. 3.4(a) and 3.4(c). As mentioned before, the validity of these approximations is guaranteed only for small damping, small forcing, and large forcing/damping ratio [138, 139]. This explains the deviations from the curves computed by numerical bifurcation and continuation which occur for PCE in the small $\sqrt{F}$ regime [damping in Eq. (3.2) is set to 1] in Fig. 3.4(c) and for comb bandwidth in the large $\sqrt{F}$ regime in Fig. 3.4(a). The comb bandwidth increases with an increasing $\sqrt{F}$ at the expense of a decreasing conversion efficiency. Additionally, one can see that with $\beta' \to 0$ the comb bandwidth increases whereas the PCE decreases.

For DSOs, the overall dependence of the conversion efficiency and comb bandwidth shows the same trends as for BSOs, see Figs. 3.4(b) and 3.4(d). In direct comparison, DSOs have a decreased bandwidth along with a higher conversion efficiency for the same values of $\sqrt{F}$ and $|\beta'|$. We attribute this to the strong constant background of the DSOs in the spatial domain which enables a more efficient power transfer from the CW pump to the soliton. However, the increased spatial width of the DSOs is also linked to a narrower frequency comb in the spectral domain. We note that the comb bandwidth of both BSOs and DSOs does not increase strictly linearly with an increasing forcing. For DSOs, the nonlinear behavior is more pronounced.

For the physical properties of soliton frequency combs in non-normalized units, the bandwidth $2\mu^\star$ as well as the conversion efficiencyη have to be converted. The physical comb bandwidth $\Omega_{3\mathrm{dB}}/(2\pi)$ is obtained by multiplying $2\mu^\star$ with

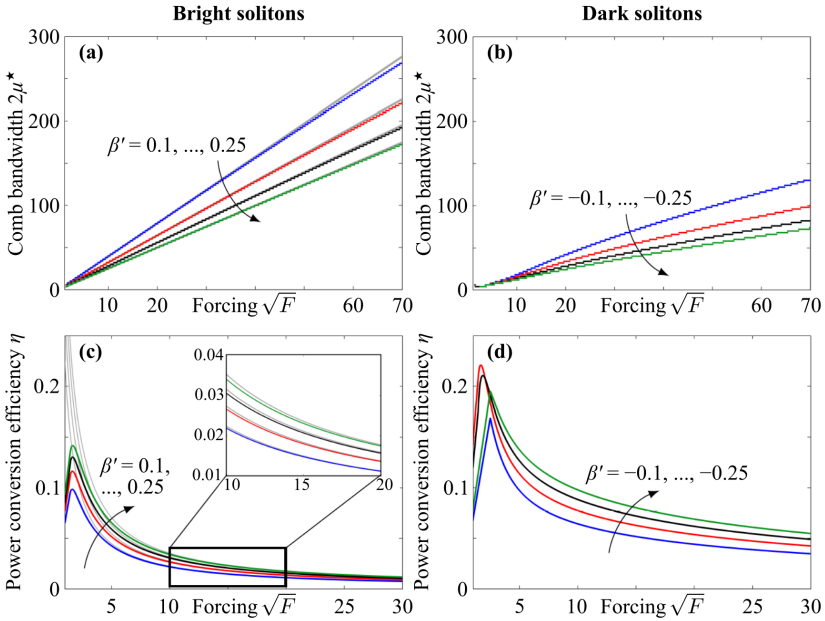

Figure 3.4: Bandwidths $2\mu^\star$ and power conversion efficiencies (PCE) η for bright-soliton combs (a), (c) and dark-soliton combs (b), (d) as a function of dispersion $\beta' = \pm 0.1, \pm 0.15, \pm 0.2, \pm 0.25$ and the forcing $\sqrt{F}$. Quantities on axes are dimensionless. (a) Bandwidth of bright-soliton combs obtained by numerical bifurcation and continuation (NBC, colored lines) along with an approximation according to Eq. (3.9a). The linear approximation is in good agreement with the numerical results and deviates only for a strong forcing. A stronger dispersion leads to a decreasing comb bandwidth. (b) Bandwidth of dark-soliton combs obtained by NBC. (c) PCE of bright-soliton states obtained by NBC (colored lines) along with an approximation according to Eq. (3.9b) (gray lines). The approximation is in good agreement with the numerical results, but deviates strongly for weak forcing. A weaker dispersion leads to a decreasing PCE. (d) PCE of dark-soliton states obtained by NBC. The PCE decreases with an increasing forcing, but is overall higher as for bright solitons. Here, weaker dispersion also leads to a decreasing PCE.

the free spectral range FSR of the resonator, i.e., the inverse of the round-trip time t_R of the light inside:

$$\Omega_{3\mathrm{dB}}/(2\pi) = \omega_{\mathrm{FSR}}/(2\pi) \times 2\mu^\star = t_\mathrm{R}^{-1} \times 2\mu^\star. \tag{3.10}$$

To determine the physical conversion efficiency outside the resonator η_{out}, the physical power coupling coefficient θ_{C} between the bus waveguide and the microresonator as well as the physical round-trip-power-loss coefficient α have to be taken into consideration via the relation

$$\eta_{\mathrm{out}} = \frac{4\theta_{\mathrm{C}}^2}{(\alpha + \theta_{\mathrm{C}})^2}\eta. \tag{3.11}$$

For details on Eq. (3.11), see Appendix B.4. To achieve high external power conversion efficiencies > 30 % as, e.g., in Ref. [140], an *overcoupled* resonator with $\alpha \ll \theta_{\mathrm{C}}$ is preferable. As visible in Figs. 3.4(c) and 3.4(d), a microresonator with normal dispersion-enabling DSO states will tend to improve the PCE. It should be noted, however that the generation of normal dispersion frequency combs generally requires an avoided mode crossing for initial modulation instability [130], which makes the design of the device more complex.

3.5 Summary

We have performed a global bifurcation analysis of the LLE and provided an overview on the structure of nontrivial solutions. We find single-soliton frequency combs both in the normal and anomalous-dispersion regime. Our investigation covers a broad space of technically relevant device and operation parameters. It allows us to identify the broadest soliton combs and to benchmark them with respect to bandwidth and pump-to-comb power conversion efficiency. Our findings are in good agreement with simplified analytic models. Comparing the results for BSOs and DSOs, we find that DSOs outperform BSOs significantly in terms of power conversion efficiency at the expense of a reduced bandwidth.

The bifurcation and continuation method allows us to determine the performance parameters of single-soliton comb states even for the cases where simplified analytic models are not valid, e.g., for certain DSOs. Our approach can be further extended to include additional effects such as two-photon absorption and to study their impact on the stationary comb states, see Ref. [141]. The results of our investigation allow for targeted design of soliton comb generators for specificapplications. In this context, the power conversion efficiency

and the comb bandwidth are key performance characteristics that need to be optimized under technical restrictions such as limited optical input power.

[End of publication [J1]]

4 Analysis of Kerr comb generation in silicon microresonators under the influence of two-photon absorption and fast free-carrier dynamics

In this chapter, an analysis of Kerr comb formation in microresonators under the influence of two-photon absorption and free-carrier absorption is performed. The content of this chapter has been published in *Physical Review A* [J2] and was adapted to fit the layout, structure and notation of this dissertation. The related appendices are given in Appendix C. This chapter assumes a negative time dependence of the optical signal of the form $\exp(-\mathrm{j}\omega t)$. Furthermore, in this chapter as well as in Appendix C the unit of electric fields is assumed to be $\sqrt{\mathrm{W}}$ [77, 86, 142]. As a consequence, magnetic fields have the unit $\sqrt{\mathrm{W}}\mathrm{A/V}$ and the power P of an electric field is given by $P = \left|\underline{\mathcal{E}}\right|^2 = \left|\underline{\mathcal{E}^*}\right|^2$.

The publication predominantly relies on the contributions of the author of this dissertation. The scope of the publication and the underlying physical model were developed by the author jointly with C. Koos and further discussed with P. Marin-Palomo, see Sections 4.1 and 4.2. The mathematical computations described in Sections 4.3, 4.4 and Appendix C.1 were verified by J. Gärtner and W. Reichel. Numerical methods used for the time integration of the Lugiato-Lefever equation, see Section 4.5 and Appendix C.5, were discussed with T. Jahnke and C. Koos. The manuscript was written by the author with support of W. Freude and C. Koos. The work was supervised by W. Freude, W. Reichel, and C. Koos.

[Start of publication [J2]]

Analysis of Kerr comb generation in silicon microresonators under the influence of two-photon absorption and fast free-carrier dynamics

Physical Review A, **103**(6), 063515 (2021)

P. Trocha,[1] J. Gärtner,[2] P. Marin-Palomo,[1] W. Freude,[1,3] W. Reichel,[2] C. Koos[1,3]

[1] Institute of Photonics and Quantum Electronics (IPQ), Karlsruhe Institute of Technology (KIT), Karlsruhe, Germany

[2] Institute for Analysis (IANA), Karlsruhe Institute of Technology (KIT), Karlsruhe, Germany

[3] Institute of Microstructure Technology (IMT), Karlsruhe Institute of Technology (KIT), Karlsruhe, Germany

Kerr frequency comb generation relies on dedicated waveguide platforms that are optimized toward ultra-low loss while offering comparatively limited functionality restricted to passive building blocks. In contrast to that, the silicon-photonic platform offers a highly developed portfolio of high-performance devices, but suffers from strong two-photon absorption (TPA) and subsequent free-carrier absorption (FCA) at near-infrared telecommunication wavelengths, thereby rendering Kerr comb generation a challenge. Here we present a model to investigate the impact of TPA and FCA on Kerr comb formation. Our model combines a modified version of the Lugiato-Lefever equation with a refined relation to precisely describe the fast space and time dependence of the free-carrier concentration along the circumference of the microresonator. Using this refined model, we derive conditions for modulation instability, in particular for necessary pump powers depending on TPA parameters and free-carrier lifetimes. We validate our analytical predictions by time integration and study the impact of fast free-carrier dynamics on Kerr comb formation. We find that silicon microresonators may be suitable for Kerr comb generation in the NIR, provided that the dwell time of the TPA-generated free carriers in the waveguide core is reduced by a reverse-biased *p-i-n*-junction and that the pump parameters are chosen appropriately.

4.1 Introduction

Generation of optical frequency combs in high-Q Kerr-nonlinear microresonators [10, 11] has the potential to unlock a wide range of applications such as timekeeping [16], frequency synthesis [88], optical communications [J5], spectroscopy [18] and optical ranging [J3] [90]. Among different frequency comb states, dissipative Kerr solitons (DKSs) [21] are particularly attractive, offering broadband optical spectra with hundreds of phase-locked optical tones spaced by free spectral ranges of tens of gigahertz. As a key advantage in comparison to conventional comb sources built from discrete components, Kerr comb generators offer a small footprint and can be integrated into robust chip-scale photonic systems that lend themselves to cost-efficient mass production. So far, integrated optical Kerr comb sources have mostly been realized using specifically optimized silica and silicon nitride based waveguides that offer ultra-low propagation loss down to $5.5\,\mathrm{dB\,m^{-1}}$ along with anomalous group-velocity dispersion [143, 144], and that can bear high power levels. The functionality of these integration platforms, however, is still limited to merely passive devices. In contrast to that, silicon photonics offers a highly developed portfolio of active and passive devices that are specifically geared toward operation at near-infrared (NIR) telecommunication wavelengths between 1200 nm and 1700 nm. These devices can be reliably fabricated at low cost on large-area silicon substrates [145–147] and lend themselves to cointegration with electronic devices [148]. Expanding the silicon-photonic integration platform by monolithically integrated Kerr comb sources could have transformative impact regarding functionality, performance, footprint and cost of comb-based optical systems. For wavelengths in the mid infrared, Kerr comb formation in silicon microresonators under the influence of three-photon absorption and free-carrier absorption was already experimentally demonstrated [149]. In contrast to that, at NIR telecommunication wavelengths, Kerr generation comb in silicon microresonators is impaired by of two-photon absorption (TPA) and subsequent free-carrier absorption (FCA) and has so far only been investigated theoretically [26–28]. Interestingly, Ref. [26] predicts that generation of NIR Kerr combs should also be possible in silicon microresonators, provided that TPA-generated free carriers are removed from the Si waveguide core by reverse-biased *p-i-n*-junctions [29]. Specifically, the effective dwell times of the carriers in the waveguide core should be reduced from 1 ... 5 ns [25, 29, 77, 149, 150] to, e.g., 100 ps , which is of the same order as

the round-trip time of the soliton pulses in the cavity [6, 11]. This conclusion, however, conflicts with the fact that Ref. [26] builds upon a formalism [77] that ignores fast carrier dynamics and assumes a spatially uniform distribution of the free carriers along the microresonator circumference.

In this paper, we expand the theoretical analysis of Kerr comb formation by including fast dynamics of TPA-generated free-carriers. Building upon an analytical model that complements the Lugiato-Lefever equation (LLE [76, 142]) by including TPA and dispersion anomalies of the ring resonances caused by avoided mode crossings, we introduce a description of the fast free-carrier dynamics based on a spatially non-uniform distribution along the microresonator circumference. Our approach allows us to describe the full spatio-temporal evolution of the free-carrier density within the ring and serves as a starting point for subsequent analysis of necessary conditions that must be fulfilled for achieving modulation instability (MI) and subsequent comb formation. Based on this analysis, we formulate simple conditions that must be fulfilled for achieving modulation instability and subsequent comb formation in dependence of the underlying TPA coefficient, the free-carrier lifetime and FCA cross-section. We describe the dependence on the MI threshold pump power on TPA and FCA parameters, and we find an upper limit for the TPA coefficient, above which comb formation is impossible even in the absence of FCA. The theoretical predictions are independently confirmed by numerical simulations that are based on time integration of the Lugiato-Lefever equation and the modified rate equation for the free carriers. While the model is general and can be broadly applied to different material platforms, we focus our investigation on silicon-photonic microresonators, in which the free-carrier dwell time can be artificially reduced by a reverse-biased *p*-*i*-*n*-junction that is built around the respective waveguide core. We find that Kerr comb generation in silicon microresonators can be achieved within technically realistic parameter ranges for free-carrier lifetime and pump power. We further develop and numerically validate a design for a silicon-photonic Kerr comb source that has a free spectral range (FSR) of 100 GHz and a threshold pump power of 12 mW and that should even be suitable for dissipative Kerr-soliton (DKS) comb formation. It turns out that the incorporation of fast free-carrier dynamics changes the behaviour of the optical waveforms in the microresonator to a notable degree, whereas the conditions for MI are essentially unaffected and remain consistent with the findings from simpler models [26–28].

4.2 Model

In our model, we describe the electric field $\mathcal{E}(z,t) = \Re\left\{\underline{\mathcal{E}}^*(z,t)\mathrm{e}^{-\mathrm{j}\omega_\mathrm{p}t}\right\}$ in the Kerr-nonlinear microresonator (MR) by a carrier at the (angular) frequency ω_p of the optical pump wave in combination with a complex slowly-varying amplitude $\underline{\mathcal{E}}^*(z,t)$ that depends on time t and on the position z along the resonator circumference. The presence of the strong pump leads to parametric gain for a pair of modes located symmetrically to both sides of the pump frequency ω_p. If the parametric gain for any of these modes exceeds the resonator losses, the corresponding mode amplitudes are amplified by resonant four-wave mixing, drawing energy from the pump wave. At the same time, the presence of a strong pump wave leads to generation of free carriers (FCs) through two-photon absorption (TPA). These carriers accumulate and lead to additional optical losses through free-carrier absorption (FCA). For silicon-photonic microresonators, the dwell time t_eff and the associated concentration N_car of the free carriers can be influenced by a reverse-biased *p-i-n*-junction [29, 151], see Fig. 4.1. In the following, we consider the evolution of the field amplitude and of the free-carrier density over multiple cavity round-trip times $t_\mathrm{R} = L_\mathrm{MR}/v_\mathrm{g} = 2\pi/\omega_\mathrm{FSR}$, where $\omega_\mathrm{FSR}/(2\pi)$ denotes the free spectral range of the cavity as defined by the perimeter L_MR and by the optical group velocity $v_\mathrm{g} = c_0/n_\mathrm{g}$ that is obtained at the pump frequency ω_p in the absence of free carriers. The number of round-trips is denoted by an integer κ, and we introduce a long time scale ("slow" time variable) $t = \kappa\, t_\mathrm{R}$, which we consider to be continuous. At the same time, we model the evolution of the complex slowly varying amplitude $\underline{\mathcal{E}}^*$ within the cavity using a short time scale ("fast" time variable) $\tau = t - z/v_\mathrm{g}$ that is retarded according to the position z inside the cavity, thus accounting for the propagation of the optical amplitude $\underline{\mathcal{E}}^*$ with optical group velocity v_g. The slowly varying amplitude $\underline{\mathcal{E}}^*(t,\tau)$ inside the resonator is modelled as a superposition of fields with complex envelopes $\underline{\mathcal{E}}^*_\mu(t)$, oscillating at equidistant angular frequencies which are offset from the pump frequency $\omega_\mathrm{p} = \omega_0$ by $\omega_{\Delta\mu} = \mu \times \omega_\mathrm{FSR}$ ($\mu = 0, \pm1, \pm2, \pm3, \ldots$) and thus given as

$$\underline{\mathcal{E}}^*(t,\tau) = \sum_\mu \underline{\mathcal{E}}^*_\mu(t)\,\mathrm{e}^{\mathrm{j}\omega_{\Delta\mu}\tau} = \sum_\mu \underline{\mathcal{E}}^*_\mu(t)\,\mathrm{e}^{\mathrm{j}2\pi\tau/t_\mathrm{R}}. \tag{4.1}$$

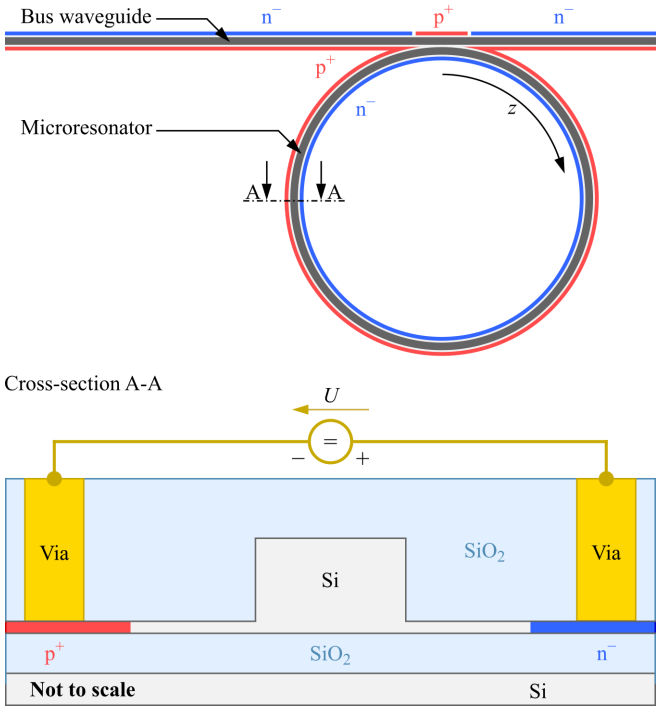

Figure 4.1: Silicon-photonic microresonator as an example of a device suffering from both TPA and FCA. The bus waveguide as well as the resonator ring waveguide are connected to p^+-doped (red) and n^--doped silicon (Si) regions (blue) that form a *p-i-n*-junction. This junction allows the reduction of the dwell time of free carriers by applying a reverse bias voltage U through contact pads and vias. At the coupling section between the bus and the ring waveguide, the doping is locally inverted from an n^--doping to a p^+-doping next to the bus waveguide to ensure maximum free-carrier removal in the microresonator [152]. The geometrical dimensions of the waveguide cross-section can be chosen such that the waveguide features anomalous group-velocity dispersion (GVD) at wavelengths near 1550 nm, see, e.g., [153]. Further, the microresonator diameter can be chosen to achieve a specific free spectral range of, e.g., $\omega_{\mathrm{FSR}}/(2\pi) = 100\,\mathrm{GHz}$, corresponding to a round-trip time $t_{\mathrm{R}} = (\omega_{\mathrm{FSR}}/(2\pi))^{-1} = 10\,\mathrm{ps}$. For details on the geometrical dimensions used in our simulations, see Section 4.5.

In contrast to the optical amplitude $\underline{\mathcal{E}}^*(t,\tau)$, generated free carriers do not move inside the microresonator. Therefore, we model them on another, stationary fast time scale $\tau_\mathrm{S} = -z/v_\mathrm{g}$ to describe their spatial distribution $N_\mathrm{car}(t,\tau_\mathrm{S})$ along the microresonator circumference. The stationary fast time scale τ_S and its retarded counterpart are related by $\tau = \tau_\mathrm{S} + t$. The optical field and the free-carrier density in the retarded time frame are transformed between the retarded and the static fast time scale via $\underline{\mathcal{E}}^*(t,\tau) = \underline{\mathcal{E}}^*(t,\tau_\mathrm{S}+t)$, and $N_\mathrm{car}(t,\tau-t) = N_\mathrm{car}(t,\tau_\mathrm{S})$. The field obeys periodic boundary conditions, $\underline{\mathcal{E}}^*(t,\tau) = \underline{\mathcal{E}}^*(t,\tau+t_\mathrm{R})$. Disregarding temperature effects, self-steepening, higher-order dispersion, and higher-order multi-photon absorption, the LLE and the stationary FC equation read [25, 77]

$$\begin{aligned} t_\mathrm{R}\frac{\partial\underline{\mathcal{E}}^*(t,\tau)}{\partial t} = \sqrt{\theta_\mathrm{C}}\mathcal{E}_\mathrm{in} + \Bigg[&-\frac{\alpha_i L_\mathrm{MR}}{2} - \frac{\theta_\mathrm{C}}{2} - \mathrm{j}\delta_0 - \mathrm{j}\frac{\beta^{(2)}L_\mathrm{MR}}{2}\frac{\partial^2}{\partial\tau^2} + \mathrm{j}\hat{\Phi}_\mathrm{AMC} \\ &+ \left(\mathrm{j}\gamma L_\mathrm{MR} - \frac{\beta_\mathrm{TPA}L_\mathrm{MR}}{2A_\mathrm{eff}}\right)\left|\underline{\mathcal{E}}^*(t,\tau)\right|^2 \\ &- \frac{\sigma_\mathrm{car}\Gamma_\mathrm{C}L_\mathrm{MR}}{2}(1+\mathrm{j}\beta_\mathrm{car})N_\mathrm{car}(t,\tau-t)\Bigg]\underline{\mathcal{E}}^*(t,\tau), \end{aligned} \tag{4.2}$$

$$\frac{\partial N_\mathrm{car}(t,\tau_\mathrm{S})}{\partial t} = \frac{\beta_\mathrm{TPA}}{2\hbar\omega_\mathrm{p}}\frac{\left|\underline{\mathcal{E}}^*(t,\tau_\mathrm{S}+t)\right|^4}{A_\mathrm{eff}^2} - \frac{N_\mathrm{car}(t,\tau_\mathrm{S})}{t_\mathrm{eff}}. \tag{4.3}$$

In these relations, the quantity $\mathcal{E}_\mathrm{in}$ denotes the electric field amplitude of the pump with power $P_\mathrm{in} = |\mathcal{E}_\mathrm{in}|^2$ in the bus waveguide, see Fig. 4.1, θ_C describes the power coupling to the microresonator, and α_i (unit m^{-1}) is the waveguide power loss coefficient inside the MR. The resonator parameters are assumed to be the same for all complex envelopes $\underline{\mathcal{E}}_\mu^*(t)$, unless specified otherwise. The detuning $\delta_0 = (\omega_{\mathrm{r},0} - \omega_\mathrm{p})\,t_\mathrm{R}$ corresponds to the offset of the pump frequency ω_p from the resonance frequency $\omega_{\mathrm{r},0}$ of the pumped mode. The coefficient $\beta^{(2)}$ describes the second-order dispersion of the cavity. The nonlinearity parameter of the resonator waveguide is denoted by $\gamma = \omega_\mathrm{p}c_0^{-1}n_2A_\mathrm{eff}^{-1}$ (unit $\mathrm{m}^{-1}\mathrm{W}^{-1}$) with the nonlinear Kerr coefficient n_2 (unit $\mathrm{m}^2\mathrm{W}^{-1}$), the vacuum speed of light c_0, and the effective mode-field area A_eff. The quantity β_TPA denotes the two-photon absorption coefficient, σ_car is the free-carrier absorption cross-section, and β_car the free-carrier dispersion parameter which describes the influence of FC on the real part of the refractive index. The reduced Planck constant is $\hbar$.

The model additionally includes a field confinement factor Γ_C which accounts for the fact that only a fraction of the optical mode field experiences the attenuation and dispersion by FCs generated in the resonator waveguide [154]. Since we consider only modes for which the field is strongly confined to the waveguide, we may assume $\Gamma_C \approx 1$, whereas other waveguide designs, e.g., slot waveguides with a nonlinear organic cladding [155, 156] may lead to values of Γ_C that are significantly smaller than 1. Finally, we include the possibility of local resonance shifts $\delta\omega_\mu$ caused by avoided mode crossings (AMCs) [61, 157, 158]. These resonance shifts lead to additional phase shifts $\delta\omega_\mu t_R$ for the respective electric field envelopes $\underline{\mathcal{E}}^*_\mu(t)$. The impact of AMCs can hence be described by an operator $\hat{\Phi}_{AMC}$ acting on the envelope field $\underline{\mathcal{E}}^*(t,\tau)$ of Eq. (4.1),

$$\begin{aligned}\hat{\Phi}_{AMC}\underline{\mathcal{E}}^*(t,\tau) &= \sum_{\tilde{\mu}}\left(\delta\omega_{\tilde{\mu}}\exp(\,\mathrm{j}2\pi\tilde{\mu}/t_R)\int_0^{t_R}\underline{\mathcal{E}}^*(t,\tau_1)\,\mathrm{e}^{-\mathrm{j}2\pi\tilde{\mu}\tau_1/t_R}\mathrm{d}\tau_1\right)\\ &= \sum_{\tilde{\mu},\mu}\left(\delta\omega_{\tilde{\mu}}t_R\underline{\mathcal{E}}^*_\mu(t)\exp(\,\mathrm{j}2\pi\tilde{\mu}\tau/t_R)\,\delta_{\tilde{\mu}\mu}\right)\\ &= \sum_{\mu'}\left(\delta\omega_{\mu'}t_R\underline{\mathcal{E}}^*_{\mu'}(t)\exp(\,\mathrm{j}2\pi\mu'\tau/t_R)\right),\end{aligned} \tag{4.4}$$

where $\delta_{\tilde{\mu}\mu}$ denotes the Kronecker delta. In the absence of AMCs, all resonance shifts $\delta\omega_\mu$ are zero and thus do not lead to any additional phase shifts $\delta\omega_\mu t_R$ for the electric field envelopes $\underline{\mathcal{E}}^*_\mu(t)$. In the following, we simplify Eq. (4.2) by assuming critical coupling , i.e., $\alpha_i L_{MR} = \theta_C$. For normalization, we multiply Eq. (4.2) with $(\gamma n_g^2/(\alpha_i^3 t_R^2 c_0^2))^{1/2}$ and Eq. (4.3) with $n_2\hbar\omega_p^2/(\alpha_i^2 c_0)$. We introduce the normalized quantities specified in Table 4.1 and reformulate Eq. (4.2), (4.3) and (4.4):

$$\begin{aligned}\frac{\partial\underline{a}(t',\tau')}{\partial t'} =&\sqrt{F}+\left[-1-\mathrm{j}\zeta+\mathrm{j}\beta'\frac{\partial^2}{\partial\tau'^2}+\mathrm{j}\hat{\Phi}'_{AMC}+(\mathrm{j}-r)\left|\underline{a}(t',\tau')\right|^2\right.\\ &\left.-\sigma'_{car}(1+\mathrm{j}\beta_{car})N'_{car}(t',\tau'-t'v')\right]\underline{a}(t',\tau'),\end{aligned} \tag{4.5}$$

$$\frac{\partial N'_{car}(t',\tau'_S)}{\partial t'} = r\left|\underline{a}(t',\tau'_S+t'v')\right|^4-\frac{N'_{car}(t',\tau'_S)}{t'_{eff}}, \tag{4.6}$$

Table 4.1: Normalized quantities and substitutions.

Slow time	t'	=	$\frac{\alpha_i L_{\mathrm{MR}}}{t_{\mathrm{R}}} t = \frac{\alpha_i c_0}{n_{\mathrm{g}}} t$
Fast time (retarded)	τ'	=	$\frac{2\pi}{t_{\mathrm{R}}} \tau$
Fast time (stationary)	τ'_{S}	=	$\frac{2\pi}{t_{\mathrm{R}}} \tau_{\mathrm{S}}$
Normalized group velocity	v'	=	$\frac{2\pi n_{\mathrm{g}}}{t_{\mathrm{R}} \alpha_i c_0}$
Optical field	$\underline{a}\,(t', \tau')$	=	$\sqrt{\frac{\gamma}{\alpha_i}}\, \underline{\mathcal{E}}^*\,(t, \tau)$
Free-carrier density	$N'_{\mathrm{car}}\,(t', \tau')$	=	$\frac{\hbar \omega_{\mathrm{p}}^2 n_2}{\alpha_i n_{\mathrm{g}}} N_{\mathrm{car}}\,(t, \tau)$
Pump field	$\sqrt{F}$	=	$\sqrt{\frac{\gamma n_{\mathrm{g}}}{c_0 \alpha_i^2 t_{\mathrm{R}}}} \sqrt{P_{\mathrm{in}}}$
Detuning	ζ	=	$\frac{n_{\mathrm{g}}}{\alpha_i t_{\mathrm{R}} c_0} \delta_0$
Phase shift operator	$\hat{\Phi}'_{\mathrm{AMC}}$	=	$\frac{n_{\mathrm{g}}}{\alpha_i t_{\mathrm{R}} c_0} \hat{\Phi}_{\mathrm{AMC}}$
Phase shifts	$\phi_{\tilde{\mu}}$	=	$\frac{n_{\mathrm{g}}}{\alpha_i c_0} \delta \omega_{\tilde{\mu}}$
Dispersion	β'	=	$-\frac{2\pi^2}{\alpha_i t_{\mathrm{R}}^2} \beta^{(2)}$
TPA parameter	r	=	$\frac{c_0}{2\omega_{\mathrm{p}} n_2} \beta_{\mathrm{TPA}}$
FC dwell time	t'_{eff}	=	$\frac{\alpha_i c_0}{n_{\mathrm{g}}} t_{\mathrm{eff}}$
FC cross-section	σ'_{car}	=	$\frac{\Gamma_{\mathrm{C}} n_{\mathrm{g}}}{2 n_2 \hbar \omega_{\mathrm{p}}^2} \sigma_{\mathrm{car}}$

$$\hat{\Phi}'_{\mathrm{AMC}} \underline{a}\,(t', \tau') = \sum_{\tilde{\mu}} \frac{\phi_{\tilde{\mu}}}{2\pi} \int_0^{2\pi} \underline{a}\,(t', \tau_1)\, \mathrm{e}^{-\mathrm{j}\tilde{\mu}\tau_1}\, \mathrm{d}\tau_1 \mathrm{e}^{\mathrm{j}\tilde{\mu}\tau'}. \tag{4.7}$$

In Equations (4.5) and (4.6), we have introduced the normalized group velocity $v' = 2\pi n_{\mathrm{g}}/(t_{\mathrm{R}} \alpha_i c_0)$ to describe the speed, at which the normalized optical field $\underline{a}\,(t', \tau') = \underline{a}\,\left(t', \tau'_{\mathrm{S}} + t' v'\right)$ propagates on the normalized stationary fast time scale τ'_{S}. In the same manner, the FC density in the normalized retarded fast time frame is described by $N'_{\mathrm{car}}\,(t', \tau' - t' v') = N'_{\mathrm{car}}\,\left(t', \tau'_{\mathrm{S}}\right)$.

4.3 Investigation of modulation instability considering fast-time free-carrier dynamics

To investigate the circumstances under which modulation instability can occur when pumping the resonator, we need to know whether any pair of resonator modes experiences a sufficiently high parametric gain to overcome the total loss in the resonator. This loss includes linear propagation loss and coupling loss, which are equal for critical coupling, $\alpha_i L_{\mathrm{MR}} = \theta_{\mathrm{C}}$, and which are expressed by -1 in Eq. (4.5), two-photon absorption, expressed by $-r\left|\underline{a}\left(t', \tau'\right)\right|^2$ in Eq. (4.5), and free-carrier absorption, expressed by $-\sigma'_{\mathrm{car}} N'_{\mathrm{car}}\left(t', \tau' - t'v'\right)$ in Eq. (4.5), where the normalized density of accumulated carriers strongly depends on the carrier dwell time t_{eff} and its normalized counterpart t'_{eff}, see Eq. (4.6). For exploring modulation instability, we use an ansatz for the normalized optical resonator field $\underline{a}\left(t', \tau'\right)$, consisting of a strong field $\underline{a}_0$ in the pumped resonator mode (normalized power $A = |\underline{a}_0|^2$) and a pair of weak fields $\underline{a}_{\pm M}$ ("sidebands" for short) in resonator modes which are offset from the pump frequency ω_{p} by $\omega_{\pm\Delta M} = \pm M \times \omega_{\mathrm{FSR}}$, $(M \in \mathbb{N}_+)$ [81]. The amplitude of these sidebands may change, which is expressed by a complex normalized gain rate $\underline{g} = g + \mathrm{j}g_{\mathrm{j}}$, $g, g_{\mathrm{j}} \in \mathbb{R}$. This leads to a three-wave ansatz of the form

$$\begin{aligned}\underline{a}\left(t', \tau'\right) = \underline{a}_0 &+ \underline{\hat{a}}_{+M} \mathrm{e}^{gt'} \mathrm{e}^{\mathrm{j}g_{\mathrm{j}}t'} \mathrm{e}^{\mathrm{j}M\tau'} \\ &+ \underline{\hat{a}}_{-M} \mathrm{e}^{gt'} \mathrm{e}^{-\mathrm{j}g_{\mathrm{j}}t'} \mathrm{e}^{-\mathrm{j}M\tau'}, \quad \left|\underline{\hat{a}}_{\pm M}\right| \ll \left|\underline{a}_0\right|. \end{aligned} \tag{4.8}$$

In the stationary fast time frame, this ansatz reads

$$\begin{aligned}\underline{a}\left(t', \tau'_{\mathrm{S}} + t'v'\right) = \underline{a}_0 &+ \underline{\hat{a}}_{+M} \mathrm{e}^{gt'} \mathrm{e}^{\mathrm{j}g_{\mathrm{j}}t'} \mathrm{e}^{\mathrm{j}M\left(\tau'_{\mathrm{S}} + t'v'\right)} \\ &+ \underline{\hat{a}}_{-M} \mathrm{e}^{gt'} \mathrm{e}^{-\mathrm{j}g_{\mathrm{j}}t'} \mathrm{e}^{-\mathrm{j}M\left(\tau'_{\mathrm{S}} + t'v'\right)}. \end{aligned} \tag{4.9}$$

We assume that the sideband amplitudes $\underline{\hat{a}}_{\pm M}$ are initially much smaller than the amplitude of the pumped mode $\underline{a}_0$, $|\underline{\hat{a}}_{\pm M}| \ll |\underline{a}_0|$, such that we can treat them as a weak perturbation by linearizing Eqs. (4.5) and (4.6) in $\underline{\hat{a}}_{+M}, \underline{\hat{a}}_{-M}$ about the strong field of the pumped mode $\underline{a}_0$. Inserting Eq. (4.8) into the linearized version of Eq. (4.5) and inserting Eq. (4.9) into Eq. (4.6) allows us to derive an expression for normalized the gain rate $\underline{g}\left(M\right)$, see Appendix C.1. Modulation instability occurs for $\Re\{\underline{g}\left(\Omega\right)\} = g\left(M\right) > 0$, in which case the sideband amplitudes at $\pm M$ grow exponentially with time. The initial field oscillates

with $\pm M$ with respect to the normalized fast time τ', and it experiences a phase shift $\pm \mathrm{j} g_\mathrm{j} t'$ with normalized slow time t'.

To identify resonator and pump parameters for which modulation instability can occur, we first derive an expression for $\underline{g}$ in terms of these parameters. To this end, we first solve the differential equation for the normalized free-carrier density, Eq. (4.6), and then substitute the resulting relation for $N'_\mathrm{car}\left(t', \tau'_\mathrm{S}\right)$ in Eq. (4.5). In this step, we assume the modulation instability to be weak, i.e., $|g| \ll 1/t'_\mathrm{eff}$. Since we are looking at the onset of MI just above its threshold, the gain parameter g is barely larger than zero and is smaller than the inverse of the free-carrier lifetime, i.e., $|g| \ll 1/t'_\mathrm{eff}$. The latter assumption is justified by the fact that, for proper choice of reverse-bias conditions, the carrier dwell time is of the order of the cavity-round-trip time, whereas the MI sidebands build up slowly over tens of cavity round-trips if the resonator is operated slightly above its MI threshold. Further details on the derivation and on the underlying approximations can be found in Appendix C.1. We further assume the imaginary part g_j of the gain parameter to be small, in particular $\left|g_\mathrm{j}\right| \ll M v'$, which is justified by the fact that MI sidebands will occur in close spectral vicinity of a ring resonance, for details see Appendix C.1. With an expression for the free-carrier density at hand (see Eqs. (C.8) and (C.9) of Appendix C.1), we substitute Eq. (4.8) in Eq. (4.5) and neglect all small second-order products of the form $\underline{\hat{a}}^2_{\pm M}$, $|\underline{\hat{a}}_{\pm M}|^2$, $\underline{\hat{a}}_{+M}\underline{\hat{a}}_{-M}$. We then solve the resulting equation for $\underline{g}$ (see Appendix C.1), and obtain two complex solutions $\underline{g}_\pm = g_\pm + \mathrm{j} g_{\mathrm{j},\pm}$. From these solutions, we select the one for which the real part g_+ can assume positive values, corresponding to modulation instability,

$$g\,(M) = -\,1 - 2rA - r t'_\mathrm{eff}\sigma'_\mathrm{car}\frac{3 + \left(M t'_\mathrm{eff} v'\right)^2}{1 + \left(M t'_\mathrm{eff} v'\right)^2}A^2 + \Re\{\underline{\Delta}\}, \quad \Re\{\underline{\Delta}\} > 0, \tag{4.10}$$

$$g_\mathrm{j}\,(M) = \frac{\phi_{+M} - \phi_{-M}}{2} + 2\frac{r t'_\mathrm{eff}\sigma'_\mathrm{car} M t'_\mathrm{eff} v'}{1 + \left(M t'_\mathrm{eff} v'\right)^2}A^2 + \Im\{\underline{\Delta}\},$$

$$\underline{\Delta} = \Bigg[A^2 \left(r + \frac{2rt'_{\mathrm{eff}}\sigma'_{\mathrm{car}}}{1+(Mt'_{\mathrm{eff}}\nu')^2} A - \mathrm{j}\frac{2rt'_{\mathrm{eff}}\sigma'_{\mathrm{car}} Mt'_{\mathrm{eff}}\nu'}{1+(Mt'_{\mathrm{eff}}\nu')^2} A \right)^2 + A^2 \left(1 - \frac{2rt'_{\mathrm{eff}}\sigma'_{\mathrm{car}}\beta_{\mathrm{car}}}{1+(Mt'_{\mathrm{eff}}\nu')^2} A + \mathrm{j}\frac{2rt'_{\mathrm{eff}}\sigma'_{\mathrm{car}}\beta_{\mathrm{car}} Mt'_{\mathrm{eff}}\nu'}{1+(Mt'_{\mathrm{eff}}\nu')^2} A \right)^2 - \Bigg(\zeta + \beta' M^2 - \frac{\phi_+ + \phi_-}{2} - 2A + rt'_{\mathrm{eff}}\sigma'_{\mathrm{car}}\beta_{\mathrm{car}} \frac{3+\left(Mt'_{\mathrm{eff}}\nu'\right)^2}{1+(Mt'_{\mathrm{eff}}\nu')^2} A^2 - \mathrm{j}\frac{2rt'_{\mathrm{eff}}\sigma'_{\mathrm{car}}\beta_{\mathrm{car}} Mt'_{\mathrm{eff}}\nu'}{1+(Mt'_{\mathrm{eff}}\nu')^2} A^2 \Bigg)^2 \Bigg]^{1/2} .$$

Both the real part g and the imaginary part g_{j} of the gain parameter show a dependence on the normalized power A of the pumped mode. For a given normalized pump power F, the normalized power A in the pumped mode can be determined by evaluating the expression

$$F = \left[\left(1 + rA + rt'_{\mathrm{eff}}\sigma'_{\mathrm{car}} A^2 \right)^2 + \underbrace{\left(A - \zeta + \phi_0 - rt'_{\mathrm{eff}}\sigma'_{\mathrm{car}}\beta'_{\mathrm{car}} A^2 \right)^2}_{(*)} \right] A. \quad (4.11)$$

A derivation of Eq. (4.11) can be found in Appendix C.1.

4.4 Parameter ranges of TPA, FCA and pump power leading to modulation instability

Using Equations (4.10) and (4.11) for a specific parameter set $\left(r, \sigma'_{\mathrm{car}}, t'_{\mathrm{eff}}, \beta_{\mathrm{car}}, \beta', \nu', \phi_\mu\right)$ and for specific operating conditions (F, ζ), we can determine whether MI can occur and at which sidebands $\mu = \pm M$ it will happen. To reduce the complexity of the evaluation, we simplify Eq. (4.10) by considering technically relevant sets of normalized parameters $\left(r \approx 1, \sigma'_{\mathrm{car}} \approx 5, t'_{\mathrm{eff}} \approx 0.05 \ldots 0.5, \beta_{\mathrm{car}} \approx 10, \nu' \approx 200, F \approx 10\right)$ and by assuming that the side modes, for which MI will occur, are not affected by AMC, i.e., $\phi_{+M} = \phi_{-M} = 0$. The normalized parameters are obtained using the relations in Table 4.1 in combination with the

physical parameters listed in Tables C.1 and C.2, see Appendix C.7. Specifically, we assume that TPA-generated free carriers are removed by a reverse-biased *p-i-n*-junction and thus have a small dwell time $t_{\mathrm{eff}} \approx (12 \ldots 100)$ ps [29], which is of the same order of magnitude as the cavity round-trip time. For estimating the normalized intracavity power A of the pumped mode, we use Eq. (4.11) and assume that a detuning $\zeta = A + \phi_0 - r t'_{\mathrm{eff}} \sigma'_{\mathrm{car}} \beta_{\mathrm{car}} A^2$ is chosen for optimized power transfer from the pump F to the pumped resonator mode, which makes the expression (*) $\left(A - \zeta + \phi_0 - r t'_{\mathrm{eff}} \sigma'_{\mathrm{car}} \beta_{\mathrm{car}} A^2\right)^2$ on the right-hand-side of Eq. (4.11) vanish. With the above-mentioned parameters, Eq. (4.11) can then be written as $F = \left(1 + rA + r t'_{\mathrm{eff}} \sigma'_{\mathrm{car}} A^2\right)^2 A$, leading to $A \approx 1$ for a large range of technically relevant normalized pump powers F between 1 and 100. Note that the following investigation aims at identifying the dominant terms in Eq. (4.10) and that the symbol "≈" is to be understood as an order-of-magnitude quantification rather than as an approximate equality.

To identify the side bands at which MI will occur first, we need to find values of the side-band offset M that maximize the gain rate g. To this end, we simplify Eq. (4.10) by reducing it to its dominant terms, assuming that the offset of the MI-generated side-bands from the pump is of the order of $M \approx 10$. With the above-mentioned parameters, this leads to

$$g(M) = -1 - r\left(2 + t'_{\mathrm{eff}} \sigma'_{\mathrm{car}} A\right) + \Re\left\{\sqrt{A^2\left(r^2+1\right) - \left(\zeta + \beta' M^2 - 2A + r t'_{\mathrm{eff}} \sigma'_{\mathrm{car}} \beta_{\mathrm{car}} A^2\right)^2}\right\}, \tag{4.12}$$

see Appendix C.2 for details. This formula was also obtained in a previous study neglecting the fast-time dynamics of free-carriers [26]. We therefore conclude that the fast-time dynamics of N'_{car} have negligible impact on MI. This can be understood by the fact that, at the onset of MI, the optical power is still uniformly distributed along the circumference of the resonator, such that fast carrier dynamics on a time scale smaller than the round-trip time do not play a big role. In the absence of FCA, i.e., for $\sigma = 0$, Eq. (4.12) is consistent with results from previous studies investigating the impact of TPA on modulation stability [27, 28]. Similarly, maintaining only FCA-related terms in Eq. (4.12) leads to relations that have previously been derived for resonators impaired by free carriers only [28]. We simplify the further analysis

of modulation instability by treating M as a continuous non-negative real-valued variable, even though it was originally defined as an integer parameter $M \in \mathbb{N}_+$. The sidebands experiencing the highest gain rate are then obtained from the condition $\zeta + \beta' M^2 - 2A + r t'_{\mathrm{eff}} \sigma'_{\mathrm{car}} \beta_{\mathrm{car}} A^2 = 0$, which is the only term depending on M in Eq. (4.12). This leads to

$$M_{\max} = \sqrt{\left(2A - r t'_{\mathrm{eff}} \sigma'_{\mathrm{car}} \beta_{\mathrm{car}} A^2 - \zeta\right) / \beta'}. \tag{4.13}$$

Note that Eq. (4.13) implies an appropriate choice of the detuning ζ such that $\left(2A - r t'_{\mathrm{eff}} \sigma'_{\mathrm{car}} \beta_{\mathrm{car}} A^2 - \zeta\right) / \beta' > 0$. Note also that a strict derivation of $M_{\max}$ by computing $\mathrm{d}g/\mathrm{d}M = 0$ will yield $M = 0$ as an additional local extremum, specifically a local maximum for $d\left(\zeta - 2A + r t'_{\mathrm{eff}} \sigma'_{\mathrm{car}} \beta_{\mathrm{car}} A^2\right) > 0$ and a local minimum for $d\left(\zeta - 2A + r t'_{\mathrm{eff}} \sigma'_{\mathrm{car}} \beta_{\mathrm{car}} A^2\right) < 0$. This extremum is not considered further, since the associated gain parameter $g(0)$ is always smaller than $g\left(M_{\max}\right)$, which is given by

$$\begin{aligned} g\left(M_{\max}\right) &= -1 - r\left(2 + t'_{\mathrm{eff}} \sigma'_{\mathrm{car}} A\right) + A\sqrt{r^2 + 1} \\ &= -1 + \left(\sqrt{r^2 + 1} - 2r\right) A - r t'_{\mathrm{eff}} \sigma'_{\mathrm{car}} A^2. \end{aligned} \tag{4.14}$$

Note also Eq. (4.14) reproduces the well-known fact that $A > 1$ is a necessary condition for MI to occur in the absence of TPA and FCA. The presence of these effects may either increase the required normalized power A to values larger than 1 or completely inhibit MI. Specifically, $g\left(M_{\max}\right)$ is negative for any value of A for sufficiently high TPA parameters $r \geq 1/\sqrt{3}$, i.e., MI cannot occur, irrespective of the pump power. On the other hand, positive values of $g\left(M_{\max}\right)$ may be found for certain normalized powers A if both of the following conditions are satisfied:

$$0 \leq r < \frac{1}{\sqrt{3}}, \qquad 0 \leq t'_{\mathrm{eff}} \sigma'_{\mathrm{car}} < \frac{1}{4r}\left(\sqrt{r^2 + 1} - 2r\right)^2. \tag{4.15}$$

Note that the upper limit of $1/\sqrt{3}$ for the TPA parameter r is exact. In a bifurcation study of the LLE [141], $r = 1/\sqrt{3}$ was also found as a threshold value for the TPA-parameter preventing bifurcations from the steady-state solution $\underline{a}\left(t', \tau'\right) = \underline{a}_0$. Further, $r < 1/\sqrt{3}$ is also a necessary condition for bistability of the continuous-wave (CW) intracavity power $A = \left|\underline{a}_0\right|^2$ as a

function of the detuning ζ [27]. Note also that other investigations previously described the impact of the TPA parameter on the intracavity power A required for MI in the presence of TPA and FCA [26] and in the presence of TPA only, see again [27] and [28]. In both cases, the required intracavity (IC) power diverges for $r \to 1/\sqrt{3}$. We therefore conclude that a TPA parameter $r \geq 1/\sqrt{3}$ prohibits a multitude of nonlinear phenomena comprising bifurcations from the steady-state solution, bistability and modulation instability. Also note that the upper limit for the free-carrier lifetime is consistent with the results of [26].

An important quantity to derive is the threshold power that leads to MI in the presence of TPA and FCA. For the values of r and $t'_{\mathrm{eff}}\sigma'_{\mathrm{car}}$ specified by Eq. (4.15), we use Eq. (4.14) to compute the minimum threshold power A_{th} of the pumped resonator mode that is required to achieve MI, i.e., $g\,(M_{\mathrm{max}}) > 0$. The forcing F_{th} required to achieve A_{th} is then determined from Eq. (4.11). For maximizing the power transfer from F_{th} to A_{th}, the detuning is chosen as $\zeta = A_{\mathrm{th}} + \phi_0 - r t'_{\mathrm{eff}}\sigma'_{\mathrm{car}}\beta_{\mathrm{car}}A_{\mathrm{th}}^2$ by appropriate adjustment of the pump frequency, thus eliminating the expression marked by a star (*) in Eq. (4.11). For this detuning, maximum gain is found for modes with offset $M_{\mathrm{max}} = \sqrt{(A_{\mathrm{th}} - \phi_0)/\beta'}$. For anomalous dispersion, $\beta' > 0$ ($\beta^{(2)} < 0$), real-valued M_{max} can be found as long as $\phi_0 < A_{\mathrm{th}}$, which includes also the complete absence of AMC, $\phi_0 = 0$. In contrast to that, normal dispersion, $d < 0$ ($\beta^{(2)} > 0$), requires $\phi_0 > A_{\mathrm{th}}$, i.e., a spectral shift of the resonance caused by sufficiently strong AMC to yield a real-valued M_{max}. For real M_{max}, Figure 4.2 displays the color-coded threshold forcing F_{th} that is required to achieve MI as a function of the normalized TPA coefficient r and the free-carrier influence $t'_{\mathrm{eff}}\sigma'_{\mathrm{car}}$. The color-coded map is limited to the ranges within which MI can be achieved, see Eq. (4.15), while the remainder of the plot is kept in gray. We find that F_{th} increases continuously with increasing r and $t'_{\mathrm{eff}}\sigma'_{\mathrm{car}}$, which is caused by both an increase of A_{th} needed to achieve positive $g\,(M_{\mathrm{max}})$ according to Eq. (4.14), and a reduced power transfer from the pump F to the pumped mode A, Eq. (4.11). In the absence of FCA, i.e., $t'_{\mathrm{eff}}\sigma'_{\mathrm{car}} = 0$, MI is possible for sufficiently weak TPA $r < 1/\sqrt{3}$, indicated by a vertical dashed line, and the associated threshold forcing F_{th} diverges for $r \to 1/\sqrt{3}$. This can be seen in Eq. (4.14), wherein the factor $\sqrt{r^2+1} - 2r \to 0$ vanishes for $r \to 1/\sqrt{3}$ and thus $A_{\mathrm{th}} \to \infty$ is needed to achieve positive $g\,(M_{\mathrm{max}})$ for $t'_{\mathrm{eff}}\sigma'_{\mathrm{car}} \to 0$. For $r < 1/\sqrt{3}$ the threshold forcing at the edge of the MI-enabling parameter space remains finite.

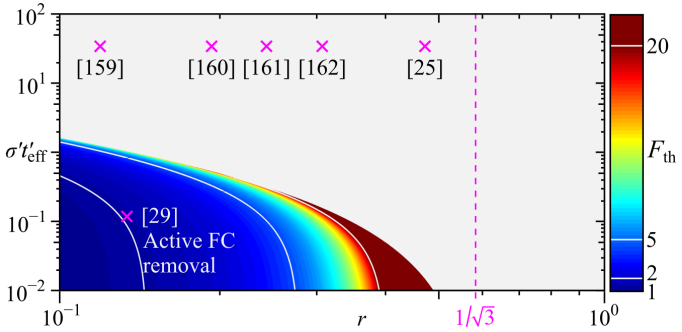

Figure 4.2: Threshold forcing needed to achieve MI as a function of r and $t'_{\mathrm{eff}}\sigma'_{\mathrm{car}}$. Modulation instability and comb formation can be observed only to the left of the vertical dashed line $r = 1/\sqrt{3}$. The gray area indicates the parameter space for which modulation instability does not occur. Magenta crosses mark data points reported for silicon photonic waveguides [25, 29, 159–162], assuming waveguide losses of $\alpha_i = 46\mathrm{m}^{-1}$ (2 dB cm^{-1}) [29]. Reference [29] reports on silicon-photonic waveguides in which free carriers are actively removed by a reverse-biased *p-i-n*-junction, leading to a dwell time of $t_{\mathrm{eff}} = 12$ ps. In all other cases, no free-carrier removal was used, leading to dwell times of the order of 1 . . . 5 ns according to [25, 29, 77, 149, 150]. Specifically, a value of 3 ns was used for the data points related to the references [159–162], which do not specify values for t_{eff}. The value for the FCA cross-section $\sigma_{\mathrm{car}} = 1.45 \times 10^{-21}$ m^2 is consistently found in various publications [25, 29, 160]. The operating wavelength is 1550 nm.

Note that all these findings are based on various approximations that make Eq. (4.10) amenable to an analytic investigation. In Appendix C.3, we check the result of Fig. 4.2 for a specific set of parameters $\sigma'_{\mathrm{car}}, \beta_{\mathrm{car}}, \nu', \beta'$ by evaluating Eqs. (4.10) and (4.11) numerically for varying r and t'_{eff} without the approximations involved in Eq. (4.14). In this investigation, we again assume that AMC is absent, i.e., $\phi_\mu = 0\,\forall\,\mu$. The relative deviation of the threshold forcing found by the numerical evaluation from its analytically approximated counterpart stays below 1 %. We hence conclude that the simplified procedure leading to Fig. 4.2 can be considered sufficiently accurate.

Figure 4.2 also shows published experimental data (magenta crosses) for the TPA coefficient r and for the product $t'_{\mathrm{eff}}\sigma'_{\mathrm{car}}$ of the FC cross-section and dwell time. The published values for r are all in the same order of magnitude [25, 29, 159–162] and stay below the limiting value of $1/\sqrt{3}$ as given in Eq. (4.15). For simple silicon-photonic waveguides without active free-carrier removal, dwell times t_{eff} are of the order of 1 . . . 5 ns [25, 29, 77, 149, 150], thereby

clearly inhibiting MI. However, active free-carrier removal by a reverse-biased *p-i-n*-junction can effectively reduce the dwell time to values of, e.g., 12 ps [29], such that modulation instability and frequency comb formation become possible at telecommunication wavelengths. The lower limit for $t'_{\mathrm{eff}}\sigma'_{\mathrm{car}}$ that is achievable by active free-carrier removal is dictated by the saturation drift velocity v_{car} of the free carriers, which is of the order of $10^5\,\mathrm{m\,s^{-1}}$ for electrons in silicon [163]. For a microresonator with an assumed waveguide width of $w = 480\,\mathrm{nm}$, the theoretically estimated carrier dwell time can be as small as $t_{\mathrm{eff}} = w/v_{\mathrm{car}} = 4.8\,\mathrm{ps}$ which leads to $t'_{\mathrm{eff}}\sigma'_{\mathrm{car}} = 0.05$ and clearly enables MI.

4.5 Silicon microresonator for Kerr comb generation at telecom wavelengths: Design study and numerical simulations

With the general model of the Section 4.4 at hand, we can now design a specific implementation of a silicon-photonic microresonator which is geared toward Kerr comb generation at telecom wavelengths around 1550 nm. Fig. 4.1 shows the general layout of the device. The silicon waveguide is undoped and is part of the intrinsic zone of a *p-i-n*-junction [149, 152]. A reverse voltage applied through vertical interconnect accesses (vias) to the p^+-doped (red) and n^--doped (blue) regions of the *p-i-n*-junction leads to efficient removal of free carriers such that dwell times of the order of the round-trip time can be achieved. To determine suitable waveguide parameters, we perform finite-element simulations for a specific waveguide geometry. We choose the width of the center waveguide as $w = 480\,\mathrm{nm}$, the height as 260 nm and the slab height as 40 nm, such that the total height amounts to $h = 300\,\mathrm{nm}$. The width of the undoped region is set to 1300 nm. This geometry of the cross-sectional design for fast carrier removal is similar to the one used in [29] and results in anomalous group velocity dispersion around 1550 nm [153]. Specifically, we obtain a second-order dispersion parameter of $\beta^{(2)} = -0.587\,\mathrm{ps^2\,m^{-1}}$ a group refractive index of $n_{\mathrm{g}} = 4.15$, and a nonlinearity parameter of $\gamma = 257\,\mathrm{W^{-1}\,m^{-1}}$ at 1550 nm, see Appendix C.4 for details. The value of the group refractive index along with a targeted free spectral range (FSR) of 100 GHz leads to a microresonator diameter of 230 μm. For the TPA and FCA parameters marked by a magenta cross in Fig. 4.2 [29], the threshold forcing for MI amounts to

$F_{\mathrm{th}} = 2.06$. Assuming a power loss coefficient of $\alpha_i = 46\,\mathrm{m}^{-1}$ ($2\,\mathrm{dB\,cm}^{-1}$) and critical coupling, which corresponds to a Q-factor of approximately 2×10^5, this threshold forcing translates into a threshold pump power of $P_{\mathrm{in}} \approx 12\,\mathrm{mW}$ measured in the on-chip bus waveguide. Q-factors of the order of 10^5 have been demonstrated using commercial silicon-photonic foundry processes [164].

Based on this resonator design, we next perform a time integration of the LLE to validate our theoretical predictions on comb formation and to study the associated impact of fast free-carrier dynamics. Our model accounts for the full dynamics of free carriers both on the slow and on the stationary fast time scale and complements previous investigations of Kerr comb generation in silicon microresonators such as [25], which formulates the free-carrier dynamics on the retarded fast time scale and accounts for the temporal evolution on the slow time scale by appropriate boundary conditions. We start our consideration from the Kerr microresonator design described before, which features a normalized group velocity $v' = 189$, a dispersion coefficient $d = 0.0025$, a TPA coefficient $r = 0.133$, an FCA cross-section $\sigma'_{\mathrm{car}} = 0.0157$, and an FC dispersion coefficient $\beta_{\mathrm{car}} = 7.5$ [25, 165], see Appendix C.7, Tables C.1 and C.2 for a list of the underlying physical microresonator parameters along with their connection to the normalized quantities. Forcing F, detuning ζ, and FC dwell time t'_{eff} are externally controllable parameters and are varied in our simulations. We use a discretization of $\Delta\tau' = 2\pi/1024$ ($\Delta\tau = 9.8\,\mathrm{fs}$) for the normalized fast time by dividing the round-trip time into 1024 parts, and we set the slow-time step-size to $\Delta t' = 64 \times \tau'/v' = 2.1 \times 10^{-3}$ ($\Delta t = 64 \times \Delta\tau = 626\,\mathrm{fs}$). Note that in order to correctly simulate the slow- and fast-time dynamics of both the optical field $\underline{a}\,(t', \tau')$ and the free-carriers $N'_{\mathrm{car}}\,(t', \tau')$, the slow-time increment and the fast-time increment are linked, see Appendix C.5 for details. We run each simulation until $t' = 150$, corresponding to 72174 time steps for the slow time. The initial field for each simulation is given by 1024 complex numbers with random phases between 0 and 2π and random amplitudes between 0 and 10^{-14}. The maximum amplitude of the initial field is chosen such that the power of the initial field is negligible compared to the forcing but can still act as a seed for starting the evolution of the differential equation system. More details on the integration of the coupled Eqs. (4.5) and (4.6) can be found in Appendix C.5. We analyze four different cases, see Figure 4.3 – 4.6 for the results.

In Figure 4.3 (*Inhibited modulation instability*), the parameters are set as follows: Forcing $F = 5$ (pump power $P_{\mathrm{in}} = 30\,\mathrm{mW}$), dwell-time $t'_{\mathrm{eff}} = 0.1665$

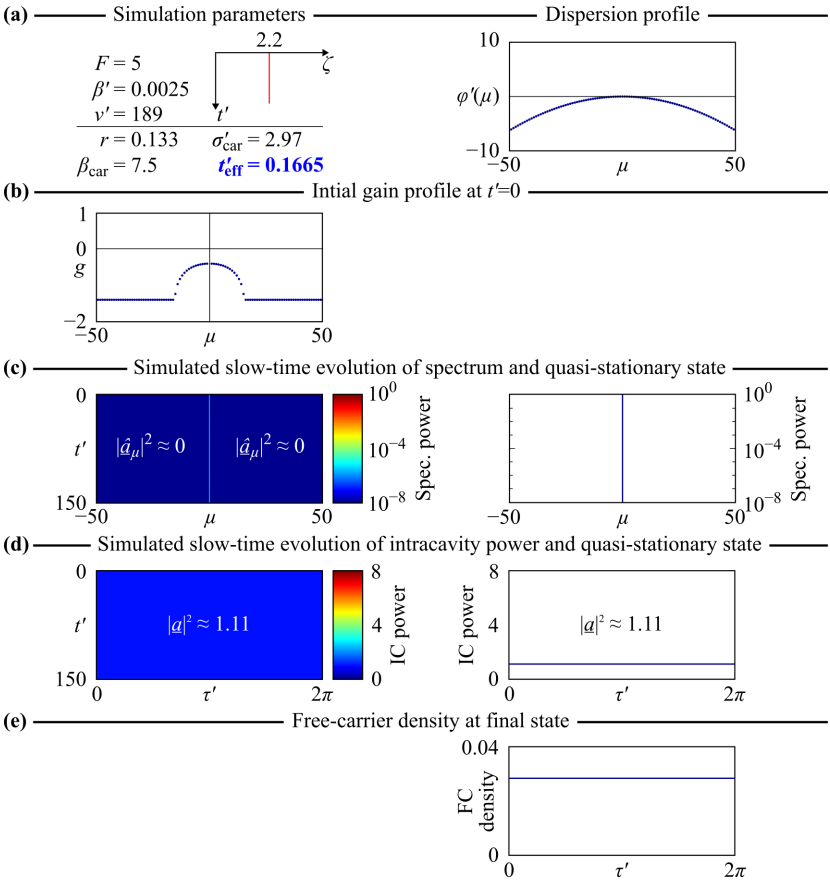

Figure 4.3: Results of time integration of the LLE: Dispersion profiles, gain rates, field and FC evolution for case I: Modulation instability inhibited by long free-carrier dwell time t_{eff}, which corresponds to five times the cavity round-trip time t_{R}. (a) Simulation parameters and dispersion profile for the central 101 modes. (b) Computed normalized gain rate at the beginning of the simulation (slow time $t' = 0$). (c) Evolution of power spectrum and spectrum at stationary state for $t' = 150$. (d) Color-coded intracavity (IC) power evolving during comb formation over t' as a function of normalized the fast time τ' and quasi-stationary IC power at $t' = 150$. (e) Free-carrier density N'_{car} $(t' = 150, \tau' - 150\nu')$ at final state.

($t_{\mathrm{eff}} = 50\,\mathrm{ps}$), detuning $\zeta = 2.2$ ($\Delta\omega = 2\pi \times 1.16\,\mathrm{GHz}$), and $\beta' = 0.0025$, corresponding to anomalous dispersion, i.e., $\beta^{(2)} < 0$, see Table 4.1. The simulation parameters are listed in Figure 4.3(a) on the l.h.s. The dispersion profile of the 101 central frequency comb modes, represented in normalized terms by $\varphi'(\mu) = -\beta'\mu^2 + \phi_\mu$, is shown in (a) on the r.h.s. as a function of the mode index μ. In physical terms, the dispersion profile $\varphi(\mu)$ corresponds to the phase deviation accumulated by each comb mode μ over a single round-trip t_{R} in the resonator due to dispersion and avoided mode crossings. This can be seen by introducing Eq. (4.1) into a reduced version of Eq. (4.2), where only the fifth and sixth term $\mathrm{j}\left[-(\beta^{(2)} L_{\mathrm{MR}}/2)\partial^2/\partial\tau^2 + \hat{\Phi}_{\mathrm{AMC}}\right] \underline{\mathcal{E}}(t,\tau)$ on the r.h.s. are maintained. Using Eq. (4.4), and the normalized quantities defined in Table 4.1, we obtain

$$\begin{aligned} \mathrm{j}\left[-\frac{\beta^{(2)} L_{\mathrm{MR}}}{2}\frac{\partial^2}{\partial\tau^2} + \hat{\Phi}_{\mathrm{AMC}}\right] \sum_{\mu} \underline{\mathcal{E}}_\mu \mathrm{e}^{\mathrm{j}2\pi\mu t/t_{\mathrm{R}}} \\ = \mathrm{j}\sum_{\mu} \varphi(\mu)\, \underline{\mathcal{E}}_\mu \mathrm{e}^{\mathrm{j}2\pi\mu t/t_{\mathrm{R}}}, \end{aligned} \tag{4.16}$$

$$\varphi(\mu) = \frac{\beta^{(2)} L_{\mathrm{MR}}}{2}\left(\mu \times \frac{2\pi}{t_{\mathrm{R}}}\right)^2 + \delta\omega_\mu t_{\mathrm{R}},$$

$$\varphi'(\mu) = \frac{n_{\mathrm{g}}}{\alpha_i t_{\mathrm{R}} c_0}\varphi(\mu) = -\beta'\mu^2 + \phi_\mu.$$

The above-mentioned choice of forcing and dwell time ensures that the normalized gain rate $g(\mu)$ (with $M = |\mu|$), Eqs. (4.10) and (4.11), is always negative, see Fig. 4.3(b). As a consequence, modulation instability cannot occur, and the only mode with nonzero power is the pumped mode at modal index $\mu = 0$. In Fig. 4.3(c) on the l.h.s., the color-coded power spectrum $|\underline{a}_\mu(t')|^2$ is shown as a function of the normalized (slow) time t' in the range $0 \le t' \le 150$ and of the modal index μ in the range $-50 \le \mu \le 50$. Fig. 4.3(c), r.h.s., displays the final power spectrum at $t' = 150$ as a function of the modal index μ. In Fig. 4.3(d) on the l.h.s., the color-coded intracavity (IC) power $|\underline{a}(t',\tau')|^2$ is depicted as a function of normalized slow time t' and normalized fast (retarded) time τ'. In the absence of modulation instability, the IC power remains constant along the circumference of the resonator, $|\underline{a}(t',\tau')|^2 = 1.11$, see Fig. 4.3(d). Similarly, the free-carrier density is also constant, as depicted in Fig. 4.3(e).

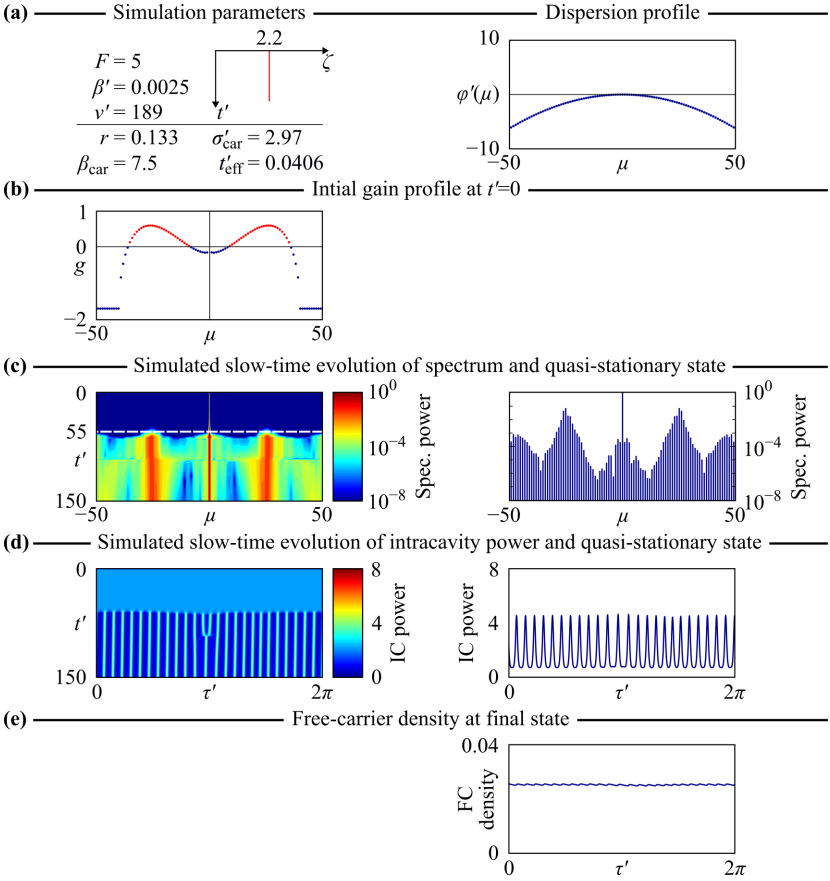

Figure 4.4: Results of time integration of the LLE: Dispersion profiles, gain rates, field and FC evolution for case II: Modulation instability with sufficiently reduced carrier dwell time $t_{\mathrm{eff}} = 1.22\times t_{\mathrm{R}}$. (a) Simulation parameters and dispersion profile for the central 101 modes. (b) Computed normalized gain rate at the beginning of the simulation (slow time $t' = 0$). (c) Evolution of power spectrum and spectrum at stationary state for $t' = 150$. (d) Color-coded intracavity (IC) power evolving during comb formation over t' as a function normalized of the fast time τ' and quasi-stationary IC power at $t' = 150$. We observe a temporal shift of the IC power distribution within the retarded time frame of the fast time axis τ', which can, e.g., be caused by FC dispersion or avoided mode crossings. Besides this shift along the τ'-axis, the IC power does not change, and we name this state "quasi-stationary". (e) Free-carrier density N'_{car} $(t' = 150, \tau' - 150\nu')$ at final state.

In Figure 4.4 (*Modulation instability*), we keep all parameters of Fig. 4.3 except for t'_{eff}, which is reduced to 0.0406. This corresponds to a physical dwell time $t_{\mathrm{eff}} = 12.2\,\mathrm{ps}$, which has previously been demonstrated in a comparable silicon-photonic waveguide [29]. In this case, the computed normalized gain rate is positive within a certain range of modal indices μ, see Fig. 4.4(b) (red dots). During the evolution of the power spectrum with slow time t', the first sidebands emerge near $t' = 55$, Fig. 4.4(c) l.h.s. A visual comparison with the gain rate plot in (b) shows that the positions $\mu \approx \pm 25$ of the initial sidebands coincide with the maxima of the gain parameter $g(\mu)$. A power spectrum at $t' = 150$ is to be seen on the r.h.s. of Fig. 4.4(c). The phase-locked modes lead to a regular temporal pulse pattern which is visible in Fig. 4.4(d). Note that there is a small slow drift of this pulse train within the retarded time frame τ', which may be inferred from the nearly vertical, but slightly inclined lines that correspond to the pulse peaks on the fast time scale, see Fig. 4.4(d) l.h.s. A possible explanation of this drift might be the fact that the rise of the free-carrier density during each pulse leads to a slightly increased attenuation of the trailing pulse edge and hence to an effectively higher propagation velocity. Mathematically, this behavior can be also seen from the terms $\exp\left(\pm \mathrm{j} g_{\mathrm{j}} t'\right) \exp\left(\pm \mathrm{j} M \tau'\right) = \exp\left(\pm \mathrm{j} M \left(g_{\mathrm{j}} t'/M + \tau'\right)\right)$ in Eq. (4.8), which describe a time shift of the optical field $\underline{a}\left(t', \tau'\right)$ that continuously increases with slow time t' within the fast time scale. The FC density $N'_{\mathrm{car}}\left(t' = 150, \tau' - 150 v'\right)$ in Fig. 4.4(e) shows modulations. These are however small, since the assumed FC lifetime of 12.2 ps is much larger than the narrow temporal spacing of the 25 optical pulses circulating in the cavity, which amounts to approximately $10\,\mathrm{ps}/25 = 0.4\,\mathrm{ps}$.

In Figure 4.5 (*Dissipative Kerr soliton generation*), we increase the forcing to $F = 8$ (48 mW). The detuning is kept constant at $\zeta = 3$ until $t' = 90$, then increased linearly to $\zeta = 3.8$ until $t' = 120$, and then kept constant again until the end of the simulation, see Fig. 4.5(a) l.h.s. Such a procedure allows generating single-soliton states [120]. In Fig. 4.5(b), the gain rate is depicted for $t' = 0$, i.e., before the detuning sweep, showing a broad range of modes that experience parametric gain. In the simulated slow-time evolution of the spectrum, Fig. 4.5(c) l.h.s., the first sidebands become visible around $t' = 70$, and the spectral position of these sidebands coincides with the maxima of computed gain rate in (b). The maximum of the gain parameter in Fig. 4.5 is slightly smaller than the one obtained for the scenario described in Fig. 4.4, and thus the sidebands only become visible at a later normalized time t'. The final power spectrum obtained at the end of the simulation, Fig. 4.5(c)

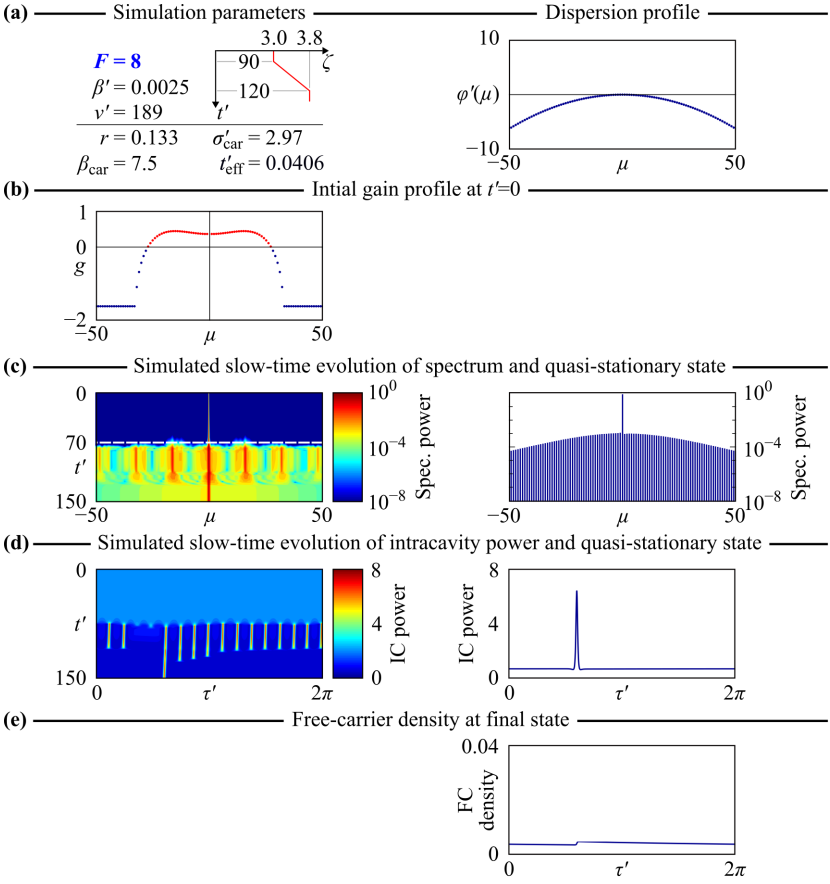

Figure 4.5: Results of time integration of the LLE: Dispersion profiles, gain rates, field and FC evolution for case III: Single soliton formation for dynamically increasing detuning. (a) Simulation parameters and dispersion profile for the central 101 modes. (b) Computed normalized gain rate at the beginning of the simulation (slow time $t' = 0$). (c) Evolution of power spectrum and spectrum at stationary state for $t' = 150$. (d) Color-coded intracavity (IC) power evolving during comb formation over t' as a function of the normalized fast time τ' and quasi-stationary IC power at $t' = 150$. We observe a temporal shift of the IC power distribution within the retarded time frame of the fast time axis τ', which can, e.g., be caused by FC dispersion or avoided mode crossings. Besides this shift along the τ'-axis, the IC power does not change, and we name this state "quasi-stationary". (e) Free-carrier density N'_{car} ($t' = 150$, $\tau' - 150\nu'$) at final state.

r.h.s., is a very regular frequency comb with a smooth envelope, which is typical for a single dissipative Kerr soliton [21] circulating in the ring. The evolution of the color-coded intracavity power, shown in Fig. 4.5(d), reveals the emergence of multiple pulses at modulation instability onset around $t' \approx 70$. Due to the swept detuning, most of the pulses vanish over time, which is in line with experimental observations [120]. The final value of ζ was chosen such that a single pulse remains in the cavity, which can be seen from the plot of the IC power $|\underline{a}(t' = 150, \tau')|^2$ in Fig. 4.5(d) r.h.s. In this simulation, FCA causes an even more pronounced change of the group velocity as compared to Fig. 4.4(d) l.h.s., leading to a stronger temporal shift of the soliton pulse within the retarded time frame τ', while the spectrum remains constant. Such drifts of soliton pulses due to FCA have been reported and investigated in [28]. At higher pump powers, this drift can be even more severe, see, e.g., Appendix C.5. Comparing the propagation of a single soliton pulse in the presence of free carriers with and without fast time dynamics, we find that this drift can only be observed when including these dynamics, see again Appendix C.5. The free-carrier density, Fig. 4.5(e), shows a stronger modulation compared to the previous case shown in Fig. 4.4. The soliton pulse increases the local free-carrier density by 28 % compared to its cavity mean value. Note that the soliton pulse is accompanied by a constant CW-background, which also a contributes a constant part to the FC density. For single-soliton states with stronger pump powers, the fast-time dynamics of the free-carrier density are more pronounced, see again Appendix C.5 for an example. Overall, the FC density is lower compared to the cases shown in Figs. 4.3 and 4.4. This is explained by a reduced FC lifetime compared to Fig 4.3 and to a significantly reduced number of pulses propagating in the cavity compared to Fig. 4.4.

In Figure 4.6 (*Modulation instability via avoided mode crossing*), the forcing is set back to $F = 5$, and the anomalous dispersion profile used in Figs. 4.3, 4.4 and 4.5 is inverted to obtain normal group-velocity dispersion, $\beta' = -0.0025$, see Fig. 4.6(a) on the l.h.s. for all parameters. Additionally, we introduce an avoided mode crossing (AMC) which causes phase shifts ϕ_μ that disturb the dispersion profile. The AMC arises due to a coupling of resonator modes with similar resonance frequency, but different transverse field distributions. The two coupled modes belong to different mode families, characterized by their respective free spectral range. Representing the dispersion profile of the second waveguide mode family in the dispersion diagram of the first mode family leads to equidistant points on an approximately straight line, which

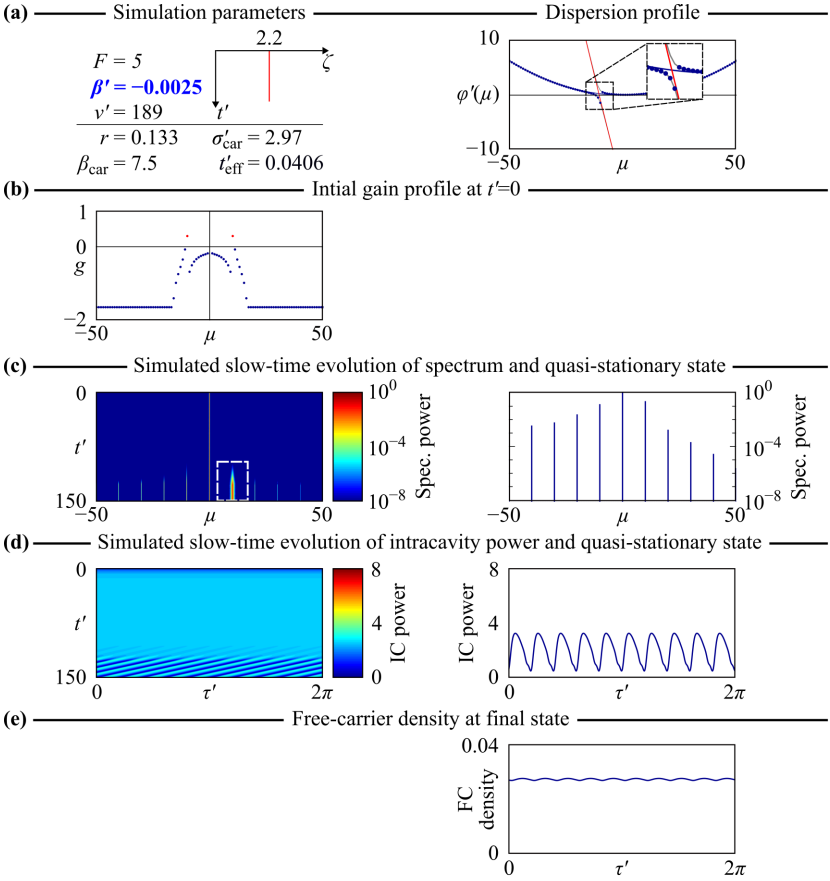

Figure 4.6: Results of time integration of the LLE: Dispersion profiles, gain rates, field and FC evolution for case IV: Comb formation in a normal-dispersion resonator with avoided mode crossing. (a) Simulation parameters and dispersion profile for the central 101 modes. (b) Computed normalized gain rate at the beginning of the simulation (slow time $t' = 0$). (c) Evolution of power spectrum and spectrum at stationary state for $t' = 150$. (d) Color-coded intracavity (IC) power evolving during comb formation over t' as a function of the normalized fast time τ' and quasi-stationary IC power at $t' = 150$. We observe a temporal shift of the IC power distribution within the retarded time frame of the fast time axis τ', which can, e.g., be caused by FC dispersion or avoided mode crossings. Besides this shift along the τ'-axis, the IC power does not change, and we name this state "quasi-stationary". (e) Free-carrier density $N'_{\mathrm{car}}\,(t' = 150, \tau' - 150\nu')$ at final state.

is indicated in red in Figure 4.6(a) r.h.s. The resonance frequencies of the coupled modes are indicated by blue filled circles connected by gray lines, which deviate from the resonance frequencies of the unperturbed modes $\omega_{\mathrm{r},\mu}$ by $\delta\omega_\mu$, see Appendix C.6 and Ref. [166] for details. The FSR of the second mode family and the coupling strength of the two transverse modes are chosen such that the strongest resonance shift amounts to $\delta\omega_{-10} = -2\pi \times 875\,\mathrm{MHz}$ ($\phi_{-10} = -1.65$, $\phi_0 = 0.06$, $\phi_{+10} = 0.03$). This corresponds to a local 1 % change of the FSR, which is the same order of magnitude as reported for experimentally investigated microresonators [157, 166]. The phase shifts ϕ_μ induced by the avoided mode crossing alter the gain parameter such that it becomes positive for certain sidebands, with a gain maximum at sidebands $\mu = \pm 10$, see Fig. 4.6(b). In the evolution of the power spectrum, Fig. 4.6(c) on the l.h.s., comb lines emerge at these positions. For better visibility, the comb line at $\mu = 10$ is framed by a broken line and horizontally enlarged. Note that pumping a resonance directly adjacent to an avoided mode crossing may allow for generation of dark soliton frequency combs, where the spacing of the comb lines is equal to a single FSR of the microresonator instead of a multiple thereof [130]. Dark solitons might even experience stronger impact from fast free-carrier dynamics than their bright counterparts.

The stationary power spectrum in Figure 4.6(c) shows a pronounced asymmetry. Compared to the previously considered scenarios, the IC power distribution exhibits a stronger temporal shift of the soliton pulse within the retarded time frame τ'. This is caused by a contribution of the AMC-induced phase shifts to the imaginary part of the gain rate, see Eq. (4.10). Apart from this time shift, the final power distribution inside the resonator exhibits a stationary regular pattern, Fig. 4.6(c) r.h.s. The FC density is again nearly constant due to the presence of multiple pulses circulating in the cavity, see Fig. 4.6(e).

Note that silicon-photonic waveguides with anomalous group-velocity dispersion around 1550 nm need a careful design and can only be achieved in a limited parameter space of widths w and heights h [153]. To ensure the technical relevance of the scenarios investigated in Figs. 4.3 – 4.5, we derived the normalized dispersion parameter along with the corresponding nonlinearity parameter from a specific waveguide design ($w = 480\,\mathrm{nm}$, $h = 300\,\mathrm{nm}$), see Table 4.11 and Appendix C.4 for details. In contrast to that, normal dispersion can be achieved for a rather large parameter range of waveguide widths and heights, including waveguides with standard heights of 220 nm or with

rather large cross-sections that support multi-mode propagation and avoided mode-crossings [153]. Silicon-photonic microresonators corresponding to the scenario considered in Fig. 4.6 may therefore by realized for multiple different waveguide geometries.

4.6 Discussion and conclusions

The simulation results indicate that modulation instability in silicon-photonic microresonators at telecommunication wavelengths is most likely to be observed if the waveguide is designed for anomalous group-velocity dispersion, if FCA is mitigated by a reverse-biased *p-i-n*-junction which leads to a sufficiently small carrier dwell time, and if the pump power and detuning are chosen properly. If an avoided mode crossing induces local dispersion shifts, microresonators with otherwise normal dispersion can also exhibit modulation instability. In both cases, moderate on-chip pump powers in the range of 10 mW to 50 mW are sufficient to initiate modulation instability and to generate frequency combs. The required pump powers depend strongly on the actual values of the TPA coefficient β_{TPA}, which is expressed by the normalized TPA parameter r, and on the actual FC dwell time t_{eff} and its normalized counterpart t'_{eff}. We illustrate this dependence in Fig. 4.7(a), where the on-chip threshold pump power P_{th} for modulation instability is displayed as a function of the TPA coefficient with the FC dwell time as a parameter. We assume critical coupling, a resonator design and waveguide properties as described in Section 4.5, a Kerr coefficient of $n_2 = 6.5 \times 10^{-18}\,\mathrm{m^2\,W^{-1}}$, and a pump wavelength of 1550 nm. We find that t_{eff} has to be of the order of 100 ps or less to enable comb formation across the range of reported values for β_{TPA} in silicon, which reach from $0.45\,\mathrm{cm\,GW^{-1}}$ [159] to $1.5\,\mathrm{cm\,GW^{-1}}$ [25] as indicated by vertical dashed lines in Fig. 4.7(a). For larger dwell times, FCA prevents comb formation, which is indicated by the fact that the green and magenta lines in Fig. 4.7(a) do not enter the range of reported values for β_{TPA}. For $t_{\mathrm{eff}} = 10$ ps (red), the threshold pump power varies between 10 mW and 60 mW, close to the threshold powers in absence of FCA ($t_{\mathrm{eff}} = 0$ ps, black curve) within the range of reported values of β_{TPA}. Note that these values for the threshold pump power only apply for an optimized detuning ζ, that minimizes the expression (*) in Eq. (4.11). Note also that the proper choice pump power and the corresponding optimum detuning ζ is an essential prerequisite for observing MI and subsequent comb formation.

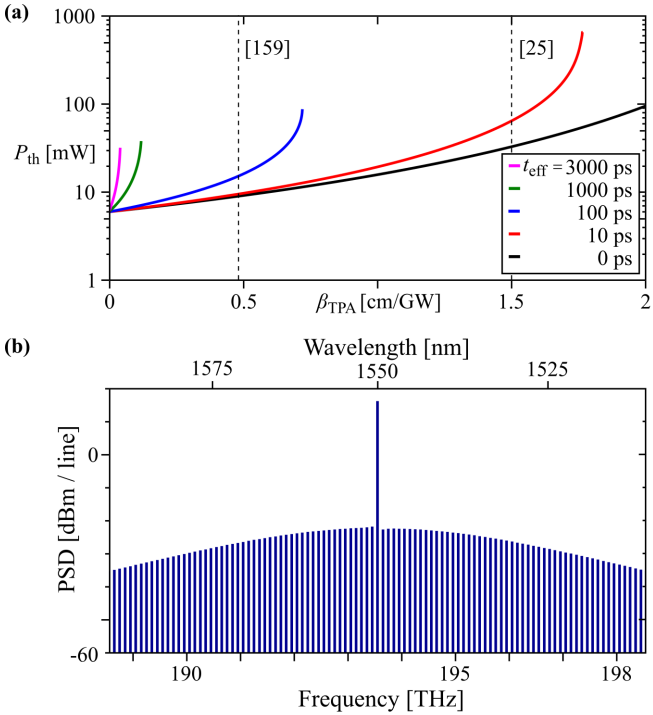

Figure 4.7: (a) On-chip threshold pump power for the onset of modulation instability as a function of TPA coefficient β_{TPA} for different FC dwell times t_{eff}. We assume a silicon microresonator with an FSR $\omega_{FSR}/(2\pi) = 100\,\text{GHz}$ at 1550 nm, see Section 4.5 for details. The microresonator is assumed to have $2\,\text{dB cm}^{-1}$ waveguide loss, anomalous dispersion and critical coupling to the bus waveguide. Reported values of β_{TPA} for silicon range from $0.45\,\text{cm GW}^{-1}$ to $1.5\,\text{cm GW}^{-1}$ as indicated by the vertical dashed lines. (b) Soliton comb spectrum obtained in the bus waveguide after the microresonator. The resonator is identical to the one considered in (a). We assume $\beta_{TPA} = 0.7\,\text{cm GW}^{-1}$, $t_{eff} = 12\,\text{ps}$, and $P_{in} = 50\,\text{mW}$. The spectrum derived from the normalized intra-cavity comb spectrum indicated in Fig.4.5(c).

For numerical simulations with non-optimum pump parameters, MI and comb formation may not be observed [25] even though the underlying device should support these processes in consideration of its TPA- and FCA-parameters.

For illustration of a specific comb source, we again assume a resonator design and waveguide properties as specified in Section 4.5, along with a Kerr coefficient of $n_2 = 6.5 \times 10^{-18}\,\mathrm{m^2\,W^{-1}}$ and a pump wavelength of 1550 nm. Based in these parameters, we calculate the physical frequency comb spectrum that is obtained in the bus waveguide after the microresonator, see Fig. 4.7(b). The TPA coefficient, the effective carrier dwell time, and the pump power are chosen as $0.7\,\mathrm{cm\,GW^{-1}}$ [29], 12 ps [29], and 50 mW, respectively. The physical spectrum shown in Fig. 4.7(b) is derived from the normalized intra-cavity comb spectrum indicated in Fig. 4.5(c) on the r.h.s.

The model presented in Eqs. (4.2), (4.3), and (4.4) can be further refined by including additional physical effect such as higher-order dispersion, Raman shift [167], or self-steepening. We expect that these effects may lead to minor corrections of the quantitative predictions on modulation instability without changing the qualitative behaviour. Note that the incorporation of such additional effects in Eq. (4.2) is straightforward, see, e.g., [25], and can be performed independently of our description of stationary free carriers, Eq. (4.3). Note also that, while the Raman effect has no significant impact on the initial comb-formation conditions [28], it severely affects the spectrum of broadband soliton frequency combs [28,168,169], as well as the power conversion efficiency [137] and the pump parameter space in which solitons can exist [28]. In addition, the results may be improved by using more accurate data for β_{TPA} and achievable ranges of t_{eff}, which will help to obtain a more precise estimate of the threshold power for MI – a key parameter from a practical point of view.

For practical devices, further reduction of the pump power is key, especially when it comes to integrated Kerr-comb modules in which the available pump power is limited [15, 22, 83, 170]. In this context, improvements in waveguide fabrication may allow reducing the linear propagation losses to values of, e.g., $0.4\,\mathrm{dB\,m^{-1}}$ [171], which is well below the $2\,\mathrm{dB\,m^{-1}}$ assumed in this work, but still far above the intrinsic absorption of silicon of less than $0.01\,\mathrm{dB\,m^{-1}}$ at telecommunication wavelengths [172]. As an alternative or an addition to reverse-biased *p-i-n*-junctions, silicon self-ion implantation may be used to reduce of the FC dwell time at the expense of slightly increased waveguide losses [173]. Alternative waveguide concepts such as, e.g., silicon-organic-

hybrid (SOH) waveguides [155, 156] with a high Kerr nonlinearity of order of $\gamma = 100\,\mathrm{m\,W^{-1}}$ and low normalized TPA absorption coefficients of $r \approx 0.036$, corresponding to $\beta_{\mathrm{TPA}} = 0.5\,\mathrm{cm\,GW^{-1}}$ for $n_2 = 1.7 \times 10^{-17}\,\mathrm{m^2\,W^{-1}}$ [155] may also be used in a microresonator.

In summary, we have presented a theoretical analysis of the impact of nonlinear loss mechanisms such as TPA and FCA on Kerr comb formation based on a model that accounts for fast-time free-carrier dynamics in a stationary frame for the fast time. Our model is based on normalized quantities and can thus be applied to wide range of resonator design, materials, and operation conditions, including devices that are affected by avoided mode crossings (AMCs). We derive the maximum two-photon absorption and free-carrier lifetime that still allow for modulation instability at sufficiently low pump powers and that can thus lead to frequency comb formation. We show that microresonators realized on the silicon-photonic platform are not necessarily unsuited for Kerr comb generation at NIR telecommunication wavelengths around 1550 nm, provided that the dwell time of the free-carriers in the waveguide core is reduced by a reverse-biased *p-i-n*-junction and that the pump parameters are chosen appropriately, and we present a specific design of a silicon microresonator with anomalous group-velocity dispersion that may even support formation of dissipative Kerr solitons. A numerical solution of the Lugiato-Lefever equation and our suggested free-carrier rate equation shows the onset of comb formation in agreement with our theoretical small-signal analysis. The impact of fast-time free-carrier dynamics is rather small as long as no comb is present or multiple pulses circulate in the microresonator. However, once single soliton pulses propagate, the FC density clearly deviates from its fast time mean value, and the optical field shows an additional fast-time drift. Both the numerical and the theoretical small-signal analysis demonstrate that modulation instability can also occur for normal-dispersion resonators if an avoided mode crossing comes into play. This would permit Kerr comb generation in silicon ring resonators with a standard waveguide height of 220 nm. We believe that our findings will help to design microresonators for Kerr comb generation on different photonic integration platforms that are affected by nonlinear loss and free-carrier absorption.

[End of publication [J2]]

5 Ultrafast optical ranging using microresonator soliton frequency combs

In this chapter, distance metrology using dissipative Kerr soliton frequency combs is described. The following text was published in *Science* [J3] and was adapted to fit the layout, structure, notation and conventions of this dissertation. The supplementary information are given in Appendix D. Parts of the results described in this chapter have been presented at conferences [C3, C4, C8, C9].

Note that the author of this dissertation, Denis Ganin and Maxim Karpov contributed equally to this publication. The idea of the experiment was conceived jointly by P. Trocha, D. Ganin, and C. Koos. The author of this dissertation and Denis Ganin jointly developed and implemented the experimental setup depicted in Figure 5.2, that is based in previous work by C. Weimann, with support of S. Wolf, J. Krockenberger, P. Marin-Palomo. D. Ganin conducted the experiments discussed in Sections 5.2 and 5.3 as well as Appendices D.1, D.5 and D.6 with support of the author. The author of this dissertation developed and implemented the digital signal processing that is described in the Appendices D.1, D.2 and D.3 and that is used to derive the results shown in Sections 5.2 and 5.3, building upon previous work by C. Weimann and supported by D. Ganin. M. Karpov, M.H.P. Pfeiffer, and A. Kordts from the Laboratory of Photonics and Quantum Measurements at École Polytechnique Fédérale de Lausanne (EPFL) developed, fabricated, and characterized the Kerr-nonlinear microresonators for comb generation as well as the soliton-generation technique described in Section 5.2 and Appendix D.7 under supervision of T. Kippenberg. The manuscript was written by the author together with D. Ganin and M. Karpov, with support of W. Freude, T.J. Kippenberg, and C. Koos. The work was jointly supervised by S. Randel, W. Freude, T.J. Kippenberg, and C. Koos.

[Start of publication [J3]]

Ultrafast optical ranging using microresonator soliton frequency combs

Science, **359**(6378), 887–891 (2018)

P. Trocha,[1] M. Karpov,[2] D. Ganin,[1] M. H. P. Pfeiffer,[2] A. Kordts,[2] S. Wolf,[1] J. Krockenberger,[1] P. Marin-Palomo,[1] C. Weimann,[1,3] S. Randel,[1,4] W. Freude,[1,4] T. J. Kippenberg,[2] C. Koos[1,4]

[1] Institute of Photonics and Quantum Electronics (IPQ), Karlsruhe Institute of Technology (KIT), Karlsruhe, Germany

[2] Laboratory of Photonics and Quantum Measurements (LPQM), École Polytechnique Fédérale de Lausanne (EPFL), Lausanne, Switzerland

[3] Carl Zeiss AG, Oberkochen, Germany

[4] Institute of Microstructure Technology (IMT), Karlsruhe Institute of Technology (KIT), Karlsruhe, Germany

Light detection and ranging is widely used in science and industry. Over the past decade, optical frequency combs were shown to offer advantages in optical ranging, enabling fast distance acquisition with high accuracy. Driven by emerging high-volume applications such as industrial sensing, drone navigation, or autonomous driving, there is now a growing demand for compact ranging systems. Here, we show that soliton Kerr comb generation in integrated silicon nitride microresonators provides a route to high-performance chip-scale ranging systems. We demonstrate dual-comb distance measurements with Allan deviations down to 12 nanometers at averaging times of 13 microseconds along with ultrafast ranging at acquisition rates of 100 megahertz, allowing for in-flight sampling of gun projectiles moving at 150 meters per second. Combining integrated soliton-comb ranging systems with chip-scale nanophotonic phased arrays could enable compact ultrafast ranging systems for emerging mass applications.

5.1 Introduction

Laser-based light detection and ranging (LiDAR) is a key technology in industrial and scientific metrology, offering high-precision, long-range, and fast

acquisition [105, 174]. LiDAR systems have found their way into a wide variety of applications, comprising, for example, industrial process monitoring, autonomous driving, satellite formation flying, or drone navigation. When it comes to fast and accurate ranging over extended distances, optical frequency combs [30] have been demonstrated to exhibit characteristic advantages, exploiting time-of-flight (ToF) schemes [175], interferometric approaches [176], or combinations thereof [19]. In early experiments [175], mode-locked fiber lasers were used for ToF ranging, thereby primarily exploiting the stability of the repetition rate. Regarding interferometric schemes, optical frequency combs were exploited to stabilize the frequency interval between continuous-wave (CW) lasers used in synthetic-wavelength interferometry [176, 177]. Dual-comb schemes, which rely on multiheterodyne detection by coherent superposition of a pair of slightly detuned frequency combs [178], allow combining of ToF measurements with optical interferometry, thereby simultaneously exploiting the radio-frequency coherence of the pulse train and the optical coherence of the individual comb tones [19]. More recently, comb-based schemes have been demonstrated as a viable path to high-speed sampling with acquisition times down to 500 ns [179].

However, besides accuracy and acquisition speed, footprint is becoming increasingly important for LiDAR systems. On the technology side, recent advances in photonic integration show that large-scale nanophotonic phased arrays [180, 181] open a promising path towards ultracompact systems for rapid high-resolution beam steering. To harness the full potential of these approaches, the optical phased arrays need to be complemented by LiDAR engines that combine high precision with ultrafast acquisition and that are amenable to chip-scale integration. Existing dual-comb LiDAR concepts cannot fulfill these requirements because they rely either on cavity-stabilized mode-locked fiber lasers [19] or on spectral broadening of initially narrowband seed combs [179], which typically require delicate fiber-based dispersion management schemes, usually in combination with intermediate amplifiers.

Here, we show that dissipative Kerr soliton (DKS) states [21, 182] in microresonator-based optical frequency combs [10, 11] provide a route to integrated LiDAR systems that combine sub-wavelength accuracy and unprecedented acquisition speed with scalable fabrication, robust implementation, and compact form factors. DKSs are solutions of a driven, damped, and detuned nonlinear Schrödinger equation, often referred to as a Lugiato-Lefever equation [78].

Such ultrashort temporal solitons can circulate continuously in the cavity, relying on a double balance of dispersion and nonlinearity as well as parametric gain and cavity loss [21]. In the frequency domain, DKS pulse trains correspond to optical frequency combs, which combine large bandwidths and smooth spectral envelopes with free spectral ranges in the range from tens of gigahertz to a few terahertz. Microresonator-based DKSs have recently been used in low-noise microwave generation [183], frequency metrology [89], dual-comb spectroscopy [18], coherent communications [J5], and optical frequency synthesis [88]. In our demonstrations, we exploit DKS combs for synthetic-wavelength interferometry with massively parallel multiheterodyne detection. Our scheme is based on a pair of free-running comb generators and does not require phase locking of the combs to each other. The large optical bandwidth of more than 11 THz leads to highly precise distance measurements with Allan deviations reaching 12 nm at an averaging time of 14 μs, whereas the large free spectral range (FSR) enables high-speed measurements at rates of up to 100 MHz. We prove the viability of our technique by sampling the naturally scattering surface of air-gun projectiles on the fly, achieving lateral spatial resolutions of more than 2 μm for object speeds of more than 150 m/s.

5.2 Experimental setup and system characterization

For DKS comb generation, we use a pair of CW-pumped silicon nitride (Si_3N_4) microring resonators on separate chips [24, 184, 185]. The devices (Fig. 5.1(a)) are fabricated using the photonic Damascene process [85], which enables crack-free fabrication of high-quality (Q) microresonators (Q > 1 million) with large waveguide dimensions (1.65 by 0.85 μm). DKS comb generation is achieved by sweeping the pump laser frequency from the effectively blue-detuned to a defined point in the effectively red-detuned regime of a selected cavity resonance, where the microresonator system supports soliton formation [21] (Fig. 5.1(b)). Once the laser scan stops, typically a multisoliton state is generated. By next applying the backward frequency tuning technique [120], a single-soliton state corresponding to an optical frequency comb with a spectrally smooth squared hyperbolic secant ($sech^2$) shape envelope (Fig. 5.1(c)) is achieved in a deterministic manner. A more detailed description of the experimental setup and of the microresonator devices can be found in Appendix D.

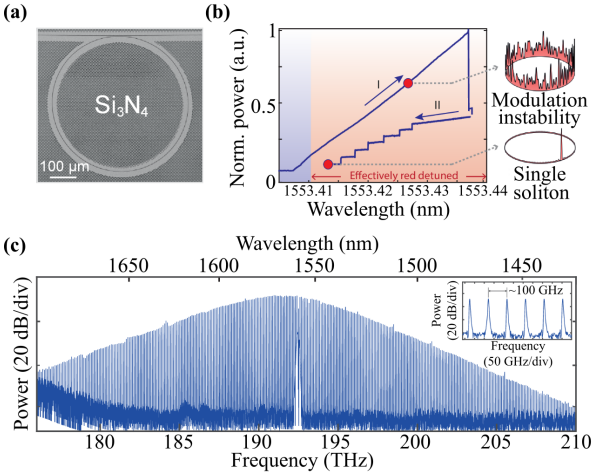

Figure 5.1: Dissipative Kerr soliton (DKS) generation in silicon nitride (Si_3N_4) microresonators. (a) Scanning electron microscopy image of a silicon nitride microresonator with a radius of 240 μm. The checkerboard pattern results from the photonic Damascene fabrication process [85]. (b) Visualization of the backward tuning technique. The pump laser wavelength is changed from an effective blue-detuning into an effective red-detuned state, thereby increasing the intracavity power and giving rise to modulation instability (arrow I). Eventually, the intracavity field switches from this chaotic state into a multisoliton state when the laser tuning is stopped. From there on, the laser wavelength is tuned toward lower wavelengths, decreasing the number of solitons until a single-soliton state is reached. The decreasing number of solitons is visible by the decreasing steps of the intracavity power (arrow II). (c) Spectrum of a DKS optical frequency comb with zoom-in. The spectrum combines large bandwidth and a smooth spectral envelope and features a line spacing of 100 GHz.

The experimental setup used for dual-comb ranging is depicted in Fig. 5.2(a). To enable multiheterodyne detection, we use two Kerr comb generators with slightly different free spectral ranges of $\omega_{\mathrm{SI,FSR}}/2\pi = 95.842\,\mathrm{GHz}$ and $\omega_{\mathrm{LO,FSR}}/2\pi = 95.746\,\mathrm{GHz}$, respectively. To demonstrate that our concept does not require phase locking of the DKS combs, we used a pair of free-running CW lasers to pump the microresonators and compensate for the stochastic phase drifts by digital signal processing, see Appendix D. The pump light for the signal and the Local oscillator (LO) comb is amplified by erbium-doped fiber amplifiers (EDFA) to power levels of 3.5 and 2.6 W, respectively, and then coupled to the microresonator chips with a coupling efficiency of 60 % per facet. The resulting combs feature overall power levels of 4.3 and 2.5 mW and

are amplified by a pair of C+L-band (1530 to 1565 nm and 1565 to 1625 nm) EDFA to 450 mW to improve the measurement precision[1]. A spectrum of an amplified comb is shown in Fig. 5.2(b). The gain bandwidth of the EDFA limits the number of usable lines to about 115, which is sufficient for our experiments.

For distance measurements, the signal comb is split by a fiber-based 50/50 coupler, and one part is routed to the target and back to a balanced measurement photodetector (Meas. PD), while the other part is directly sent to the balanced reference detector (Ref. PD); see Fig. 5.2(a). Measurement and reference PDs feature bandwidths of 43 GHz. Similarly, the LO comb is split into two portions, which are routed to the measurement PD and the reference PD for multiheterodyne detection. The resulting baseband signal contains discrete beat notes, which are recorded by a 33-GHz real-time sampling oscilloscope and separated by means of a numerically calculated Fourier transform. The distance to the target is extracted from the phase of the baseband beat notes. Data processing and evaluation are performed offline; see Appendix D for details of the underlying algorithms.

Figure 5.2(c) shows the Fourier transform of a recorded baseband signal, revealing the various beat notes between the signal and LO comb lines. The spacing of the beat notes is given by the difference of the line spacing of the LO and the signal comb and amounts to $\Delta f_{\mathrm{FSR}} = \Delta\omega_{\mathrm{FSR}}/2\pi = 96.4\,\mathrm{MHz}$, thereby dictating a minimum possible acquisition time of $T_{\mathrm{min}} = 1/\Delta f_{\mathrm{FSR}} = 10.4\,\mathrm{ns}$ and a maximum possible distance acquisition rate of 96.4 MHz.

For a thorough stability and precision analysis of our dual-comb scheme, we measure the distance to a static mirror and evaluate the Allan deviation. The entire measurement contains a series of $\approx 1.1\times10^6$ individual data points taken at an acquisition time of 10.4 ns per point, leading to a total duration of $\approx$ 12 ms. The extracted Allan deviation is plotted in Fig. 5.2(d). At an averaging time of 10.4 ns, the Allan deviation amounts to 284 nm, and it decreases to 12 nm for an averaging time of 13 μs. At small averaging times, the Allan deviation decreases with increasing averaging time, as expected for dominating white noise such as shot noise or amplified spontaneous emission (ASE) originating from the EDFA. For larger averaging times, the Allan deviation increases,

[1] In [J3], the text refers to the measurement "accuracy", however in the terminology of this thesis, the underlying physical quantity is the measurement "precision" and therefore the text changed where applicable, see also Appendix D.

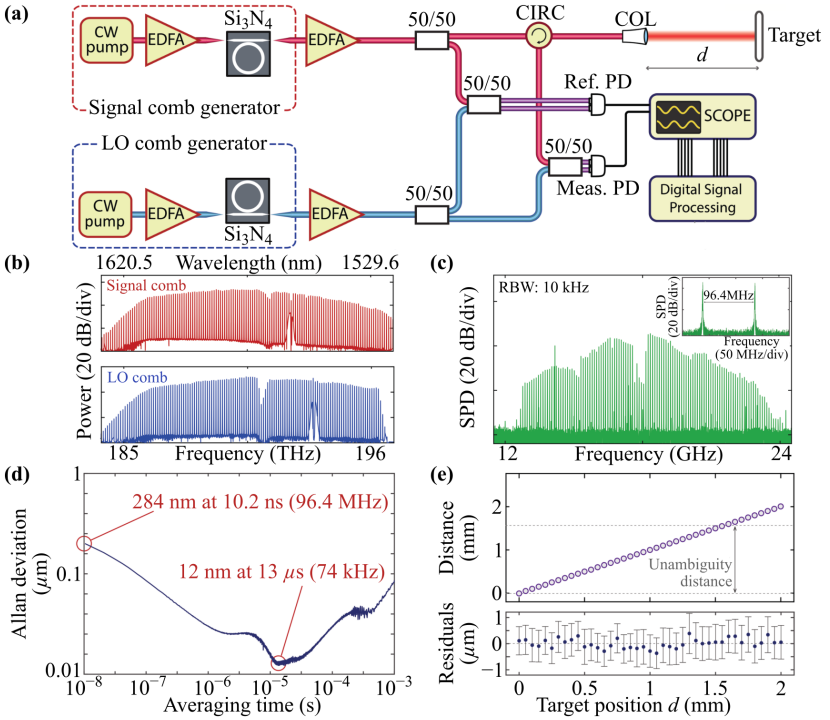

Figure 5.2: Experimental demonstration and performance characterization. (a) Experimental setup. DKS combs are generated by a pair of silicon nitride (Si_3N_4) microresonators, which are pumped by free-running CW lasers and EDFA. After suppressing residual pump light by fiber Bragg gratings (not shown), the combs are amplified by another pair of EDFA. The signal comb (red) is split, and one part is routed to the target and back to a balanced measurement photodetector (Meas. PD) by optical fibers, an optical circulator (CIRC), and a collimator (COL), while the other part is directly sent to the balanced reference detector (Ref. PD). Similarly, the LO comb is split into two portions, which are routed to the measurement PD and the reference PD for multi-heterodyne detection. The resulting baseband beat signals are recorded by a 33-GHz real-time sampling oscilloscope. Digital signal processing is performed offline. (b) Optical spectra of the signal comb (red) and the local oscillator comb (blue) after amplification. (c) Numerically calculated Fourier transform of a recorded time-domain signal. (d) Allan deviation of measured distances as a function of averaging time. The increase toward longer averaging times is attributed to drifts and to mechanical vibrations of the fibers that lead to the target, see Appendix D. (e) (Top) Scan of measured position versus set position in steps of 50 μm over the full unambiguity distance (marked by dashed lines). (Bottom) Residual deviations ("residuals") between measured and set positions, with standard deviations as error bars.

which we attribute to thermal drift of the fibers and to mechanical vibrations at acoustic frequencies. The current measurement precision is hence only limited by a nonideal implementation of the system. Further improvements are possible by reducing the ASE noise floor of the EDFA and by avoiding thermal drift and mechanical vibrations. Fundamentally, the measurement precision is only limited by inevitable shot noise and possibly by additional ASE noise of ideal EDFA. For comb powers of 10 mW, this would allow for measurement precisions of better than 10 nm at the highest acquisition rate of 100 MHz; see Appendix D for details.

Besides the Allan deviation, we also estimated the accuracy of our technique by measuring variable distances to a target that is moved over a full unambiguity distance[2] $d_{\mathrm{ua}} = \frac{c}{2}\frac{2\pi}{\omega_{\mathrm{SLFSR}}}$ (Fig. 5.2(e)). In this experiment, the target mirror is stepped in increments of 50 μm using a feedback-stabilized stage with a positioning accuracy of more than 50 nm. To reduce the impact of fiber drift, the distance measurement is continuously switched between the movable target mirror and a static calibration mirror in quick succession, taking between 6500 and 9500 measurements with the full acquisition rate of $\approx$ 96 MHz on each mirror; see Appendix D. From these measurements, we extract the distance to the target mirror and the associated standard deviation; see Appendix D for details. In the upper part of Fig. 5.2(e), the measured distance is plotted as a function of the distance set by the translation state. Measured distances exceeding the unambiguity distance of $d_{\mathrm{ua}} = 1.56$ mm are unwrapped manually. The bottom part of Fig. 5.2(e) shows the residual deviations of the measured positions from the set positions along with the respective standard deviations indicated as error bars. Importantly, no cyclic error is observed throughout the unambiguity distance. We determine the accuracy of our measurement to 188 nm, defined as the standard deviation of the residuals, which are of the same order of magnitude as the 50-nm positioning accuracy of the stage specified by the manufacturer. In this measurement, the refractive index of air is considered according to Ciddor's formula for ambient laboratory conditions. The measured 188 nm standard deviation of the residuals is still dominated by drift and acoustic vibrations of the measurement setup rather than by the measurement system itself, despite compensation via the static calibration

[2] In the formalism presented in [J3] and therefore in this chapter, the refractive index of light is considered in the speed of light $c = c_0/n_{\mathrm{air}}$ at this position in the text. This definition of the unambiguity distance is consistent with the definition presented in Section 2.4.2, Eq. (2.73).

mirror. This can be inferred from the fact that the standard deviation of 188 nm is still much larger than the intrinsic system-related errors of 5 nm that should be expected for the averaging time of 100 μs; see Appendix D for a more detailed discussion.

5.3 Distance data reproducibity and ultrafast ranging

To validate the reproducibility of our system and to benchmark the results with respect to existing techniques, we measured the profile of a quickly rotating disk with grooves of different depths on its surface (see Fig. 5.3(a)). In this experiment, the measurement beam is focused to the surface near the edge of the disk, which rotates at a frequency of about 600 Hz, thus resulting in an edge velocity of 160 m/s. The distance acquisition rate in this experiment amounts to 96.5 MHz, limited by the spectral spacing of $\Delta\omega_{\mathrm{FSR}}/(2\pi)$ of the beat notes in the baseband photocurrent but not by the acquisition speed of our oscilloscopes. The resulting profiles are shown in Fig. 5.3(b) for two measurements, which were taken independently from one another during different round-trips of the disc. Measurement points close to the edges of the grooves may suffer from strong scattering and low power levels, which lead to unreliable distance information. Using the fit error of the linear phase characteristic as a quality criterion, our technique allows identification of such nonusable measurement points and allows automatically discarding them from the data; see Appendix D for details. The raw data of both measurements was further subject to vibrations of the disk arising from the driving engine. These vibrations have been removed by fitting a polynomial to the top surface of the disk and by using it for correction of the overall measurement data. In a first experiment, we analyze the reproducibility of the technique by a detailed comparison of the results obtained from the two measurements (see Fig. 5.3(b), Inset 1). The measured profiles exhibit good agreement regarding macroscopic features such as the groove depth, as well as microscopic features such as surface texture and a decrease of depth toward the edge of the groove. Deviations are attributed to the fact that the two measurements have been taken independently and might hence not have sampled the exact same line across the groove. In addition, we benchmark our technique by comparing the obtained profile of a single groove with a profile obtained from an industrial optical coordinate-measuring

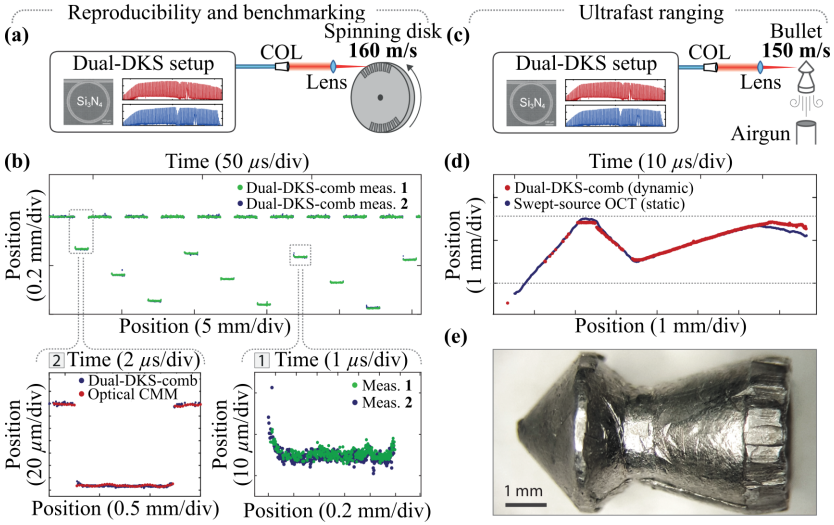

Figure 5.3: Reproducibility, benchmarking, and ultrafast ranging demonstration. (a) Setup for reproducibility and benchmarking experiments. The measurement beam is focused on the surface of a spinning disk with grooves of different depths. (b) Measured surface profile of the disk as a function of position (bottom scale) and time (top scale). The plot contains two independent measurements depicted in blue and green. (Inset 1) Reproducibility demonstration by detailed comparison of the two independent measurements plotted in (b). The measured profiles exhibit good agreement regarding both macroscopic features, such as the groove depth, and microscopic features. (Inset 2) Benchmarking of the high-speed dual-DKS-comb measurement to the results obtained from an industrial optical CMM. (c) Setup of ultrafast ranging experiment. (d) Measured profile of the projectile obtained from single-shot in-flight dual-DKS-comb measurement (red), along with a swept-source optical coherence tomography (OCT) profile scan that was recorded on the static projectile after recovery from the backstop. The deviations toward the back end of the projectile are attributed to strong corrugations in this area; see (e). (e) Image of the projectile after recovery from the backstop.

machine (CMM, Werth VideoCheck HA) (Fig. 5.3(b), Inset 2). Both profiles are in good agreement, with some minor deviations that we again attribute to slightly different measurement positions along the analyzed groove.

Ultrafast ranging is demonstrated by measuring the profile of a flying air-gun bullet that is shot through the focus of the measurement beam (see Fig. 5.3(c)). The projectile moves at a speed of 150 m/s (Mach 0.47), which, together with the acquisition rate of 96.2 MHz, results in a lateral distance of 1.6 μm between

neighboring sampling points on the surface of the bullet. The full profile of the projectile is taken during a single shot and depicted in red in Fig. 5.3(d) along with a reference measurement obtained from the static bullet using a swept-source optical coherence tomography system (dark blue). For better comparison, the two profiles were rotated and an actual speed of the bullet of 149 m/s was estimated for best agreement. Both curves clearly coincide and reproduce the shape of the fired projectile. Missing data points in the dual-DKS comb measurement at the tip of the projectile are caused by low power levels of the back-coupled signal, which is inevitable for such steep surfaces in combination with the limited numerical aperture of the lens used for collecting the backscattered light. As before, these measurement points have been discarded from the data based on a large fit error of the linear phase characteristic, see Appendix D. An image of the projectile after recovery from the backstop exhibits a strong corrugation of the bullet toward its back (Fig. 5.3(e)). This leads to deviations of the measured profiles in Fig. 5.3(d) toward the right-hand side, since the strongly corrugated surface of the projectile in this area has very likely been sampled at two different positions.

To make dual-DKS-comb ranging a viable option for practical applications, the limited unambiguity distance of 1.56 mm must be overcome. This can be achieved, for example, by switching the role of the LO comb and the measurement comb [19] or by sending the LO comb also to the target while evaluating not only the difference signal of the balanced photodetectors but also the sum [186]. Using such techniques, high-precision ranging over extended distances should be possible, only limited by coherence lengths of the individual comb lines, which amount to several kilometers. The high acquisition rate allows tracking continuous movements of objects at any practical speed, with an unambiguity limit of ~145 000 m/s.

5.4 Summary and outlook

Our experiments demonstrate the viability of chip-scale DKS comb generators to act as optical sources for high-performance ranging systems and are a key step toward fully integrated chip-scale LiDAR engines, as illustrated as an artist's view in Fig. 5.4. In this vision, the LiDAR system is realized as a photonic multichip assembly, in which all photonic integrated circuits are con-

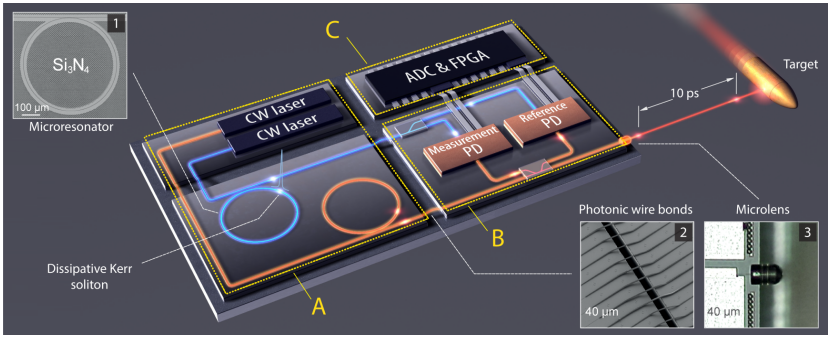

Figure 5.4: Artist's view of a dual-comb chip-scale LiDAR engine. The system consists of a dual-frequency comb source (A), a photonic integrated circuit (PIC) for transmission and detection of the LiDAR signal [114] (B), and data acquisition and signal processing electronics (C). The system is realized as a photonic multichip assembly that combines the distinct advantages of different photonic integration platforms. The insets show various technologies that could be used to realize the envisioned LiDAR engine. (Inset 1) Si_3N_4 microresonator for comb generation [85,185]. (Inset 2) Photonic wire bonds for chip-chip connections [187]. (Inset 3) Facet-attached microlens for collimation of the emitted free-space beam [188].

nected by photonic wire bonds (Fig. 5.4, Inset 2) [187]. The comb generators are pumped by integrated CW lasers, and a dedicated optical chip is used to transmit and receive the optical signals [114]. The receiver is equipped with a chip-attached microlens that collimates the emitted light toward the target (Fig. 5.4, Inset 3) [188]. The electrical signals generated by the photodetectors are sampled by analog-to-digital converters (ADC) and further evaluated by digital signal processing in powerful field-programmable gate arrays (FPGA) or application-specific integrated circuits. Free-running pump lasers greatly simplify the implementation in comparison with configurations where two comb generators are simultaneously pumped by a single light source. Although most of the technological building blocks for realizing this vision have already been demonstrated, one of the remaining key challenges is to reduce the power levels required for DKS generation to typical output power levels of state-of-the-art diode lasers. This requires silicon nitride microresonators with higher quality factors that can be achieved by optimizing the waveguide geometry and the fabrication processes. We expect that such optimizations will allow increasing the Q-factor by about one order of magnitude, thus reducing the pump power requirements by two orders of magnitude. Alternatively, other

integration platforms, such as silicon oxide or AlGaAs, can be used, permitting comb generation with only a few milliwatts of pump power [48]. These power levels are realistically achievable with integrated pump laser diodes. Based on these findings, we believe that DKS-based dual-comb LiDAR could have a transformative impact on all major application fields that require compact LiDAR systems and high-precision ranging, in particular when combined with large-scale nanophotonic phased arrays [180, 181]. Acquisition rates of hundreds of megahertz could enable ultrafast three-dimensional imaging with megapixel resolution and update rates of hundreds of frames per second.

[End of publication [J3]]

6 Ultrafast optical ranging using quantum-dash mode-locked laser diodes

In this chapter, distance metrology using optical frequency combs emitted by quantum-dash mode-locked laser diodes (QD-MLLDs) is described. The following text [J4] was published in *Scientific Reports* and was adapted to fit the layout, structure and notation of this dissertation. The related supplementary information are given in Appendix E, Sections E.1 to E.6.

The scope of the manuscript was developed by the author of this dissertation together with C. Koos. The experiments described in Sections 6.3, 6.4 and 6.5 as well as Appendices E.1, E.5 and E.6 were conducted by the author of this dissertation. The laser diodes described in Section 6.3 were fabricated and provided by Q. Gaimard, G. Aubin, F. Lelarge, and A. Ramdane from the Centre de Nanosciences et de Nanotechnologies at Université Paris-Saclay and from Almae Technologies, Marcoussis. Setups for operating the QD-MLLDs were developed and implemented by J. Kemal with support of the author. The author of this dissertation developed the digital signal processing (DSP) required for data evaluation, which is an advanced version of the DSP used in the experiments described in Chapter 5, see Sections 6.3 and 6.4 and Appendix E.5. The analysis of fundamental limitations of the distance measurement system described in the Appendices E.3 and E.4 was performed by the author of this dissertation under supervision and in discussion with C. Koos, S. Randel, and W. Freude. The manuscript was written by the author with support of W. Freude and C. Koos. The work was supervised by W. Freude, S. Randel, and C. Koos.

[Start of manuscript [J4]]

Ultra-fast optical ranging using quantum-dash mode-locked laser diodes

Scientific Reports, **12**(1076), 1–12 (2022)

P. Trocha,[1] J. Kemal,[1] Q. Gaimard,[2] G. Aubin,[2] F. Lelarge,[3] A. Ramdane,[2] W. Freude,[1] S. Randel,[1] C. Koos,[1,4]

[1] Institute of Photonics and Quantum Electronics (IPQ), Karlsruhe Institute of Technology (KIT), Karlsruhe, Germany

[2] Centre de Nanosciences et de Nanotechnologies, Centre national de la recherche scientifique, Université Paris-Saclay, Palaiseau, France

[3] Almae Technologies, Marcoussis, France

[4] Institute of Microstructure Technology (IMT), Karlsruhe Institute of Technology (KIT), Karlsruhe, Germany

Laser-based light detection and ranging (LiDAR) is key to many applications in science and industry. For many use cases, compactness and power efficiency are key, especially in high-volume applications such as industrial sensing, navigation of autonomous objects, or digitization of 3D scenes using hand-held devices. In this context, comb-based ranging systems are of particular interest, combining high accuracy with high measurement speed. However, the technical complexity of miniaturized comb sources is still prohibitive for many applications, in particular when high optical output powers and high efficiency are required. Here we show that quantum-dash mode-locked laser diodes (QD-MLLD) offer a particularly attractive route towards high-performance chip-scale ranging systems. QD-MLLD are compact, can be easily operated by a simple DC drive current, and provide spectrally flat frequency combs with bandwidths in excess of 2 THz – thus lending themselves to coherent dual-comb ranging. In our experiments, we show measurement rates of up to 500 MHz, which corresponds to the highest rate demonstrated with any ranging system so far. We attain reliable measurement results with optical return powers of only −40 dBm, corresponding to a total loss of 49 dB in the ranging path – the highest loss tolerance demonstrated so far for dual-comb ranging with chip-scale comb sources. Combing QD-MLLD with advanced silicon photonic receivers offers an attractive route towards robust and technically simple chip-scale LiDAR systems.

6.1 Introduction

Optical distance metrology is key to many applications in science and industry [101, 103, 189–191]. Among various techniques, dual-comb ranging based on multi-heterodyne detection [J3] [19, 179, 192] stands out due to a unique combination of measurement accuracy and acquisition speed. As an example, dual-comb ranging based on mode-locked fiber lasers was demonstrated to provide a measurement precision of 5 nm, achieved by combining a time-of-flight scheme with optical interferometry [19]. More recently soliton Kerr comb generators have gained importance as light sources for optical ranging [193, 194], permitting measurement rates of up to 100 MHz with sub-micrometer precision when used in dual-comb multi-heterodyne detection [J3]. However, while these experiments demonstrate impressive performance parameters, the underlying comb sources are still rather complex, involving, e.g., discrete components such as fiber ring lasers [19], high-power optical amplifiers [J3], or fiber-coupled electro-optic modulators [179, 192]. It might hence be challenging for these schemes to fulfil the stringent requirements with respect to robustness, size, weight and power consumption that are associated with many technically relevant applications. In addition, only few publications explicitly [192, 195] address the optical loss tolerance of comb-based ranging systems, which is a key performance metric in many ranging applications.

In this paper, we demonstrate that high-precision dual-comb ranging can be greatly simplified by using quantum-dash mode-locked laser diodes (QD-MLLD) as light sources. These devices are compact and robust and offer easy operation by a simple DC drive current [92, 93]. QD-MLLD provide spectrally flat frequency combs with line spacings of tens of gigahertz and have previously been used for high-speed optical communications [J6, J7] [196]. In our experiments, we use a pair of QD-MLLDs with slightly detuned free spectral ranges (FSR) of approximately 50 GHz and demonstrate measurement rates of up to 500 MHz with a precision of 1.7 μm. To the best of our knowledge, this is the highest measurement rate demonstrated with any ranging system so far. When reducing the measurement rate to 10 kHz, the precision improves to 23 nm. We further demonstrate reliable ranging with optical return powers of only −40 dBm, corresponding to a total round-trip loss of 49 dB in the free-space measurement path. To the best or our knowledge, this is the highest loss tolerance demonstrated so far for a comb-based measurement system that

relies on chip-scale comb sources. When using an erbium-doped fiber amplifier (EDFA) for boosting the transmitted power, the maximum tolerable round-trip loss increases to 71 dB, without any impairment of the achievable precision. We demonstrate the measurement speed of our system by high-precision in-flight sampling of air-gun pellets moving at a speed of 150 m s^{-1}. We believe that our experiments pave the path towards practically viable chip-scale ranging systems that combine robust and technically simple frequency comb sources with advanced silicon photonic receivers [197] and solid-state beam-steering circuits [180, 191, 198], thus providing an unprecedented combination of compactness, accuracy, measurement speed, and loss tolerance.

6.2 Comb-based integrated LiDAR systems and quantum-dash mode locked laser diodes

An application scenario of an ultrafast chip-scale LiDAR system is illustrated in Fig. 6.1(a). Due to its compact and lightweight implementation, the chip-scale LiDAR module can be mounted to autonomously navigating carrier systems such as drones, offering, e.g., new perspectives in structural health monitoring of large buildings or critical infrastructures such as bridges. In such applications, high-speed ranging is crucial for fast scanning of 3D surface profiles with sub-millimeter or even micrometer-scale precision during movement of the carrier system. The 3D surface profiles may complement 2D camera images for a reliable quantitative analysis of damage patterns.

Figure 6.1(b) illustrates the concept of a fully integrated dual-comb LiDAR system that exploits multi-heterodyne reception for high-speed high-precision ranging [J3] [114]. The system is realized as a multi-chip assembly that combines a pair of MLLD-based frequency comb sources (A), silicon photonic transmitter and receiver circuits (B), as well as processing electronics (C) in a compact lightweight package. One MLLD emits the so-called signal frequency comb (SI MLLD, red) while the other one generates the local-oscillator (LO) comb (LO MLLD, blue). Photonic wire bonds [199, 200] are used to couple the frequency combs to the transmitter and receiver circuit, where they are split in two parts each. One part of the SI comb leaves the LiDAR system through a micro-lens directly attached to the chip [188], is collimated by a macroscopic lens and directed towards the target. Note that the beam scanning

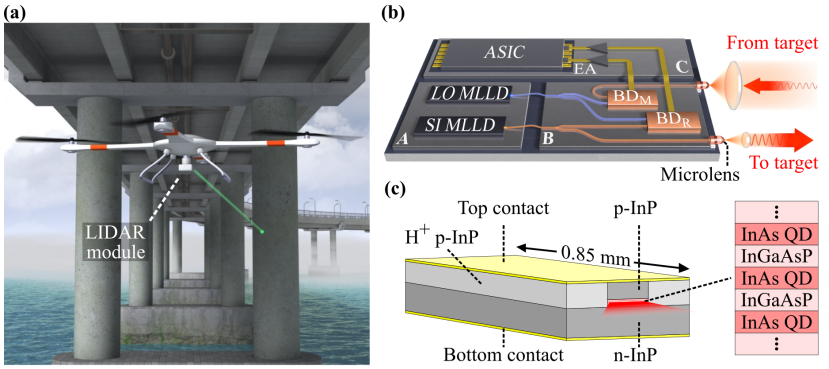

Figure 6.1: Application scenario and technical concept of an ultrafast chip-scale LiDAR system. (a) Compact lightweight LiDAR modules lend themselves to application in autonomously navigating carrier systems such as drones. High-resolution scanning of 3D surface profiles may complement 2D camera images for a reliable quantitative analysis of damage patterns, e.g., in structural health monitoring of large buildings or critical infrastructures. (b) Concept of a fully integrated dual-comb LiDAR system realized as a multi-chip assembly that combines a pair of MLLD-based frequency comb sources realized on InP substrates (A), silicon photonic transmitter and receiver circuits (B), and processing electronics (C) in a compact lightweight package. For distance measurements, light is emitted through a micro-lens directly attached to the chip, collimated by a macroscopic lens and directed towards the target via a beam scanner (not shown). The back-scattered light is coupled back to the chip and sent to a balanced photodetector (BD_M) for multi-heterodyne reception. An electronic application-specific integrated circuit (ASIC) is used for digital signal processing and extraction of the distance information. (c) Schematic of the QD-MLLD. The active medium comprises a stack of three InAs QD layers separated by InGaAsP layers. The pump current is applied via the bottom and top contact. The cavity is formed by the cleaved end facets of the chip with roughly 30 % reflectivity each. Due to the inhomogeneously broadened gain spectrum of the QD material, multiple longitudinal lasing modes can oscillate simultaneously in the laser cavity, mode-locked by self-induced carrier density modulations. This leads to a time-periodic optical signal with a comb-like spectrum, where the FSR is determined by the round-trip time and hence the length of the cavity.

system is omitted in Fig. 6.1(b) for simplicity. The other part of the SI comb is superimposed with one part of the LO comb and received by a balanced reference photodetector (BD_R). The LO MLLD and the SI MLLD are slightly detuned in center frequency and free-spectral range, leading to a photocurrent with comb-like spectrum that reveals the phase relations of the various optical tones [J3] [114]. The light backscattered from the target is collected by a large lens, focused into a waveguide of the receiver chip via a micro-lens [188], and guided to another balanced measurement photodetector (BD_M), where

it is superimposed with the second portion of the LO comb. The distance can be extracted by comparing the phases of the spectral components in the comb-like photocurrent of the measurement detector to the phases extracted from the photocurrent of the reference detector. In the concept illustrated in Fig. 6.1(b), the electrical output signals from BD_R and BD_M are transferred to chip (C) by electrical wire bonds, amplified, and processed by an application specific integrated circuit (ASIC). The data evaluation scheme exploits the concept of synthetic-wavelength interferometry and is described in more detail in Refs. [J3] [114].

The MLLD rely on InAs/InGaAsP quantum-dash (QD) structures on InP substrates and are driven by a simple DC pump current, see Fig. 6.1(c). The active medium consists of three stacked layers of InAs QD, which are separated by InGaAsP barriers, such that charge carriers injected into the layer stack become trapped in the QD-layers and recombine radiatively. The optical field is vertically and laterally confined to the InAs-QD / InGaAsP stack through the surrounding low-index InP material. The cavity is formed by the cleaved end facets with roughly 30 % reflectivity each. Multiple longitudinal lasing modes can oscillate simultaneously in this Fabry-Pérot laser cavity. These longitudinal modes experience mode-locking due to self-induced carrier density modulations of the gain medium [92], leading to a time-periodic optical signal with a comb-like spectrum, where the FSR of the comb lines is determined by the roundtrip-time and hence the length of the cavity. The comb spectrum is centered around a photon energy of approximately 0.81 eV (195 THz, 1538 nm), with a relatively large optical bandwidth of more than 1.5 . . . 2 THz, owing to the inhomogeneously broadened gain spectrum arising from the shape and size variations of the quantum dashes.

In the following, we denote the comb-line frequencies by $\omega_{\mathrm{SI},\mu}$ for the SI MLLD and by $\omega_{\mathrm{LO},\mu'}$ for the LO MLLD,

$$\omega_{\mathrm{SI},\mu} = \omega_{\mathrm{SI},0} + \mu\,\omega_{\mathrm{SI,FSR}}, \tag{6.1}$$

$$\omega_{\mathrm{LO},\mu'} = \omega_{\mathrm{LO},0} + \mu'\omega_{\mathrm{LO,FSR}}. \tag{6.2}$$

In these relations, $\omega_{\mathrm{SI},0}$ and $\omega_{\mathrm{LO},0}$ are the center comb lines, the integer comb line indices are denoted as μ for the SI comb and as μ' for the LO comb, and the corresponding free spectral ranges are $\omega_{\mathrm{SI,FSR}}$ and $\omega_{\mathrm{LO,FSR}}$, respectively. Spectra of the SI-MLLD comb and the LO-MLLD comb are

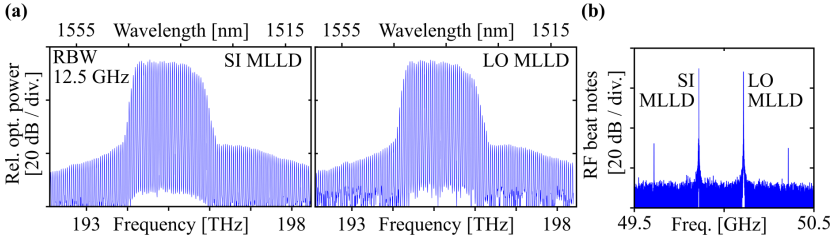

Figure 6.2: Optical spectra and RF beat notes of QD-MLLDs. (a) Left: Emission spectrum of the MLLD used as signal comb (SI MLLD), having an FSR of 49.72 GHz. Right: Emission spectrum of MLLD used as local oscillator (LO MLLD), for which the FSR amounts to 50.21 GHz. (b) RF beat notes of both MLLDs. The narrow RF linewidth of the order of 10 kHz indicates stable mode-locking of neighboring optical tones. The noise floor in this measurement is limited by the effective number of bits (ENOB $\approx$ 5) of the high-speed oscilloscopes (Keysight UXR0804A) that were used to digitize the signals, see Appendix E, Section E.3 for a more detailed discussion.

shown in Fig. 6.2(a). To determine the FSR of the combs experimentally, we connect both combs simultaneously to a balanced photodetector with a 3 dB-bandwidth of 43 GHz, record the photocurrent and compute the Fourier transform. Due to the limited photodetector bandwidth, only mixing products of directly neighboring comb lines are visible in the RF beat signal, see Fig. 6.2(b). The left beat signal corresponds to the FSR $\omega_{\mathrm{SI,FSR}} = 2\pi \times 49.72$ GHz of the SI MLLD, and the right beat signal reveals the FSR $\omega_{\mathrm{LO,FSR}} = 2\pi \times 50.21$ GHz of the LO MLLD. The 3 dB-bandwidth of the individual beat notes, also referred to as the RF linewidth of the QD MLLD comb, is typically of the order of 10 kHz [J6], which indicates efficient mode-locking of the longitudinal modes. Note that the RF linewidth only indicates low relative phase noise of neighboring comb tones. The absolute phase noise of the tones, as, e.g., measured with respect to an ultra-stable continuous-wave (CW) reference tone, is usually much stronger, indicated by optical linewidth of 10 MHz [J6] or more, see Section 6.3 for details. In contrast to other comb generators, QD-MLLD emit frequency combs by simply applying a DC current [92, 93], without the need for high-speed RF devices [114, 179, 192] or fiber-based amplifiers [J3] [19]. Typically, QD-MLLD offer around 50 comb lines with FSR in the range of 10 GHz to 100 GHz. In our devices, the total comb power amounts to 20 mW with an average line power of 400 μW. The simple operation of QD-MLLD and their relatively large power per comb line along with the potential for hybrid

or monolithic integration with photonic integrated circuits make the devices attractive for chip-scale LiDAR systems.

6.3 System, operation principle and digital signal processing

In our proof-of-principle experiments we use the setup depicted in Fig. 6.3, which consists of a transmitter (Tx) and a receiver (Rx) part. The SI MLLD at the transmitter is driven by a DC pump current of 200 mA at a voltage of 1.8 V, leading to a single-facet optical output power of 13 dBm. This corresponds to a wall-plug efficiency (WPE) of 5.6 %, which compares well to that of continuous-wave laser diodes. The output of the SI MLLD is coupled into a lensed fiber (LF) with a coupling loss of approximately 1 dB. A fiber-optic circulator (not shown) attached to the lensed fiber prevents spurious back-reflections into the MLLD. Optionally, the signal comb power can be amplified using an erbium-doped fiber amplifier (EDFA, dashed). The LO comb is generated in an equivalent setup, which does not contain an amplifier. We split the SI comb in two parts using a 90/10 coupler. Light leaving the 90 %-port is collimated (COL_O) and radiated towards the target located at a distance d. The emitted optical power amounts to 9 dBm without and to 31 dBm with EDFA. The collimated signal beam is scattered back from the target and collected by a second collimator (COL_I) after traversing the measurement path with a free-space length of $2d$. A more detailed description of the free-space optics is given in Appendix E, Section E.1.

In the receiver, the LO comb is split by a 50/50 coupler. Signal light returning from the measurement path is superimposed with light of the LO comb in another 50/50 coupler and received with a balanced photodetector (BD_M). The second fraction of the SI comb does not leave the setup and is directly superimposed with the second fraction of the LO comb in another 50/50 coupler and sent to a balanced reference photodetector (BD_R). The electrical signals are amplified by electrical amplifiers (EA) and recorded using a high-speed oscilloscope (Keysight UXR0804A) with an analog-to-digital converter (ADC) operated at a sampling rate of 128 GSa s^{-1}, such that the RF beat notes of the individual combs at approximately 50 GHz can be extracted for exact determination of the respective FSR, see Fig 6.2. More detailed information

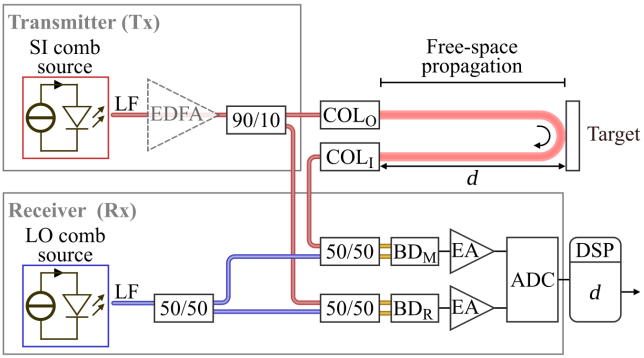

Figure 6.3: Experimental setup of our proof-of-concept demonstration. In the transmitter (Tx), the signal (SI) comb generated by a first MLLD is coupled into a lensed fiber (LF), optionally amplified in an EDFA (dashed lines), and then split by a 90/10 coupler. A first portion is emitted towards the target through an output collimator (COL$_O$). After free-space propagation and reflection at the target, the comb re-enters the system at the input collimator (COL$_I$). In the receiver (Rx), the captured light is sent to a 50/50 coupler where it is superimposed with a first portion of the local oscillator (LO) comb emitted by a second MLLD. The superimposed signals are then sent to a balanced photodetector, which is referred as the measurement detector (BD$_M$). An electrical amplifier (EA) boosts the electrical signal, which is captured by a high-speed analog-to-digital converter (ADC). The second portion of the SI comb is superimposed with a second portion of the LO comb in another 50/50 coupler, detected by a reference photodetector (BD$_R$), and fed to a second channel of the ADC. Digital signal processing (DSP) of the recorded signals is performed offline to obtain the distance d from the recorded signals. Details regarding the components used in the experimental setup can be found in Appendix E, Section E.7.

regarding the components used in the experimental setup can be found in Appendix E, Section E.7. Digital signal processing (DSP) is performed offline to extract the target distance d. Figure 6.4(a) shows the power spectral density (PSD) of the RF beat signal between the SI-MLLD and the LO-MLLD as extracted from BD$_R$. In general, the PSD contains all RF beat notes of the SI comb lines, Eq. (6.1), (index μ) and the LO comb lines, Eq. (6.1), (index μ'), appearing at RF frequencies [J3]

$$\Delta\omega_{\mu',\mu} = \left|\omega_{\mathrm{LO},0} - \omega_{\mathrm{SI},0} + (\mu' - \mu)\,\omega_{\mathrm{SI,FSR}} + \mu' \left|\omega_{\mathrm{LO,FSR}} - \omega_{\mathrm{SI,FSR}}\right|\right| . \quad (6.3)$$

After low-pass filtering of the RF signal, only beat notes of LO comb lines with the respective nearest SI comb lines are retained, which are represented by $\mu' = \mu$ in Eq. (6.3), such that $\Delta\omega_\mu = \left|\omega_{\mathrm{LO},0} - \omega_{\mathrm{SI},0} + \mu \left|\omega_{\mathrm{LO,FSR}} - \omega_{\mathrm{SI,FSR}}\right|\right|$, see

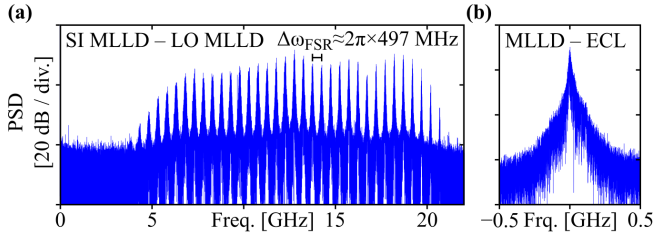

Figure 6.4: Measured RF spectra of our proof-of-concept demonstration. (a) Power spectral density (PSD) of the electric signal emitted, as obtained from the measurement photodetector for an incident signal power of −5 dBm. The spectrum shows discrete RF tones that are generated by mixing of pairs of optical tones of the SI MLLD and the LO MLLD. The comb line spacing is approximately 497 MHz, corresponding to the FSR difference of the two comb sources. The RF tones exhibit substantial linewidths of 10 MHz and more, which vary across the spectrum and which are caused by the rather high optical linewidth of the corresponding comb lines. Also here, the noise floor is limited by the effective number of bits (ENOB $\approx$ 5) of the high-speed oscilloscopes (Keysight UXR0804A) that were used to digitize the signals, see Appendix E, Section E.3 for a more detailed discussion.(b) Beat note of a QD-MLLD comb line with a narrow-linewidth ECL, showing an optical 3-dB linewidth of approximately 15 MHz.

Fig. 6.4(a). In our measurement, the center frequency $\left|\omega_{\mathrm{LO},0} - \omega_{\mathrm{SI},0}\right| = \Delta\omega_0$ is located at $2\pi \times 12$ GHz and is adjusted by temperature tuning of the MLLDs via small pump current changes such that the mixing products of the two combs can be clearly separated. The spectral separation $\left|\omega_{\mathrm{LO,FSR}} - \omega_{\mathrm{SI,FSR}}\right| = \Delta\omega_{\mathrm{FSR}}$ of the beat signals is approximately about $2\pi \times 497$ MHz. This FSR difference may drift by a few MHz on a long time-scale, unless stabilization techniques are used [201].

For extracting the distance, we evaluate the phases $\Phi_{\mathrm{meas},\mu}$ of the RF beat notes at the output of $\mathrm{BD_M}$ and compare them to the corresponding phases $\Phi_{\mathrm{ref},\mu}$ extracted from $\mathrm{BD_R}$. The phases $\Phi_{\mathrm{meas},\mu}(d)$ depend on the target distance d, whereas the phases $\Phi_{\mathrm{ref},\mu}$ are independent of d and serve as a reference for the initial phases of the various tones, see [J3] for a detailed mathematical description of the measurement technique. The free-space distance d can be determined from the phases differences $\delta\Phi_\mu(d) = \Phi_{\mathrm{meas},\mu}(d) - \Phi_{\mathrm{ref},\mu}$ of the various RF beat notes [J3],

$$\delta\Phi_\mu(d) = \mu\omega_{\mathrm{SI,FSR}}\frac{n_{\mathrm{air}}}{c_0}\,2\,(d - d_0)\,,\; n_{\mathrm{air}} = 1.000266. \tag{6.4}$$

In this relation, c_0 denotes the vacuum speed of light, and the refractive index of air n_{air} was obtained from Ciddor's formula [107]. The quantity d_0 denotes a constant distance offset dictated by the lengths of the various fibers between the comb sources and the balanced detectors, see [J3] for details.

Note that the RF beat notes shown in Fig. 6.4(a) exhibit substantial linewidths of 10 MHz and more, which vary across the spectrum and which are caused by the rather high optical linewidth of the individual comb lines. For comparison, we also record a beat note of an MLLD comb line with a highly stable tunable external-cavity laser (ECL, linewidth < 10 kHz), see Fig.6.4(b), which exhibits an optical linewidth of approximately 15 MHz. These numbers are typical for QD-MLLD, see [J6] for a more detailed discussion. For the measurements presented in this work, phase noise does not have a significant impact on the result since the path differences are much smaller than the coherence length $c_0/15\,\mathrm{MHz} = 20\,\mathrm{m}$. The phase-noise of the beat notes on the reference and the measurement detector is hence strongly correlated and does not have strong impact on the phase differences $\delta\Phi_\mu(d) = \Phi_{\mathrm{meas},\mu}(d) - \Phi_{\mathrm{ref},\mu}$. For larger measurement distances, it is possible to additionally apply linewidth-reduction techniques for the MLLDs, exploiting, e.g., external-cavity feedback [196, 202, 203] or injection locking [93].

For extracting the distance information from the measured phases, we numerically unwrap the measured phases by adding integer multiples of 2π to each phase difference $\delta\Phi_\mu(d)$ such that the pairs $\big(\mu, \delta\Phi_\mu(d)\big)$ can be fitted by a straight line according to Eq. (6.4). From the slope of this fit, we then determine d. Note that the 2π-unambiguity of the phase differences $\delta\Phi_\mu(d)$ leads to an unambiguity of the slope of 2π and hence to an unambiguity distance $d_{\mathrm{ua}} = 2\pi c_0/\big(2n_{\mathrm{air}}\omega_{\mathrm{SI,FSR}}\big) = 3.01\,\mathrm{mm}$ of the measured distance d. The minimum observation time needed for evaluating the phases $\Phi_{\mathrm{meas},\mu}(d)$ and $\Phi_{\mathrm{ref},\mu}$ is the period $T_{\mathrm{r}} = 2\pi/\Delta\omega_{\mathrm{FSR}} = 2.02\,\mathrm{ns}$ of the SI-MLLD – LO-MLLD beat signal generated on the two balanced photodetectors. For smaller evaluation times T_{eval}, the frequency resolution T_{eval}^{-1} would be insufficient to discriminate neighboring RF beat notes at frequencies $\Delta\omega_\mu$. Figure 6.4(a) shows the calculated power spectrum of a sequence of $N_{\mathrm{eval}} = 4000$ pulse periods T_{r} at a received signal comb power of -5 dBm. The evaluation time $T_{\mathrm{eval}} = N_{\mathrm{eval}}T_{\mathrm{r}}$ and the corresponding frequency resolution T_{eval}^{-1} define the effective noise-filtering bandwidth, which we call evaluation bandwidth and which, in case of Fig. 6.4(a), amounts to $B_{\mathrm{eval}} = (N_{\mathrm{eval}}T_{\mathrm{r}})^{-1} = 124\,\mathrm{kHz}$. While this narrow

noise-filtering bandwidth B_{eval} suppresses noise effectively and therefore results in an accurate spectrum, it is not the setting of choice if evaluation speed is important. For high-speed measurements, we may choose $N_{\mathrm{eval}} = 1$, i.e., $B_{\mathrm{eval}} = 497\,\mathrm{MHz}$, which can be increased to $N_{\mathrm{eval}} = 10$, i.e., $B_{\mathrm{eval}} = 49.5\,\mathrm{MHz}$ in case an increased signal-to-noise power ratio is needed.

The measured phase differences $\delta\Phi_\mu(d)$ of the N_{b} beat notes are subject to various impairments such as shot noise, electronic noise of the receiver circuits, or impairments of the ADC, which makes the extracted distances d unreliable, see Sections E.3 and E.4 of Appendix E for details. As a reliability metric for each measured distance, we extract the residual errors of the data points $\left(\mu, \delta\Phi_\mu(d)\right)$ with respect to the linear fit. We define an overall fit error ε as the root-mean-square of the fit errors of the $N_{\mathrm{b}} \approx 25$ fitted beat note phases

$$\varepsilon\left(d_i\right) = \sqrt{\frac{1}{N_{\mathrm{b}} - 1} \sum_{\mu=-\lfloor N_{\mathrm{b}}/2 \rfloor + 1}^{\lfloor N_{\mathrm{b}}/2 \rfloor} \left(\delta\Phi_{\mu,\mathrm{meas}}(d_i) - \delta\Phi_{\mu,\mathrm{fit}}(d_i)\right)^2}, \tag{6.5}$$

where the floor operator $\lfloor \bullet \rfloor$ denotes the nearest smaller integer. If $\varepsilon(d_i)$ is small, the linear fit is a good approximation to the measured phase differences $\delta\Phi_\mu(d)$, and the result should be reliable. In contrast, if $\varepsilon(d_i)$ is high, impairment due to noise may be substantial. We define a limit $\varepsilon_{\mathrm{th}}(d_i)$ to distinguish between reliable distance data points, where $\varepsilon(d_i) < \varepsilon_{\mathrm{th}}(d_i)$, and unreliable distance data points defined by $\varepsilon(d_i) \geq \varepsilon_{\mathrm{th}}(d_i)$, which are eventually discarded. For details on the determination of the fit error threshold $\varepsilon_{\mathrm{th}}(d_i)$, see Appendix E, Section E.2.

6.4 System precision and accuracy

In our experiments, we characterize the achievable precision of the system by repeatedly measuring the distance to a fixed target mirror. We record time series of an overall duration of 1.56 ms, limited by the memory size of the oscilloscope. For finding the distance, we evaluate the same recording for two different evaluation times $T_{\mathrm{eval}} = N_{\mathrm{eval}} T_{\mathrm{r}}$ with $N_{\mathrm{eval}} = 1$ ($B_{\mathrm{eval}} = 495\,\mathrm{MHz}$), and $N_{\mathrm{eval}} = 10$ ($B_{\mathrm{eval}} = 49.5\,\mathrm{MHz}$). We extract N_{d} distance values, $10^5 \leq$

$N_\mathrm{d} \leq 10^6$, and compute the Allan deviation σ_A as a function of the averaging time T_av. To this end introduce the number of averaged distance values

$$N_\mathrm{av} = \lfloor T_\mathrm{av} B_\mathrm{eval} \rfloor = \left\lfloor \frac{T_\mathrm{av}}{N_\mathrm{eval} T_\mathrm{r}} \right\rfloor, \tag{6.6}$$

The number N_av of averaged samples leads to the averaged distance values $\overline{d}_j\,(N_\mathrm{av})$,

$$\overline{d}_j\,(N_\mathrm{av}) = \frac{1}{N_\mathrm{av}} \sum_{i=0}^{N_\mathrm{av}-1} d_{jN_\mathrm{av}+i}, \tag{6.7}$$

based on which we calculate the Allan deviation [204],

$$\sigma_\mathrm{A}^2\,(N_\mathrm{av}) = \frac{1}{2} \frac{1}{\lfloor N_\mathrm{d}/N_\mathrm{av} \rfloor - 1} \sum_{j=1}^{\lfloor N_\mathrm{d}/N_\mathrm{av} \rfloor - 1} \left(\overline{d}_{j+1}\,(N_\mathrm{av}) - \overline{d}_j\,(N_\mathrm{av}) \right)^2. \tag{6.8}$$

For comparison, we also compute the standard deviation $\sigma_{\overline{d}}\,(N_\mathrm{av})$ of all measured distances to the fixed target mirror as a function of number of averaged samples,

$$\sigma_{\overline{d}}^2\,(N_\mathrm{av}) = \frac{1}{2} \frac{1}{\lfloor N_\mathrm{d}/N_\mathrm{av} \rfloor - 1} \sum_{j=1}^{\lfloor N_\mathrm{d}/N_\mathrm{av} \rfloor} \left(\overline{d}_j\,(N_\mathrm{av}) - \overline{\overline{d}_j\,(N_\mathrm{av})} \right)^2, \tag{6.9}$$

$$\overline{\overline{d}_j\,(N_\mathrm{av})} = \frac{1}{\lfloor N_\mathrm{d}/N_\mathrm{av} \rfloor} \sum_{j=1}^{\lfloor N_\mathrm{d}/N_\mathrm{av} \rfloor} \overline{d}_j\,(N_\mathrm{av})\,.$$

Note that distance points d_i for which the fit error $\varepsilon(d_i)$ exceeds the threshold $\varepsilon_\mathrm{th}(d_i)$ are not considered when evaluating Eqs. (6.6)... (6.9).

To quantify the sensitivity of our system with respect to low optical return power, we characterize the Allan deviation and the standard deviation of the measured distances for three different optical power levels, which are adjusted by introducing attenuators and neutral-density (ND) filters in the free-space beam path. The table in Fig. 6.5 lists the parameters of the three measurements, i.e., the optical return power, the free-space loss, the number N_eval of pulse repetition periods per distance data point, and the corresponding evaluation

Performance without optical amplifier

Opt. return pwr	+7 dBm		−20 dBm		−40 dBm	
Free-space loss	2 dB		29 dB		49 dB	
N_{eval}	1	10	1	10	1	10
B_{eval} [MHz]	495	49.5	497	49.7	487	48.7
Accepted [%]	99.9	99.6	86.1	97.3	–	59.8
Color					–	

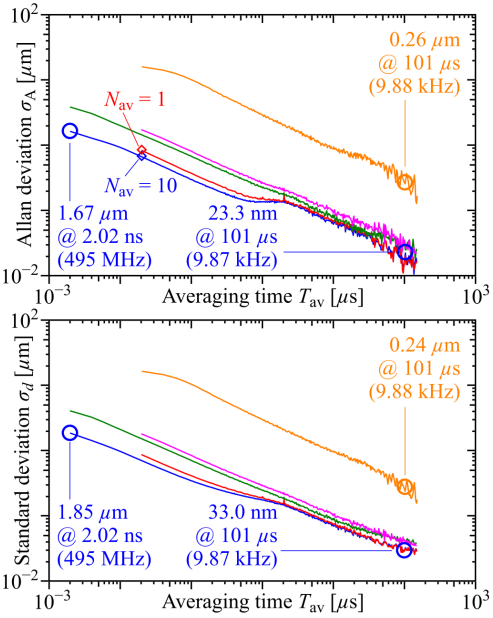

Figure 6.5: Performance of ranging system for varying optical return powers without booster EDFA, see Fig. 6.3 for the underlying experimental setup and Section E.7 of Appendix E for further details. The table lists the optical return power, the associated round-trip loss in the free-space path, the number of repetition periods N_{eval} used for signal evaluation per distance data point, the corresponding evaluation bandwidth B_{eval}, and the percentage of accepted data points. The upper plot shows the Allan deviation as a function of distance averaging time T_{av} for all five configurations, and the lower diagram depicts the standard deviation. Deviations of less than 2 μm were demonstrated at record-high effective measurement rates of up to 495 MHz.

bandwidth $B_{\mathrm{eval}} = (N_{\mathrm{eval}} T_{\mathrm{r}})^{-1}$ along with the percentage of accepted data points. Note that the evaluation bandwidth may slightly vary between the measurements due to a slow drift of the FSR difference $\Delta\omega_{\mathrm{FSR}} = 2\pi/T_{\mathrm{r}}$.

The lowest return power in our experiments is −40 dBm. At this power level, the beat signals in the electric spectrum are barely detectable, and we did not included the recordings at maximum bandwidth ($N_{\mathrm{eval}} = 1$), which are subject to large standard deviations of 500 μm or more with less than 5 % of the data points accepted according to the criteria discussed after Eq. (6.5). The upper graph of Fig. 6.5 shows the Allan deviation as a function of averaging time $T_{\mathrm{av}} = N_{\mathrm{av}} N_{\mathrm{eval}} T_{\mathrm{r}}$. For the highest optical return power and for a measurement bandwidth of $B_{\mathrm{meas}} = B_{\mathrm{eval}} = 495$ MHz (blue curve), the Allan deviation for $T_{\mathrm{av}} = 2.02$ ns ($N_{\mathrm{eval}} = 1$) amounts to 1.67 μm (blue circle). To the best of our knowledge, this is the highest measurement bandwidth demonstrated with any ranging system. Specifically, this measurement bandwidth can well compete with recently demonstrated values of up to 400 MHz, which were achieved with highly stable, but bulky and technically complex mode-locked fiber lasers [205,206]. When averaging over $N_{\mathrm{av}} > 1$ consecutively measured distances, the Allan deviation decreases to $\sigma_{\mathrm{A}} = 23$ nm for an effective measurement rate of meas $B_{\mathrm{meas}} = 9.87$ kHz ($T_{\mathrm{av}} = 101\,\mu$s, $N_{\mathrm{av}} = 50\,119$, $B_{\mathrm{eval}} = 495$ MHz). Similar results are achieved when the same data record is evaluated at $B_{\mathrm{eval}} = 49.5$ MHz (red curve) beginning at $T_{\mathrm{av}} = 20.2$ ns with $N_{\mathrm{av}} = 1$. The red and the blue curves approximately coincide, confirming that averaging over, e.g., $N_{\mathrm{av}} = 10$ distance samples subsequently acquired at a high evaluation bandwidth and sufficiently high return power leads to approximately the same result as 10-fold increased evaluation period T_{eval} for each distance measurement.

Reducing the optical return power leads to an increase of the Allan deviation for all averaging times and evaluation bandwidths. At −20 dBm optical return power (green and magenta line), the Allan deviation increases to 3.9 μm for an effective measurement rate of $B_{\mathrm{meas}} = B_{\mathrm{eval}} = 497$ MHz ($T_{\mathrm{av}} = 2.01$ ns, $N_{\mathrm{av}} = 1$), and reduces to 26 nm for $B_{\mathrm{meas}} = 9.91$ kHz ($T_{\mathrm{av}} = 101\,\mu$s, $N_{\mathrm{av}} = 50\,119$). At even lower return power levels, proper phase unwrapping for distance reconstruction according to Eq. (6.4) is not possible at the highest evaluation bandwidths, since the accuracy of the phase differences $\delta\Phi_{\mu}(d)$ suffers from electrical noise. To still obtain reliable distance values at a return power of −40 dBm, we reduce the evaluation bandwidth to $B_{\mathrm{eval}} = (10\,T_{\mathrm{r}})^{-1} = 48.7$ MHz

(orange curve). To the best or our knowledge, this represents the highest loss tolerance demonstrated so far for dual-comb distance metrology that fully relies on chip-scale frequency comb generators. We believe that the loss tolerance of such systems can be further improved, considering the outstanding sensitivity levels that have been demonstrated for ranging with comb sources built from fiber-optic or discrete components [207–210]. At $B_{\mathrm{meas}} = B_{\mathrm{eval}}$ ($T_{\mathrm{av}} = 20.5\,\mathrm{ns}$, $N_{\mathrm{av}} = 1$), i.e., without averaging of subsequently acquired distance samples, the Allan deviation amounts to 16 μm, and reduces to 0.26 μm for $T_{\mathrm{av}} = 101\,\mu\mathrm{s}$ ($N_{\mathrm{av}} = 4\,898$), corresponding to an effective measurement rate of $B_{\mathrm{meas}} = 9.95\,\mathrm{kHz}$.

The lower graph of Fig. 6.5 shows the standard deviation of the distance measurements with the same color coding as in the upper graph. Allan deviation and standard deviation are nearly identical. This indicates that the distance measurement errors can be described by spectrally white noise and are not impaired by any drift processes [204]. For an optical return power of 7 dBm, orange line, the measurement accuracy is limited by the noise floor of our ADC, whereas shot noise and the thermal noise of the detector electronics represent the dominant limitation for the lower received power levels of −20 dBm and −40 dBm. The theoretically achievable precision of all measurements is approximately a factor of 3 ... 10 better than the values we demonstrated here, indicating that the system can benefit from a further optimized implementation. A more detailed discussion can be found in Appendix E, Sections E.3 and E.4.

In a second set of experiments, we boost the SI comb power in the receiver by an EDFA and repeat the measurements for larger target distances corresponding to higher free-space losses. To avoid damaging the reference balanced photodetector ($\mathrm{BD_R}$) depicted in Fig. 6.3, we additionally include a variable optical attenuator (VOA) between the 90/10 coupler after the EDFA and the 50/50 coupler before $\mathrm{BD_R}$. We set the attenuation at the VOA such that the power of the SI comb reaching $\mathrm{BD_R}$ is approximately 0 dBm, which is sufficient for the detection of reference beat signals and read-out of the corresponding phase. The measurement and evaluation parameters are again listed in the table at the top of Fig. 6.6, and the corresponding Allan deviations and standard deviations are shown in the graphs below the table. At highest optical return powers of +5 dBm (26 dB free-space loss), the Allan deviation increases by approximately a factor of 2 compared to the measurement without an EDFA. We attribute this to the ASE noise of the EDFA, for which a noise figure of

approximately 5 dB is specified by the manufacturer. At lower optical return powers, however, both the Allan deviation and the standard deviation become comparable to the measurement without an EDFA, see see Figs. 6.5 and 6.6 (orange curves), which supports the notion that the phase measurement errors in this case are dominated by shot noise caused by the LO comb and by thermal noise of the receiver electronics, see Section E.3 of Appendix E for a more detailed analysis. An Allan deviation of 0.26 μm for an effective measurement rate of $B_{\mathrm{meas}} = 9.95\,\mathrm{kHz}$ ($T_{\mathrm{av}} = 100\,\mu\mathrm{s}$, $N_{\mathrm{av}} = 5\,012$) is achieved at a free-space loss of 71 dB. Note that the standard deviation of the measurement at +5 dBm (Fig. 6.6, lower graph, blue and red curve) does not continuously decrease when increasing the averaging time, but reaches a plateau of $\sigma_d = 70\,\mathrm{nm}$ near $T_{\mathrm{av}} = 100\,\mu\mathrm{s}$. We relate this to a drift of the optical path lengths in our setup during this specific measurement.

Next we move the target mirror in Fig. 6.3 with a feedback-stabilized stage (Physik Instrumente, M511.HD) to $N_{\mathrm{p}} = 16$ positions and record the distances obtained with our ranging system. The $N_{\mathrm{p}} = 16$ mirror positions are evenly spaced by $\Delta z = 200\,\mu\mathrm{m}$, and the absolute positioning accuracy of the stage is specified to be better than 50 nm. The range of distances covers the full unambiguity distance of our system. To eliminate the impact of fiber drift on the measured distance [J3], we periodically compare the measured free-space distance d_{tar} to the target mirror with the distance d_{fix} to a second fixed reference mirror by alternating the measurement paths at a rate of 2 kHz, see Appendix E, Section E.1 for details of the underlying setup. At each mirror position, 4 970 distance values are acquired for d_{tar} and d_{fix} over a period of 100 μs at an evaluation bandwidth of $B_{\mathrm{eval}} = 1/(10\,T_{\mathrm{r}}) \approx 49.7\,\mathrm{MHz}$. Out of these 4 970 measurements, a number of $N_{\mathrm{accept}} \approx 4\,100$ values are accepted based on the associated fit errors $\varepsilon(d_i)$, Eq. (6.5). Examples of measured and evaluated data can be found in Appendix E, Figs. E.5 and E.6. For evaluating the accuracy of the ranging system, we first calculate the measured position z_{tar} of the target mirror at each of the $N_{\mathrm{p}} = 16$ stage positions, which is given by the path-length differences of the individual measurements. In the following, the mirror position is indicated by a subscript $m = 1 \ldots N_{\mathrm{p}}$ and a subscript $l = 1 \ldots N_{\mathrm{accept}}$ is used to refer to the individual pairs of measured distances to the target and the reference mirror, $z_{\mathrm{tar},m,l} = d_{\mathrm{tar},m,l} - d_{\mathrm{fix},l}$. To quantify the precision and the accuracy of our ranging system, we first calculate the average of the measured target position $\overline{z}_{\mathrm{tar},m}$ for each stage position m along with

Performance including optical amplifier

Opt. return pwr	+5 dBm		−20 dBm		−40 dBm	
Free-space loss	26 dB		51 dB		71 dB	
N_{eval}	1	10	1	10	1	10
B_{eval} [MHz]	495	49.5	500	50.0	499	49.9
Accepted [%]	99.8	99.5	92.0	97.9	–	60.9
Color					–	

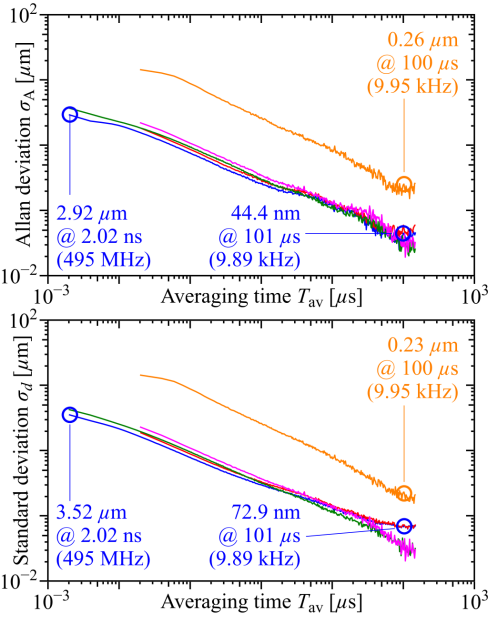

Figure 6.6: Performance of ranging system for varying optical return powers with an optical booster amplifier (EDFA), see Fig. 6.3 for the underlying experimental setup and Section E.7 of Appendix E for further details. The table lists the optical return power, the associated round-trip loss in the free-space path, the number of repetition periods N_{eval} used for signal evaluation per distance data point, the corresponding evaluation bandwidth B_{eval}, and the percentage of accepted data points. The upper plot shows the Allan deviation as a function of distance averaging time T_{av} for all five configurations, and the lower diagram depicts the standard deviation. The optical booster amplifier increases the loss tolerance and therefore permits a longer measurement reach compared to Fig. 6.5. At an effective measurement rate of 10 kHz, we demonstrate reliable ranging with standard deviations of less than 1 μm for free-space losses of more than 70 dB.

the associated measurement uncertainty, quantified by the standard deviation $\sigma_{z_{\mathrm{tar}},m}$,

$$\begin{aligned}\overline{z}_{\mathrm{tar},m} &= \frac{1}{N_{\mathrm{accept}}} \sum_{l=1}^{N_{\mathrm{accept}}} d_{\mathrm{tar},m,l} - d_{\mathrm{fix},l},\\ \sigma^2_{z_{\mathrm{tar}},m} &= \frac{1}{N_{\mathrm{accept}}-1} \sum_{l=1}^{N_{\mathrm{accept}}} \left(z_{\mathrm{tar},m,l} - \overline{z}_{\mathrm{tar},m}\right)^2 .\end{aligned} \tag{6.10}$$

Each of the measured target-mirror positions $\overline{z}_{\mathrm{tar},m}$ is associated with a nominal position $z_{\mathrm{stage},m} = m\Delta z + z_0$ of the mirror as set by the translation stage, where z_0 accounts for constant offset between the z-scale of our ranging system and the z-scale of the stage encoder. For each mirror position m, we then calculate the distance error, i.e., the deviation of averaged measured mirror positions $\overline{z}_{\mathrm{tar},m}$ to the nominal positions $\overline{z}_{\mathrm{stage},m}$ set by the stage,

$$\varepsilon_{z,m} = \overline{z}_{\mathrm{tar},m} - m\Delta z - z_0. \tag{6.11}$$

For simplicity, the constant offset z_0 is chosen to achieve a zero-mean deviation of the nominal mirror position from its measured counterpart when averaging over all of the N_{p} mirror positions, $\sum_{m=1}^{N_{\mathrm{p}}} \varepsilon_{z,m} = 0$.

To quantify the performance of our ranging system, we extract the distance error $\varepsilon_{z,m}$ along with the associated measurement uncertainty $\sigma_{z_{\mathrm{tar}},m}$ at each mirror position m. This procedure is repeated for a wide range of optical return powers with and without EDFA, see Figs. 6.7 and 6.8. For each measurement, the return power and the evaluation parameters are listed in the top tables of Figs. 6.7 and 6.8. The plots below these tables show the distance errors $\varepsilon_{z,m}$ according to Eq. (6.11) as a function of the target position $m\Delta z$, recorded over a full unambiguity distance $d_{\mathrm{ua}} = 3.01\,\mathrm{mm}$ centered at $z_0 \approx 1\,\mathrm{m}$. The error bars represent the standard deviations $\sigma_{z_{\mathrm{tar}},m}$ according to Eq. (6.10). We do not observe any outliers throughout our measurements, which demonstrates the reliability of the approach. Moreover, we do no observe any cyclic errors, which would lead to a systematic variation of $\varepsilon_{z,m}$ over the unambiguity distance. For the system without optical amplifier, we find measurement uncertainties $\sigma_{z_{\mathrm{tar}},m}$ of approximately 19 μm even for return power levels as low as $-40\,\mathrm{dBm}$. For the system with optical amplifier, the measurement uncertainties $\sigma_{z_{\mathrm{tar}},m}$

increase to approximately 25 μm for the same power level, corresponding to a free-space loss of 70 dB.

As an additional performance metric, we calculate the variance $\sigma^2_{\varepsilon_z}$ of the distance errors $\varepsilon_{z,m}$ for the various mirror positions by determining the variance

$$\sigma^2_{\varepsilon_z} = \frac{1}{N_\mathrm{p} - 1} \sum_{m=1}^{N_\mathrm{p}} \varepsilon^2_{z,m}. \tag{6.12}$$

This figure is an indicator of the overall accuracy of ranging system and is specified in the second to last row of the tables in Figs. 6.7 and 6.8. We find this number to be approximately 1 μm, merely independent of the optical return power. We attribute this observation to additional ranging errors which are caused by the periodic alternation between target and reference mirror, see Appendix E, Section E.5, and which are independent of the return power levels. The quantity σ_{ε_z} does hence not represent the fundamental accuracy limitation of our optical ranging system, but is rather to be understood as an upper boundary of the achievable measurement accuracy, dictated by the specific experimental setup.

To overcome the limited unambiguity distance d_ua = 3.01 mm of our system, several approaches can be used. Evidently, it is always possible to combine the dual-comb scheme with a simple time-of-flight system for coarse ranging. Alternatively switching the role of the LO comb and the SI comb allows to greatly extend the unambiguity distance via the Vernier effect [19]. In another approach, the LO comb can also be sent to the target and the sum of the resulting phases detected at the balanced photodetectors can be evaluated [186]. These approaches allow for high-precision ranging over distances that are limited only by the coherence length of the QD-MLLD. For the devices used in our current experiments, the coherence length is in the order of tens of meters and can be increased further by applying linewidth-reduction techniques [93, 196, 202, 203].

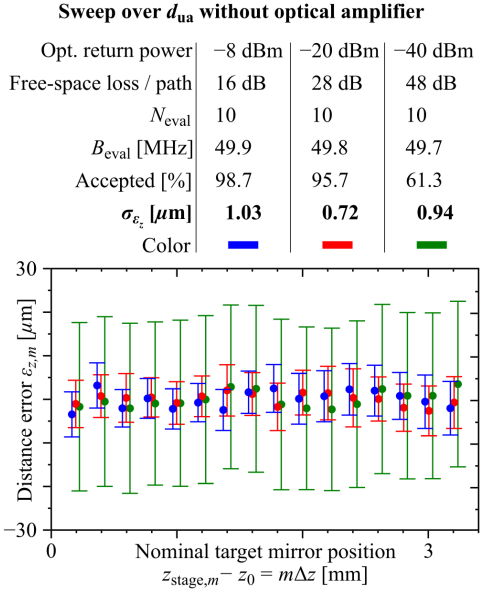

Figure 6.7: Unambiguity-distance sweep for varying free-space losses without EDFA, see Fig. 6.3 for the underlying experimental setup and Section E.7 of Appendix E for further details. The table lists the optical return power, the associated optical loss per path, the amount of considered pulse repetition periods per distance data point N_{eval}, the corresponding evaluation bandwidth B_{eval} averaged over the measurement series, the percentage of accepted data points, and the variance σ_{ε_z} of the distance errors $\varepsilon_{z,m}$ for three different measurement series. The figure shows the residual distance error of each target mirror position, i.e., the difference between the set and the mean of the measured position as a function of the nominal target mirror position $z_{stage,m} - z_0 = m\Delta z$ as set by the stage over the unambiguity distance of the system. Error bars indicate the standard deviation $\sigma_{z_{tar},m}$ of the point-wise computed difference between the beam-path length to the static reference mirror and the beam-path length to the target mirror. For better readability, the data points and error bars belonging to the same position $z_{stage,m} - z_0 = m\Delta z, m = 1 \ldots 16, \Delta z = 200\,\mu$m of the target mirror are slightly offset horizontally with respect to each other. Further details on the experiment and the data evaluation can be found in Section E.5 of Appendix E.

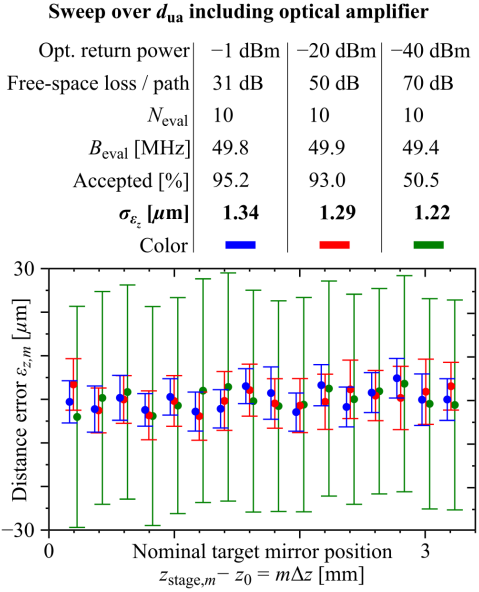

Figure 6.8: Unambiguity-distance sweep for varying free-space losses with EDFA, see Fig. 6.3 for the underlying experimental setup and Section E.7 of Appendix E for further details. The table lists the optical return power, the associated optical loss per path, the amount of considered pulse repetition periods per distance data point N_{eval}, the corresponding evaluation bandwidth B_{eval} averaged over the measurement series, the percentage of accepted data points, and the variance σ_{ε_z} of the distance errors $\varepsilon_{z,m}$ for three different measurement series. The figure shows the residual distance error of each target mirror position, i.e., the difference between the set and the mean of the measured position as a function of the nominal target mirror position $z_{stage,m} - z_0 = m\Delta z$ as set by the stage over the unambiguity distance of the system. Error bars indicate the standard deviation $\sigma_{z_{tar},m}$ of the point-wise computed difference between the beam-path length to the static reference mirror and the beam-path length to the target mirror. For better readability, the data points and error bars belonging to the same position $z_{stage,m} - z_0 = m\Delta z$, $m = 1 \ldots 16$, $\Delta z = 200\,\mu$m of the target mirror are slightly offset horizontally with respect to each other. Further details on the experiment and the data evaluation can be found in Section E.5 of Appendix E.

6.5 High-speed ranging

To demonstrate the ultrafast-sampling capabilities of our ranging system, we measure the profile of a flying air-gun projectile. To simplify free-space beam alignment, we replace the two separated collimators of Fig. 6.3 with a single collimator and a fiber-optic circulator, see Section E.6 see of Appendix E for further details of the experiment. We focus the free-space beam at the anticipated projectile trajectory. In Fig. 6.9(a), we depict the recorded profile of a projectile that is shot through the measurement beam at a speed of approximately $150\,\mathrm{m\,s^{-1}}$. We use a measurement bandwidth of $B_{\mathrm{meas}} = B_{\mathrm{eval}} = (10\,T_{\mathrm{r}})^{-1} = 49.1\,\mathrm{MHz}$ and perform the experiment without an EDFA (red trace) and with EDFA (green trace). For the given projectile speed, this corresponds to a separation of neighboring sample points of approximately $3\,\mu\mathrm{m}$. For the measurement without EDFA, an average of 61 % of the evaluated distance data points are accepted using the fit-error criterion according to Eq. (6.5). The black dashed line on top of the red trace is the result of an optical coherence tomography (OCT) measurement that was performed on the static projectile after recovery from the back-stop. For better comparison, the OCT-based profile and the profile obtained from the flying projectile were rotated with respect to each other, and an actual speed of the projectile of $151\,\mathrm{m\,s^{-1}}$ was estimated for best agreement. The same procedure was performed for the measurement with EDFA, for which the signal comb power emitted from the collimator amounts to 22 dBm. In this experiment, 65 % of the measured distance points are accepted, and a speed of $153\,\mathrm{m\,s^{-1}}$ was estimated by comparing the profile on the flying projectile to the OCT measurement. Figure 6.9(b) shows a photograph of the projectile used in the ranging experiments without EDFA.

6.6 Summary and Outlook

We have demonstrated high-precision dual-comb ranging with quantum-dash mode-locked laser diodes (QD-MLLD) as particularly compact and efficient frequency comb sources. The devices offer easy operation by a simple DC drive current and provide spectrally flat frequency combs with line spacings of tens of gigahertz. We demonstrate measurement rates up to 500 MHz, corresponding

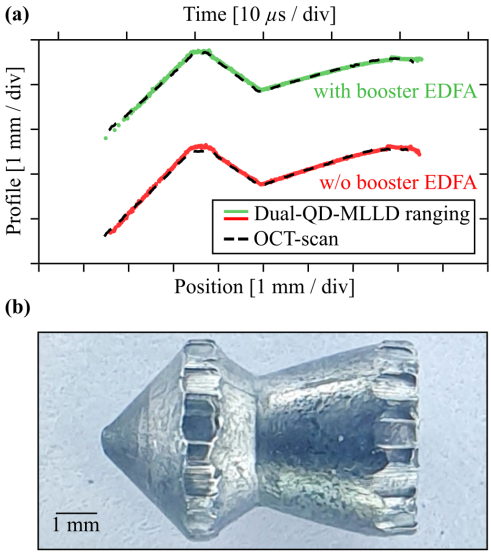

Figure 6.9: Surface profile measurements of air-gun projectile passing the measurement beam at a speed of approximately 150 m s^{-1}. (a) Surface profiles measured on the flying projectile, using the one port ranging system Appendix E, Fig. E.7, with EDFA (green) and without EDFA (red). The free space signal beam power amounts to 9 dBm and 22 dBm for the measurement with and without EDFA, respectively. For better visibility, the red and the green curve are separated by a vertical offset. The black dashed curves denote the profiles of both investigated projectiles, obtained from an optical coherence tomography (OCT) measurement on the static projectile after recovery from the back stop. (b) Photo graph of the projectile measured in (a), red curve.

to the highest measurement rate demonstrated with any ranging system so far. In comparison to other chip-scale comb sources, QD-MLLDs provide comparatively high comb line powers of the order of 500 μW – more than one order of magnitude higher than those of Kerr soliton frequency comb generators [15, 22, 23]. This leads to high tolerance with respect to optical loss in the free-space path of a ranging system. In our experiments, we find a high loss tolerance of 49 dB without optical amplifiers and of 71 dB in case a booster EDFA is used. To the best of our knowledge, this is the highest loss tolerance demonstrated so far for a comb-based measurement system that relies on chip-scale light sources. The loss tolerance can be further improved by increasing the free-space beam power and by reducing the measurement

rate, see Sections E.3 and E.4 of Appendix E for a more detailed analysis of the noise limitations in dual-comb ranging systems. We demonstrate the measurement speed of our system by high-precision in-flight sampling of air-gun pellets moving at a speed of $150\,\mathrm{m\,s^{-1}}$. Based on our findings, we believe that quantum-dash mode-locked laser diodes (MLLD) are an attractive option for comb generation in compact power-efficient LiDAR systems.

[End of manuscript [J4]]

7 Summary and future work

7.1 Summary

Chip-scale frequency comb generators are unique tools that have the potential to unlock compact LiDAR systems with exceptional performance. In this work, optical ranging systems were demonstrated that make use of Kerr microresonators and quantum-dash mode-locked laser diodes as chip-scale comb generators. The large free spectral range and the large number of comb lines of microresonator-based Kerr soliton frequency combs enables ultrafast measurements with sampling rates up to 96 MHz at a precision of 280 nm. This unique combination was demonstrated by measuring the profile of a flying air-gun projectile. In a comparative ranging experiment, quantum-dash mode-locked laser diodes were used in the same manner. Here, a precision of 1.7 μm was achieved at a sampling rate of 500 MHz. In direct comparison, the QD-MLLD-based system has a worse relative precision $\sigma_d/d_{\mathrm{ua}} = 950\,\mathrm{nm}/3\,\mathrm{mm} = 3.2\times10^{-4}$ at a distance sampling rate of 100 MHz[1] compared to the soliton Kerr comb-based system, with $\sigma_d/d_{\mathrm{ua}} = 280\,\mathrm{nm}/1.5\,\mathrm{mm} = 1.9\times10^{-4}$. Still, considering the achieved absolute precision and accuracy, both comb sources may be viable options for comb-based LiDAR systems. From a practical point of view, the simple operation of QD-MLLDs for comb generation is an additional advantage compared to Kerr comb generators. Furthermore the high comb line power of approximately 400 μW of QD-MLLD combs enables distance measurements at higher losses compared to Kerr soliton frequency combs, where the average comb line power is in the order of 10 μW. Given these considerations, both comb sources may be viable options in LiDAR systems. For measurements at the highest precision, Kerr soliton frequency combs are better suited, whereas

[1] The value $\sigma_d = 950\,\mathrm{nm}$ is taken from Fig. 6.5, blue curve in the lower plot for the standard deviation of distance measurements at an averaging time of $T_{\mathrm{av}} = (100\,\mathrm{MHz})^{-1} = 10\,\mathrm{ns}$.

QD-MLLDs are favourable, if a simple comb source operation and a higher loss-tolerance are required.

While these results show the enormous potential of existing microresonator-based comb generators, there are still many aspects of this technology that require further research and development. In this work, two theoretical studies were performed that aim at the optimization of Kerr-nonlinear microresonators under practical considerations. First, in a joint effort with scientists of the Institute for Analysis (IANA) and the Institute for Applied and Numerical Mathematics (IANM), Karlsruhe Institute of Technology (KIT), a method was developed that allows to benchmark single-soliton Kerr combs in terms of their bandwidth and pump-to-comb power conversion efficiency for arbitrary pump and microresonator parameters. This allows for the targeted design of Kerr comb generators for given application-specific comb requirements. Second, the impact of two-photon absorption and free-carrier absorption on Kerr comb formation in a microresonator in consideration of fast-time free-carrier dynamics was investigated. Limits were derived, below which these loss mechanisms are weak enough, such that modulation instability may still occur. Based on these insights, a silicon microresonator design was developed that may support comb formation at telecommunication wavelengths despite presence of TPA and FCA. Silicon is the most common material platform for integrated photonics, and therefore silicon-based Kerr-nonlinear microresonators could significantly boost the wide-spread application of Kerr combs.

7.2 Future work

The research carried out in this work can be continued on both its experimental as well as its theoretical aspects. In the following, several different topics are discussed.

Advanced comb-based distance measurements

After the proof-of-principle experiments using chip-scale frequency comb sources for optical distance measurements, one can either improve their performance further or improve their applicability. A potentially massive increase in

precision could by achieved by not only relying on synthetic wavelength interferometry, but also simultaneously on optical interferometry of the individual comb lines when measuring distances. Comb-based synthetic wavelength interferometry achieves already sub-μm precision and accuracy, therefore it should be possible to relate the distance information obtained from both methods similar as, e.g., in [19] while keeping high sampling rates. Optical interferometry, executed simultaneously for 100 comb lines or more could provide extreme precision and accuracy in the order of 1 nm or better over a comparatively large ambiguity distance of a few millimeters when combined with synthetic wavelength interferometry.

A different route to follow is the integration of comb-based LiDAR systems. As comb sources, one can rely either on already integrated Kerr comb generators [15], QD-MLLDs or others [192, 211]. The integration of further photonic circuits required in ranging systems has already been demonstrated [114]. A remaining challenge is the design of suitable optics for light emission and collection by the photonic integrated circuits, considering the high optical round-trip losses during the distance measurement. In particular, large receiver apertures are necessary to maximize the signal received from the target. Furthermore, both the receiver and the transmitter optics may need to be combined with scanning mirrors that allow for beam steering, unless optical phased arrays are used [180, 181]. This will add further complexity to the design of optical components.

Kerr comb generation in nonlinear absorbing microresonators

Following the research presented in Chapter 4, the next step is the experimental verification of comb generation in silicon microresonators at telecommunication wavelengths. To this end, photonic chips with silicon microresonators need to be designed and characterized. The design proposed in [J2] can be used, provided that silicon waveguides with a height of up to 300 nm can be fabricated, which is key to achieve waveguides with anomalous dispersion [153]. If only standard silicon waveguides with a height of 220 nm [212] are available, the microresonator design needs to be altered. To enable comb formation, multi-mode waveguides with appropriate width need to be designed, such that avoided mode crossings can occur and local dispersion anomalies can induce locally anomalous dispersion.

In both cases, the waveguides need to be part of a cointegrated, reverse-biased *p-i-n*-junction for free-carrier removal according to, e.g., the layout demonstrated in [29]. Furthermore, the chip section, where the microresonator is coupled to the bus waveguide requires careful design to ensure free-carrier removal in the microresonator and the bus waveguide [149, 152], as well as to ensure efficient optical coupling. Finally, the maximum tolerable length of the bus waveguide needs to be estimated in consideration of TPA and FCA. All these crucial design aspects were investigated in a separate Master thesis, and multiple chip designs were derived [213]. In this thesis, the presence of avoided mode crossings in passive silicon microresonators with multi-mode waveguides was confirmed, and shifts of resonance frequencies in the order of 2 GHz (approx. 2 % of the microresonator FSR) were observed.

With chip-designs at hand, devices can be fabricated and characterized, thereby building the base for comb generation experiments. If Kerr comb generation should prove successful, these comb generators could be integrated with other active and passive devices for application-specific comb-based photonic integrated circuits operated at 1550 nm. However, if no frequency combs can be obtained, an in-depth analysis of the different optical loss mechanisms should reveal the cause. In particular, this may result in a more precise determination of the normalized TPA parameter r, whose measured or assumed value varies by more than half an order of magnitude across literature.

Quasi-stationary drifting field distributions in Kerr-nonlinear microresonators and third-order dispersion

It was noted that the inclusion of free-carrier dynamics in the Lugiato-Lefever equation leads to quasi-stationary field distributions $\underline{a}_{\mathrm{QS}}$, see Chapter 4, Figs. 4.4, 4.5 and 4.6. These field distributions do not show a dependence on the slow time t', i.e., the natural time, aside from a constant drift along the fast time τ', i.e., the retarded spatial coordinate. This drift is characterized by the field drift velocity v_{D}, such that the optical field circulating in the microresonator can be written as $\underline{a}(t', \tau') = \underline{a}_{\mathrm{QS}}(\tau' - v_{\mathrm{D}} t')$. Such drifts were also observed in simulations where third-order dispersion (TOD) was included in the LLE [214, 215]. Here, it would be interesting to understand how the field drift velocity v_{D} is related to other parameters in the LLE, how such a drift affects comb formation and which single-soliton Kerr comb states can be

obtained in presence of TOD. From a practical point of view, this becomes relevant when microresonators are designed to achieve the largest possible frequency comb bandwidths. According to Fig. 3.4(a) and (b), these are obtained for vanishing second-order dispersion $\beta' \to 0$. In this case, third-order dispersion will dominate and therefore needs to be understood.

Since the quasi-stationary field distributions $\underline{a}_{\mathrm{QS}}(\tau' - v_{\mathrm{D}} t')$ are assumed to not show any further dependence on the slow time t' aside from a drift, a derivative with respect to the slow time can be written as

$$\frac{\partial \underline{a}\,(t', \tau')}{\partial t'} = \frac{\partial \underline{a}_{\mathrm{QS}}\,(\tau' - v_{\mathrm{D}} t')}{\partial t'} = -v_{\mathrm{D}} \frac{\partial \underline{a}_{\mathrm{QS}}\,(\tau' - v_{\mathrm{D}} t')}{\partial \tau'}. \tag{7.1}$$

Introducing the drifting fast time coordinate $\tau'_{\mathrm{D}} = \tau' - v_{\mathrm{D}} t'$, the normalized LLE, see Eq. (2.45), including third-order dispersion [25] for the quasi-stationary field $\underline{a}(t', \tau') = \underline{a}_{\mathrm{QS}}(\tau'_{\mathrm{D}})$ reads

$$\begin{aligned} 0 = \sqrt{F} - (1 + \mathrm{j}\zeta)\, \underline{a}_{\mathrm{QS}}\left(\tau'_{\mathrm{D}}\right) + v_{\mathrm{D}} \frac{\partial}{\partial \tau'_{\mathrm{D}}} \underline{a}_{\mathrm{QS}}\left(\tau'_{\mathrm{D}}\right) + \mathrm{j}\beta' \frac{\partial^2}{\partial \tau'^2_{\mathrm{D}}} \underline{a}_{\mathrm{QS}}\left(\tau'_{\mathrm{D}}\right) \\ + \beta^{(3)\prime} \frac{\partial^3}{\partial \tau'^3_{\mathrm{D}}} \underline{a}_{\mathrm{QS}}\left(\tau'_{\mathrm{D}}\right) + \mathrm{j} \left|\underline{a}_{\mathrm{QS}}\left(\tau'_{\mathrm{D}}\right)\right|^2 \underline{a}_{\mathrm{QS}}\left(\tau'_{\mathrm{D}}\right). \end{aligned} \tag{7.2}$$

Here $\beta^{(3)\prime} = \beta^{(3)} L_{\mathrm{MR}} \left(2\pi / t_{\mathrm{R}}\right)^3 / \left(3\left(\alpha_i L_{\mathrm{MR}} + \theta_{\mathrm{C}}\right)\right)$ is the normalized third-order dispersion coefficient. Equation (7.2) can be further investigated, in particular with respect to possible soliton comb states. Approximate expressions for bright solitons have been derived [216], however a description with the same universal scope as done in Chapter 3 is still lacking.

Ultimately, a method to deterministically derive the spectrum, power conversion efficiency and other properties of DKS combs generated in Kerr-nonlinear microresonators with arbitrary dispersion profiles would be desirable. "Reversing" such a method could enable designing microresonators with specific properties of the generated DKS frequency combs in mind.

Pumping of multiple modes of a microresonator and time-dependent pump terms

It was observed that pumping multiple resonances of a microresonator with multiple phase-locked pump tones leads to the formation of frequency combs in a normal-dispersive microresonator [217]. This is usually difficult to achieve, unless avoided mode crossings are exploited. From a theoretical point of view, additional pump tones can be desribed as additional terms in the coupled-mode equations, see Eqs. (2.32). In the following, the inclusion of a single additional pump term is considered. This second forcing, described by its frequency $\omega_{\mathrm{p},\kappa}$ and amplitude $\mathcal{E}_{\mathrm{in},\kappa} = \sqrt{P_{\mathrm{in},\kappa}}$, is applied to the microresonator resonance with index κ. The resulting coupled-mode equations read

$$\begin{aligned} t_{\mathrm{R}} \frac{\partial \underline{\mathcal{E}}_{\mathrm{r},\mu}(t)}{\partial t} = &- \frac{\alpha_i L_{\mathrm{MR}} + \theta_{\mathrm{C}}}{2} \underline{\mathcal{E}}_{\mathrm{r},\mu} \\ &+ \delta_{\mu 0} \sqrt{\theta_{\mathrm{C}} P_{\mathrm{in}}} \mathrm{e}^{\mathrm{j}\left(\omega_{\mathrm{p}} - \omega_{\mathrm{r},0}\right) t} + \delta_{\mu\kappa} \sqrt{\theta_{\mathrm{C}} P_{\mathrm{in},\kappa}} \mathrm{e}^{\mathrm{j}\left(\omega_{\mathrm{p},\kappa} - \omega_{\mathrm{r},\kappa}\right) t} \\ &- \mathrm{j}\gamma L_{\mathrm{MR}} \sum_{\mu',\mu''} \underline{\mathcal{E}}_{\mathrm{r},\mu'} \underline{\mathcal{E}}_{\mathrm{r},\mu''} \underline{\mathcal{E}}^{*}_{\mathrm{r},\mu'+\mu''-\mu} \\ &\times \mathrm{e}^{\mathrm{j}\left(\omega_{\mathrm{r},\mu'} + \omega_{\mathrm{r},\mu''} - \omega_{\mathrm{r},\mu'+\mu''-\mu} - \omega_{\mathrm{r},\mu}\right) t}. \end{aligned} \tag{7.3}$$

For simplicity, we assume the coupling coefficient θ_{C} to be the same for both pump terms. Following the same procedure that leads to the final form of the coupled-mode equations, see Eqs. (2.32) to (2.35), leads to

$$\begin{aligned} t_{\mathrm{R}} \frac{\partial \underline{\mathcal{E}}_{\mu}(t)}{\partial t} = &- \left(\frac{\alpha_i L_{\mathrm{MR}} + \theta_{\mathrm{C}}}{2} - \mathrm{j}\delta_0 \right) \underline{\mathcal{E}}_{\mu} - \mathrm{j} \frac{\beta^{(2)} L_{\mathrm{MR}}}{2} \left(\mu\, \omega_{\mathrm{FSR}}\right)^2 \underline{\mathcal{E}}_{\mu} \\ &+ \delta_{\mu 0} \sqrt{\theta_{\mathrm{C}} P_{\mathrm{in}}} + \delta_{\mu\kappa} \sqrt{\theta_{\mathrm{C}} P_{\mathrm{in},\kappa}} \mathrm{e}^{\mathrm{j}\left(\omega_{\mathrm{p},\kappa} - \omega_{\mathrm{p}} - \kappa\, \omega_{\mathrm{FSR}}\right) t} \\ &- \mathrm{j}\gamma L_{\mathrm{MR}} \sum_{\mu',\mu''} \underline{\mathcal{E}}_{\mu'} \underline{\mathcal{E}}_{\mu''} \underline{\mathcal{E}}^{*}_{\mu'+\mu''-\mu}. \end{aligned} \tag{7.4}$$

We introduce the detuning of the second pump, $\delta_\kappa = (\omega_{\mathrm{p},\kappa} - \omega_\mathrm{p} - \kappa\,\omega_\mathrm{FSR})t_\mathrm{R}$ and insert the Eqs. (7.4) into Eq. (2.37) to obtain an equation for the field envelope $\underline{\mathcal{E}}(t,\tau)$,

$$\begin{aligned} t_\mathrm{R}\frac{\partial\underline{\mathcal{E}}\,(t,\tau)}{\partial t} &= \sum_\mu t_\mathrm{R}\frac{\partial\underline{\mathcal{E}}_\mu\,(t)}{\partial t}\mathrm{e}^{-\mathrm{j}2\pi\mu\tau/t_\mathrm{R}} \\ &= -\left(\frac{\alpha_i L_\mathrm{MR}+\theta_\mathrm{C}}{2}-\mathrm{j}\delta_0\right)\underline{\mathcal{E}}(t,\tau)+\mathrm{j}\frac{\beta^{(2)}L_\mathrm{MR}}{2}\frac{\partial^2}{\partial\tau^2}\underline{\mathcal{E}}(t,\tau) \\ &\quad+\sqrt{\theta_\mathrm{C}P_\mathrm{in}}+\sqrt{\theta_\mathrm{C}P_{\mathrm{in},\kappa}}\mathrm{e}^{\mathrm{j}(\delta_\kappa t-2\pi\kappa\tau)/t_\mathrm{R}}-\mathrm{j}\gamma L_\mathrm{MR}\left|\underline{\mathcal{E}}(t,\tau)\right|^2\underline{\mathcal{E}}(t,\tau). \end{aligned} \tag{7.5}$$

Complex-conjugating Eq. (7.5) to an equation for electric fields with negative time dependence of the form $\exp(-\mathrm{j}\omega t)$ and normalizing the result, see Table 2.1, leads to the LLE with a second pump term,

$$\begin{aligned} \frac{\partial\underline{a}\,(t',\tau')}{\partial t'} &= \sqrt{F}+\sqrt{F_\kappa}\mathrm{e}^{-\mathrm{j}(\zeta_\kappa t'-\kappa\tau')}-(1+\mathrm{j}\zeta)\,\underline{a}(t',\tau') \\ &\quad+\mathrm{j}\beta'\frac{\partial^2}{\partial\tau'^2}\underline{a}(t',\tau')+\mathrm{j}\left|\underline{a}(t',\tau')\right|^2\underline{a}(t',\tau'). \end{aligned} \tag{7.6}$$

Here, the second forcing $F_\kappa = P_{\mathrm{in},\kappa}8\gamma L_\mathrm{MR}\theta_\mathrm{C}/(\alpha_i L_\mathrm{MR}+\theta_\mathrm{C})^3$ and the second normalized detuning $\zeta_\kappa = \delta_\kappa 2/(\alpha_i L_\mathrm{MR}+\theta_\mathrm{C})$ were introduced in the same manner as F and ζ before, see Table 2.1. Generally, the field $\underline{a}\,(t',\tau')$ cannot be stationary in such a system due to the slow-time dependence of the second pump term in Eq. (7.6). However, in principle the detuning ζ_κ of the second pump can be zero, if the two pump frequencies $\omega_{\mathrm{p},0}$ and $\omega_{\mathrm{p},\kappa}$ are separated by a multiple of the FSR ω_FSR of the frequency comb (that is assumed to be nearly equal to the microresonator FSR). In this case, the total forcing $\sqrt{F}+\sqrt{F_\kappa}\mathrm{e}^{\mathrm{j}\kappa\tau'}$ is constant in slow time t' and shows a periodic fast-time dependence with period κ.

Experimentally, such a precisely defined forcing, consisting of multiple coherent signals, could be generated by modulating a CW laser to generate sidebands, see, e.g., [217]. In conjunction with optical amplifiers, attenuators and spectral filters, an adjustment of the pump parameters F, F_κ, κ, and ζ_κ would be possible.

From this point on, the investigation can be continued by considering slow- and fast-time dependent, complex forcings $\underline{F}(t', \tau')$ both experimentally and theoretically. The generation of frequency combs in a microresonator pumped by optical pulses was already studied numerically and experimentally [218] and offers many different directions for further research.

Bibliography

[1] T. Udem, J. Reichert, R. Holzwarth, and T. Hänsch, "Absolute optical frequency measurement of the cesium D_1 line with a mode-locked laser," *Physical Review Letters*, vol. 82, no. 18, pp. 3568–3571, 1999.

[2] N. Nemitz, T. Ohkubo, M. Takamoto, I. Ushijima, M. Das, N. Ohmae, and H. Katori, "Frequency ratio of Yb and Sr clocks with 5×10^{-17} uncertainty at 150 seconds averaging time," *Nature Photonics*, vol. 10, no. 4, pp. 258–261, 2016.

[3] M. S. Safronova, D. Budker, D. Demille, D. F. Kimball, A. Derevianko, and C. W. Clark, "Search for new physics with atoms and molecules," *Reviews of Modern Physics*, vol. 90, no. 2, p. 025008, 2018.

[4] S. A. Diddams, "The evolving optical frequency comb," *Journal of the Optical Society of America B*, vol. 27, no. 11, pp. B51–B62, 2010.

[5] T. Wilken, G. L. Curto, R. A. Probst, T. Steinmetz, A. Manescau, L. Pasquini, J. I. González Hernández, R. Rebolo, T. W. Hänsch, T. Udem, and R. Holzwarth, "A spectrograph for exoplanet observations calibrated at the centimetre-per-second level," *Nature*, vol. 485, no. 5, pp. 611–614, 2012.

[6] T. Fortier and E. Baumann, "20 years of developments in optical frequency comb technology and applications," *Communications Physics*, vol. 2, no. 12, p. 153, 2019.

[7] T. W. Hänsch, "Nobel lecture: passion for precision," *Reviews of Modern Physics*, vol. 78, no. 4, pp. 1297–1309, 2006.

[8] J. L. Hall, "Nobel lecture: defining and measuring optical frequencies," *Reviews of Modern Physics*, vol. 78, no. 4, pp. 1279–1295, 2006.

[9] M. Giunta, R. Holzwarth, M. Fischer, W. Hansel, T. Steinmetz, M. Lessing, S. Holzberger, C. Cleff, T. W. Hansch, and M. Mei, "20 years and 20 decimal digits: a journey with optical frequency combs," *IEEE Photonics Technology Letters*, vol. 31, no. 23, pp. 1898–1901, 2019.

[10] P. Del'Haye, A. Schliesser, O. Arcizet, T. Wilken, R. Holzwarth, and T. J. Kippenberg, "Optical frequency comb generation from a monolithic microresonator," *Nature*, vol. 450, no. 7173, pp. 1214–1217, 2007.

[11] T. J. Kippenberg, R. Holzwarth, and S. A. Diddams, "Microresonator-based optical frequency combs," *Science*, vol. 332, no. 6029, pp. 555–559, 2011.

[12] M. H. P. Pfeiffer, C. Herkommer, J. Liu, H. Guo, M. Karpov, E. Lucas, M. Zervas, and T. J. Kippenberg, "Octave-spanning dissipative Kerr soliton frequency combs in Si_3N_4 microresonators," *Optica*, vol. 4, no. 7, pp. 684–691, 2017.

[13] V. Brasch, E. Lucas, J. D. Jost, M. Geiselmann, and T. J. Kippenberg, "Self-referenced photonic chip soliton Kerr frequency comb," *Light: Science and Applications*, vol. 6, no. 1, p. e16202, 2017.

[14] J. Pfeifle, V. Brasch, M. Lauermann, Y. Yu, D. Wegner, T. Herr, K. Hartinger, P. Schindler, J. Li, D. Hillerkuss, R. Schmogrow, C. Weimann, R. Holzwarth, W. Freude, J. Leuthold, T. J. Kippenberg, and C. Koos, "Coherent terabit communications with microresonator Kerr frequency combs," *Nature Photonics*, vol. 8, no. 5, pp. 375–380, 2014.

[15] B. Stern, X. Ji, Y. Okawachi, A. L. Gaeta, and M. Lipson, "Battery-operated integrated frequency comb generator," *Nature*, vol. 562, no. 10, pp. 401–405, 2018.

[16] S. B. Papp, K. Beha, P. DelHaye, F. Quinlan, H. Lee, K. J. Vahala, and S. A. Diddams, "A microresonator frequency comb optical clock," *Optica*, vol. 1, no. 1, pp. 10–14, 2014.

[17] F. Ferdous, H. Miao, D. E. Leaird, K. Srinivasan, J. Wang, L. Chen, L. T. Varghese, and A. M. Weiner, "Spectral line-by-line pulse shaping of on-chip microresonator frequency combs," *Nature Photonics*, vol. 5, no. 12, pp. 770–776, 2011.

[18] M.-G. Suh, Q.-F. Yang, K. Y. Yang, X. Yi, and K. Vahala, "Microresonator soliton dual-comb spectroscopy," *Science*, vol. 354, no. 6312, pp. 600–603, 2016.

[19] I. Coddington, W. C. Swann, L. Nenadovic, and N. R. Newbury, "Rapid and precise absolute distance measurements at long range," *Nature Photonics*, vol. 3, no. 6, pp. 351–356, 2009.

[20] C. Weimann, F. Hoeller, Y. Schleitzer, C. A. Diez, B. Spruck, W. Freude, Y. Boeck, and C. Koos, "Measurement of length and position with frequency combs," *Journal of Physics: Conference Series*, vol. 605, p. 012030, 2015.

[21] T. Herr, V. Brasch, J. D. Jost, C. Y. Wang, N. M. Kondratiev, M. L. Gorodetsky, and T. J. Kippenberg, "Temporal solitons in optical microresonators," *Nature Photonics*, vol. 8, no. 2, pp. 145–152, 2014.

[22] A. S. Raja, A. S. Voloshin, H. Guo, S. E. Agafonova, J. Liu, A. S. Gorodnitskiy, M. Karpov, N. G. Pavlov, E. Lucas, R. R. Galiev, A. E. Shitikov, J. D. Jost, M. L. Gorodetsky, and T. J. Kippenberg, "Electrically pumped photonic integrated soliton microcomb," *Nature Communications*, vol. 10, no. 2, p. 680, 2019.

[23] J. Liu, A. S. Raja, M. Karpov, B. Ghadiani, M. H. P. Pfeiffer, B. Du, N. J. Engelsen, H. Guo, M. Zervas, and T. J. Kippenberg, "Ultralow-power chip-based soliton microcombs for photonic integration," *Optica*, vol. 5, no. 10, pp. 1347–1353, 2018.

[24] J. S. Levy, A. Gondarenko, M. a. Foster, A. C. Turner-Foster, A. L. Gaeta, and M. Lipson, "CMOS-compatible multiple-wavelength oscillator for on-chip optical interconnects," *Nature Photonics*, vol. 4, no. 8, pp. 37–40, 2010.

[25] R. K. W. Lau, M. R. E. Lamont, Y. Okawachi, and A. L. Gaeta, "Effects of multiphoton absorption on parametric comb generation in silicon microresonators," *Optics Letters*, vol. 40, no. 12, pp. 2778–2781, 2015.

[26] R. Hamerly, D. Gray, C. Rogers, and K. Jamshidi, "Conditions for parametric and free-carrier oscillation in silicon ring cavities," *Journal of Lightwave Technology*, vol. 36, no. 19, pp. 4671–4677, 2018.

[27] R. Haldar, A. Roy, P. Mondal, V. Mishra, and S. K. Varshney, "Free-carrier-driven Kerr frequency comb in optical microcavities: Steady state, bistability, self-pulsation, and modulation instability," *Physical Review A*, vol. 99, no. 3, p. 033848, 2019.

[28] A. Sahoo and S. Roy, "Stability and variational analysis of cavity solitons under various perturbations," *Physical Review A*, vol. 100, no. 5, p. 053814, 2019.

[29] A. C. Turner-Foster, M. a. Foster, J. S. Levy, C. B. Poitras, R. Salem, A. L. Gaeta, and M. Lipson, "Ultrashort free-carrier lifetime in low-loss silicon nanowaveguides," *Optics Express*, vol. 18, no. 4, pp. 3582–3591, 2010.

[30] T. Udem, R. Holzwarth, and T. W. Hänsch, "Optical frequency metrology," *Nature*, vol. 416, no. 3, pp. 233–237, 2002.

[31] S. T. Cundiff and J. Ye, "Colloquium: Femtosecond optical frequency combs," *Reviews of Modern Physics*, vol. 75, no. 1, pp. 325–342, 2003.

[32] T. Udem, J. Reichert, R. Holzwarth, and T. Hänsch, "Accurate measurement of large optical frequency differences with a mode-locked laser," *Optics Letters*, vol. 24, no. 13, pp. 881–883, 1999.

[33] B. R. Washburn, S. A. Diddams, N. R. Newbury, J. W. Nicholson, M. F. Yan, and C. G. Jørgensen, "Phase-locked, erbium-fiber-laser-based frequency comb in the near infrared," *Optics Letters*, vol. 29, no. 3, pp. 250–252, 2004.

[34] J. Rauschenberger, T. Fortier, D. Jones, J. Ye, and S. Cundiff, "Control of the frequency comb from a mode-locked erbium-doped fiber laser," *Optics Express*, vol. 10, no. 24, pp. 1404–1410, 2002.

[35] U. Keller, "Recent developments in compact ultrafast lasers," *Nature*, vol. 424, no. 8, pp. 831–838, 2003.

[36] W. T. Silfvast, *Laser Fundamentals*. Cambridge University Press, second ed., 2004.

[37] O. Okhotnikov, A. Grudinin, and M. Pessa, "Ultra-fast fibre laser systems based on SESAM technology: New horizons and applications," *New Journal of Physics*, vol. 6, no. 177, pp. 1–22, 2004.

[38] Y. Takushima, H. Sotobayashi, M. E. Grein, E. P. Ippen, and H. A. Haus, "Linewidth of mode combs of passively and actively mode-locked semiconductor laser diodes," *Proc. SPIE , Active and Passive Optical Components for WDM Communications IV*, vol. 5595, pp. 213–227, 2004.

[39] G. Cerullo, S. De Silvestri, and V. Magni, "Self-starting Kerr-lens mode locking of a Ti:sapphire laser," *Optics Letters*, vol. 19, no. 14, pp. 1040–1042, 1994.

[40] F. Salin, M. Piché, and J. Squier, "Mode locking of Ti:Al_2O_3 lasers and self-focusing: a Gaussian approximation," *Optics Letters*, vol. 16, no. 21, pp. 1674–1676, 1991.

[41] J. P. Van Der Ziel, "Active mode locking of double heterostructure lasers in an external cavity," *Journal of Applied Physics*, vol. 52, no. 7, pp. 4435–4446, 1981.

[42] K. Sato, I. Kotaka, Y. Kondo, and M. Yamamoto, "Active mode locking at 50 GHz repetition frequency by half-frequency modulation of monolithic semiconductor lasers integrated with electroabsorption modulators," *Applied Physics Letters*, vol. 69, no. 18, pp. 2626–2628, 1996.

[43] R. Holzwarth, T. Udem, T. W. Hänsch, J. C. Knight, W. J. Wadsworth, and P. S. J. Russell, "Optical frequency synthesizer for precision spectroscopy," *Physical Review Letters*, vol. 85, no. 11, pp. 2264–2267, 2000.

[44] S. A. Diddams, T. Udem, J. C. Bergquist, E. A. Curtis, R. E. Drullinger, L. Hollberg, W. M. Itano, W. D. Lee, C. W. Oates, K. R. Vogel, D. J. Wineland, J. Reichert, and R. Holzwarth, "An optical clock based on a single trapped $^{199}Hg^{+}$ ion," *Science*, vol. 293, no. 5531, pp. 825–828, 2001.

[45] C. Wu and N. K. Dutta, "High-repetition-rate optical pulse generation using a rational harmonic mode-locked fiber laser," *IEEE Journal of Quantum Electronics*, vol. 36, no. 2, pp. 145–150, 2000.

[46] M. Yu, Y. Okawachi, A. G. Griffith, M. Lipson, and A. L. Gaeta, "Modelocked mid-infrared frequency combs in a silicon microresonator," *Optica*, vol. 3, no. 8, pp. 854–860, 2016.

[47] B. J. Hausmann, I. Bulu, V. Venkataraman, P. Deotare, and M. Loncar, "Diamond nonlinear photonics," *Nature Photonics*, vol. 8, no. 5, pp. 369–374, 2014.

[48] M. Pu, L. Ottaviano, E. Semenova, and K. Yvind, "Efficient frequency comb generation in AlGaAs-on-insulator," *Optica*, vol. 3, no. 8, pp. 8–11, 2016.

[49] H. Jung, C. Xiong, K. Y. Fong, X. Zhang, and H. X. Tang, "Optical frequency comb generation from aluminum nitride microring resonator," *Optics Letters*, vol. 38, no. 15, pp. 2810–2813, 2013.

[50] W. Liang, A. A. Savchenkov, A. B. Matsko, V. S. Ilchenko, D. Seidel, and L. Maleki, "Generation of near-infrared frequency combs from a MgF_2 whispering gallery mode resonator," *Optics Letters*, vol. 36, no. 12, pp. 2290–2292, 2011.

[51] A. A. Savchenkov, A. B. Matsko, V. S. Ilchenko, I. Solomatine, D. Seidel, and L. Maleki, "Tunable optical frequency comb with a crystalline whispering gallery mode resonator," *Physical Review Letters*, vol. 101, no. 9, p. 093902, 2008.

[52] A. Chiasera, Y. Dumeige, P. Féron, M. Ferrari, Y. Jestin, G. N. Conti, S. Pelli, S. Soria, and G. C. Righini, "Spherical whispering-gallery-mode microresonators," *Laser and Photonics Reviews*, vol. 4, no. 3, pp. 457–482, 2010.

[53] D. K. Armani, T. J. Kippenberg, S. M. Spillane, and K. J. Vahala, "Ultra-high-Q toroid microcavity on a chip," *Nature*, vol. 421, no. 2, pp. 925–928, 2003.

[54] M. L. Gorodetsky and V. S. Ilchenko, "High-Q optical whispering-gallery microresonators: precession approach for spherical mode analysis and emission patterns with prism couplers," *Optics Communications*, vol. 113, no. 1-3, pp. 133–143, 1994.

[55] S. M. Spillane, T. J. Kippenberg, O. J. Painter, and K. J. Vahala, "Ideality in a fiber-taper-coupled microresonator system for application to cavity quantum electrodynamics," *Physical Review Letters*, vol. 91, no. 4, p. 043902, 2003.

[56] I. Chremmos, O. Schwelb, and N. Uzunoglu, *Photonic Microresonator Research and Applications*. Springer US, 2010.

[57] D. G. Rabus, *Integrated Ring Resonators: The Compendium*. Springer Berlin Heidelberg, 2007.

[58] R. Hunsperger, *Integrated Optics: Theory and Technology*. Springer New York, sixth ed., 2009.

[59] B. M. Rahman and J. B. Davies, "Finite-Element Solution of Integrated Optical Waveguides," *Journal of Lightwave Technology*, vol. 2, no. 5, pp. 682–688, 1984.

[60] C. R. Pollock and M. Lipson, *Integrated Photonics*. Springer US, second ed., 2003.

[61] X. Xue, M. Qi, and A. M. Weiner, "Normal-dispersion microresonator Kerr frequency combs," *Nanophotonics*, vol. 5, no. 2, pp. 244–262, 2016.

[62] E. Lucas, H. Guo, J. D. Jost, M. Karpov, and T. J. Kippenberg, "Detuning-dependent properties and dispersion-induced instabilities of temporal dissipative Kerr solitons in optical microresonators," *Physical Review A*, vol. 95, no. 4, p. 043822, 2017.

[63] P. S. Kuo, J. Bravo-Abad, and G. S. Solomon, "Second-harmonic generation using 4-quasi-phasematching in a GaAs whispering-gallery-mode microcavity," *Nature Communications*, vol. 5, no. 1, p. 3109, 2014.

[64] M. Parisi, N. Morais, I. Ricciardi, S. Mosca, T. Hansson, S. Wabnitz, G. Leo, and M. D. Rosa, "AlGaAs waveguide microresonators for efficient generation of quadratic frequency combs," *Journal of the Optical Society of America B*, vol. 34, no. 9, pp. 1842–1847, 2017.

[65] G. Agrawal, *Nonlinear Fiber Optics*. Elsevier, fifth ed., 2013.

[66] C. Koos, L. Jacome, C. G. Poulton, J. Leuthold, and W. Freude, "Nonlinear silicon-on-insulator waveguides for all-optical signal processing," *Optics Express*, vol. 15, no. 10, pp. 5976–5990, 2007.

[67] R. Boyd, *Nonlinear Optics*. Academic Press, third ed., 2008.

[68] T. Kremp, *Split-step wavelet collocation methods for linear and nonlinear optical wave propagation*. Cuvillier, 2002.

[69] H. Bao, A. Cooper, M. Rowley, L. Di Lauro, J. S. Totero Gongora, S. T. Chu, B. E. Little, G. L. Oppo, R. Morandotti, D. J. Moss, B. Wetzel, M. Peccianti, and A. Pasquazi, "Laser cavity-soliton microcombs," *Nature Photonics*, vol. 13, no. 6, pp. 384–389, 2019.

[70] A. R. Johnson, Y. Okawachi, M. R. E. Lamont, J. S. Levy, M. Lipson, and A. L. Gaeta, "Microresonator-based comb generation without an external laser source," *Optics Express*, vol. 22, no. 2, pp. 1394–1401, 2014.

[71] S. B. Papp, P. Del'Haye, and S. A. Diddams, "Parametric seeding of a microresonator optical frequency comb," *Optics Express*, vol. 21, no. 15, pp. 17615–17624, 2013.

[72] W. Weng, E. Lucas, G. Lihachev, V. E. Lobanov, H. Guo, M. L. Gorodetsky, and T. J. Kippenberg, "Spectral purification of microwave signals with disciplined dissipative Kerr solitons," *Physical Review Letters*, vol. 122, no. 1, p. 13902, 2019.

[73] Y. K. Chembo and N. Yu, "Modal expansion approach to optical-frequency-comb generation with monolithic whispering-gallery-mode resonators," *Physical Review A*, vol. 82, no. 3, p. 033801, 2010.

[74] T. Herr, K. Hartinger, J. Riemensberger, C. Y. Wang, E. Gavartin, R. Holzwarth, M. L. Gorodetsky, and T. J. Kippenberg, "Universal formation dynamics and noise of Kerr-frequency combs in microresonators," *Nature Photonics*, vol. 6, no. 7, pp. 480–487, 2012.

[75] T. Hansson, D. Modotto, and S. Wabnitz, "On the numerical simulation of Kerr frequency combs using coupled mode equations," *Optics Communications*, vol. 312, no. 2, pp. 134–136, 2014.

[76] Y. K. Chembo and C. R. Menyuk, "Spatiotemporal Lugiato-Lefever formalism for Kerr-comb generation in whispering-gallery-mode resonators," *Physical Review A*, vol. 87, no. 5, p. 053852, 2013.

[77] T. Hansson and S. Wabnitz, "Dynamics of microresonator frequency comb generation: Models and stability," *Nanophotonics*, vol. 5, no. 2, pp. 231–243, 2016.

[78] L. A. Lugiato and R. Lefever, "Spatial dissipative structures in passive optical systems," *Physical Review Letters*, vol. 58, no. 21, pp. 2209–2211, 1987.

[79] G. D'Aguanno and C. R. Menyuk, "Coupled Lugiato-Lefever equation for nonlinear frequency comb generation at an avoided crossing of a microresonator," *European Physical Journal D*, vol. 71, no. 3, p. 74, 2017.

[80] T. Kobatake, T. Kato, H. Itobe, Y. Nakagawa, and T. Tanabe, "Thermal effects on Kerr comb generation in a CaF_2 whispering-gallery mode microcavity," *IEEE Photonics Journal*, vol. 8, no. 2, pp. 1–9, 2016.

[81] T. Hansson, D. Modotto, and S. Wabnitz, "Dynamics of the modulational instability in microresonator frequency combs," *Physical Review A*, vol. 88, no. 2, p. 023819, 2013.

[82] R. Irving, *Beyond the Quadratic Formula*. Mathematical Association of America, 2013.

[83] M.-G. Suh, C. Y. Wang, C. Johnson, and K. J. Vahala, "Directly pumped 10 GHz microcomb modules from low-power diode lasers," *Optics Letters*, vol. 44, no. 7, pp. 1841–1843, 2019.

[84] M.-G. Suh and K. Vahala, "Gigahertz-repetition-rate soliton microcombs," *Nature Communications*, vol. 5, no. 1, pp. 65–66, 2018.

[85] M. H. P. Pfeiffer, A. Kordts, V. Brasch, M. Zervas, M. Geiselmann, J. D. Jost, and T. J. Kippenberg, "Photonic Damascene process for integrated high-Q microresonator based nonlinear photonics," *Optica*, vol. 3, no. 1, pp. 20–25, 2016.

[86] V. Torres-Company, D. Castelló-Lurbe, and E. Silvestre, "Comparative analysis of spectral coherence in microresonator frequency combs," *Optics Express*, vol. 22, no. 4, pp. 4678–4691, 2014.

[87] D. C. Cole, E. S. Lamb, P. D. Haye, S. A. Diddams, and S. B. Papp, "Soliton crystals in Kerr resonators," *Nature Photonics*, vol. 11, no. 10, pp. 671–676, 2017.

[88] D. T. Spencer, T. Drake, T. C. Briles, J. Stone, L. C. Sinclair, C. Fredrick, Q. Li, D. Westly, B. R. Ilic, A. Bluestone, N. Volet, T. Komljenovic, L. Chang, S. H. Lee, D. Y. Oh, M. G. Suh, K. Y. Yang, M. H. Pfeiffer, T. J. Kippenberg, E. Norberg, L. Theogarajan, K. Vahala, N. R. Newbury, K. Srinivasan, J. E. Bowers, S. A. Diddams, and S. B. Papp, "An optical-frequency synthesizer using integrated photonics," *Nature*, vol. 557, no. 7703, pp. 81–85, 2018.

[89] J. D. Jost, T. Herr, C. Lecaplain, E. Lucas, V. Brasch, H. P. Pfeiffer, and T. J. Kippenberg, "Counting the cycles of light using an optical microresonator," *Optica*, vol. 2, no. 8, pp. 706–711, 2014.

[90] M.-G. Suh and K. Vahala, "Soliton microcomb range measurement," *Science*, vol. 359, no. 6378, pp. 884–887, 2018.

[91] Y. Geng, W. Cui, J. Sun, X. Chen, and X. Yin, "Enhancing the long-term stability of dissipative Kerr soliton microcomb," *Optics Letters*, vol. 45, no. 18, pp. 5073–5076, 2020.

[92] R. Rosales, K. Merghem, A. Martinez, A. Akrout, J. P. Tourrenc, A. Accard, F. Lelarge, and A. Ramdane, "InAs/InP quantum-dot passively mode-locked lasers for 1.55-μm applications," *IEEE Journal on Selected Topics in Quantum Electronics*, vol. 17, no. 5, pp. 1292–1301, 2011.

[93] E. Sooudi, S. Sygletos, A. D. Ellis, G. Huyet, J. G. McInerney, F. Lelarge, K. Merghem, R. Rosales, A. Martinez, A. Ramdane, and S. P. Hegarty, "Optical frequency comb generation using dual-mode injection-locking of quantum-dash mode-locked lasers: Properties and applications," *IEEE Journal of Quantum Electronics*, vol. 48, no. 10, pp. 1327–1338, 2012.

[94] F. Lelarge, B. Dagens, J. Renaudier, R. Brenot, A. Accard, F. Van Dijk, D. Make, O. Le Gouezigou, J. G. Provost, F. Poingt, J. Landreau, O. Drisse, E. Derouin, B. Rousseau, F. Pommereau, and G. H. Duan, "Recent advances on InAs/InP quantum dash based semiconductor lasers and optical amplifiers operating at 1.55 μm," *IEEE Journal on Selected Topics in Quantum Electronics*, vol. 13, no. 1, pp. 111–123, 2007.

[95] Z. G. Lu, J. R. Liu, S. Raymond, P. J. Poole, P. J. Barrios, and D. Poitras, "312-fs pulse generation from a passive C-band InAs/InP quantum dot mode-locked laser," *Optics Express*, vol. 16, no. 14, pp. 10835–10840, 2008.

[96] A. Akrout, A. Shen, A. Enard, G. H. Duan, F. Lelarge, and A. Ramdane, "Low phase noise all-optical oscillator using quantum dash modelocked laser," *Electronics Letters*, vol. 46, no. 1, pp. 73–74, 2010.

[97] A. Shen, J. G. Provost, A. Akrout, B. Rousseau, F. Lelarge, O. Legouezigou, F. Pommereau, F. Poingt, L. Legouezigou, G. H. Duan, and A. Ramdane, "Low confinement factor quantum dash (QD) modelocked fabry-perot (FP) laser diode for tunable pulse generation," *Conference on Optical Fiber Communication/National Fiber Optic Engineers Conference*, p. OThK1, 2008.

[98] K. Merghem, A. Akrout, A. Martinez, G. Aubin, A. Ramdane, F. Lelarge, and G. H. Duan, "Pulse generation at 346 GHz using a passively mode locked quantum-dash-based laser at 1.55 μm," *Applied Physics Letters*, vol. 94, no. 2, p. 021107, 2009.

[99] A. Willner, *Optical Fiber Telecommunications*. Elsevier, 2019.

[100] B. Schwarz, "Lidar: Mapping the world in 3D," *Nature Photonics*, vol. 4, no. 7, pp. 429–430, 2010.

[101] X. Liang, V. Kankare, J. Hyyppä, Y. Wang, A. Kukko, H. Haggrén, X. Yu, H. Kaartinen, A. Jaakkola, F. Guan, M. Holopainen, and M. Vastaranta, "Terrestrial laser scanning in forest inventories," *ISPRS Journal of Photogrammetry and Remote Sensing*, vol. 115, pp. 63–77, 2016.

[102] Y. Cui, S. Schuon, D. Chan, S. Thrun, and C. Theobalt, "3D shape scanning with a time-of-flight camera," in *Proceedings of the IEEE*

Computer Society Conference on Computer Vision and Pattern Recognition, pp. 1173–1180, IEEE, 2010.

[103] J. U. Eitel, B. Höfle, L. A. Vierling, A. Abellán, G. P. Asner, J. S. Deems, C. L. Glennie, P. C. Joerg, A. L. LeWinter, T. S. Magney, G. Mandlburger, D. C. Morton, J. Müller, and K. T. Vierling, "Beyond 3-D: The new spectrum of lidar applications for earth and ecological sciences," *Remote Sensing of Environment*, vol. 186, pp. 372–392, 2016.

[104] D. F. Pierrottet, F. Amzajerdian, L. Petway, B. Barnes, G. Lockard, and M. Rubio, "Linear FMCW laser radar for precision range and vector velocity measurements," in *MRS Proceedings*, vol. 1076, pp. 1076–K04–06, Cambridge University Press, 2008.

[105] G. Berkovic and E. Shafir, "Optical methods for distance and displacement measurements," *Advances in Optics and Photonics*, vol. 4, no. 4, pp. 441–471, 2012.

[106] P. Bhargava, T. Kim, C. V. Poulton, J. Notaros, A. Yaacobi, E. Timurdogan, C. Baiocco, N. Fahrenkopf, S. Kruger, T. Ngai, Y. Timalsina, M. R. Watts, and V. Stojanovic, "Fully integrated coherent LiDAR in 3D-integrated silicon photonics/65 nm CMOS," *IEEE Symposium on VLSI Circuits, Digest of Technical Papers*, pp. C262–C263, 2019.

[107] P. E. Ciddor, "Refractive index of air: new equations for the visible and near infrared," *Applied Optics*, vol. 35, no. 9, pp. 1566–1573, 1996.

[108] A. Gelbart, B. C. Redman, R. S. Light, C. A. Schwartzlow, and A. J. Griffis, "Flash lidar based on multiple-slit streak tube imaging lidar," *Laser Radar Technology and Applications VII*, vol. 4723, no. 7, pp. 9–18, 2002.

[109] A. Medina, F. Gayá, and F. del Pozo, "Compact laser radar and three-dimensional camera," *Journal of the Optical Society of America A*, vol. 23, no. 4, pp. 800–805, 2006.

[110] C. Spiegelberg, J. Geng, Y. Hu, Y. Kaneda, S. Jiang, and N. Peyghambarian, "Low-noise narrow-linewidth fiber laser at 1550 nm," *Journal of Lightwave Technology*, vol. 22, no. 1, pp. 57–62, 2004.

[111] M. Pisani, "A homodyne Michelson interferometer with sub-picometer resolution," *Measurement Science and Technology*, vol. 20, no. 8, p. 084008, 2009.

[112] C. Weimann, M. Fratz, H. Wölfelschneider, W. Freude, H. Höfler, and C. Koos, "Synthetic-wavelength interferometry improved with frequency calibration and unambiguity range extension," *Applied Optics*, vol. 54, no. 20, pp. 6334–6343, 2015.

[113] P. Hariharan, *Optical Interferometry*. Elsevier Science, second ed., 2003.

[114] C. Weimann, M. Lauermann, F. Hoeller, W. Freude, and C. Koos, "Silicon photonic integrated circuit for fast and precise dual-comb distance metrology," *Optics Express*, vol. 25, no. 24, pp. 30091–30104, 2017.

[115] J. Gärtner, *Continuation and bifurcation of frequency combs modeled by the Lugiato-Lefever equation*. KIT, 2019.

[116] J. Pfeifle, A. Coillet, R. Henriet, K. Saleh, P. Schindler, C. Weimann, W. Freude, I. V. Balakireva, L. Larger, C. Koos, and Y. K. Chembo, "Optimally coherent Kerr combs generated with crystalline whispering gallery mode resonators for ultrahigh capacity fiber communications," *Physical Review Letters*, vol. 114, no. 9, p. 093902, 2015.

[117] C. Joshi, J. K. Jang, K. Luke, X. Ji, S. A. Miller, A. Klenner, Y. Okawachi, M. Lipson, and A. L. Gaeta, "Thermally controlled comb generation and soliton modelocking in microresonators," *Optics Letters*, vol. 41, no. 11, pp. 2565–2568, 2016.

[118] C. Godey, I. V. Balakireva, A. Coillet, and Y. K. Chembo, "Stability analysis of the spatiotemporal Lugiato-Lefever model for Kerr optical frequency combs in the anomalous and normal dispersion regimes," *Physical Review A*, vol. 89, no. 6, p. 063814, 2014.

[119] P. Parra-Rivas, D. Gomila, L. Gelens, and E. Knobloch, "Bifurcation structure of localized states in the Lugiato-Lefever equation with anomalous dispersion," *Physical Review E*, vol. 97, no. 4, p. 042204, 2018.

[120] H. Guo, M. Karpov, E. Lucas, A. Kordts, M. H. P. Pfeiffer, G. Lichachev, V. E. Lobanov, M. L. Gorodetsky, and T. J. Kippenberg, "Universal dynamics and deterministic switching of dissipative Kerr solitons in optical microresonators," *Nature Physics*, vol. 13, no. 1, pp. 94–102, 2017.

[121] X. Yi, Q.-F. Yang, K. Y. Yang, M.-G. Suh, and K. Vahala, "Soliton frequency comb at microwave rates in a high-Q silica microresonator," *Optica*, vol. 2, no. 12, pp. 1078–1085, 2015.

[122] C. Godey, "A bifurcation analysis for the Lugiato-Lefever equation," *The European Physical Journal D*, vol. 71, no. 5, p. 131, 2017.

[123] P. Parra-Rivas, D. Gomila, M. A. Matías, S. Coen, and L. Gelens, "Dynamics of localized and patterned structures in the Lugiato-Lefever equation determine the stability and shape of optical frequency combs," *Physical Review A*, vol. 89, no. 4, p. 043813, 2014.

[124] P. Parra-Rivas, E. Knobloch, D. Gomila, and L. Gelens, "Dark solitons in the Lugiato-Lefever equation with normal dispersion," *Physical Review A*, vol. 93, no. 6, p. 063839, 2016.

[125] R. Mandel and W. Reichel, "A priori bounds and global bifurcation results for frequency combs modeled by the Lugiato-Lefever equation," *SIAM Journal on Applied Mathematics*, vol. 77, no. 1, pp. 315–345, 2017.

[126] T. Miyaji, I. Ohnishi, and Y. Tsutsumi, "Bifurcation analysis to the Lugiato-Lefever equation in one space dimension," *Physica D*, vol. 239, no. 23, pp. 2066 – 2083, 2010.

[127] L. Delcey and M. Haraguss, "Periodic waves of the Lugiato-Lefever equation at the onset of Turing instability," *Philosophical Transactions of the Royal Society A*, vol. 376, no. 2117, p. 20170188, 2018.

[128] N. Périnet, N. Verschueren, and S. Coulibaly, "Eckhaus instability in the Lugiato-Lefever model," *The European Physical Journal D*, vol. 71, no. 9, p. 243, 2017.

[129] M. Stanislavova and A. G. Stefanov, "Asymptotic stability for spectrally stable Lugiato-Lefever solitons in periodic waveguides," *Journal of Mathematical Physics*, vol. 59, no. 10, p. 101502, 2018.

[130] X. Xue, Y. Xuan, Y. Liu, P.-H. Wang, S. Chen, J. Wang, D. E. Leaird, M. Qi, and A. M. Weiner, "Mode-locked dark pulse Kerr combs in normal-dispersion microresonators," *Nature Photonics*, vol. 9, no. 9, pp. 594–600, 2015.

[131] H. Kielhöfer, *Bifurcation Theory*. Springer New York, second ed., 2012.

[132] P. H. Rabinowitz, "Some global results for nonlinear eigenvalue problems," *Journal of Functional Analysis*, vol. 7, no. 3, pp. 487 – 513, 1971.

[133] R. Mandel, "Global secondary bifurcation, symmetry breaking and period-doubling," *Topological Methods in Nonlinear Analysis*, vol. 53, no. 2, pp. 779–800, 2019.

[134] H. Uecker, D. Wetzel, and J. D. M. Rademacher, "pde2path – a matlab package for continuation and bifurcation in 2d elliptic systems," *Numerical Mathematics: Theory, Methods and Applications*, vol. 7, no. 1, pp. 58–106, 2014.

[135] T. Dohnal, J. D. M. Rademacher, H. Uecker, and D. Wetzel, "pde2path–V2: multi-parameter continuation and periodic domains," *Proceedings of 8th European Nonlinear Dynamics Conference*, p. 373, 2014.

[136] S. Coen and M. Erkintalo, "Universal scaling laws of Kerr frequency combs," *Optics Letters*, vol. 38, no. 11, pp. 1790–1792, 2013.

[137] C. Bao, L. Zhang, A. Matsko, Y. Yan, Z. Zhao, G. Xie, A. M. Agarwal, L. C. Kimerling, J. Michel, L. Maleki, and A. E. Willner, "Nonlinear conversion efficiency in Kerr frequency comb generation," *Optics Letters*, vol. 39, no. 21, pp. 6126–6129, 2014.

[138] K. Nozaki and N. Bekki, "Chaotic solitons in a plasma driven by an rf field," *Journal of the Physical Society of Japan*, vol. 54, no. 7, pp. 2363–2366, 1985.

[139] K. Nozaki and N. Bekki, "Low-dimensional chaos in a driven damped nonlinear Schrödinger equation," *Physica D*, vol. 21, no. 2–3, pp. 381–393, 1986.

[140] X. Xue, P.-H. Wang, Y. Xuan, M. Qi, and A. M. Weiner, "Microresonator Kerr frequency combs with high conversion efficiency," *Laser & Photonics Reviews*, vol. 11, no. 1, p. 1600276, 2017.

[141] J. Gärtner, R. Mandel, and W. Reichel, "The Lugiato-Lefever equation with nonlinear damping caused by two photon absorption," *Journal of Dynamics and Differential Equations*, pp. 1–21, 2021.

[142] S. Coen, H. G. Randle, T. Sylvestre, and M. Erkintalo, "Modeling of octave-spanning Kerr frequency combs using a generalized mean-field Lugiato-Lefever model," *Optics Letters*, vol. 38, no. 1, pp. 37–39, 2013.

[143] H. Lee, T. Chen, J. Li, K. Y. Yang, S. Jeon, O. Painter, and K. J. Vahala, "Chemically etched ultrahigh-Q wedge-resonator on a silicon chip," *Nature Photonics*, vol. 6, no. 6, pp. 369–373, 2012.

[144] M. H. P. Pfeiffer, C. Herkommer, J. Liu, T. Morais, M. Zervas, M. Geiselmann, and T. J. Kippenberg, "Photonic damascene process for low-loss, high-confinement silicon nitride waveguides," *IEEE Journal of Selected Topics in Quantum Electronics*, vol. 24, no. 4, p. 6101411, 2018.

[145] X. Chen, M. M. Milosevic, S. Stanković, S. Reynolds, T. D. Bucio, K. Li, D. J. Thomson, F. Gardes, and G. T. Reed, "The emergence of silicon photonics as a flexible technology platform," *Proceedings of the IEEE*, vol. 106, no. 12, pp. 2101–2116, 2018.

[146] D. Thomson, A. Zilkie, J. E. Bowers, T. Komljenovic, G. T. Reed, L. Vivien, D. Marris-Morini, E. Cassan, L. Virot, J. M. Fédéli, J. M. Hartmann, J. H. Schmid, D. X. Xu, F. Boeuf, P. O'Brien, G. Z. Mashanovich, and M. Nedeljkovic, "Roadmap on silicon photonics," *Journal of Optics*, vol. 18, no. 7, p. 073003, 2016.

[147] A. Rickman, "The commercialization of silicon photonics," *Nature Photonics*, vol. 8, no. 8, pp. 579–582, 2014.

[148] C. Sun, M. T. Wade, Y. Lee, J. S. Orcutt, L. Alloatti, M. S. Georgas, A. S. Waterman, J. M. Shainline, R. R. Avizienis, S. Lin, B. R. Moss, R. Kumar, F. Pavanello, A. H. Atabaki, H. M. Cook, A. J. Ou, J. C. Leu, Y. H. Chen, K. Asanović, R. J. Ram, M. A. Popović, and V. M. Stojanović, "Single-chip microprocessor that communicates directly using light," *Nature*, vol. 528, no. 12, pp. 534–538, 2015.

[149] A. G. Griffith, R. K. W. Lau, J. Cardenas, Y. Okawachi, A. Mohanty, R. Fain, Y. Ho, D. Lee, M. Yu, C. T. Phare, C. B. Poitras, A. L. Gaeta, and M. Lipson, "Silicon-chip mid-infrared frequency comb generation," *Nature Communications*, vol. 6, no. 2, p. 6299, 2015.

[150] C. Koos, P. Vorreau, T. Vallaitis, P. Dumon, W. Bogaerts, R. Baets, B. Esembeson, I. Biaggio, T. Michinobu, F. Diederich, W. Freude, and J. Leuthold, "All-optical high-speed signal processing with silicon–organic hybrid slot waveguides," *Nature Photonics*, vol. 3, no. 4, pp. 216–219, 2009.

[151] S. F. Preble, Q. Xu, B. S. Schmidt, and M. Lipson, "Ultrafast all-optical modulation on a silicon chip.," *Optics letters*, vol. 30, no. 21, pp. 2891–2893, 2005.

[152] A. G. Griffith, M. Yu, Y. Okawachi, J. Cardenas, A. Mohanty, A. L. Gaeta, and M. Lipson, "Coherent mid-infrared frequency combs in silicon-microresonators in the presence of Raman effects," *Optics Express*, vol. 24, no. 12, pp. 13044–13050, 2016.

[153] A. C. Turner, C. Manolatou, B. S. Schmidt, M. Lipson, M. A. Foster, Y. Okawachi, and A. L. Gaeta, "Tailored anomalous group-velocity dispersion in silicon waveguides," *Optics Express*, vol. 14, no. 10, pp. 4357–4362, 2006.

[154] N. Feng, J. Michel, and L. C. Kimerling, "Optical field concentration in low-index waveguides," *IEEE Journal of Quantum Electronics*, vol. 42, no. 9, pp. 885–890, 2006.

[155] T. Vallaitis, S. Bogatscher, L. Alloatti, P. Dumon, R. Baets, M. L. Scimeca, I. Biaggio, F. Diederich, C. Koos, W. Freude, and J. Leuthold, "Optical properties of highly nonlinear silicon-organic hybrid (SOH)

waveguide geometries," *Optics Express*, vol. 17, no. 20, pp. 17357–17368, 2009.

[156] C. Koos, P. Vorreau, P. Dumon, R. Baets, B. Esembeson, I. Biaggio, T. Michinobu, F. Diederich, W. Freude, and J. Leuthold, "Highly-nonlinear silicon photonics slot waveguide," in *Optical Fiber Communication Conference*, p. PDP25, 2008.

[157] C. Bao, Y. Xuan, D. E. Leaird, S. Wabnitz, M. Qi, and A. M. Weiner, "Spatial mode-interaction induced single soliton generation in microresonators," *Optica*, vol. 4, no. 9, pp. 1011–1014, 2017.

[158] Y. Liu, Y. Xuan, X. Xue, P.-H. Wang, S. Chen, A. J. Metcalf, J. Wang, D. E. Leaird, M. Qi, and A. M. Weiner, "Investigation of mode coupling in normal-dispersion silicon nitride microresonators for Kerr frequency comb generation," *Optica*, vol. 1, no. 3, pp. 137–144, 2014.

[159] H. K. Tsang and Y. Liu, "Nonlinear optical properties of silicon waveguides," *Semiconductor Science and Technology*, vol. 23, no. 6, p. 064007, 2008.

[160] X. Gai, Y. Yu, B. Kuyken, P. Ma, S. J. Madden, J. Van Campenhout, P. Verheyen, G. Roelkens, R. Baets, and B. Luther-Davies, "Nonlinear absorption and refraction in crystalline silicon in the mid-infrared," *Laser and Photonics Reviews*, vol. 7, no. 6, pp. 1054–1064, 2013.

[161] Q. Lin, O. J. Painter, and G. P. Agrawal, "Nonlinear optical phenomena in silicon waveguides : Modeling and applications," *Optics Express*, vol. 15, no. 25, pp. 16604–16644, 2007.

[162] A. D. Bristow, N. Rotenberg, and H. M. Van Driel, "Two-photon absorption and Kerr coefficients of silicon for 850-2200 nm," *Applied Physics Letters*, vol. 90, no. 19, p. 191104, 2007.

[163] C. Jacoboni, C. Canali, G. Otiaviani, and A. A. Quaranta, "A review of some charge transport properties of silicon," *Solid-State Electronics*, vol. 20, no. 2, pp. 77–89, 1977.

[164] W. Bogaerts, P. de Heyn, T. van Vaerenbergh, K. de Vos, S. Kumar Selvaraja, T. Claes, P. Dumon, P. Bienstman, D. van Thourhout, and

R. Baets, "Silicon microring resonators," *Laser and Photonics Reviews*, vol. 6, no. 1, pp. 47–73, 2012.

[165] L. Yin and G. P. Agrawal, "Impact of two-photon absorption on self-phase modulation in silicon waveguides," *Optics Letters*, vol. 32, no. 14, pp. 2031–2033, 2007.

[166] Q.-F. Yang, X. Yi, K. Y. Yang, and K. Vahala, "Spatial-mode-interaction-induced dispersive-waves and their active tuning in microresonators," *Optica*, vol. 3, no. 10, pp. 1132–1135, 2016.

[167] C. Milián, A. V. Gorbach, M. Taki, A. V. Yulin, and D. V. Skryabin, "Solitons and frequency combs in silica microring resonators: Interplay of the Raman and higher-order dispersion effects," *Physical Review A*, vol. 92, no. 3, p. 033851, 2015.

[168] T. Hansson, D. Modotto, and S. Wabnitz, "Mid-infrared soliton and Raman frequency comb generation in silicon microrings," *Optics Letters*, vol. 39, no. 23, pp. 6747–6750, 2014.

[169] M. Karpov, H. Guo, A. Kordts, V. Brasch, M. H. Pfeiffer, M. Zervas, M. Geiselmann, and T. J. Kippenberg, "Raman self-frequency shift of dissipative Kerr solitons in an optical microresonator," *Physical Review Letters*, vol. 116, no. 10, p. 103902, 2016.

[170] A. S. Raja, J. Liu, N. Volet, R. N. Wang, J. He, E. Lucas, R. Bouchand, and P. Morton, J. Bowers, and T. J. Kippenberg, "Chip-based soliton microcomb module using a hybrid semiconductor laser," *Optics Express*, vol. 28, no. 3, pp. 2714–2721, 2020.

[171] T. Horikawa, D. Shimura, and T. Mogami, "Low-loss silicon wire waveguides for optical integrated circuits," *MRS Communications*, vol. 6, no. 1, pp. 9–15, 2016.

[172] J. Steinlechner, C. Krüger, N. Lastzka, S. Steinlechner, A. Khalaidovski, and R. Schnabel, "Optical absorption measurements on crystalline silicon test masses at 1550 nm," *Classical and Quantum Gravity*, vol. 30, no. 9, p. 095007, 2013.

[173] N. M. Wright, D. J. Thomson, K. L. Litvinenko, W. R. Headley, A. J. Smith, A. P. Knights, F. Y. Gardes, G. Z. Mashanovich, R. Gwilliam,

and G. T. Reed, "Free carrier lifetime modification for silicon waveguide based devices," *Optics Express*, vol. 16, no. 24, pp. 19779–19784, 2008.

[174] M.-C. Amann, T. Bosch, M. Lescure, R. Myllyla, and M. Rioux, "Laser ranging: a critical review of usual techniques for distance measurement," *Optical Engineering*, vol. 40, no. 1, pp. 10–19, 2001.

[175] K. Minoshima and H. Matsumoto, "High-accuracy measurement of 240-m distance in an optical tunnel by use of a compact femtosecond laser.," *Applied Optics*, vol. 39, no. 30, pp. 5512–5517, 2000.

[176] N. Schuhler, Y. Salvadé, S. Lévêque, R. Dändliker, and R. Holzwarth, "Frequency-comb-referenced two-wavelength source for absolute distance measurement," *Optics Letters*, vol. 31, no. 21, pp. 3101–3103, 2006.

[177] Y. S. Jang, G. Wang, S. Hyun, H. J. Kang, B. J. Chun, Y. J. Kim, and S. W. Kim, "Comb-referenced laser distance interferometer for industrial nanotechnology," *Scientific Reports*, vol. 6, no. 31770, pp. 1–10, 2016.

[178] F. Keilmann, C. Gohle, and R. Holzwarth, "Time-domain mid-infrared frequency-comb spectrometer," *Optics Letters*, vol. 29, no. 13, pp. 1542–1544, 2004.

[179] V. Ataie, P. P. Kuo, A. Wiberg, Z. Tong, C. Huynh, N. Alic, and S. Radic, "Ultrafast absolute ranging by coherent parametric comb," *Optical Fiber Communication Conference/National Fiber Optic Engineers Conference*, p. OTh3D.2, 2013.

[180] J. Sun, E. Timurdogan, A. Yaacobi, E. S. Hosseini, and M. R. Watts, "Large-scale nanophotonic phased array," *Nature*, vol. 493, no. 7431, pp. 195–199, 2013.

[181] J. C. Hulme, J. K. Doylend, M. J. R. Heck, J. D. Peters, M. L. Davenport, J. T. Bovington, L. A. Coldren, and J. E. Bowers, "Fully integrated hybrid silicon two dimensional beam scanner," *Optics Express*, vol. 23, no. 5, pp. 5861–5874, 2015.

[182] N. Akhmediev and A. Ankiewicz, *Dissipative Solitons*. Springer Berlin Heidelberg, 2005.

[183] W. Liang, D. Eliyahu, V. S. Ilchenko, A. A. Savchenkov, A. B. Matsko, D. Seidel, and L. Maleki, "High spectral purity Kerr frequency comb radio frequency photonic oscillator," *Nature Communications*, vol. 6, no. 7957, pp. 1–8, 2015.

[184] D. J. Moss, R. Morandotti, A. L. Gaeta, and M. Lipson, "New CMOS-compatible platforms based on silicon nitride and Hydex for nonlinear optics," *Nature Photonics*, vol. 7, no. 8, pp. 597–607, 2013.

[185] V. Brasch, T. Herr, M. Geiselmann, G. Lihachev, M. H. P. Pfeiffer, M. L. Gorodetsky, and T. J. Kippenberg, "Photonic chip-based optical frequency comb using soliton Cherenkov radiation," *Science*, vol. 351, no. 6271, pp. 357–360, 2016.

[186] C. Koos, C. Weimann, and J. Leuthold, "Multiscale distance measurement with frequency combs," U.S. Patent 20150070685, 2013.

[187] N. Lindenmann, G. Balthasar, D. Hillerkuss, R. Schmogrow, M. Jordan, J. Leuthold, W. Freude, and C. Koos, "Photonic wire bonding: a novel concept for chip-scale interconnects," *Optics Express*, vol. 20, no. 16, pp. 17667–17677, 2012.

[188] P. I. Dietrich, M. Blaicher, I. Reuter, M. Billah, T. Hoose, A. Hofmann, C. Caer, R. Dangel, B. Offrein, U. Troppenz, M. Moehrle, W. Freude, and C. Koos, "In situ 3D nanoprinting of free-form coupling elements for hybrid photonic integration," *Nature Photonics*, vol. 12, no. 4, pp. 241–247, 2018.

[189] W. Y. Yan, A. Shaker, and N. El-Ashmawy, "Urban land cover classification using airborne LiDAR data: A review," *Remote Sensing of Environment*, vol. 158, pp. 295–310, 2015.

[190] J. Hecht, "Lidar for self-driving cars," *Optics & Photonics News*, vol. 29, no. 1, pp. 26–33, 2018.

[191] C. Rogers, A. Y. Piggott, D. J. Thomson, R. F. Wiser, I. E. Opris, S. A. Fortune, A. J. Compston, A. Gondarenko, F. Meng, X. Chen, G. T.

Reed, and R. Nicolaescu, "A universal 3D imaging sensor on a silicon photonics platform," *Nature*, vol. 590, no. 2, pp. 256–261, 2021.

[192] C. Weimann, A. Messner, T. Baumgartner, S. Wolf, F. Hoeller, W. Freude, and C. Koos, "Fast high-precision distance metrology using a pair of modulator-generated dual-color frequency combs," *Optics Express*, vol. 26, no. 26, pp. 34305–34335, 2018.

[193] J. Riemensberger, A. Lukashchuk, M. Karpov, W. Weng, E. Lucas, J. Liu, and T. J. Kippenberg, "Massively parallel coherent laser ranging using a soliton microcomb," *Nature*, vol. 581, no. 5, pp. 164–170, 2020.

[194] C. Bao, M.-G. Suh, and K. Vahala, "Microresonator soliton dual-comb imaging," *Optica*, vol. 6, no. 9, pp. 1110–1116, 2019.

[195] D. Hu, Z. Wu, H. Cao, Y. Shi, R. Li, H. Tian, Y. Song, and M. Hu, "Dual-comb absolute distance measurement of non-cooperative targets with a single free-running mode-locked fiber laser," *Optics Communications*, vol. 482, p. 126566, 2021.

[196] J. N. Kemal, P. Marin-Palomo, K. Merghem, G. Aubin, F. Lelarge, A. Ramdane, S. Randel, W. Freude, and C. Koos, "32QAM WDM transmission at 12 Tbit/s using a quantum-dash mode-locked laser diode (QD-MLLD) with external-cavity feedback," *Optics Express*, vol. 28, no. 16, pp. 23594–23608, 2020.

[197] S. Schneider, M. Lauermann, P.-I. Dietrich, C. Weimann, W. Freude, and C. Koos, "Optical coherence tomography system mass-producible on a silicon photonic chip," *Optics Express*, vol. 24, no. 2, p. 1573, 2016.

[198] C. V. Poulton, A. Yaacobi, D. B. Cole, M. J. Byrd, M. Raval, D. Vermeulen, and M. R. Watts, "Coherent solid-state LIDAR with silicon photonic optical phased arrays," *Optics Letters*, vol. 42, no. 20, pp. 4091–4094, 2017.

[199] M. Blaicher, M. R. Billah, J. Kemal, T. Hoose, P. Marin-Palomo, A. Hofmann, Y. Kutuvantavida, C. Kieninger, P. I. Dietrich, M. Lauermann, S. Wolf, U. Troppenz, M. Moehrle, F. Merget, S. Skacel, J. Witzens, S. Randel, W. Freude, and C. Koos, "Hybrid multi-chip assembly

of optical communication engines by in situ 3D nano-lithography," *Light: Science and Applications*, vol. 9, no. 1, p. 71, 2020.

[200] M. R. Billah, M. Blaicher, T. Hoose, P.-I. Dietrich, P. Marin-Palomo, N. Lindenmann, A. Nesic, A. Hofmann, U. Troppenz, M. Moehrle, S. Randel, W. Freude, and C. Koos, "Hybrid integration of silicon photonics circuits and InP lasers by photonic wire bonding," *Optica*, vol. 5, no. 7, pp. 876–883, 2018.

[201] K. Merghem, C. Calò, V. Panapakkam, A. Martinez, F. Lelarge, and A. Ramdane, "Long-term frequency stabilization of 10-GHz quantum-dash passively mode-locked lasers," *IEEE Journal of Selected Topics in Quantum Electronics*, vol. 21, no. 6, p. 1101407, 2015.

[202] T. Verolet, G. Aubin, Y. Lin, C. Browning, K. Merghem, F. Lelarge, C. Calo, A. Demalde, K. Mekhazni, E. Giacoumidis, A. Shen, L. P. Barry, and A. Ramdane, "Mode locked laser phase noise reduction under optical feedback for coherent DWDM communication," *Journal of Lightwave Technology*, vol. 38, no. 20, pp. 5708–5715, 2020.

[203] Z. G. Lu, J. R. Liu, P. J. Poole, C. Y. Song, and S. D. Chang, "Ultra-narrow linewidth quantum dot coherent comb lasers," *Optics Express*, vol. 26, no. 9, pp. 11909–11914, 2018.

[204] D. V. Land, A. P. Levick, and J. W. Hand, "The use of the Allan deviation for the measurement of the noise and drift performance of microwave radiometers," *Measurement Science and Technology*, vol. 18, no. 7, pp. 1917–1928, 2007.

[205] D. Huang, F. Li, Z. He, Z. Cheng, C. Shang, and P. K. A. Wai, "400 MHz ultrafast optical coherence tomography," *Optics Letters*, vol. 45, no. 24, pp. 6675–6678, 2020.

[206] Y. Na, C. G. Jeon, C. Ahn, M. Hyun, D. Kwon, J. Shin, and J. Kim, "Ultrafast, sub-nanometre-precision and multifunctional time-of-flight detection," *Nature Photonics*, vol. 14, no. 6, pp. 355–360, 2020.

[207] H. Wu, T. Zhao, Z. Wang, K. Zhang, B. Xue, J. Li, M. He, and X. Qu, "Long distance measurement up to 1.2 km by electro-optic dual-comb interferometry," *Applied Physics Letters*, vol. 111, no. 25, p. 251901, 2017.

[208] B. Lin, X. Zhao, M. He, Y. Pan, J. Chen, S. Cao, Y. Lin, Q. Wang, Z. Zheng, and Z. Fang, "Dual-comb absolute distance measurement based on a dual-wavelength passively mode-locked laser," *IEEE Photonics Journal*, vol. 9, no. 6, p. 7106508, 2017.

[209] Y. Li, Y. Cai, R. Li, H. Shi, H. Tian, M. He, Y. Song, and M. Hu, "Large-scale absolute distance measurement with dual free-running all-polarization-maintaining femtosecond fiber lasers," *Chinese Optics Letters*, vol. 17, no. 9, p. 091202, 2019.

[210] X. Ren, B. Xu, Q. Fei, Y. Liang, J. Ge, X. Wang, K. Huang, M. Yan, and H. Zeng, "Single-Photon Counting Laser Ranging with Optical Frequency Combs," *IEEE Photonics Technology Letters*, vol. 33, no. 1, pp. 27–30, 2021.

[211] M. D. G. Pascual, V. Vujicic, J. Braddell, F. Smyth, P. Anandarajah, and L. Barry, "Photonic integrated gain switched optical frequency comb for spectrally efficient optical transmission systems," *IEEE Photonics Journal*, vol. 9, no. 3, pp. 1–8, 2017.

[212] D. X. Xu, J. H. Schmid, G. T. Reed, G. Z. Mashanovich, D. J. Thomson, M. Nedeljkovic, X. Chen, D. Van Thourhout, S. Keyvaninia, and S. K. Selvaraja, "Silicon photonic integration platform – Have we found the sweet spot?," *IEEE Journal on Selected Topics in Quantum Electronics*, vol. 20, no. 4, pp. 189–205, 2014.

[213] D. Bauer, *Design and Application of Kerr-microresonator Frequency Combs*. Master thesis, Karlsruhe Institute of Technology, 2020.

[214] P. Parra-Rivas, D. Gomila, F. Leo, S. Coen, and L. Gelens, "Third-order chromatic dispersion stabilizes Kerr frequency combs," *Optics Letters*, vol. 39, no. 10, pp. 2971–2974, 2014.

[215] V. E. Lobanov, A. V. Cherenkov, A. E. Shitikov, I. A. Bilenko, and M. L. Gorodetsky, "Dynamics of platicons due to third-order dispersion," *European Physical Journal D*, vol. 71, no. 7, p. 185, 2017.

[216] A. V. Cherenkov, V. E. Lobanov, and M. L. Gorodetsky, "Dissipative Kerr solitons and Cherenkov radiation in optical microresonators with third-order dispersion," *Physical Review A*, vol. 95, no. 3, p. 033810, 2017.

[217] H. Liu, S.-W. Huang, J. Yang, M. Yu, D.-L. Kwong, and C. Wong, "Bright square pulse generation by pump modulation in a normal GVD microresonator," *Conference on Lasers and Electro-Optics*, p. FTu3D.3, 2017.

[218] E. Obrzud, S. Lecomte, and T. Herr, "Temporal solitons in microresonators driven by optical pulses," *Nature Photonics*, vol. 11, no. 9, pp. 600–607, 2017.

[219] M. G. Crandall and P. H. Rabinowitz, "Bifurcation from simple eigenvalues," *Journal of Functional Analysis*, vol. 8, no. 2, pp. 321 – 340, 1971.

[220] H. Brezis, *Functional Analysis, Sobolev Spaces and Partial Differential Equations*. Springer, 2011.

[221] M. Haelterman, S. Trillo, and S. Wabnitz, "Additive-modulation-instability ring laser in the normal dispersion regime of a fiber," *Optics Letters*, vol. 17, no. 10, pp. 745–747, 1992.

[222] I. H. Malitson, "Interspecimen comparison of the refractive index of fused silica," *Journal of the Optical Society of America*, vol. 55, no. 10, pp. 1205–1209, 1965.

[223] C. D. Salzberg and J. J. Villa, "Infrared refractive indexes of silicon germanium and modified selenium glass," *Journal of the Optical Society of America*, vol. 47, no. 3, pp. 244–246, 1957.

[224] A. Kordts, M. Pfeiffer, H. Guo, V. Brasch, and T. J. Kippenberg, "Higher order mode suppression in high-Q anomalous dispersion SiN microresonators for temporal dissipative Kerr soliton formation," *Optics Letters*, vol. 41, no. 3, pp. 452–455, 2015.

[225] D. Montgomery, E. Peck, and G. Vining, *Introduction to Linear Regression Analysis*. Wiley, fifth ed., 2012.

[226] J. Ronnau, S. Haimov, and S. P. Gogineni, "The effect of signal-to-noise ratio on phase measurements with polarimetric radars," *Remote Sensing Reviews*, vol. 9, no. 1–2, pp. 27–37, 1994.

[227] F. L. Pedrotti, L. M. Pedrotti, and L. S. Pedrotti, *Introduction to Optics*. Cambridge University Press, third ed., 2017.

[228] S. Juds, *Photoelectric Sensors and Controls: Selection and Applications*. Taylor & Francis, 1988.

[229] R. J. Muenster, "FMCW: The future of lidar," 2019. Called on 02.06.2020 from *https://www.novuslight.com/fmcw-the-future-of-lidar_N9691.html*.

Journal publications

[J1] J. Gärtner, P. Trocha, R. Mandel, C. Koos, T. Jahnke, and W. Reichel, "Bandwidth and conversion efficiency analysis of dissipative Kerr soliton frequency combs based on bifurcation theory," *Physical Review A*, vol. 100, no. 3, p. 033819, 2019.

[J2] P. Trocha, J. Gärtner, P. Marin-Palomo, W. Freude, W. Reichel, and C. Koos, "Analysis of Kerr comb generation in silicon microresonators under the influence of two-photon absorption and fast free-carrier dynamics," *Physical Review A*, vol. 103, no. 6, p. 063515, 2021.

[J3] P. Trocha, M. Karpov, D. Ganin, M. H. P. Pfeiffer, A. Kordts, S. Wolf, J. Krockenberger, P. Marin-Palomo, C. Weimann, S. Randel, W. Freude, T. J. Kippenberg, and C. Koos, "Ultrafast optical ranging using microresonator soliton frequency combs," *Science*, vol. 359, no. 6378, pp. 887–891, 2018.

[J4] P. Trocha, J. Kemal, Q. Gaimard, G. Aubin, F. Lelarge, A. Ramdane, W. Freude, S. Randel, and C. Koos, "Ultra-fast optical ranging using quantum-dash mode-locked laser diodes," *Scientific Reports*, vol. 12, no. 1076, pp. 1–12, 2022.

[J5] P. Marin-Palomo, J. N. Kemal, M. Karpov, A. Kordts, J. Pfeifle, M. H. P. Pfeiffer, P. Trocha, S. Wolf, V. Brasch, M. H. Anderson, R. Rosenberger, K. Vijayan, W. Freude, T. J. Kippenberg, and C. Koos, "Microresonator-based solitons for massively parallel coherent optical communications," *Nature*, vol. 546, no. 7657, pp. 274–279, 2017.

[J6] P. Marin-Palomo, J. N. Kemal, P. Trocha, S. Wolf, K. Merghem, F. Lelarge, A. Ramdane, W. Freude, S. Randel, and C. Koos, "Comb-based

WDM transmission at 10 Tbit/s using a DC-driven quantum-dash mode-locked laser diode," *Optics Express*, vol. 27, no. 22, pp. 31110–31129, 2019.

[J7] J. N. Kemal, P. Marin-Palomo, V. Panapakkam, P. Trocha, S. Wolf, K. Merghem, F. Lelarge, A. Ramdane, S. Randel, W. Freude, and C. Koos, "Coherent WDM transmission using quantum-dash mode-locked laser diodes as multi- wavelength source and local oscillator," *Optics Express*, vol. 27, no. 22, pp. 31164–31175, 2019.

Conference publications

[C1] P. Marin-Palomo, J. N. Kemal, P. Trocha, S. Wolf, A. Kordts, and M. Karpov, "34.6 Tbit/s WDM transmission using soliton Kerr frequency combs as optical source and local oscillator," in *European Conference on Optical Communication*, pp. 415–417, 2016.

[C2] P. Marin-Palomo, J. Pfeifle, M. Karpov, P. Trocha, R. Rosenberger, K. Vijayan, S. Wolf, J. Kemal, A. Kordts, M. Pfeiffer, V. Brasch, W. Freude, T. J. Kippenberg, and C. Koos, "50 Tbit/s massively parallel WDM transmission in C and L band using interleaved cavity-soliton Kerr combs," in *Conference on Lasers and Electro-Optics*, p. STu1G.1, 2016.

[C3] C. Koos, T. J. Kippenberg, L. P. Barry, A. Ramdane, R. Brenot, W. Freude, S. Randel, P. Marin-Palomo, J. N. Kemal, P. Trocha, D. Ganin, C. Weimann, S. Wolf, J. Pfeifle, M. Karpov, A. Kordts, V. Vujicic, and K. Merghem, "Optical frequency combs and photonic integrated circuits – tools for high-speed communications and advanced distance metrology," in *SPIE Photonics West; Quantum Sensing and Nano Electronics and Photonics XV*, pp. 10540–74, SPIE, 2018.

[C4] C. Koos, S. Randel, W. Freude, T. J. Kippenberg, P. Marin-Palomo, J. N. Kemal, P. Trocha, D. Ganin, C. Weimann, S. Wolf, J. Pfeifle, M. Karpov, A. Kordts, and V. Vujicic, "Optical frequency combs: tools for high-speed communications and optical distance metrology," in *Sino-German Joint Symposium on Opto- and Microelectronic Devices and Circuits*, p. 17, 2018.

[C5] J. N. Kemal, P. Marin-Palomo, V. Panapakkam, P. Trocha, S. Wolf, K. Merghem, F. Lelarge, A. Ramdane, S. Randel, W. Freude, and C. Koos, "WDM transmission using quantum-dash mode-locked laser diodes as multi-wavelength source and local oscillator," in *Optical Fiber Communications Conference and Exhibition*, p. Th3F.6, 2017.

[C6] C. Koos, W. Freude, L. Dalton, T. J. Kippenberg, L. P. Barry, A. Ramdane, F. Lelarge, S. Wolf, H. Zwickel, M. Lauermann, C. Weimann, W. Hartmann, J. N. Kemal, P. Marin, P. Trocha, J. Pfeifle, T. Herr, V. Brasch, R. T. Watts, D. Elder, A. Martinez, V. Panapakkam, and N. Chimot, "Silicon-organic hybrid (SOH) devices and their use in comb-based communication systems," in *IEEE International Conference on Group IV Photonics*, p. ThC1, 2016.

[C7] C. Koos, T. J. Kippenberg, L. P. Barry, L. Dalton, A. Ramdane, F. Lelarge, W. Freude, J. N. Kemal, P. Marin, S. Wolf, P. Trocha, J. Pfeifle, C. Weimann, M. Lauermann, T. Herr, V. Brasch, R. T. Watts, D. Elder, A. Martinez, V. Panapakkam, and N. Chimot, "Multi-terabit/s transmission using chip-scale frequency comb sources," in *International Conference on Transparent Optical Networks*, p. We.A5.1, IEEE, 2016.

[C8] D. Ganin, P. Trocha, M. Pfeiffer, M. Karpov, A. Kordts, J. Krockenberger, P. Marin, S. Randel, W. Freude, T. J. Kippenberg, and C. Koos, "Ultrafast dual-comb distance metrology using dissipative Kerr solitons," in *Conference on Lasers and Electro-Optics*, p. STh4L.6, 2017.

[C9] C. Koos, T. J. Kippenberg, L. P. Barry, A. Ramdane, F. Lelarge, W. Freude, P. Marin, J. N. Kemal, C. Weimann, S. Wolf, P. Trocha, J. Pfeifle, M. Karpov, A. Kordts, V. Brasch, R. T. Watts, V. Vujicic, A. Martinez, V. Panapakkam, and N. Chimot in *SPIE Nonlinear Frequency Generation and Conversion: Materials and Devices XVI*, vol. 10090-15.

Glossary

List of abbreviations

ADC	Analogue-to-digital converter
ASE	Amplified spontaneous emission
ASIC	Application-specific integrated circuit
ATT	Attenuator
BD	Balanced photodetector
BS	Beam splitter
BSO	Bright dissipative Kerr soliton
CIRC	Circulator
CM	Calibration mirror
CMM	Coordinate measuring machine
COL	Collimator
CPW	Chopper wheel
CW	Continuous-wave
DC	Direct current
DFT	Discrete Fourier transform
DKS	Dissipative Kerr soliton
DSO	Dark dissipative Kerr soliton

DSP	Digital signal processing
EA	Electric amplifier
ECL	External cavity laser
EDFA	Erbium-doped fiber amplifier
ENOB	Effective number of bits
FC	Free carriers
FCA	Free-carrier absorption
FCD	Free-carrier density
FFT	Fast Fourier transform
FMCW	Frequency-modulated continuous-wave
FPGA	Field programmable gate array
FSR	Free spectral range
FWHM	Full width at half maximum
GVD	Group velocity dispersion
IANA	Institute for Analysis
IANM	Institute for Applied and Numerical Mathematics
IC	Intracavity
IMT	Institute of Microstructure Technology
IPQ	Institute of Photonics and Quantum Electronics
KIT	Karlsruhe Institute of Technology
LF	Lensed fiber
LiDAR	Light detection and ranging
LLE	Lugiato-Lefever equation
LO	Local oscillator

MEMS	Micro-electro-mechanical systems
MI	Modulation instability
MLL	Mode-locked laser
MLLD	Mode-locked laser diode
MR	Microresonator
NBC	Numeric bifurcation and continuation
ND	Neutral-density
NIR	Near-infrared
NLSE	Nonlinear Schrödinger equation
OCT	Optical coherence tomography
OSA	Optical spectrum analyzer
OSC	(Electric) oscillator
P-MOD	Phase modulator
PC	Polarization controller
PCE	Power conversion efficiency
PD	Photodiode
PDE	Partial differential equation
PIC	Photonic integrated circuit
PR	Photoreceiver
PSD	Power spectral density
QD	Quantum-dash
RBW	Resolution bandwidth
RCW	Rotating chopper wheel
RF	Radio frequency

RMS	Root mean square
RX	Receiver
SI	Signal
SLS	Swept laser source
SNR	Signal-to-noise power ratio
SOH	Silicon-organic-hybrid
SPD	Spectral power density
SPM	Self-phase modulation
SWI	Synthetic wavelength interferometry
TE	Transverse electric
TEC	Temperature controller
TM	Target mirror
ToF	Time of flight
TPA	Two-photon absorption
TX	Transmitter
VOA	Variable optical attenuator
WG	Waveguide
WPE	Wall-plug efficiency
XPM	Cross-phase modulation
XYZ	XYZ stage

Latin symbols

$\underline{a}(t', \tau')$	Amplitude of normalized optical field propagating in a microresonator
$\underline{a}_\mu(t')$, $\hat{\underline{a}}_\mu(t')$	Fourier coefficients of normalized field $\underline{a}$
A	Power $\left\lvert\underline{a}\right\rvert^2$ of normalized field
A_{beam}	Cross-sectional area of a free-space laser beam
A_{eff}	Effective mode field area
A_{illum}	Illuminated area on distance measurement target
A_{PD}	Photosensitive area of photodetector
B_{eval}	Evaluation bandwidth / rate of a ranging system for a distance data point
B_{meas}	Effective measurement bandwidth / rate of a ranging system after averaging of distance data points
c	Speed of light in a medium
$\underline{c}$	Complex constant function
c_0	Speed of light in vacuum: 299 792 458 $\frac{\mathrm{m}}{\mathrm{s}}$
d	Geometric free-space distance
d_{ua}	Geometric unambiguity distance
$D(d, d_0)$	Linear fit coefficient of a fit to a set of unwrapped phases
D_2	Second-order microresonator dispersion coefficient
D_λ	Second-order dispersion coefficient
$\hat{D}$	Dispersive operator
e	Euler's number: 2.718 281 828 . . .
$\mathbf{e}_z$	Unit vector along microresonator waveguide (z-) direction

$\underline{\mathbf{E}}$	Vectorial electric field components of optical signal
$\underline{E}, \underline{E}(t)$	Electric field amplitude of an optical signal
$\underline{E}_\mathrm{P}(t)$	Field envelope of a single pulse of a pulsed optical signal
$\hat{\underline{E}}, \hat{\underline{E}}(\omega)$	Fourier transform of $\underline{E}(t)$
$\hat{\underline{E}}_\mathrm{P}(t)$	Fourier transform of $\underline{E}_\mathrm{P}(t)$
$\underline{\mathcal{E}}, \underline{\mathcal{E}}(t)$	Complex amplitude of the electric field with unit $\sqrt{\mathrm{W}}$
$\underline{\mathcal{E}}(t,\tau)$, $\underline{\mathcal{E}}_z(z,\tau)$	Field envelope of electric field propagating in a waveguide / microresonator with unit $\sqrt{\mathrm{W}}$
$\underline{\mathcal{E}}_\mathrm{in}$	Amplitude of input pump field with unit $\sqrt{\mathrm{W}}$
$\underline{\mathcal{E}}_{\mathrm{r},\mu}(t)$	Electric field amplitude of optical signal oscillating at the resonance frequency $\omega_{\mathrm{r},\mu}$ of a microresonator with unit $\sqrt{\mathrm{W}}$
$\underline{\mathcal{E}}_\mu(t)$	Kerr comb mode oscillating in μth microresonator resonance with unit $\sqrt{\mathrm{W}}$
f	Frequency
f_ADC	Bandwidth of an analogue-to-digital (ADC) converter
f_CEO	Carrier-envelope offset frequency
f_rep	Pulse repetition rate of a pulsed optical signal
F	Normalized pump power or forcing coupled into a Kerr-nonlinear microresonator
F_n	Noise figure of an electric amplifier
F_th	Normalized threshold pump power or forcing for modulation instability in a Kerr-nonlinear microresonator
FWHM_a	Full width at half maximum
FWHM_i	Full width at half minimum

$\underline{g}$	Complex gain parameter of sidebands growing due to modulation instability in a pumped Kerr-nonlinear microresonator
g, g_{j}	Real part and imaginary part of gain parameter
G / G_{eff}	Gain / effective gain of an electric amplifier
$\underline{\mathbf{H}}$	Vectorial magnetic field components of optical signal
$\hbar$	Reduced Planck constant: $6.626\,070\,15 \times 10^{-34}/(2\pi)$ Js
i	Electric current
I	Intensity of an optical signal
I_{R}	Near-field intensity of reflected light on a reflecting surface
Id	Identity matrix
j	Imaginary unit: $\sqrt{-1}$
k_{B}	Boltzmann constant: $1.380\,649 \times 10^{-23}$ J/K
L	Radiance of reflected light on a reflecting surface
L_{MR}	Geometric circumference of a microresonator
L_{obj}	Optical path length of an object allowing for optical signal propagation
$L_{\mathrm{obj}}^{(\mathrm{g})}$	Geometric path length of an object allowing for optical signal propagation
$\hat{L}$	Linearized operator
M	Normalized spectral separation between the primary sidebands of an emerging Kerr comb and the pumped mode
n	Integer
n_0	Refractive index
n_2	Nonlinear refractive index
n_{air}	Refractive index of air: $\approx$ 1.000266 under ambient conditions

n_e	Effective refractive index
n_{eg}, n_g	(Effective) group refractive refractive index
N_{accept}	Number of accepted distance data points from a larger set of distance data points
N_{av}	Number of averaged distance data points used to obtain a single, more reliable distance data point
N_b	Number of beat notes used in a SWI scheme for the determination of a distance between a target and a ranging system
N_{car}	Free-carrier density
N'_{car}	Normalized free-carrier density
N_d	Number of distance measurements
N_{eval}	Number of pulses / number of pulse repetition periods used for the determination of a distance
N_{FC}	Number of lines of a frequency comb
N_p	Number of set positions of a mirror on a moving stage
$\hat{N}$	Nonlinear operator
p	Parameter of a curve parametrization
P	Power of an optical signal received by photodetector
$\underline{P}/\underline{P}(t)$	Amplitude of the polarization in a material
P_{beam}	Power of a free-space laser beam
$P_{beam,R}$	Power of a free-space laser beam after reflection at a surface
P_F	Far-field intensity of an optical signal
P_{FC}	Power of a frequency comb
P_{in}	Power of the pump field coupled in a Kerr-nonlinear microresonator

$P_{\mathrm{lin}}(t)$	Scalar linear polarization induced by a scalar electric field in a medium
$P_{\mathrm{n,shot}}$	Shot noise power in an electric receiver system
$P_{\mathrm{n,ther}}$	Thermal noise power in an electric receiver system
$P_{\mathrm{nl}}(t)$	Scalar nonlinear polarization induced by a scalar electric field in a medium
P_{th}	Power of pump field coupled in microresonator required for modulation instability
$P_{\mathrm{tot}}(t)$	Scalar total polarization induced by a scalar electric field in a medium
P_{μ}	Power of the μth mode of a frequency comb
q_{e}	Elementary charge: $1.602\,176\,634 \times 10^{-19}$C
Q	Microresonator quality factor
r	Normalized two-photon absorption parameter
r_{A}	Radius of the input aperture of an optical ranging system
$\mathcal{R}$	Photodetector responsivity
s	Normalized free-carrier cross-section
t	Physical time / slow time
t'	Normalized physical time / slow time
$\underline{t}$	Complex transmission coefficient of an optical waveguide coupler
t_{eff}	Free-carrier lifetime / dwell time in a waveguide
t'_{eff}	Normalized free-carrier lifetime / dwell time in a waveguide
t_{R}	Round-trip time of an optical signal in a microresonator
T	Temperature

T_{av}	Averaging period of a ranging system, inverse of its effective measurement rate B_{meas}
T_{eval}	Evaluation period of a ranging system required for measuring a distance, inverse of its evaluation bandwidth B_{eval}
T_{min}	Minimum acquisition time of a ranging system required for measuring a distance
T_{O}	Observation time defined in digital signal processing of a ranging system for the evaluation of multiple consecutive distances
T_{r}	Repetition period of a periodic (baseband) signal
U	Voltage
v'	Normalized group velocity of a field in a microresonator
v_{car}	Saturation drift velocity of free carriers in a *p*-*i*-*n*-junction
v_{D}	Drift velocity of an optical signal in a retarded time frame moving a the group velocity of the optical signal
v_{g}	Group velocity of an optical signal propagating in a waveguide
w	Width of a waveguide
x	Spatial coordinate
y	Spatial coordinate
z	Spatial coordinate, longitudinal coordinate in microresonator waveguide
z_{tar}	Position of a target mirror used in optical ranging experiments
Z	Impedance of an electric component
Z_0	Impedance of free space: 376.730 313 . . . Ω

Greek symbols

α	Coefficient of round-trip power-loss of an optical field due to linear waveguide losses in a microresonator
α_i	Power-loss coefficient of an optical waveguide accounting for linear propagation losses
$\beta, \beta(\omega)$	Propagation constant of an optical field in a waveguide
β'	Normalized second-order dispersion coefficient
$\beta^{(n)}$	nth Taylor-expansion coefficient of the propagation constant $\beta(\omega)$ / nth-order dispersion coefficient
β_{car}	Free-carrier dispersion parameter
β_{TPA}	Two-photon absorption parameter
γ	Nonlinearity parameter of a Kerr-nonlinear waveguide
Γ_{C}	Confinement factor of a transversal field distribution in a waveguide
$\delta(\omega)$	Dirac delta function
δ_0	Detuning, i.e., spectral separation of the frequency of pump light coupled in a Kerr-nonlinear microresonator and the center of the pumped microresonator resonance
$\delta_{\mu\nu}$	Kronecker-delta for indices μ, ν
$\delta\Phi_\mu(d)$	Phase difference of two beat notes generated on a measurement and a reference detector at frequency $\Delta\omega_\mu$ in a multi-heterodyne SWI ranging system
$\delta\omega_{\tilde{\mu}}$	Spectral shift of a microresonator resonance frequency $\omega_{\mathrm{r},\mu}$ caused by avoided mode crossings
Δf_{n}	Noise bandwidth of shot noise and thermal noise impairing multi-heterodyne SWI distance measurements

Δt	Slow-time (physical time) increment in time integrations of the Lugiato-Lefever equation
$\Delta t'$	Normalized slow-time (physical time) increment in time integrations of the normalized Lugiato-Lefever equation
$\Delta\tau, \Delta\tau_S$	Fast-time (intracavity coordinate) increment in time integrations of the Lugiato-Lefever equation in the retarded and stationary fast-time frame
$\Delta\tau', \Delta\tau'_S$	Normalized fast-time (intracavity coordinate) increment in time integration of the normalized Lugiato-Lefever equation in the retarded and stationary fast-time frame
$\Delta\Phi_\mu(d, d_0)$	Phase difference of two beat notes generated on a measurement and a reference detector at frequency ω_μ in a multi-heterodyne SWI ranging system, referenced with respect to a reference distance d_0
$\Delta\omega_\mu$, $\Delta\omega_{\mu,\mu'}$	Frequencies of beat notes caused by superposition of two frequency combs with frequencies ω_μ and $\omega_{\mu'}$ on a photodetector
$\Delta\omega_{FSR}$	Difference of free spectral ranges of two frequency combs
ϵ_0	Vacuum permittivity: $8.854\,187\,813\ldots \times 10^{-12}\,\frac{\mathrm{As}}{\mathrm{V\,m}}$
ϵ_r	Relative permittivity
ε	Root-mean-square (RMS) of errors of a linear fit to a set of unwrapped phase differences $\delta\Phi_\mu(d)$ or $\Delta\Phi_\mu(d, d_0)$ in a multi-heterodyne SWI ranging system
ε_{th}	Upper boundary the RMS error ε of each distance data point for allowing for its acceptance
$\varepsilon_{th,lo}$	Globally defined lowest value (lower limit) for local upper boundary $\varepsilon_{th,loc}$ of the RMS error ε
$\varepsilon_{th,loc}$	Local upper boundary of RMS error ε of each distance data point for its acceptance, neglecting global limits and an additional offset for ε_{th}

$\varepsilon_{\mathrm{th,o}}$	Constant offset added to the local upper boundary $\varepsilon_{\mathrm{th,loc}}$ of the RMS error ε
$\varepsilon_{\mathrm{th,up}}$	Globally defined upper value (upper limit) for local upper boundary $\varepsilon_{\mathrm{th,loc}}$ of the RMS error ε
ε_z	Distance error, i.e., the difference between the true distance and the measured distance between a target and a ranging system
ζ	Normalized detuning, i.e., spectral separation of the frequency of pump light coupled in a Kerr-nonlinear microresonator and the center of the pumped microresonator resonance
η	Normalized pump-to-frequency comb power conversion efficiency in a Kerr-nonlinear microresonator
η_{out}	Physical pump-to-comb power conversion efficiency in the bus waveguide attached to a Kerr-nonlinear microresonator
θ	Angular coordinate
θ_{C}	Power coupling coefficient between a bus waveguide and a microresonator
$\theta_{\mathrm{C,M}}$	Coupling coefficient of transverse mode families of a microresonator
κ	Integer
$\underline{\kappa}$	Complex coupling coefficient of an optical waveguide coupler
λ	Wavelength of an optical signal
Λ_{S}, $\Lambda_{\mathrm{S},\mu}$	Synthetic wavelength of an SWI ranging system
Λ	Eigenvalue
μ	Integer
ν	Integer
π	Pi: 3.141 592 654 . . .
ρ	Reflectivity of a surface

σ_{A}	Allan deviation
σ_{car}	Free-carrier cross-section
σ'_{car}	Normalized free-carrier cross-section
$\sigma_d^2, \sigma_{\overline{d}}^2$	Variance of a set of measured (and averaged) distances d
$\sigma_{d,\mathrm{shot}}^2$	Variance of a set of measured distances d induced by shot noise
$\sigma_{\mathrm{n,shot}}^2$	Variance of an electric current induced by shot noise
σ_r^2	Variance of a set of measured distances normalized to the squared unambiguity distance d_{ua}^2
σ_{ε_z}	Standard deviation of distance errors ε_z
σ_ϕ^2	Variance of a set of measured phases of an electric signal
τ, τ_{S}	Microresonator intracavity coordinate in a retarded (stationary) time frame
τ', τ'_{S}	Normalized microresonator intracavity coordinate in a retarded (stationary) time frame
ϕ_{n}	Phase noise of measured phase differences $\Delta\Phi_\mu(d, d_0)$
ϕ_μ	Normalized phase shift affecting μth Kerr comb mode over one round-trip in a Kerr-nonlinear microresonator, induced by an avoided mode crossing
Φ_μ	Phase of the μth beat note at frequency $\omega_{\mu,\,\mathrm{comb\,1}} - \omega_{\mu,\,\mathrm{comb\,2}}$ generated by the superposition of two combs on a photodetector
$\hat{\Phi}_{\mathrm{AMC}}$	Phase shift operator describing the accumulated phase shifts of all Kerr comb modes over one round-trip in a microresonator, induced by avoided mode crossings
$\hat{\Phi}'_{\mathrm{AMC}}$	Normalized shift operator describing the normalized accumulated phase shifts of all Kerr comb modes over one round-trip in a microresonator, induced by avoided mode crossings
φ	Angular coordinate

$\varphi(\mu)$	Phase accumulated by μth Kerr comb mode during one round-trip in a microresonator due to second-order dispersion and avoided mode crossings
$\varphi'(\mu)$	Normalized phase accumulated by μth Kerr comb mode during one round-trip in a microresonator due to second-order dispersion and avoided mode crossings
$\chi^{(n)}$	nth order nonlinear susceptibility
$\chi_{\mathrm{h}}^{(n)}$	nth order impulse response function
ω	Frequency of optical field
ω_{FSR}	Free spectral range of a frequency comb
ω_{p}	Frequency of the pump field coupled in Kerr-nonlinear microresonator
$\omega_{\mathrm{r},\mu}$	μth resonance frequency of a microresonator
$\omega_{\mathrm{r,FSR}}$	Free spectral range of the resonance frequencies of a microresonator around a given optical frequency
$\omega_{\Delta\mu}$	Frequency difference between the frequency ω_μ of the μth comb line of a Kerr comb and its pumped comb line $\omega_{\mathrm{p}} = \omega_0$
ω_μ	Frequency of the μth line of a frequency comb
Ω	Solid angle
Ω_{3dB}	3dB-comb bandwidth
Ω_{tot}	Total comb bandwidth

A Kerr comb dynamics

A.1 Parameter regions of modulation instability and thermal effects on comb formation

In practice Kerr combs are usually generated in microresonators with (at least partial) anomalous dispersion, since comb generation in normal-dispersive devices is more difficult [61]. Considering Eqs. (2.54) and (2.51) from Section 2.2.2, theoretically a positive gain $\Re\{\underline{g}(M)\} > 0$ can be observed for normal dispersion ($\beta' < 0$) for certain sidebands μ located at spectral positions $\mu = \pm M$, if the pump parameters ζ and F are chosen properly. In literature, thermal effects are said to play a crucial role on this difference between theory and experimental observations [61]. In this section, this statement is explained more in-depth using the normalized LLE, Eq. (2.45). An explanation is given, why modulation instability for normal dispersive microresonators is difficult to achieve even when excluding thermal effects and how thermal effects prevent comb formation experimentally.
According to Eq. (2.54), sidebands μ at $\mu = \pm M_{\max}$ with the highest gain are defined by the condition $\zeta + \beta' M_{\max}^2 - 2A = 0$, which leads to

$$M_{\max} = \sqrt{(2A - \zeta)/\beta'}. \tag{A.1}$$

Note that $M_{\max}$ is an integer, see Eq. (2.47), so in practice the (non-integer) expression on the r.h.s. of Eq. (A.1) has to be rounded to find the sidebands with the highest gain. Equation (A.1) implies that the following condition must be fulfilled such that the underlying ansatz for modulation instability is valid:

$$(2A - \zeta)/\beta' > 0. \tag{A.2}$$

For further investigation of this condition, we note that the intracavity power (IC) power $A = \left|\underline{a}_0\right|^2$ of a constant solution $\underline{a}_0$ of the LLE, Eq. (2.45), depends

on the detuning ζ, as well as the forcing F, see Eq. (2.51). A change of the IC power A caused by a changing detuning can always be compensated by an increase or decrease of the forcing F. Therefore, we consider A and ζ as independent parameters, whose combinations (ζ, A) may or may not fulfill the condition for MI defined in Eq. (A.2). For anomalous dispersion $\beta' > 0$, this leads to the condition $2A > \zeta$ for modulation instability. For normal dispersion $\beta' < 0$, one finds $\zeta > 2A$. Together with the necessary prequisite $A = 1$ for a positive real part g of the gain parameter, see Sec. 2.2.2, Eq. (2.56), this leads to the following regions of modulation instability in a (ζ, A) parameter space:

$$\beta' > 0: \quad 1 < \zeta/2 < A \tag{A.3}$$

$$\beta' < 0: \quad 1 < A < \zeta/2 \tag{A.4}$$

These regions of modulation instability are depicted in Fig. A.1 as blue (anomalous dispersion, $\beta' > 0$) and red (normal dispersion, $\beta' < 0$) shaded areas. In addition, several curves are depicted in gray that represent the IC power $A(\zeta)$ of constant solutions $\underline{a}_0(\zeta)$ for varying forcings F. These curves are obtained by numerically solving Eq. (2.51).

In an experiment or in a numeric time-integration of the LLE, specific points $(\zeta, A(\zeta))$ can be reached by, e.g., choosing a fixed pump power F and an initial pump frequency (detuning) ζ that is usually far off the s-shaped part of the curves depicted in Fig. A.1. Then, the detuning is increased or decreased, until a specific point $(\zeta, A(\zeta))$ has been reached that is within the regions of modulation instability. With this procedure, the center branch in the s-shaped region can however not be accessed. Furthermore, even if by any means a point on the center branch would be reached, small perturbations would lead to a drop to a state of the field to the lower branch, since the center branch is unstable [61]. The center branch is defined by the turning points of the curve $A(\zeta)$, where $\mathrm{d}A/\mathrm{d}\zeta$ diverges. The turning points can only occur, if for a given forcing F and a given ζ multiple values of the intracavity power A exist. In formal terms, this corresponds to the condition that the function $F(A, \zeta)$, given by Eq. (2.51), has the same value F for three different A and therefore there must be values for $A(\zeta)$ where $\mathrm{d}F/\mathrm{d}A = 0$:

$$\begin{aligned} \frac{\mathrm{d}F}{\mathrm{d}A} &= 1 + (\zeta - A)^2 + A\,(1 - 2\,(\zeta - A)) \\ &= 3A^2 - 4\zeta A + 1 + \zeta^2 = 0. \end{aligned} \tag{A.5}$$

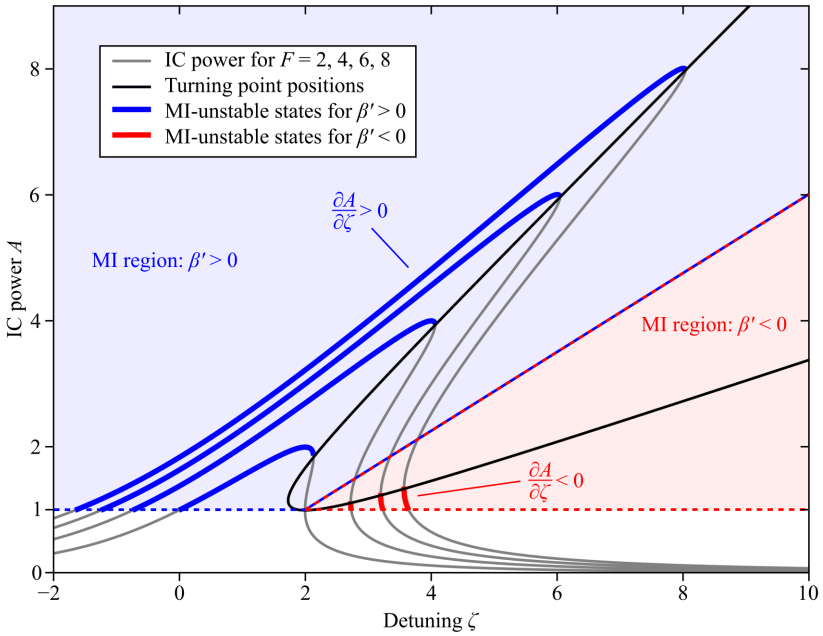

Figure A.1: Modulation instability regions for anomalous and normal dispersion defined by Eqs. (A.3) and (A.4) along with intracavity CW states for different forcings F. The blue-shaded area shows the parameter space (ζ, A) for which modulation instability can occur, provided that the microresonator features anomalous dispersion ($\beta' > 0$) and that the detuning ζ and the forcing F are chosen such that the power A of the IC field is within this area. In the same manner, the red shaded area indicates the region where MI can occur in a normal-dispersive microresonator ($\beta' < 0$). The gray lines show the intracavity power $A(\zeta)$ for different applied forcings $F = 2, 4, 6, 8$. Higher values for the forcing lead to a higher IC power $A(\zeta)$ for a given detuning ζ. The black curve marks turning points of the curves of $A(\zeta)$, where the curve transitions between three different branches. The center branch, located in the area framed by the black curve, cannot be accessed in time-integrations of the LLE or experimentally. Accessible states on the upper and the lower branch that are located in the MI regions are highlighted in blue and red. If the IC power $A(\zeta)$ field is located on these positions for a given detuning ζ, MI may occur, provided that the dispersion has the matching sign.

Equation (A.5) can be solved for A, which yields the curve of the upper turning points $(\zeta, A_+(\zeta))$ and the lower turning points $(\zeta, A_-(\zeta))$ of the curves $A(\zeta)$ depicted in Fig. A.1:

$$A_\pm(\zeta) = \frac{1}{3}\left(2\zeta \pm \sqrt{\zeta^2 - 3}\right). \tag{A.6}$$

Computing the turning point locations yields the black curve shown in Fig. A.1. Stable states of the IC power $A(\zeta)$ that can be accessed in time integrations of the LLE or in an experiment for different forcings F are located outside of this black framed area.

Therefore, the effective regions of modulation instability are reduced. In Figure A.1, blue and red sections on the gray curves $A(\zeta)$ mark points $(\zeta, A(\zeta))$ that lead to modulation instability for either anomalous or normal dispersion. One can see that for any F, the detuning range for normal dispersion allowing for MI is roughly two orders of magnitude smaller than the range for for anomalous dispersion. This explains why MI is difficult to achieve in time-integrations of the LLE for $\beta' < 0$. The pump parameters ζ and F have to be chosen very carefully.

Thermal effects occurring in an experiment can be considered in this formalism by considering the influence of temperature changes on the detuning ζ[1]. When light is coupled in a microresonator, its temperature T will increase due to absorption of light in the material. Mathematically, this can be expressed as $\partial T/\partial A > 0$ or equivalently $\partial A/\partial T > 0$. An increase of the temperature leads to an expansion of the microresonator, and as a result, the pumped resonance frequency $\omega_{\mathrm{r},0}$ will decrease. Consequently, the detuning, which given as $\zeta = (\omega_{\mathrm{r},0} - \omega_\mathrm{p})2t_\mathrm{R}/(\alpha_i L_\mathrm{MR} + \theta_\mathrm{C})$, will also decrease[2], and therefore we can write $\partial\zeta/\partial T < 0$, or $\partial T/\partial\zeta < 0$. Thus, there is a temperature-induced link between the IC power A and the detuning ζ, for which we can write $\partial A/\partial\zeta = \partial A/\partial T \; \partial T/\partial\zeta < 0$.

[1] Thermal effects can also be included in the LLE explicitly [80].

[2] Assuming critical coupling $\alpha_i L_\mathrm{MR} = \theta_\mathrm{C}$, the detuning reads $\zeta = (\omega_{\mathrm{r},0} - \omega_\mathrm{p})t_\mathrm{R}/(\alpha_i L_\mathrm{MR}) = (\omega_{\mathrm{r},0} - \omega_\mathrm{p})n_\mathrm{eg}/(\alpha_i c_0)$. Here, the temperature dependence of $n_\mathrm{eg}/(\alpha_i c_0)$ is negligible compared to the temperature dependence of $\omega_{\mathrm{r},0}$, according to experimentally observed behaviours.

This relation between A and ζ can now be compared to their dependence given by the nonlinear microresonator in the two different MI regions for normal and anomalous dispersion in Fig. A.1: For normal dispersion (red curves), the the derivative $\partial A/\partial\zeta$ has the same sign as the temperature dependence. This means that fluctuations of A induced by temperature fluctuations are reinforced by the nonlinearity of the system. As a result, IC states in the red region are unstable experimentally and the system will drift out of the (small) MI region. For the MI region for anomalous dispersion, the opposite holds: Here, IC power A is linked to the detuning ζ according to $\partial A/\partial\zeta > 0$ for essentially every part of all blue curves, except for very small regions right to their respective maxima $A_{\max} = \zeta$. Consequently, fluctuations of A induced by temperature changes are counter-balanced by the nonlinearity of the system. As a result, an equilibrium state of the IC power is possible, such that MI may occur for anomalous dispersion in presence of thermal effects.

A.2 Power spikes during soliton Kerr comb breakdown

In experiments, it was observed that single-soliton comb states may spontaneously break down in a laboratory environment. Possible reasons for this are slow thermal drifts or vibrations, which lead to a misalignment of the optics used for coupling pump light into the photonic chip containing Kerr-nonlinear microresonators and therefore a reduction of the available pump power. Measurements showed that a soliton breakdown is accompanied by a short, but very strong increase of the comb power (excluding the pump). Such power spikes may be harmful for optical devices, in which light of the soliton Kerr comb is coupled in.

In Figure A.2(a) top, the power of a soliton comb with suppressed pump, measured in an optical fiber following the Kerr-nonlinear microresonator, is depicted before, during and after a soliton breakdown. The peak in the center is the moment at which the soliton comb disappears. At that point in time, the comb power in the fiber increases from 5 dBm to 18 dBm for a period in the order of 1 μs. While such a power level is tolerable for most devices for a short period of time, the power spike effect becomes more severe when the soliton comb with suppressed pump is amplified in an EDFA. The power

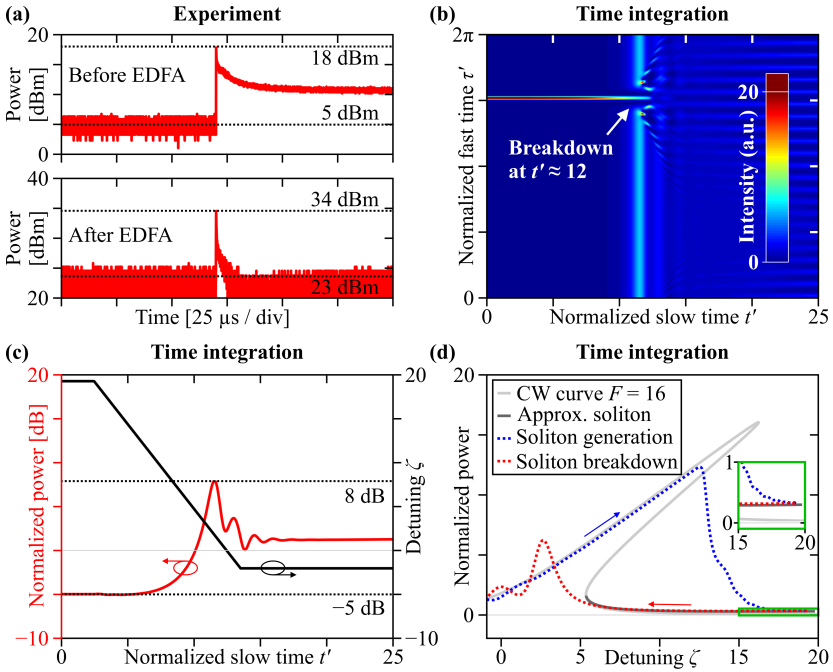

Figure A.2: Investigation of soliton-breakdown in Kerr-nonlinear microresonators accompanied by power-spikes. (a) Experimentally observed power spikes. Top: Comb power as a function of time, with the soliton breakdown in the center of the figure. Bottom: Same as top, but with the comb power monitored after the comb has been amplified in an EDFA. (b) – (d): Results of time integration of the LLE. (b) Evolution of IC field, plotted as a function of normalized fast time τ' describing the IC field distribution inside the microresonator and as a function of normalized slow time t'. At the beginning of the simulation, a single soliton located at $\tau' = 1.5\pi$ circulates in the cavity. Around $t' = 12$, the soliton breaks down. (c) Normalized IC power and detuning ζ as a function of normalized time t'. The soliton breakdown is accompanied by a strong increase of the IC power in the order of 10 dB, as the detuning is decreased over time. The forcing is kept constant at $F = 16$. (d) Soliton generation and breakdown on a map showing the mean IC power $(2\pi)^{-1} \int_0^{2\pi} \left|\underline{a}(t', \tau')\right|^2 \mathrm{d}\tau'$ as a function of the slow-time dependent detuning ζ. The light gray curve shows the CW curve $A(\zeta)$ for $F = 16$ based on Eq. (2.51) and the dark gray curve shows the analytical approximation for single-soliton states, see Eq. (2.59). The blue-dotted curve shows the transition of the IC field into a single-soliton state during initial single-soliton generation. The final state is located on the dark gray curve, as visible in the green zoom-in. The red-dotted curve shows the simulation already depicted in (b) and (c). As soon as the dark gray soliton branch ends and detuning is further decreased, a transition to the upper branch of the CW curve occurs, which is accompanied by a strong increase of the IC comb power.

spike during soliton breakdown can also be observed after amplification of the comb, as shown in Fig. A.2(a) bottom. Here, the power increases from 23 dBm to 34 dBm. Power levels of several Watts can damage optical devices even when applied only over short periods of time.

Time integrations of the LLE with F and ζ varying over time showed that a decreasing ζ will cause the break-down of a soliton and the associated increase of the IC power. This behaviour is depicted in Fig. A.2(b) and (c). In Figure A.2(b) the IC power distribution is plotted as a function of the normalized fast time τ' and normalized slow time t'. The initial IC state is a single soliton, as visible by the vertical power distribution at $t' = 0$. The forcing is set to $F = 16$ and the detuning decreased linearly over t', as depicted in black in A.2(c). Figure A.2(c) also shows the mean IC power $\frac{1}{2\pi}\int_0^{2\pi} \left|\underline{a}(t', \tau')\right|^2 \, \mathrm{d}\tau'$ as a function of normalized time t' in red. Around $t' = 12$, the soliton breaks down, and this is accompanied by a strong increase of the IC power from -5 dB, to 8 dB, see Fig. A.2(c), which is roughly the same increase as observed in the experiment. Increasing ζ, or changing the forcing F over time can also lead to the break-down of a soliton, however these do not show short increases of the IC power (not shown).

For a better understanding of the occurrence of this power spike, one can consider a map that shows the mean IC power as a function of the detuning ζ for different comb states, see Fig. A.2(d). Here, the curve of a constant field (CW curve), $\underline{a}(\tau') = \underline{a}_0$, is plotted in light gray and the curve of a single-soliton state $\underline{a}_{\mathrm{soliton}}$ in dark gray, assuming a forcing of $F = 16$ and varying values of ζ. The CW curve is again obtained by numerically solving Eq. (2.51) and the single-soliton curve is obtained by computing the power of the single-soliton states approximated by Eq. (2.59). For this, the field of the pumped mode $\underline{a}_0(\zeta, F)$ is obtained by numerically solving Eq. (2.48). The remaining expression on the r.h.s of Eq. (2.59) can computed for given parameters (ζ, F), with the soliton centered at $\tau'_0 = \pi$.

In Fig. A.2(d), the single-soliton curve (dark gray) is very close to the lower branch of the CW curve (light gray). The soliton curve reaches from the lower turning point of the CW curve near $\zeta \approx 5$ up to the maximum value that permits a single soliton $\zeta_{\mathrm{max}} = \pi^2 F/8 \approx 19.7$ [21]. The green inset shows a zoom to the region near the maximum detuning. It can be seen that the normalized power difference between the soliton curve and the CW curve amounts to less than 1 and therefore these curves nearly overlap in Fig. A.2(d).

The dotted curves show the mean IC power obtained from time integrations of the LLE. First, a single-soliton state is generated from a weak, random initial state by increasing the detuning from a negative value $\zeta < 0$ to positive values for a constant forcing $F = 16$, see blue-dotted curve. The IC power follows the CW curve, until modulation instability significantly alters the IC power around $\zeta = 13$. The IC field enters different comb states and remains constant, once it has reached the single-soliton state. The final IC power of this simulation is located closely to the theoretical obtained IC power of a single-soliton, see green zoom-in in Fig. A.2(d). From here, the soliton breakdown described in (b) and (c) is also visualized by a red-dotted curve in (d). For a decreasing detuning, the IC field follows the theoretically expected single-soliton IC power, as indicated by an overlap of the red-dotted curve and the dark gray curve. Near the lower turning point of the CW curve, which marks the end of the theoretical expected single-soliton curve, the time-integration IC power begins to transition to the upper branch of the CW curve. This transition is accompanied a strong increase of the comb, which is visible by an overshoot of the red-dotted curve over the CW curve in Figure A.2(d) around $\zeta = 3$.

These simulations show that the nonlinearity of the system likely causes the power-spike during a soliton-breakdown, when the detuning of the system is decreased. Noteworthy, it is not necessary to include any other effects such as, e.g., the influence of temperature changes or additional resonances to reproduce power spikes numerically.

B Bifurcation theory applied to the Lugiato-Lefever equation and properties of dissipative Kerr soliton combs

The text in this chapter has been published as appendix of the publication [J1]. It was adapted to fit the layout, structure and notation of this dissertation. This appendix assumes a negative time dependence of the optical signal of the form $\exp(-\mathrm{j}\omega t)$.

[Start of appendix of publication [J1]]

B.1 Identification of bifurcation branches

Here we derive the expression that allows us to identify bifurcation points on the curve of trivial solutions to the stationary LLE with Neumann boundary conditions:

$$-\beta' \frac{d^2}{d\tau'^2}\underline{a} - (\mathrm{j} - \zeta)\underline{a} - |\underline{a}|^2\underline{a} + \mathrm{j}\sqrt{F} = 0, \tag{B.1}$$

$$\frac{d\underline{a}}{d\tau'}(0) = \frac{d\underline{a}}{d\tau'}(\pi) = 0. \tag{B.2}$$

The structure of the solutions $\underline{a} : [0, \pi] \to \mathbb{C}$ near a point $\big(\zeta_0, \underline{a}_0(\zeta_0)\big)$ on the trivial curve depends on the properties of the linearized operator $\hat{L}$

$$\hat{L}\underline{a}_\phi := -\beta' \frac{d^2}{d\tau'^2}\underline{a}_\phi - (\mathrm{j} - \zeta_0)\underline{a}_\phi - 2|\underline{a}_0|^2\underline{a}_\phi - \underline{a}_0^2\overline{\underline{a}}_\phi, \tag{B.3a}$$

$$\frac{d\underline{a}_\phi}{d\tau'}(0) = \frac{d\underline{a}_\phi}{d\tau'}(\pi) = 0, \tag{B.3b}$$

where we write $\underline{a}_0$ instead of $\underline{a}_0(\zeta_0)$, but we keep the notation $\underline{a}_0(\zeta)$ whenever we want to stress the ζ-dependence of the trivial solution. We denote the kernel of the differential operator $\hat{L}$ by

$$\mathrm{Ker}\hat{L} = \{\underline{a}_\phi : \hat{L}\underline{a}_\phi = 0, \frac{d\underline{a}_\phi}{d\tau'}(0) = \frac{d\underline{a}_\phi}{d\tau'}(\pi) = 0\}$$

and its range by

$$\mathrm{Rg}\hat{L} = \{\hat{L}\underline{a}_\phi : \frac{d\underline{a}_\phi}{d\tau'}(0) = \frac{d\underline{a}_\phi}{d\tau'}(\pi) = 0\},$$

where the functions $\underline{a}_\phi : [0, \pi] \to \mathbb{C}$ are twice continuously differentiable. For such a function $\underline{a}_\phi \neq 0$, we denote by $\mathrm{span}\{\underline{a}_\phi\} = \{m\underline{a}_\phi : m \in \mathbb{R}\}$ the one-dimensional space of all real multiples of $\underline{a}_\phi$ and by $\mathrm{span}\{\underline{a}_\phi\}^\perp = \{\underline{\psi} : \int_0^\pi \underline{a}_\phi(x)\overline{\underline{\psi}}(x)\,dx = 0\}$ its L^2-orthogonal complement. Let us abbreviate the nonlinearity in Eq. (B.1) by $\mathcal{N}(\underline{a}) = |\underline{a}|^2\underline{a} - \mathrm{j}\sqrt{F}$. The derivative $D\mathcal{N}(\underline{a})\underline{z} := \frac{d}{dm}\mathcal{N}(\underline{a} + m\underline{z})|_{m=0} = 2|\underline{a}|^2\underline{z} + \underline{a}^2\overline{\underline{z}}$ for $\underline{a}, \underline{z} \in \mathbb{C}$ appeared in Eq. (B.3) in the definition of the linearized operator $\hat{L}$. It can also be written in the form

$$D\mathcal{N}(\underline{a})\underline{z} = \begin{pmatrix} 3(\Re\{\underline{a}\})^2 + (\Im\{\underline{a}\})^2 & 2\Re\{\underline{a}\}\Im\{\underline{a}\} \\ 2\Re\{\underline{a}\}\Im\{\underline{a}\} & (\Re\{\underline{a}\})^2 + 3(\Im\{\underline{a}\})^2 \end{pmatrix} \begin{pmatrix} \Re\{\underline{z}\} \\ \Im\{\underline{z}\} \end{pmatrix}. \tag{B.4}$$

Besides the linearized operator $\hat{L}$ given in Eq. (B.3), we also consider its adjoint operator,

$$\hat{L}^* \underline{a}_\phi = -\beta' \frac{d^2}{d\tau'^2} \underline{a}_\phi + (\mathrm{j} + \zeta_0) \underline{a}_\phi - \overline{DN(\underline{a}_0(\zeta_0))} \underline{a}_\phi, \tag{B.5a}$$

$$\frac{d\underline{a}_\phi}{d\tau'}(0) = \frac{d\underline{a}_\phi}{d\tau'}(\pi) = 0, \tag{B.5b}$$

which will be used below. Next we will compute the spaces $\mathrm{Ker}\hat{L}$, $\mathrm{Ker}\hat{L}^*$, which have the same finite dimension since both $\hat{L}$ and $\hat{L}^*$ are Fredholm operators. Owing to the Neumann boundary conditions, any element $\underline{a}_\phi \in \mathrm{Ker}\hat{L}$ can be expanded in the form $\underline{a}_\phi(\tau') = \sum_{\kappa=0}^{\infty} \underline{\alpha}_\kappa \cos(\kappa\tau')$. Since $\{\cos(\kappa\tau')\}_{\kappa\in\mathbb{N}_0}$ is a basis and $\hat{L}$ is linear the condition that $\underline{a}_\phi \in \mathrm{Ker}\hat{L}$ means that there is at least one integer $\mu \in \mathbb{N}_0$ such that $\hat{L}(\underline{\alpha}\cos(\mu\tau')) = (\beta'\mu^2 - \mathrm{j} + \zeta_0 - DN(\underline{a}_0))\underline{\alpha}\cos(\mu\tau') = 0$ for some $\underline{\alpha} = (\Re\{\underline{\alpha}\}, \Im\{\underline{\alpha}\}) \in \mathbb{C} \setminus \{0\}$. Using Eq. (B.4), it follows that $\beta'\mu^2$ must be an eigenvalue of the matrix

$$\mathrm{M}_{\underline{\alpha}} = \begin{pmatrix} -\zeta_0 + 3(\Re\{\underline{a}_0\})^2 + (\Im\{\underline{a}_0\})^2 & 2\Re\{\underline{a}_0\}\Im\{\underline{a}_0\} - 1 \\ 2\Re\{\underline{a}_0\}\Im\{\underline{a}_0\} + 1 & -\zeta_0 + (\Re\{\underline{a}_0\})^2 + 3(\Im\{\underline{a}_0\})^2 \end{pmatrix}, \tag{B.6}$$

with eigenvector $\underline{\alpha}$. Nonzero elements in $\mathrm{Ker}\hat{L}$ exist if $\det(-\beta'\mu^2\mathrm{Id} + \mathrm{M}_{\underline{\alpha}}) = 0$ and computing this determinant yields

$$(\zeta_0 + \beta'\mu^2)^2 - 4|\underline{a}_0(\zeta_0)|^2(\zeta_0 + \beta'\mu^2) + 1 + 3|\underline{a}_0(\zeta_0)|^4 = 0. \tag{B.7}$$

Solving for μ leads to $\mu_{1,2}$, given by the following equation:

$$\mu_{1,2} := \sqrt{\frac{2|\underline{a}_0(\zeta_0)|^2 - \zeta_0 \pm \sqrt{|\underline{a}_0(\zeta_0)|^4 - 1}}{\beta'}}. \tag{B.8}$$

Likewise, nonzero elements in $\mathrm{Ker}\hat{L}^*$ exist if $\det(-\beta'\tilde{\mu}^2\mathrm{Id} + \mathbf{M}_{\underline{\alpha}}^T) = 0$ for some integer $\tilde{\mu} \in \mathbb{N}_0$. Since $\det(-\beta'\tilde{\mu}^2\mathrm{Id} + \mathbf{M}_{\underline{\alpha}}^T) = \det(-\beta'\tilde{\mu}^2\mathrm{Id} + \mathbf{M}_{\underline{\alpha}})$, this leads to the same formula Eq. (B.8) for $\tilde{\mu}_{1,2}$. In the remaining part of this section, we write μ as a shorthand for one of the two values $\mu_{1,2}$. Consequently, under

the condition from Eq. (B.7) there is a vector $\underline{\alpha}$ and a vector $\underline{\alpha}^*$ such that $\underline{\alpha}\cos(\mu\tau') \in \mathrm{Ker}\hat{L}$ and $\underline{\alpha}^*\cos(\mu\tau') \in \mathrm{Ker}\hat{L}^*$.

Now we determine $\underline{\alpha}$ and $\underline{\alpha}^*$ under the condition from Eq. (B.7). In the matrix $\mathbf{M}_{\underline{\alpha}} - \beta'\mu^2\mathrm{Id}$, the first or the second line could be zero (but not both). Therefore, the eigenvector $\underline{\alpha}$ of the matrix in Eq. (B.6) is given in the form

$$\underline{\alpha} = \begin{pmatrix} 2\Re\{\underline{a}_0\}\Im\{\underline{a}_0\} - 1 \\ \zeta + \beta'\mu^2 - 3(\Re\{\underline{a}_0\})^2 - (\Im\{\underline{a}_0\})^2 \end{pmatrix} \text{ or}$$
$$\underline{\alpha} = \begin{pmatrix} \zeta + \beta'\mu^2 - (\Re\{\underline{a}_0\})^2 - 3(\Im\{\underline{a}_0\})^2 \\ 2\Re\{\underline{a}_0\}\Im\{\underline{a}_0\} + 1 \end{pmatrix}, \tag{B.9}$$

such that $(-\beta'\mu^2\mathrm{Id} + \mathbf{M}_{\underline{\alpha}})\underline{\alpha} = 0$, and hence $\underline{\alpha}\cos(\mu\tau')$ belongs to $\mathrm{Ker}\hat{L}$. The first choice can be taken if $2\Re\{\underline{a}_0\}\Im\{\underline{a}_0\} - 1 \neq 0$ and the second choice if $2\Re\{\underline{a}_0\}\Im\{\underline{a}_0\} + 1 \neq 0$. Likewise,

$$\underline{\alpha}^* = \begin{pmatrix} \zeta + \beta'\mu^2 - (\Re\{\underline{a}_0\})^2 - 3(\Im\{\underline{a}_0\})^2 \\ 2\Re\{\underline{a}_0\}\Im\{\underline{a}_0\} - 1 \end{pmatrix} \text{ or}$$
$$\underline{\alpha}^* = \begin{pmatrix} 2\Re\{\underline{a}_0\}\Im\{\underline{a}_0\} + 1 \\ \zeta + \beta'\mu^2 - 3(\Re\{\underline{a}_0\})^2 - (\Im\{\underline{a}_0\})^2 \end{pmatrix}, \tag{B.10}$$

with $\underline{\alpha}^* = (\Re\{\underline{\alpha}^*\}, \Im\{\underline{\alpha}^*\}) \in \mathbb{C}$ satisfies $(-\beta'\mu^2\mathrm{Id} + \mathbf{M}^T_{\underline{\alpha}})\underline{\alpha}^* = 0$ and leads to an element $\underline{\alpha}^*\cos(\mu\tau') \in \mathrm{Ker}\hat{L}^*$. As before, the first choice can be taken if $2\Re\{\underline{a}_0\}\Im\{\underline{a}_0\} - 1 \neq 0$ and the second choice if $2\Re\{\underline{a}_0\}\Im\{\underline{a}_0\} + 1 \neq 0$.
We can exclude the case $\mu_1 = 0$ or $\mu_2 = 0$ in the bifurcation condition from Eq. (B.7) since it would only lead to bifurcation of trivial solutions, and we are interested in nontrivial solutions. The kernel of $\hat{L}$ will be one-dimensional provided that in Eq. (B.7) we have $\mu_1 \in \mathbb{N}$ and $\mu_2 \notin \mathbb{N}$ or vice versa, and two-dimensional if both $\mu_1, \mu_2 \in \mathbb{N}$. If neither μ_1 or μ_2 are in $\mathbb{N}$, then $\mathrm{Ker}\hat{L} = \mathrm{Ker}\hat{L}^* = \{0\}$, and the implicit function theorem (cf. Ref. [131], Theorem I.1.1]) implies that solutions nearby the point $(\zeta_0, \underline{a}_0)$ are unique, and therefore trivial. Hence, $(\zeta_0, \underline{a}_0)$ cannot be a bifurcation point in this case, and therefore the necessary bifurcation condition is that $\mu_1 \in \mathbb{N}$ or $\mu_2 \in \mathbb{N}$. The same condition, expressed in the form of Eq. (B.7), is given in Ref. [125], Proposition 10.

B.2 Transversality condition

According to the Crandall-Rabinowitz theorem (cf. Refs. [219], Theorem I.5.1 and [131]), two conditions are sufficient for bifurcation. The first is that $\mathrm{Ker}\hat{L}$ is one-dimensional, i.e., with μ_1, μ_2 from Eq. (B.8), we need that $\mu_1 \in \mathbb{N}$, $\mu_2 \notin \mathbb{N}$ or vice versa, and we write μ for the one which is the integer. As we will see, the second condition (the transversality condition) is given by

$$2|\underline{a}_0(\zeta_0)|^4(|\underline{a}_0(\zeta_0)|^2 - \zeta_0) \mp (1 + \zeta_0^2 - |\underline{a}_0(\zeta_0)|^4)\sqrt{|\underline{a}_0(\zeta_0)|^4 - 1} \neq 0 \quad \text{(B.11)}$$

with "−" if $\mu_1 \in \mathbb{N}$ and "+" if $\mu_2 \in \mathbb{N}$. To verify that Eq. (B.11) together with the one-dimensionality of the kernel is really sufficient for bifurcation, we need to bring our problem into the form used in Ref. [219]. Nontrivial solutions of Eqs. (B.1) and (B.2) may be written as

$$\underline{a}(\tau') = \underline{a}_0(\zeta) + \underline{b}(\tau') \quad \text{with} \quad \frac{d\underline{b}}{d\tau'}(0) = \frac{d\underline{b}}{d\tau'}(\pi) = 0.$$

From Eqs. (B.1) and (B.2), we derive the equation for the function $\underline{b}$ in the form

$$F(\zeta, \underline{b}) := -\beta' \frac{d^2}{d\tau'^2}\underline{b} - (\mathrm{j} - \zeta)(\underline{a}_0(\zeta) + \underline{b}) - \mathcal{N}(\underline{a}_0(\zeta) + \underline{b}) = 0, \quad \text{(B.12)}$$

where $F(\zeta, \underline{b})$ is defined on $\mathbb{R} \times H$ with H given as the real Hilbert space of twice almost everywhere differentiable functions

$$\underline{b} : [0, \pi] \to \mathbb{C} \quad \text{with} \quad \frac{d\underline{b}}{d\tau'}(0) = \frac{d\underline{b}}{d\tau'}(\pi) = 0$$

and $\underline{b}$, $d^2\underline{b}/d\tau'^2$ being square integrable. Notice that $F(\zeta, 0) = 0$ for all ζ, i.e., the curve of trivial solutions $(\zeta, \underline{a}_0(\zeta))$ for Eqs. (B.1) and (B.2) has now become the line of zero solutions $(\zeta, 0)$ for Eq. (B.12). Let us write $D^2_{\underline{b},\zeta}F(\zeta_0, 0)$ for the mixed second derivative of $F(\zeta, \underline{b})$ with respect to $\underline{b}$ and ζ at the point

$(\zeta_0, 0)$. In our case, where $F(\zeta, \underline{b})$ is defined by Eq. (B.12), we find for the mixed second derivative

$$\begin{aligned} D^2_{\underline{b},\zeta} F(\zeta_0, 0)\underline{a}_\phi =& \underline{a}_\phi - D^2\mathcal{N}(\underline{a}_0)(\underline{a}_\phi, \dot{a}_0) \\ =& \underline{a}_\phi - 2\overline{\underline{a}}_0 \underline{a}_\phi \dot{a}_0 - 2\underline{a}_0 \underline{a}_\phi \overline{\dot{\underline{a}}_0} - 2\underline{a}_0 \overline{\underline{a}_\phi} \dot{a}_0, \end{aligned} \tag{B.13}$$

where $\underline{\dot{a}}_0 = \frac{d}{d\zeta}\underline{a}_0(\zeta)|_{\zeta=\zeta_0}$ is the tangent direction along the curve $\zeta \mapsto \underline{a}_0(\zeta)$ at the point ζ_0. According to Ref. [219], the transversality condition is expressed by

$$D^2_{\underline{b},\zeta} F(\zeta_0, 0)\underline{a}_\phi \notin \mathrm{Rg}(D_{\underline{b}} F(\zeta_0, 0)),$$

with $\underline{a}_\phi$ such that $\mathrm{Ker}(D_{\underline{b}} F(\zeta_0, 0)) = \mathrm{span}\{\underline{a}_\phi\}$. In our case, $D_{\underline{b}} F(\zeta_0, 0) = \hat{L}$, where $\hat{L}$ is the linearized operator given in Eq. (B.3). By the Fredholm alternative, cf. Ref. [220], $\mathrm{Rg}\hat{L} = (\mathrm{Ker}\hat{L}^*)^\perp = \mathrm{span}\{\underline{a}^*_\phi\}^\perp$, where $\underline{a}_\phi(\tau') = \underline{\alpha}\cos(\mu\tau')$, $\underline{a}^*_\phi(\tau') = \underline{\alpha}^*\cos(\mu\tau')$ with $\underline{\alpha}$ from Eqs. (B.9) and $\underline{\alpha}^*$ from Eqs. (B.10). Here orthogonality $\underline{u} \perp \underline{v}$ of two functions $\underline{u}, \underline{v} \in H$ is understood as vanishing of the inner product $\langle \underline{u}, \underline{v} \rangle = \Re\{\int_0^\pi \underline{u}(\tau')\overline{\underline{v}}(\tau')\,\mathrm{d}\tau'\}$. Hence, transversality is expressed as

$$\langle D^2_{\underline{b},\zeta} F(\zeta_0, 0)\underline{a}_\phi, \underline{a}^*_\phi \rangle = \Re\left\{\int_0^\pi \left(D^2_{\underline{b},\zeta} F(\zeta_0, 0)\underline{a}_\phi\right)\overline{\underline{a}^*_\phi}\,\mathrm{d}\tau'\right\} \neq 0, \tag{B.14}$$

and we will show next that this amounts to

$$\begin{aligned} \langle D^2_{\underline{b},\zeta} F(\zeta_0, 0)\underline{a}_\phi, \underline{a}^*_\phi \rangle =& \frac{-\pi(2\Re\{\underline{a}_0\}\Im\{\underline{a}_0\} \mp 1)}{3|\underline{a}_0|^4 - 4|\underline{a}_0|^2\zeta_0 + \zeta_0^2 + 1} \\ & \times \Big((\beta'\mu^2 - \zeta_0)|\underline{a}_0|^4 + (\zeta_0^2 + 1)(2|\underline{a}_0|^2 - \beta'\mu^2 - \zeta_0\Big). \end{aligned} \tag{B.15}$$

To evaluate $D^2_{\underline{b},\zeta} F(\zeta_0, 0)\underline{a}_\phi$, we first need to determine the tangent $\underline{\dot{a}}_0 = \frac{d}{d\zeta}\underline{a}_0(\zeta)|_{\zeta=\zeta_0}$. Differentiating the equation $(\mathrm{j} - \zeta)\underline{a}_0(\zeta) + \mathcal{N}(\underline{a}_0(\zeta)) = 0$ with respect to ζ and evaluating the derivative at ζ_0, we get

$$\big(D\mathcal{N}(\underline{a}_0) + \mathrm{j} - \zeta_0\big)\underline{\dot{a}}_0 = \underline{a}_0.$$

Recalling that $D\mathcal{N}(\underline{a}_0)\underline{z} = 2|\underline{a}_0|^2\underline{z} + \underline{a}_0^2\overline{\underline{z}}$, we thus find

$$(2|\underline{a}_0|^2 + \mathrm{j} - \zeta_0)\dot{\underline{a}}_0 + \underline{a}_0^2\overline{\dot{\underline{a}}_0} = \underline{a}_0$$

and hence

$$\dot{\underline{a}}_0 = \underline{\mathcal{T}}\,\underline{a}_0 \quad \text{with} \quad \underline{\mathcal{T}} = \frac{|\underline{a}_0|^2 - \zeta_0 - \mathrm{j}}{3|\underline{a}_0|^4 - 4|\underline{a}_0|^2\zeta_0 + \zeta_0^2 + 1}. \tag{B.16}$$

Inserting $\dot{\underline{a}}_0$ from Eq. (B.16) into Eq. (B.13), we deduce that the transversality condition Eq. (B.14) becomes

$$\langle D^2_{\underline{b},\zeta} F(\zeta_0, 0)\underline{a}_\phi, \underline{a}^*_\phi\rangle = \frac{\pi}{2}\Re\left\{\underline{\alpha}\,\overline{\underline{\alpha}^*} - 4\Re\{\underline{\mathcal{T}}\}|\underline{a}_0|^2\underline{\alpha}\,\overline{\underline{\alpha}^*} - 2\underline{\mathcal{T}}\,\underline{a}_0^2\overline{\underline{\alpha}}\,\overline{\underline{\alpha}^*}\right\} \neq 0. \tag{B.17}$$

Depending on the alternatives in Eqs. (B.9) and (B.10) for the actual form of $\underline{\alpha}, \underline{\alpha}^*$, we obtain

$$\Re\left\{\underline{\alpha}\,\overline{\underline{\alpha}^*}\right\} = (2\Re\{\underline{a}_0\}\Im\{\underline{a}_0\} \mp 1)(2\zeta_0 + 2\beta'\mu^2 - 4|\underline{a}_0|^2).$$

Likewise,

$$\begin{aligned}
&\overline{\underline{\alpha}}\,\overline{\underline{\alpha}^*}\\
=&(2\Re\{\underline{a}_0\}\Im\{\underline{a}_0\} \mp 1)\left(\zeta_0 + \beta'\mu^2 - (\Re\{\underline{a}_0\})^2 - 3(\Im\{\underline{a}_0\})^2\right)\\
&- (2\Re\{\underline{a}_0\}\Im\{\underline{a}_0\} \mp 1)\left(\zeta_0 + \beta'\mu^2 - 3(\Re\{\underline{a}_0\})^2 - (\Im\{\underline{a}_0\})^2\right)\\
&- \mathrm{j}\Big((2\Re\{\underline{a}_0\}\Im\{\underline{a}_0\} \mp 1)^2\\
&+ \Big(\zeta_0 + \beta'\mu^2 - 3(\Re\{\underline{a}_0\})^2 - (\Im\{\underline{a}_0\})^2\Big)\\
&\quad \underbrace{\times \Big(\zeta_0 + \beta'\mu^2 - (\Re\{\underline{a}_0\})^2 - 3(\Im\{\underline{a}_0\})^2\Big)\Big)}_{\overset{\text{Eq. B.7}}{=} 4(\Re\{\underline{a}_0\})^2(\Im\{\underline{a}_0\})^2 - 1}\\
=&(2\Re\{\underline{a}_0\}\Im\{\underline{a}_0\} \mp 1)2\overline{\underline{a}_0}^2,
\end{aligned}$$

where we have used the necessary bifurcation condition from Eq. (B.7). Taking the expressions for $\Re\{\underline{\alpha}\,\overline{\underline{\alpha}^*}\}$ and $\overline{\underline{\alpha}}\,\overline{\underline{\alpha}^*}$ the transversality condition from Eq (B.17) finally leads to

$$\begin{aligned}\langle D^2_{\underline{b},\zeta} F(\zeta_0,0)\underline{a}_\phi, \underline{a}^*_\phi\rangle =& \frac{\pi}{2}\Re\left\{\underline{\alpha}\,\overline{\underline{\alpha}^*} - 4\Re\{\underline{\mathcal{T}}\}|\underline{a}_0|^2\underline{\alpha}\,\overline{\underline{\alpha}^*} - 2\underline{\mathcal{T}}\,\underline{a}_0^2\overline{\underline{\alpha}}\,\overline{\underline{\alpha}^*}\right\}\\ =& \frac{\pi}{2}(2\Re\{\underline{a}_0\}\Im\{\underline{a}_0\} \mp 1)\Big((2\zeta_0 + 2\beta'\mu^2 - 4|\underline{a}_0|^2)\\ &\times(1 - 4\Re\{\underline{\mathcal{T}}\}|\underline{a}_0|^2) - 4\Re\{\underline{\mathcal{T}}\}|\underline{a}_0|^4\Big) \neq 0.\end{aligned}$$

Since the choices in Eqs. (B.9) and (B.10) were made such that the factor $(2\Re\{\underline{a}_0\}\,\Im\{\underline{a}_0\} \mp 1)$ is nonzero, the nonvanishing of the expression in brackets amounts to (after inserting $\Re\{\underline{\mathcal{T}}\} = (|\underline{a}_0|^2 - \zeta_0)/(3|\underline{a}_0|^4 - 4|\underline{a}_0|^2\zeta_0 + \zeta_0^2 + 1)$)

$$(\beta'\mu^2 - \zeta_0)|\underline{a}_0|^4 + (\zeta_0^2 + 1)(2|\underline{a}_0|^2 - \beta'\mu^2 - \zeta_0) \neq 0.$$

We have therefore verified Eq. (B.15), and using the definition μ_1, μ_2 from Eq. (B.8), we obtain the transversality condition in its final form Eq. (B.11), where only $\underline{a}_0$ and ζ_0 appear.

B.3 Approximations for the bright-soliton power conversion efficiency and comb bandwidth

For BSOs, a closed form approximation [21, 136–139] of the intracavity field is given by

$$\underline{a}(\tau') \approx \underline{a}_0 + \underline{a}_{\mathrm{BSO}}(\tau') = \underline{a}_0 + B\mathrm{e}^{\mathrm{j}\varphi_{0,\mathrm{BSO}}}\operatorname{sech}\left(\frac{B}{\sqrt{2\beta'}}\tau'\right). \tag{B.18}$$

Here, $\underline{a}_{\mathrm{BSO}}(\tau')$ represents the field of a BSO on top of a constant background field $\underline{a}_0$, $B \approx \sqrt{2\zeta}$ defines the width and the amplitude of the soliton, and $\varphi_{0,\mathrm{BSO}} = \arccos(\sqrt{8\zeta}/(\pi\sqrt{F}))$ is the relative phase of the soliton with respect to $\underline{a}_0$. For strong solitons, the intracavity field will be dominated by the soliton itself, such that $\underline{a}(\tau') \approx \underline{a}_{\mathrm{BSO}}(\tau')$. For a given forcing, the maximum detuning can be derived by the condition that the argument of the arccos function may not

exceed 1, cf. supplementary information in Ref. [21]. With maximum detuning $\zeta_{\max} = \pi^2 F/8$, $\varphi_{0,\mathrm{BSO}} = 0$, we find that the intracavity field reads

$$\underline{a}(\tau') \approx \frac{\pi}{2}\sqrt{F}\,\mathrm{sech}\left(\frac{\pi}{2}\sqrt{\frac{F}{2\beta'}}\tau'\right). \tag{B.19}$$

Given this expression, the power conversion efficiency at the maximum detuning for BSOs can be computed by an integral in the spatial domain:

$$\begin{aligned}\eta_{\mathrm{BSO,max}} =& \frac{\frac{1}{2\pi}\int_{-\pi}^{\pi}\left|\frac{\pi}{2}\sqrt{F}\,\mathrm{sech}\left(\frac{\pi}{2}\sqrt{\frac{F}{2\beta'}}\tau'\right)\right|^2 \mathrm{d}\tau'}{F}\\ =& \sqrt{\frac{\beta'}{2F}}\tanh\left(\frac{\pi}{2}\sqrt{\frac{F}{2\beta'}}\pi\right) \approx \sqrt{\frac{\beta'}{2F}}.\end{aligned} \tag{B.20}$$

To determine the comb bandwidth, we calculate the Fourier coefficients associated with the various comb lines. The power spectrum is given by the magnitude square of these coefficients:

$$\begin{aligned}\left|\underline{a}_\mu\right|^2 =& \left|\frac{1}{2\pi}\int_{-\pi}^{\pi}\frac{\pi}{2}\sqrt{F}\,\mathrm{sech}\left(\frac{\pi}{2}\sqrt{\frac{F}{2\beta'}}\tau'\right)\mathrm{e}^{-\mathrm{j}\mu\tau'}\,\mathrm{d}\tau'\right|^2\\ \approx& \left|\frac{1}{2\pi}\int_{-\infty}^{\infty}\frac{\pi}{2}\sqrt{F}\,\mathrm{sech}\left(\frac{\pi}{2}\sqrt{\frac{F}{2\beta'}}\tau'\right)\mathrm{e}^{-\mathrm{j}\mu\tau'}\,\mathrm{d}\tau'\right|^2\\ =& \frac{\beta'}{2}\mathrm{sech}^2\left(\sqrt{\frac{2\beta'}{F}}\mu\right).\end{aligned} \tag{B.21}$$

The (FWHM$_a$) bandwidth x_{FWHM} of the sech^2 function is given by the condition

$$\mathrm{sech}^2\left(\frac{x_{\mathrm{FWHM}}}{2}\right) = \frac{1}{2}, \tag{B.22}$$

which leads to $x_{\mathrm{FWHM}} = 2\ln\left(1+\sqrt{2}\right)$. This leads to the FWHM bandwidth $2\mu^{\star}_{\mathrm{BSO,max}}$,

$$2\mu^{\star}_{\mathrm{BSO,max}} = \sqrt{\frac{F}{2\beta'}}x_{\mathrm{FWHM}} = \sqrt{\frac{2F}{\beta'}}\ln\left(1+\sqrt{2}\right). \tag{B.23}$$

For a representation of the Eqs. (B.20) and (B.23) in physical, i.e., non-normalized units, see, e.g., Refs. [136, 137].

B.4 Physical power conversion efficiency outside of the microresonator

In physical terms, the time-dependent LLE [77] is given by

$$\begin{aligned} t_{\mathrm{R}}\frac{\partial\underline{\mathcal{E}}^{*}(t,\tau)}{\partial t} =& \sqrt{\theta_{\mathrm{C}}}\sqrt{P_{\mathrm{in}}} + \left(-\frac{\alpha+\theta_{\mathrm{C}}}{2} - \mathrm{j}\delta_0\right)\underline{\mathcal{E}}^{*}(t,\tau) \\ &+ \left(-\mathrm{j}\frac{\beta^{(2)}}{2}L_{\mathrm{MR}}\frac{\partial^2}{\partial\tau^2} + \mathrm{j}\gamma L_{\mathrm{MR}}\left|\underline{\mathcal{E}}^{*}(t,\tau)\right|^2\right)\underline{\mathcal{E}}^{*}(t,\tau). \end{aligned} \tag{B.24}$$

Here, t_{R} is the round-trip time of light circulating in the resonator, $\underline{\mathcal{E}}^{*}$ the electric field, t the physical time, τ the round-trip position inside the resonator, θ_{C} the power-coupling coefficient of the bus waveguide and the microresonator, P_{in} the power of the pump light, α the power round-trip loss, $\beta^{(2)}$ the second order dispersion coefficient, L_{MR} the circumference, and γ the nonlinearity coefficient of the microresonator. The detuning $\delta_0 = \left(\omega_{\mathrm{r},0} - \omega_{\mathrm{p}}\right)t_{\mathrm{R}}$ is defined by the difference between the angular frequency of the pump laser ω_{p}, the angular resonance frequency $\omega_{\mathrm{r},0}$ and the round-trip time.
The normalized field $\underline{a}(t',\tau')$ for $\tau' \in [0, 2\pi)$ and the normalized quantities ζ and β' satisfy the time-dependent normalized LLE,

$$\frac{\partial\underline{a}(t',\tau')}{\partial t'} = \sqrt{F} + \left(-1 - \mathrm{j}\zeta + \mathrm{j}\beta'\frac{\partial^2}{\partial\tau'^2} + \mathrm{j}|\underline{a}(t',\tau')|^2\right)\underline{a}(t',\tau'), \tag{B.25}$$

and are related to the physical parameters $\underline{\mathcal{E}}^*$ and P_{in}, γ, α, θ_{C}, δ_0, t_{R} and $\beta^{(2)}$ via

$$\underline{a}(t',\tau') = \sqrt{\frac{2\gamma L_{\mathrm{MR}}}{\alpha+\theta_{\mathrm{C}}}}\,\underline{\mathcal{E}}^*(t,\tau) \tag{B.26}$$

$$t' = \frac{\alpha+\theta_{\mathrm{C}}}{2}\frac{t}{t_{\mathrm{R}}}, \tag{B.27}$$

$$\tau' = \frac{2\pi}{t_{\mathrm{R}}}\tau, \tag{B.28}$$

$$\sqrt{F} = \sqrt{\frac{2\gamma L_{\mathrm{MR}}}{\alpha+\theta_{\mathrm{C}}}}\,\frac{2\sqrt{\theta_{\mathrm{C}}}}{\alpha+\theta_{\mathrm{C}}}\sqrt{P_{\mathrm{in}}}, \tag{B.29}$$

$$\zeta = \frac{2\delta_0}{\alpha+\theta_{\mathrm{C}}}, \tag{B.30}$$

$$\beta' = \frac{-4\pi^2\beta^{(2)}L_{\mathrm{MR}}}{(\alpha+\theta_{\mathrm{C}})t_{\mathrm{R}}^2}. \tag{B.31}$$

For the field $\underline{\mathcal{E}}^*(t,\tau) = \sum_{\mu\in\mathbb{Z}}\underline{\mathcal{E}}^*_\mu(t)\mathrm{e}^{\mathrm{j}\mu 2\pi\tau/t_{\mathrm{R}}}$, the intracavity power is given by $\frac{1}{t_{\mathrm{R}}}\int_0^{t_{\mathrm{R}}}|\underline{\mathcal{E}}^*(t,\tau)|^2\,\mathrm{d}\tau = \sum_{\mu\in\mathbb{Z}}|\underline{\mathcal{E}}^*_\mu|^2$. The power of the frequency comb is defined as the power of the intracavity-field excluding the pumped mode, $P_{\mathrm{FC}} = \sum_{\mu\in\mathbb{Z}\setminus\{0\}}|\underline{\mathcal{E}}^*_\mu|^2$. The pumped mode is excluded since it will have a nonzero value even if no frequency comb is formed. The physical power conversion efficiency η_{in} inside the microresonator can then be expressed as

$$\eta_{\mathrm{in}} = \frac{P_{\mathrm{FC}}}{P_{\mathrm{in}}} = \frac{\sum_{\mu\in\mathbb{Z}\setminus\{0\}}|\underline{\mathcal{E}}^*_\mu|^2}{P_{\mathrm{in}}}. \tag{B.32}$$

When the comb is coupled out of the microresonator, the field amplitude is decreased by the square root of the power-coupling coefficient θ_{C}. Therefore, the physical conversion efficiency with respect to the comb power outside of the resonator η_{out} is given by

$$\eta_{\mathrm{out}} := \frac{\sum_{\mu\in\mathbb{Z}\setminus\{0\}}|\sqrt{\theta_{\mathrm{C}}}\underline{\mathcal{E}}^*_\mu|^2}{P_{\mathrm{in}}} = \theta_{\mathrm{C}}\eta_{\mathrm{in}}. \tag{B.33}$$

Given the relations from Eqs. (B.26) and (B.29), the normalized power conversion efficiency η defined as the ratio between the power of the normalized

frequency comb $\sum_{\mu\in\mathbb{Z}\setminus\{0\}} |\hat{\underline{a}}_\mu|^2$ and the normalized forcing power F can be expressed by physical quantities as follows:

$$\eta = \frac{\sum_{\mu\in\mathbb{Z}\setminus\{0\}} |\underline{a}_\mu|^2}{F} = \frac{\sum_{\mu\in\mathbb{Z}\setminus\{0\}} \left|\sqrt{\frac{2\gamma L_{\mathrm{MR}}}{\alpha+\theta_{\mathrm{C}}}}\underline{\mathcal{E}}^*_\mu\right|^2}{\left(\sqrt{\frac{2\gamma L_{\mathrm{MR}}}{\alpha+\theta_{\mathrm{C}}}}\frac{2\sqrt{\theta_{\mathrm{C}}}}{\alpha+\theta_{\mathrm{C}}}\sqrt{P_{\mathrm{in}}}\right)^2}$$
$$= \frac{(\alpha+\theta_{\mathrm{C}})^2}{4\theta_{\mathrm{C}}}\eta_{\mathrm{in}} = \frac{(\alpha+\theta_{\mathrm{C}})^2}{4\theta_{\mathrm{C}}^2}\eta_{\mathrm{out}}. \tag{B.34}$$

This is equivalent to Eq (3.11) of Chapter 3.

B.5 Bifurcation maps, stability and multi-peak solutions

In this appendix, we explain and illustrate details on the global bifurcation maps of Figs. 3.1(a) and 3.2(a). In particular, we comment on the topics of *connectedness of branches, secondary bifurcations, and transition between soliton classes*, the use of a *different norm* to display certain aspects of the branches, and finally on the issue of *stability*.

Connectedness of branches, secondary bifurcations, and transition between soliton classes At bifurcation points, branches of solutions intersect. Those bifurcation points that lie on the curve of constant solutions are called primary bifurcation points and they were described in Sec. 3.2. Bifurcation points which are not lying on the curve of constant solutions are called secondary bifurcation points and they occur whenever two curves of nonconstant solutions join. In Figs. B.1(a) (anomalous dispersion $\beta' = 0.1$, forcing $\sqrt{F} = 2$) and B.2(a) (normal dispersion $\beta' = -0.1$, forcing $\sqrt{F} = 2$), we show which of the bifurcation curves are connected to each other by secondary bifurcations. Curves connected to each other by secondary bifurcations are plotted with the same color. Note that in a trivial sense all curves are connected to the curve of constant solutions via primary bifurcations – but these connections are not used for our coloring. All bifurcation points in Figs. B.1(a) and B.2(a)

are marked as unfilled circles. The bifurcation points on the black curve of constant solutions are primary bifurcation points. Most secondary bifurcation points in Fig. B.1(a) occur at turning points with the exception of one secondary bifurcation point that occurs on the blue curve near $\zeta = 0.8$. In Fig. B.2(a), three secondary bifurcation points occur at $\zeta = 2.73$ (cf. zoom), $\zeta = 2.84$, and $\zeta = 3.36$.

Near secondary bifurcation points one can observe the transition between solutions of a different number of peaks, e.g., in the case of BSOs in Fig. B.1(b) a secondary bifurcation occurs at the turning point C'. Taking the 1-solitons at points A, C, B from Fig. 3.1(b) one can see their transition through U, V, W in Fig. B.1(d) into equally spaced 2-solitons shown at Fig. B.1(c) on the branch with A', C', B'. Following the branch A', C', B' further up, one finds another secondary bifurcation at a turning point where one meets the branch of 4-solitons. Similar observations can be made in the case of DSOs. Fig. B.2(a) and B.2(b) show a secondary bifurcation near $\zeta = 3.36$. One can see how dark 1-solitons at points D, F, E known from Fig. B.1(e) transform through X, Y, Z in Fig. B.2(d) into equally spaced 2-solitons shown at Fig. B.2(c) on the branch with D', F', E'. The state Z approximates a two soliton somewhere between F' and E'. We also show in the zoom of Fig. B.2(a) how the curve of 1-solitons undergoes a secondary bifurcation with the curve of 3-solitons near $\zeta = 2.73$. Right after this bifurcation, the curves split up again. Since this happens close to the trivial curve, the visible effects on the solutions are marginal and are therefore not displayed.

Secondary bifurcations coming with the phenomenon period-doubling, period-tripling etc. were found earlier in Refs. [119], Fig. 7(b) or [128], Fig. 5 for anomalous dispersion and in Ref. [124], Fig. 12 for normal dispersion. An abstract result related to global secondary bifurcations with applications to Eqs. (3.2) and (3.3) can be found in Ref. [133].

Branches displayed in a different norm In the case of anomalous dispersion, Fig. B.1(a) shows the branches in the conventional norm $\|\underline{a}\|_2^2$ which represents the intracavity power of the states. This norm does not capture well the fact that eight branches snake back and forth after having reached maximal values of ζ. In fact, comparing states on a fixed branch for the same value of ζ, one finds that the state obtained on the way out toward the maximal value of ζ is different compared with the state obtained on the way back. This effect

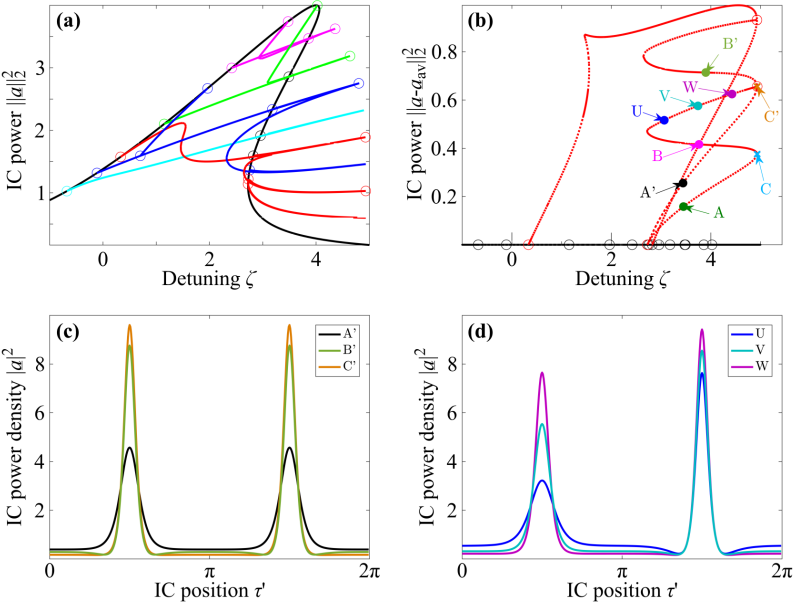

Figure B.1: Connected components of bifurcation graphs (top) and selected bright solitons (bottom) in anomalous dispersion for $\sqrt{F} = 2$ and $\beta' = 0.1$. Quantities on axes are dimensionless. (a) Same graph as in Fig. 3.1(a) shows normalized intracavity power $\|\underline{a}\|_2^2$ vs normalized detuning ζ. Bifurcation points are marked as unfilled circles. Primary bifurcation points lie on the black curve of constant solutions, secondary bifurcation points lie off the black curve. Branches connected through secondary bifurcation points are plotted with the same color. (b) Detailed resolution of red connected component from (a) using the norm $\|\underline{a} - \underline{a}_{\mathrm{av}}\|_2^2$ vs ζ. The black curve of constant solutions is now on the ζ-axis. Stable states lie on solid lines, unstable states on dashed lines. The curve of 1-solitons runs through the states A, C, B whose spatial power distribution was shown in Fig. 3.1(b). Following this branch further leads to states U, V, W marking the transition from 1-solitons to 2-solitons before meeting the branch of 2-solitons through A', C', B' at the secondary bifurcation point C'. Following the A', C', B' curve further up leads to another secondary bifurcation with the branch of 4-solitons that eventually meets the trivial curve again near $\zeta_0 = 0.3325$. (c) shows the spatial power distribution of selected 2-solitons and (d) shows how on the branch of 1-solitons the transition towards 2-solitons occurs before the two branches join at point C'.

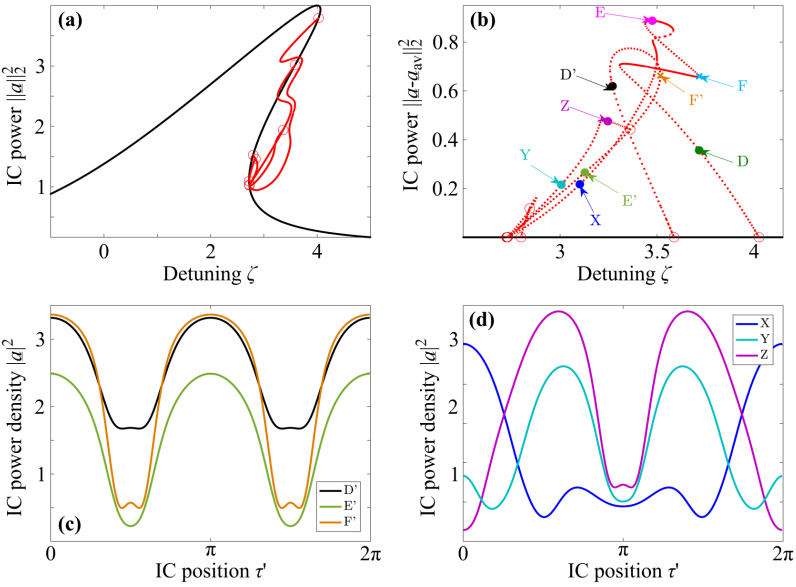

Figure B.2: Connected components of bifurcation graphs (top) and selected dark solitons (bottom) in normal dispersion for $\sqrt{F} = 2$ and $\beta' = -0.1$. Quantities on axes are dimensionless. (a) Same graph as in Fig. 3.2(a) showing normalized intracavity power $\|\underline{a}\|_2^2$ vs normalized detuning ζ restricted to the relevant range. Bifurcation points are marked as unfilled circles. There are six primary bifurcation points lying on the black curve of constant solutions, and three secondary bifurcation points lying off the black curve. All branches are connected to each other and are therefore shown in red. The zoom shows how the branch of 1-solitons starting on the trivial curve near$\zeta = 4$ almost meets the curve of constant solutions near $\zeta = 2.73$. Instead, it connects at a secondary bifurcation point near $\zeta = 2.73$ with the curve of 3-solitons and immediately detaches from it again and then finally connects to the 2-solitons at the secondary bifurcation point near $\zeta = 3.36$. (b) Detailed resolution of red connected component from (a) using the norm $\|\underline{a} - \underline{a}_{\mathrm{av}}\|_2^2$ vs ζ. The black curve of constant solutions is now on the ζ-axis. Stable states lie on solid lines, unstable states on dashed lines. The curve of 1-solitons runs through the states D, F, E whose spatial power distribution was shown in Fig. 3.2(b). Following this branch further leads to states X, Y, Z marking the transition from 1-solitons to 2-solitons before meeting the branch of 2-solitons through D', F', E' at a secondary bifurcation point near $\zeta = 3.36$. (c) shows the spatial power distribution of selected 2-solitons and (d) shows how on the branch of 1-solitons the transition toward 2-solitons occurs before the two branches meet near $\zeta = 3.36$.

can be visualized much better in Fig. B.1(b), where instead of $\|\underline{a}\|_2^2$ we use the norm

$$\|\underline{a} - \underline{a}_{\mathrm{av}}\|_2^2 \text{ with } \underline{a}_{\mathrm{av}} := \frac{1}{2\pi}\int_0^{2\pi} \underline{a}(\tau')\,\mathrm{d}\tau' \tag{B.35}$$

with the average value $\underline{a}_{\mathrm{av}}$ being subtracted from a before the intracavity power measure is taken. This has the effect of squeezing the black curve of trivial solutions onto the ζ-axis. On the other hand, it visualizes more clearly that the states before and after the turning points are different. One may even observe the snaking behavior of the branches with respect to the detuning in the range $\zeta > 2$, which is quite similar to the "foliated snaking" with respect to the forcing parameter discussed in Ref. [119], Section V.B. Notice that in both cases secondary bifurcations occur at turning points of the curves, i.e., at local extrema of the bifurcation parameter along the curve. For the case of normal dispersion, the same comparison between $\|\underline{a}\|_2^2$ and $\|\underline{a} - \underline{a}_{\mathrm{av}}\|_2^2$ has been done in Figs. B.2(a) and B.2(b). Again, a snaking behavior can be seen on the branch of 1-solitons as well as on the 2-soliton branch, and a similar behavior (collapsed defect-mediated snaking) is described in Ref. [124] in case of bifurcation with respect to the forcing.

Stability In Figs. B.1(b) and Fig. B.2(b), stable states are depicted with solid lines and unstable states are shown with dashed lines. Here, stability of a stationary state $\underline{a}$ means nonlinear stability, i.e., solutions of the evolution equation (3.1) starting in a small neighbourhood of $\underline{a}$ stay inside this neighbourhood for all times. A necessary (but not sufficient) condition for nonlinear stability of $\underline{a}$ is the spectral stability, by which we mean that the spectrum of $-\mathrm{j}\hat{L}$ lies in the left complex plane, where $\hat{L}$ is the linearized operator defined in Eqs. (3.4) with $\underline{a}_0$ replaced by $\underline{a}$. Indeed, one of the main results of Ref. [129] is that for the special case of the LLE, Eq. (3.1) spectral stability and nonlinear stability are equivalent. Notice that the shift-invariance of solutions $\underline{a}$ of Eq. (3.2) generates the eigenvalue 0 of the linearized operator $\hat{L}$ at any nontrivial solution. This is the reason why in Ref. [129] only orbital stability of stationary states can be deduced. In our case, we have imposed Neumann boundary conditions at $\tau' = 0$ and $\tau' = \pi$ together with the even symmetry around $\tau' = \pi$. This eliminates the shift invariance so that 0 is an eigenvalue of $\hat{L}$ only at bifurcation points, and hence (with the exception of bifurcation points) proper nonlinear

stability statements can be deduced. For the purpose of indicating nonlinear stability or instability in our graphs, we computed the finite spectrum of the finite-element discretization of the operator $\hat{L}$ and checked whether it belongs entirely to the lower complex plane or not.

[End of supplementary information of publication [J1]]

C Modulation instability in silicon microresonators at telecommunication wavelengths

The text in this chapter is added as appendix to the publication [J2]. It was adapted to fit the layout, structure and notation of this dissertation. This appendix assumes a negative time dependence of the optical signal of the form $\exp(-\mathrm{j}\omega t)$.

[Start of appendix of publication [J2]]

C.1 Lugiato-Lefever equation for modeling modulation instability

When pumping a nonlinear system with a sinusoidal waveform of constant amplitude, spectral sidebands can develop, and the pump amplitude appears modulated. This so-called modulation instability (MI) is the starting point of frequency comb formation in a pumped Kerr-nonlinear optical microresonator. We determine the onset of MI in the presence of two-photon absorption (TPA) and free-carrier absorption (FCA) analytically by a small-signal approximation of the modified Lugiato-Lefever equation (LLE). In the following analysis, we use normalized quantities, see Table 4.1 in Chapter 4.

The complex optical field amplitude $\underline{\mathcal{E}}^*(t,\tau)$ (Eq. (4.1) in Chapter 4) is defined with respect to the pump frequency ω_p. It depends on a "slow" time variable $t = \kappa\, t_\mathrm{R}$ expressed in multiples κ of the fixed round-trip time $t_\mathrm{R} = L_\mathrm{MR}/v_\mathrm{g}$ for a given resonator perimeter L_MR and a group velocity v_g at the pump frequency ω_p, as well as on a "fast" time $\tau = t - z/v_\mathrm{g}$, defined by a retarded

time frame that depends on the local position z inside the resonator. The corresponding normalized optical field according to Table 4.1 is $\underline{a}\,(t', \tau')$, where the slow normalized time t' is assumed to be continuous and where the short normalized time variable τ' defines the position within the cavity in the retarded fast time frame, $\tau' \in [0, 2\pi)$. The resonator is driven by a normalized pump field amplitude $\sqrt{F}$. Due to TPA, the optical field generates free carriers (FCs) with a normalized density N'_{car}. The free carriers are stationary in the microresonator, and we hence describe them as a function of a stationary (non-retarded) fast time $\tau_{\mathrm{S}} = -z/v_{\mathrm{g}}$, that only depends on the position z within the resonator. Both the optical field and the free-carrier density can be transformed between the stationary and the retarded fast time frame via $\underline{a}\,(t', \tau') = \underline{a}\left(t', \tau'_{\mathrm{S}} + t'v'\right)$ and $N'_{\mathrm{car}}\,(t', \tau' - t'v') = N'_{\mathrm{car}}\left(t', \tau'_{\mathrm{S}}\right)$, where v' is the normalized group velocity. Each rapidly varying time-harmonic component $\mathrm{e}^{\mathrm{j}\omega_\mu \tau}$ ($\omega_\mu = \mu\,(2\pi/t_{\mathrm{R}})$, $\mu = 0, \pm1, \pm2, \pm3, \ldots$) in Eq. (4.1) of Chapter 4 is periodic in τ with the round-trip time, leading to periodic boundary conditions $\underline{a}\,(t', \tau') = \underline{a}\,(t', \tau' + 2\pi)$ for the dependence of the complex field amplitude on the normalized fast time τ', which can hence be represented as a Fourier series, $\underline{a}\,(t', \tau') = \sum_\mu \underline{a}_\mu\,(t')\,\mathrm{e}^{\mathrm{j}\mu\tau'}$. In the following, we describe the slow-time evolution of the optical field $\underline{a}\,(t', \tau')$ in the retarded time frame τ' using the normalized LLE, Eq. (4.5) in Chapter 4. Further, we describe the slow-time evolution of the free carriers $N'_{\mathrm{car}}\left(t', \tau'_{\mathrm{S}}\right)$ in the stationary time frame τ'_{S}. The normalized LLE and the differential equation describing the evolution of the free-carrier density ("free-carrier equation") are given in Eqs. (4.5) and (4.6) in Chapter 4,

$$\frac{\partial \underline{a}\,(t', \tau')}{\partial t'} = \sqrt{F} + \Bigg[-1 - \mathrm{j}\zeta + \mathrm{j}\beta' \frac{\partial^2}{\partial \tau'^2} + \mathrm{j}\hat{\Phi}'_{\mathrm{AMC}} + (\mathrm{j} - r)\left|\underline{a}\,(t', \tau')\right|^2 - \sigma'_{\mathrm{car}}\,(1 + \mathrm{j}\beta_{\mathrm{car}})\,N'_{\mathrm{car}}\,(t', \tau' - t'v')\Bigg]\,\underline{a}\,(t', \tau')\,, \tag{C.1}$$

$$\frac{\partial N'_{\mathrm{car}}\left(t', \tau'_{\mathrm{S}}\right)}{\partial t'} = r\left|\underline{a}\left(t', \tau'_{\mathrm{S}} + t'v'\right)\right|^4 - \frac{N'_{\mathrm{car}}\left(t', \tau'_{\mathrm{S}}\right)}{t'_{\mathrm{eff}}}, \tag{C.2}$$

The normalized difference between the pump frequency ω_{p} and the closest resonance frequency $\omega_{\mathrm{r},0}$ of an unpumped resonator is ζ. The second-order dispersion of the microresonator is represented by the normalized dispersion parameter β'. The quantity r denotes the normalized TPA coefficient. For the

TPA-generated FC, the quantities $\sigma'_{\mathrm{car}}, \beta_{\mathrm{car}}, t'_{\mathrm{eff}}$ define the normalized absorption cross-section, the contribution to the refractive index, and the normalized dwell-time inside the microresonator waveguide, respectively. The relationship between normalized parameters and physical quantities are summarized in Table 4.1 of Chapter 4. We further include an operator $\hat{\Phi}'_{\mathrm{AMC}}$ describing phase shifts ϕ_μ experienced by individual components $\underline{a}_\mu\,(t')$ of the optical field for frequencies μ. These phase shifts take into account local resonance frequency shifts caused by mode coupling of different transverse modes, an effect known as avoided mode crossing [166]. The operator can be written as

$$\hat{\Phi}'_{\mathrm{AMC}}\underline{a}\,(t',\tau') = \sum_{\tilde{\mu}} \frac{\phi_{\tilde{\mu}}}{2\pi} \int_0^{2\pi} \underline{a}\,(t',\tau_1)\,\mathrm{e}^{-\mathrm{j}\tilde{\mu}\tau_1}\,\mathrm{d}\tau_1 \mathrm{e}^{\mathrm{j}\tilde{\mu}\tau'}. \tag{C.3}$$

In our simulations shown in Chapter 4, the strength of the mode coupling, which defines the exact values $\phi_{\tilde{\mu}}$, was chosen to reflect typical experimental results.

To investigate the condition for the onset of MI, we assume that the optical field consists of a constant pumped mode $\underline{a}_0$ and two infinitesimally small sidebands $\underline{a}_{\pm M}$ ($M = 1, 2, 3, \ldots$) [221], the temporal evolution of which is described by complex gain parameter $\underline{g} = g + \mathrm{j}g_\mathrm{j}$,

$$\begin{aligned} \underline{a}\,(t',\tau') &= \underline{a}_0 + \underline{a}_{+M} + \underline{a}_{-M}, \quad \left|\hat{\underline{a}}_{\pm M}\right| \ll \left|\underline{a}_0\right|, \\ \underline{a}_{+M} &= \hat{\underline{a}}_{+M}\mathrm{e}^{gt'}\mathrm{e}^{\mathrm{j}g_\mathrm{j}t'}\mathrm{e}^{\mathrm{j}M\tau'}, \\ \underline{a}_{-M} &= \hat{\underline{a}}_{-M}\mathrm{e}^{gt'}\mathrm{e}^{-\mathrm{j}g_\mathrm{j}t'}\mathrm{e}^{-\mathrm{j}M\tau'}. \end{aligned} \tag{C.4}$$

In the stationary fast time frame, this optical field is then given by

$$\begin{aligned} \underline{a}\left(t',\tau'_\mathrm{S}+t'v'\right) &= \underline{a}_0 + \underline{a}_{+M,\mathrm{S}} + \underline{a}_{-M,\mathrm{S}}, \\ \underline{a}_{+M,\mathrm{S}} &= \hat{\underline{a}}_{+M}\mathrm{e}^{gt'}\mathrm{e}^{+\mathrm{j}g_\mathrm{j}t'}\mathrm{e}^{+\mathrm{j}M\tau'_\mathrm{S}}\mathrm{e}^{+\mathrm{j}M\,t'v'}, \\ \underline{a}_{-M,\mathrm{S}} &= \hat{\underline{a}}_{-M}\mathrm{e}^{gt'}\mathrm{e}^{-\mathrm{j}g_\mathrm{j}t'}\mathrm{e}^{-\mathrm{j}M\tau'_\mathrm{S}}\mathrm{e}^{-\mathrm{j}M\,t'v'}. \end{aligned} \tag{C.5}$$

We further assume that right at the onset of MI at $t' = 0$, the normalized free-carrier density according to Eq. (C.2) has reached a stationary value of

$N'_{\mathrm{car}}\left(0,\tau'_{\mathrm{S}}\right) = rt'_{\mathrm{eff}}\left|\underline{a}_0\right|^4$ dictated by the strong pump $\underline{a}_0$. Solving Eq. (C.2) with this initial condition leads to

$$N'_{\mathrm{car}}\left(t',\tau'_{\mathrm{S}}\right) = \exp\left(-\frac{t'}{t'_{\mathrm{eff}}}\right)\left[rt'_{\mathrm{eff}}\left|\underline{a}_0\right|^4 + r\int_0^{t'}\left|\underline{a}\left(t_1,\tau'_{\mathrm{S}}+t_1v'\right)\right|^4\exp\left(\frac{t'}{t'_{\mathrm{eff}}}\right)\mathrm{d}t_1\right]. \quad \text{(C.6)}$$

We then insert Eq. (C.5) into Eq. (C.6) and apply a small-signal approximation of the form $\left|\underline{a}\left(t',\tau'_{\mathrm{S}}+t'v'\right)\right|^4 \approx \left|\underline{a}_0\right|^4 + 2\left|\underline{a}_0\right|^2\left(\underline{a}_0^*\,\underline{a}_{+M,\mathrm{S}} + \underline{a}_0\,\underline{a}_{-M,\mathrm{S}}^*\right) + 2\left|\underline{a}_0\right|^2\left(\underline{a}_0^*\,\underline{a}_{-M,\mathrm{S}} + \underline{a}_0\,\underline{a}_{+M,\mathrm{S}}^*\right)$, where the star (*) denotes the complex conjugate. Keeping only terms up to linear order in $\underline{\hat{a}}_{\pm M}$ or $\underline{\hat{a}}_{\pm M}^*$, we solve the integral in Eq. (C.6) and obtain

$$\begin{aligned} N'_{\mathrm{car}}\left(t',\tau'_{\mathrm{S}}\right) = rt_{\mathrm{eff}}\left|\underline{a}_0\right|^2\Bigg[&\left|\underline{a}_0\right|^2 \\ &+ 2\left(\underline{a}_0^*\,\underline{\hat{a}}_{+M} + \underline{a}_0\,\underline{\hat{a}}_{-M}^*\right)\mathrm{e}^{+\mathrm{j}M\tau'_{\mathrm{S}}}\frac{\mathrm{e}^{gt'}\mathrm{e}^{+\mathrm{j}\left(g_{\mathrm{j}}+Mv'\right)t'} - \mathrm{e}^{-t'/t'_{\mathrm{eff}}}}{t'_{\mathrm{eff}}g + 1 + \mathrm{j}t'_{\mathrm{eff}}\left(g_{\mathrm{j}}+Mv'\right)} \\ &+ 2\left(\underline{a}_0^*\,\underline{\hat{a}}_{-M} + \underline{a}_0\,\underline{\hat{a}}_{+M}^*\right)\mathrm{e}^{-\mathrm{j}M\tau'_{\mathrm{S}}}\frac{\mathrm{e}^{gt'}\mathrm{e}^{-\mathrm{j}\left(g_{\mathrm{j}}+Mv'\right)t'} - \mathrm{e}^{-t'/t'_{\mathrm{eff}}}}{t'_{\mathrm{eff}}g + 1 - \mathrm{j}t'_{\mathrm{eff}}\left(g_{\mathrm{j}}+Mv'\right)}\Bigg]. \end{aligned} \quad \text{(C.7)}$$

Over time, exponentially decaying terms $\mathrm{e}^{-t'/t'_{\mathrm{eff}}}$ can be neglected since normalized free-carrier lifetimes are of the order of $t'_{\mathrm{eff}} \approx 0.1 \ldots 1$ (corresponding to physical FC lifetimes of the order of 100 ps or less for our microresonator design) such that the decay of $\mathrm{e}^{-t'/t'_{\mathrm{eff}}}$ occurs much faster than the increase of $\mathrm{e}^{gt'}$ with typical values of $g \approx 0.1$ for the gain parameter. Similarly, for short normalized free-carrier lifetimes $t'_{\mathrm{eff}} \approx 0.1 \ldots 1$ and small gain parameters$g \approx 0.1$, we may approximate $t'_{\mathrm{eff}}g + 1 \approx 1$ in the denominators in Eq. (C.7). In the same manner, we may approximate $g_{\mathrm{j}} + Mv' \approx Mv'$ in the denominators of Eq. (C.7). This is justified by the fact that g_{j} represents the normalized frequency offset of the MI sideband from the center of the corresponding resonance and is thus much smaller than the offset from the pump, which corresponds to multiple

FSRs and is represented by Mv', i.e., $g_\mathrm{j} \ll Mv'$. The remaining expression for the free-carrier density reads

$$N'_\mathrm{car}\left(t', \tau'_\mathrm{S}\right) = rt'_\mathrm{eff}\left|\underline{a}_0\right|^2 \left[\left|\underline{a}_0\right|^2 + 2\frac{1 - \mathrm{j}Mt'_\mathrm{eff}v'}{1 + \left(Mt'_\mathrm{eff}v'\right)^2}\left(\underline{a}_0^*\,\underline{a}_{+M,\mathrm{S}} + \underline{a}_0\,\underline{a}_{-M,\mathrm{S}}^*\right) + 2\frac{1 + \mathrm{j}Mt'_\mathrm{eff}v'}{1 + \left(Mt'_\mathrm{eff}v'\right)^2}\left(\underline{a}_0^*\,\underline{a}_{-M,\mathrm{S}} + \underline{a}_0\,\underline{a}_{+M,\mathrm{S}}^*\right)\right]. \tag{C.8}$$

Via $N'_\mathrm{car}\left(t', \tau' - t'v'\right) = N'_\mathrm{car}\left(t', \tau'_\mathrm{S}\right)$, this result is now transformed into the retarded time frame, which yields

$$N'_\mathrm{car}\left(t', \tau' - t'v'\right) = rt'_\mathrm{eff}\left|\underline{a}_0\right|^2 \left[\left|\underline{a}_0\right|^2 + 2\frac{1 - \mathrm{j}Mt'_\mathrm{eff}v'}{1 + \left(Mt'_\mathrm{eff}v'\right)^2}\left(\underline{a}_0^*\,\underline{a}_{+M} + \underline{a}_0\,\underline{a}_{-M}^*\right) + 2\frac{1 + \mathrm{j}Mt'_\mathrm{eff}v'}{1 + \left(Mt'_\mathrm{eff}v'\right)^2}\left(\underline{a}_0^*\,\underline{a}_{-M} + \underline{a}_0\,\underline{a}_{+M}^*\right)\right]. \tag{C.9}$$

The expression for the free-carrier density in the retarded fast time frame is substituted in Eq. (C.1) along with the ansatz for $\underline{a}\left(t', \tau'\right)$, Eq. (C.4). Again, we keep only terms up to linear order in $\underline{\hat{a}}_{\pm M}$ or $\underline{\hat{a}}_{\pm M}^*$. We separate non-oscillating terms from terms oscillating with $\mathrm{e}^{\mathrm{j}M\tau'}$ and $\mathrm{e}^{-\mathrm{j}M\tau'}$, and obtain

$$0 = \sqrt{F} + \left[-1 - \mathrm{j}\zeta + \mathrm{j}\phi_0 + (\mathrm{j} - r)\left|\underline{a}_0\right|^2 - \sigma'_\mathrm{car}\left(1 + \mathrm{j}\beta_\mathrm{car}\right) rt'_\mathrm{eff}\left|\underline{a}_0\right|^4\right]\underline{a}_0, \tag{C.10}$$

$$\begin{aligned}\underline{g}\,\underline{a}_{+M} = &\left[-1-\mathrm{j}\zeta-\mathrm{j}\beta' M^2+\mathrm{j}\phi_{+M}\right]\underline{a}_{+M}\\ &+(\mathrm{j}-r)\left[2\left|\underline{a}_0\right|^2\underline{a}_{+M}+\left(\underline{a}_0\right)^2\underline{a}^*_{-M}\right]\\ &-(1+\mathrm{j}\beta_{\mathrm{car}})\frac{\sigma'_{\mathrm{car}}rt'_{\mathrm{eff}}\left|\underline{a}_0\right|^2}{1+\left(Mt'_{\mathrm{eff}}v'\right)^2}\Bigg[\left(3+\left(Mt'_{\mathrm{eff}}v'\right)^2\right)\left|\underline{a}_0\right|^2\underline{a}_{+M}\\ &+2\left(\underline{a}_0\right)^2\underline{a}^*_{-M}-\mathrm{j}2Mt'_{\mathrm{eff}}v'\left(\left|\underline{a}_0\right|^2\underline{a}_{+M}+\left(\underline{a}_0\right)^2\underline{a}^*_{-M}\right)\Bigg],\end{aligned}\tag{C.11}$$

$$\begin{aligned}\underline{g}^*\,\underline{a}_{-M} = &\left[-1-\mathrm{j}\zeta-\mathrm{j}\beta' M^2+\mathrm{j}\phi_{-M}\right]\underline{a}_{-M}\\ &+(\mathrm{j}-r)\left[2\left|\underline{a}_0\right|^2\underline{a}_{-M}+\left(\underline{a}_0\right)^2\underline{a}^*_{+M}\right]\\ &-(1+\mathrm{j}\beta_{\mathrm{car}})\frac{\sigma'_{\mathrm{car}}rt'_{\mathrm{eff}}\left|\underline{a}_0\right|^2}{1+\left(Mt'_{\mathrm{eff}}v'\right)^2}\Bigg[\left(3+\left(Mt_{\mathrm{eff}}v'\right)^2\right)\left|\underline{a}_0\right|^2\underline{a}_{-M}\\ &+2\left(\underline{a}_0\right)^2\underline{a}^*_{+M}+\mathrm{j}2Mt'_{\mathrm{eff}}v'\left(\left|\underline{a}_0\right|^2\underline{a}_{-M}+\left(\underline{a}_0\right)^2\underline{a}^*_{+M}\right)\Bigg].\end{aligned}\tag{C.12}$$

We divide Eq. (C.11) by $\mathrm{e}^{gt'}\mathrm{e}^{\mathrm{j}g_{\mathrm{j}}t'}\mathrm{e}^{\mathrm{j}M\tau'}$ and Eq. (C.12) by $\mathrm{e}^{gt'}\mathrm{e}^{-\mathrm{j}g_{\mathrm{j}}t'}\mathrm{e}^{-\mathrm{j}M\tau'}$ and we introduce $\overline{\phi}=(\phi_{+M}+\phi_{-M})/2$ and $\Delta\phi=(\phi_{+M}-\phi_{-M})/2$. Both equations are then expressed in terms of $\underline{\hat{a}}_{\pm M}$ instead of in terms of $\underline{a}_{\pm M}$,

$$\begin{aligned}\underline{g}\,\hat{\underline{a}}_{+M} = &\left[-1-\mathrm{j}\zeta-\mathrm{j}\beta' M^2+\mathrm{j}\overline{\phi}+\mathrm{j}\Delta\phi\right]\hat{\underline{a}}_{+M}\\ &+(\mathrm{j}-r)\left[2\left|\underline{a}_0\right|^2\hat{\underline{a}}_{+M}+\left(\underline{a}_0\right)^2\hat{\underline{a}}^*_{-M}\right]\\ &-(1+\mathrm{j}\beta_{\mathrm{car}})\frac{\sigma'_{\mathrm{car}}rt'_{\mathrm{eff}}\left|\underline{a}_0\right|^2}{1+\left(Mt'_{\mathrm{eff}}v'\right)^2}\Bigg[\left(3+\left(Mt'_{\mathrm{eff}}v'\right)^2\right)\left|\underline{a}_0\right|^2\hat{\underline{a}}_{+M}\\ &+2\left(\underline{a}_0\right)^2\hat{\underline{a}}^*_{-M}-\mathrm{j}2Mt'_{\mathrm{eff}}v'\left(\left|\underline{a}_0\right|^2\hat{\underline{a}}_{+M}+\left(\underline{a}_0\right)^2\hat{\underline{a}}^*_{-M}\right)\Bigg],\end{aligned}\tag{C.13}$$

$$
\begin{aligned}
\underline{g}^{*}\,\underline{a}_{-M} = {} & \left[-1-\mathrm{j}\zeta-\mathrm{j}\beta' M^2+\mathrm{j}\overline{\phi}-\mathrm{j}\Delta\phi\right]\underline{\hat{a}}_{-M} \\
& +(\mathrm{j}-r)\left[2\left|\underline{a}_0\right|^2\underline{\hat{a}}_{-M}+\left(\underline{a}_0\right)^2\underline{\hat{a}}^{*}_{+M}\right] \\
& -(1+\mathrm{j}\beta_{\mathrm{car}})\,\frac{\sigma'_{\mathrm{car}} r t'_{\mathrm{eff}}\left|\underline{a}_0\right|^2}{1+\left(M t'_{\mathrm{eff}} v'\right)^2}\Bigg[\left(3+\left(M t_{\mathrm{eff}} v'\right)^2\right)\left|\underline{a}_0\right|^2\underline{\hat{a}}_{-M} \\
& +2\left(\underline{a}_0\right)^2\underline{\hat{a}}^{*}_{+M}+\mathrm{j}2M t'_{\mathrm{eff}} v'\left(\left|\underline{a}_0\right|^2\underline{\hat{a}}_{-M}+\left(\underline{a}_0\right)^2\underline{\hat{a}}^{*}_{+M}\right)\Bigg].
\end{aligned}
\tag{C.14}
$$

We subtract $\mathrm{j}\Delta\phi\underline{\hat{a}}_{+M}$ in Eq. (C.13), add $\mathrm{j}\Delta\phi\underline{\hat{a}}_{-M}$ in Eq. (C.14) and introduce $\underline{g}' = g+\mathrm{j}g'_{\mathrm{j}} = g+\mathrm{j}\left(g_{\mathrm{j}}-\Delta\phi\right)$. Then, we compute the complex conjugate of the resulting Eq. (C.14). We obtain a matrix equation of the form

$$
\begin{aligned}
\underline{g}'\begin{pmatrix}\underline{\hat{a}}_{+M}\\ \underline{\hat{a}}^{*}_{-M}\end{pmatrix} = {} & \begin{pmatrix}-1-2r\left|\underline{a}_0\right|^2 & -r\left(\underline{a}_0\right)^2\\ -r\left(\underline{a}^{*}_0\right)^2 & -1-2r\left|\underline{a}_0\right|^2\end{pmatrix}\begin{pmatrix}\underline{\hat{a}}_{+M}\\ \underline{\hat{a}}^{*}_{-M}\end{pmatrix} \\
& +\mathrm{j}\begin{pmatrix}-\zeta-\beta' M^2+\overline{\phi}+2\left|\underline{a}_0\right|^2 & \left(\underline{a}_0\right)^2\\ -\left(\underline{a}^{*}_0\right)^2 & \zeta+\beta' M^2-\overline{\phi}-2\left|\underline{a}_0\right|^2\end{pmatrix}\begin{pmatrix}\underline{\hat{a}}_{+M}\\ \underline{\hat{a}}^{*}_{-M}\end{pmatrix} \\
& -\frac{\sigma'_{\mathrm{car}} r t'_{\mathrm{eff}}\left|\underline{a}_0\right|^2}{1+\left(M t'_{\mathrm{eff}} v'\right)^2}\Bigg[\begin{pmatrix}\left(3+\left(M t'_{\mathrm{eff}} v'\right)^2\right)\left|\underline{a}_0\right|^2 & 2\left(\underline{a}_0\right)^2\\ 2\left(\underline{a}^{*}_0\right)^2 & \left(3+\left(M t'_{\mathrm{eff}} v'\right)^2\right)\left|\underline{a}_0\right|^2\end{pmatrix} \\
& +\mathrm{j}\beta_{\mathrm{car}}\begin{pmatrix}\left(3+\left(M t'_{\mathrm{eff}} v'\right)^2\right)\left|\underline{a}_0\right|^2 & 2\left(\underline{a}_0\right)^2\\ -2\left(\underline{a}^{*}_0\right)^2 & -\left(3+\left(M t'_{\mathrm{eff}} v'\right)^2\right)\left|\underline{a}_0\right|^2\end{pmatrix}\Bigg]\begin{pmatrix}\underline{\hat{a}}_{+M}\\ \underline{\hat{a}}^{*}_{-M}\end{pmatrix} \\
& +\mathrm{j}\frac{\sigma'_{\mathrm{car}} r t'_{\mathrm{eff}}\left|\underline{a}_0\right|^2}{1+\left(M t'_{\mathrm{eff}} v'\right)^2}2M t'_{\mathrm{eff}} v' \\
& \times\begin{pmatrix}\left(1+\mathrm{j}\beta_{\mathrm{car}}\right)\left|\underline{a}_0\right|^2 & \left(1+\mathrm{j}\beta_{\mathrm{car}}\right)\left(\underline{a}_0\right)^2\\ \left(1-\mathrm{j}\beta_{\mathrm{car}}\right)\left(\underline{a}^{*}_0\right)^2 & \left(1-\mathrm{j}\beta_{\mathrm{car}}\right)\left|\underline{a}_0\right|^2\end{pmatrix}\begin{pmatrix}\underline{\hat{a}}_{+M}\\ \underline{\hat{a}}^{*}_{-M}\end{pmatrix}.
\end{aligned}
\tag{C.15}
$$

This equation can be represented as

$$\begin{aligned}
\underline{g}' \begin{pmatrix} \underline{\hat{a}}_{+M} \\ \underline{\hat{a}}^*_{-M} \end{pmatrix} &= \begin{pmatrix} \underline{m}_{A,1} + \mathrm{j}\underline{m}_{B,1} & \underline{m}_{A,2} + \mathrm{j}\underline{m}_{B,2} \\ \underline{m}^*_{A,2} + \mathrm{j}\underline{m}^*_{B,2} & \underline{m}^*_{A,1} + \mathrm{j}\underline{m}^*_{B,1} \end{pmatrix} \begin{pmatrix} \underline{\hat{a}}_{+M} \\ \underline{\hat{a}}^*_{-M} \end{pmatrix} \\
&= \mathbf{M} \begin{pmatrix} \underline{\hat{a}}_{+M} \\ \underline{\hat{a}}^*_{-M} \end{pmatrix}, \quad \text{where} \\
\underline{m}_{A,1} &= -1 - \mathrm{j}\zeta - \mathrm{j}\beta' M^2 + \mathrm{j}\overline{\phi} + (\mathrm{j} - r)\, 2 \left|\underline{a}_0\right|^2 \\
&\quad - \frac{\sigma'_{\mathrm{car}} r t'_{\mathrm{eff}} \left|\underline{a}_0\right|^2}{1 + \left(M t'_{\mathrm{eff}} \nu'\right)^2} (1 + \mathrm{j}\beta_{\mathrm{car}}) \left(3 + \left(M t'_{\mathrm{eff}} \nu'\right)^2\right) \left|\underline{a}_0\right|^2, \\
\underline{m}_{A,2} &= (\mathrm{j} - r) \left(\underline{a}_0\right)^2 - \frac{\sigma'_{\mathrm{car}} r t'_{\mathrm{eff}} \left|\underline{a}_0\right|^2}{1 + \left(M t'_{\mathrm{eff}} \nu'\right)^2} (1 + \mathrm{j}\beta_{\mathrm{car}})\, 2 \left(\underline{a}_0\right)^2, \\
\underline{m}_{B,1} &= \frac{\sigma'_{\mathrm{car}} r t'_{\mathrm{eff}} \left|\underline{a}_0\right|^2}{1 + \left(M t'_{\mathrm{eff}} \nu'\right)^2} 2 M t'_{\mathrm{eff}} \nu' (1 + \mathrm{j}\beta_{\mathrm{car}}) \left|\underline{a}_0\right|^2, \\
\underline{m}_{B,2} &= \frac{\sigma'_{\mathrm{car}} r t'_{\mathrm{eff}} \left|\underline{a}_0\right|^2}{1 + \left(M t'_{\mathrm{eff}} \nu'\right)^2} 2 M t'_{\mathrm{eff}} \nu' (1 + \mathrm{j}\beta_{\mathrm{car}}) \left(\underline{a}_0\right)^2.
\end{aligned} \tag{C.16}$$

Computing the eigenvalues of $\mathbf{M}$ results in

$$\begin{aligned}
\underline{g}'_{\pm} &= \Re\{\underline{m}_{A,1}\} + \mathrm{j}\Re\{\underline{m}_{B,1}\} \pm \sqrt{\underline{\Delta}}, \\
\underline{\Delta} &= \left(\Re\{\underline{m}_{A,2}\} + \mathrm{j}\Re\{\underline{m}_{B,2}\}\right)^2 + \left(\Im\{\underline{m}_{A,2}\} + \mathrm{j}\Im\{\underline{m}_{B,2}\}\right)^2 \\
&\quad - \left(\Im\{\underline{m}_{A,1}\} + \mathrm{j}\Im\{\underline{m}_{B,1}\}\right)^2.
\end{aligned} \tag{C.17}$$

We back-substitute $\underline{m}_{A,1}$, $\underline{m}_{A,2}$, $\underline{m}_{B,1}$, $\underline{m}_{B,2}$, g'_{j}, $\overline{\phi}$ and $\Delta\phi$, and introduce the power of the pumped mode $A = \left|\underline{a}_0\right|^2$ to obtain expressions for the real part and the imaginary part of the gain parameter, see Eq. (4.10) in Chapter 4. From Eq. (C.10) we derive the relation between the pump power F and the power of the pumped mode A, see Eq. (4.11) in Chapter 4.

C.2 Approximation of the gain parameter for technically relevant values for TPA, FCA and pump parameters

In Chapter 4, Section 4.4 we simplify the expression for the real part of the gain parameter g given in Eq. (4.10) of Chapter 4 by assuming technically relevant values for the TPA, FCA, and pump parameters $\left(r \approx 1,\, t'_{\mathrm{eff}} \approx 0.05 \ldots 0.5,\right.$ $\left.\sigma'_{\mathrm{car}} \approx 5,\, \beta_{\mathrm{car}} \approx 10, v' \approx 200,\, F \approx 10,\, A \approx 1\right)$, as well as $M \approx 10$. Here we specify the magnitude of specific terms occurring in Eq. (4.10) of Chapter 4 for the given parameter ranges. We consider two different cases $t'_{\mathrm{eff}} \approx 0.05$ (left value below the respective term) and $t'_{\mathrm{eff}} \approx 0.5$ (right value below the respective term), and we neglect all terms that are either at least three orders of magnitude smaller than competing terms or that are at least two orders of magnitude smaller and that are approximately constant in t'_{eff}. The remaining terms are highlighted in blue. In the following relations, the symbol "≈" used is to be understood as an order-of-magnitude quantification rather than as an approximate equality.

$$g\,(M) = -\underbrace{1}_{\approx 1} - \underbrace{2rA}_{\approx 2} - \underbrace{rt'_{\mathrm{eff}}\sigma'_{\mathrm{car}}A}_{\approx 3\times10^{-1}\ldots 3\times10^{0}} \underbrace{\frac{3+\left(Mt'_{\mathrm{eff}}v'\right)^2}{1+\left(Mt'_{\mathrm{eff}}v'\right)^2}}_{\approx 1} + \Re\{\underline{\Delta}\}, \qquad \text{(C.18)}$$

$$
\begin{aligned}
\underline{\Delta} = \Bigg[& \underbrace{A^2}_{\approx 1} \Bigg(\underbrace{r}_{\approx 1} + \underbrace{\frac{2rt'_{\mathrm{eff}}\sigma'_{\mathrm{car}}}{1+(Mt'_{\mathrm{eff}}\nu')^2}A}_{\approx 5\times10^{-5}\ldots 5\times10^{-6}} - \mathrm{j}\,\underbrace{\frac{2rt'_{\mathrm{eff}}Mt'_{\mathrm{eff}}\nu'\sigma'_{\mathrm{car}}}{1+(Mt'_{\mathrm{eff}}\nu')^2}A}_{\approx 5\times10^{-3}\ldots 5\times10^{-3}} \Bigg)^2 \\
& + \underbrace{A^2}_{\approx 1} \Bigg(\underbrace{1}_{=1} - \underbrace{\frac{2rt'_{\mathrm{eff}}\sigma'_{\mathrm{car}}\beta_{\mathrm{car}}}{1+(Mt'_{\mathrm{eff}}\nu')^2}A}_{\approx 5\times10^{-4}\ldots 5\times10^{-5}} + \mathrm{j}\,\underbrace{\frac{2rt'_{\mathrm{eff}}Mt'_{\mathrm{eff}}\nu'\sigma'_{\mathrm{car}}\beta_{\mathrm{car}}}{1+(Mt'_{\mathrm{eff}}\nu')^2}A}_{\approx 5\times10^{-2}\ldots 5\times10^{-2}} \Bigg)^2 \\
& - \Bigg(\underbrace{\zeta + \beta' M^2 - \frac{\phi_+ + \phi_-}{2}}_{\text{Arbitrarily large}} - \underbrace{2A}_{\approx 2} + \underbrace{rt'_{\mathrm{eff}}\sigma'_{\mathrm{car}}\beta_{\mathrm{car}}A^2}_{\approx 3\times10^{0}\ldots 3\times10^{1}} \underbrace{\frac{3+\left(Mt'_{\mathrm{eff}}\nu'\right)^2}{1+(Mt'_{\mathrm{eff}}\nu')^2}}_{\approx 1} \\
& - \mathrm{j}\,\underbrace{\frac{2rt'_{\mathrm{eff}}Mt'_{\mathrm{eff}}\nu'\sigma'_{\mathrm{car}}\beta_{\mathrm{car}}}{1+(Mt'_{\mathrm{eff}}\nu')^2}A^2}_{\approx 5\times10^{-2}\ldots 5\times10^{-2}} \Bigg)^2 \Bigg]^{1/2} .
\end{aligned}
$$

These approximations are equivalent to approximating the optical field $\underline{a}(t', \tau')$ generating free carriers by $\left|\underline{a}(t', \tau'_{\mathrm{S}} + t'\nu')\right|^4 \approx \left|\underline{a}_0\right|^4$ in Eq. (C.6), such that only the first term on the r.h.s. of Eq. (C.8) remains. This is consistent with the fact that, at the onset of MI, the instantaneous free-carrier density is still dictated by the unperturbed CW pump. The expression for the real part g of the complex gain parameter then reads

$$
\begin{aligned}
g\,(M) \approx & -1 - 2rA - rt'_{\mathrm{eff}}\sigma'_{\mathrm{car}}A^2 \\
& + \Re\Bigg\{ \Bigg(A^2r^2 + A^2 \\
& \qquad - \left(\zeta + \beta' M^2 - \frac{\phi_+ + \phi_-}{2} - 2A + rt'_{\mathrm{eff}}\sigma'_{\mathrm{car}}\beta_{\mathrm{car}}A^2 \right)^2 \Bigg)^{1/2} \Bigg\}.
\end{aligned}
\tag{C.19}
$$

In the absence of AMC, $\phi_{+M} = \phi_{-M} = 0$, this leads to Eq. (4.12) of Chapter 4.

C.3 Threshold pump power for modulation instability: Approximate vs. numerical evaluation

In Chapter 4, Figure 4.2, we analytically evaluate an approximation of the threshold pump power F_{th} needed to achieve modulation instability, based on realistic values for t'_{eff}, A, M, r, σ'_{car}, β_{car}, v', and for anomalous dispersion $\beta' > 0$ with $\beta' M^2 - A = 0$ at $g\left(M_{\mathrm{max}}\right) = 0$. We further assume that mode coupling is absent or sufficiently weak such that avoided mode crossings do not need to be considered ($\phi_\mu = 0 \,\forall\, \mu$). In the following, we validate this approximation by a numerical investigation. To this end, we find the associated threshold pump power $F_{\mathrm{th,num}}$ by minimizing F according to Eq. (4.11) of Chapter 4 when varying A, M and ζ under the constraint $g\left(M_{\mathrm{max}}\right) = 0$, Eq. (4.10). We choose $\beta' = 0.0025$, $\beta_{\mathrm{car}} = 7.5$ and sweep the quantities r and $t'_{\mathrm{eff}}\sigma'_{\mathrm{car}}$ to cover the same parameter space as in Fig. 4.2. Figure C.1(a) shows the result of the analytic approximation and corresponds to Fig. 4.2, while Fig. C.1(b) displays the numerical result. No difference is visible from the two graphs. The relative difference $\left|\Delta F_{\mathrm{th}}\right| / F_{\mathrm{th,num}} = \left|F_{\mathrm{th}} - F_{\mathrm{th,num}}\right| / F_{\mathrm{th,num}}$ is smaller than 10^{-2} in the whole region, see Figure C.1(c).

C.4 Waveguide field simulations for nonlinearity parameter, group refractive index and dispersion parameter

To determine realistic values for the waveguide nonlinearity, the group refractive index, and the dispersion of a microresonator waveguide according to Fig. 4.1 in Chapter 4, we perform finite-element simulations using commercial tools (RSoft Photonics CAD suite, FemSIM). We assume a pump wavelength of 1550 nm along with the waveguide dimensions specified in Fig. C.2. The waveguide in these simulations is either straight or has a bend radius of 115 μm, corresponding to the resonator design shown in Chapter 4, Fig. 4.1. The refractive indices of silica $n_{\mathrm{SiO_2}}$ and silicon n_{Si} are included according to Sellmeier's equation [222, 223]. The modulus squared of the electric field of the quasi-TE mode field within the silicon waveguide is shown in Fig. C.2. The undoped

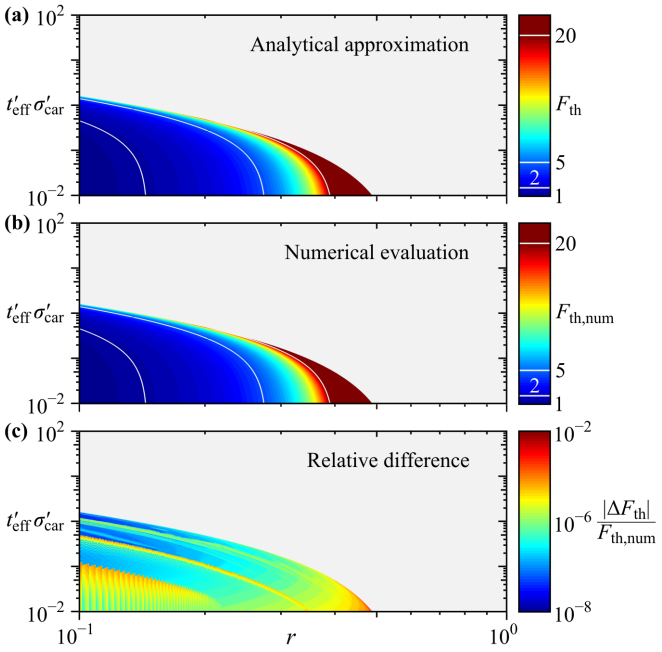

Figure C.1: Threshold pump power for modulation instability. (a) Approximate analytical evaluation, see also Chapter 4, Fig. 4.2. (b) Corresponding numerical calculation. (c) Relative color-coded difference in threshold pump powers when comparing the analytical and the numerical method. The deviation is smaller than 1 % in the whole region.

silicon portion of the waveguide is marked with a white outline, and the mode is essentially confined to this region such that the optical field will not be affected by doping associated with the *p-i-n*-junction or by the vertical interconnect accesses (vias) shown in Chapter 4, Fig. 4.1. Since the bend radius $R_B \gg w$ is large relative to the waveguide width w and because $\sqrt{n_{\mathrm{Si}}^2 - n_{\mathrm{SiO_2}}^2}\, R_B \gg \lambda$ holds, the field appears symmetrical in the horizontal direction. Given the field distributions $\mathbf{E}\,(x,\ y), \mathbf{H}\,(x,\ y)$ we compute the nonlinear waveguide parameter γ using [66]

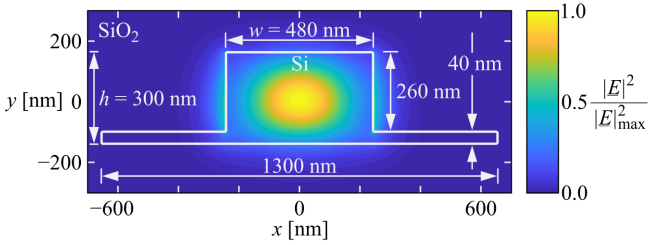

Figure C.2: Normalized modulus squared of the total electric field of the quasi-TE mode at 1550 nm. We assume a waveguide bent to the left with bend radius of 115 μm. The white outline marks the undoped silicon part of the waveguide.

$$\gamma = \frac{\omega_\mathrm{p}\epsilon_0 n_\mathrm{Si}^2 n_\mathrm{2,Si}}{Z_0} \frac{\int\int_\mathrm{Si} \left|\underline{\mathbf{E}}\,(x,\,y)\right|^4 \mathrm{d}x\mathrm{d}y}{\left|\int\int_\mathrm{total} \Re\{\underline{\mathbf{E}}\,(x,\,y) \times \underline{\mathbf{H}}\,(x,\,y)\} \cdot \mathbf{e}_z \mathrm{d}x\mathrm{d}y\right|^2}. \tag{C.20}$$

Here, ω_p is the angular frequency of the optical pump field, Z_0 is the free space impedance, and $\mathbf{e}_z$ the unit vector along a perimeter of the ring-shaped waveguide. We assume that the third-order nonlinear susceptibility of silicon is a scalar quantity and can be expressed by the corresponding Kerr coefficient $n_\mathrm{2,Si} = 6.5 \times 10^{-18}\,\mathrm{m^2\,W^{-1}}$ [29]. The resulting nonlinearity parameter at a wavelength of 1550 nm amounts to $\gamma = 257\,\mathrm{W^{-1}m^{-1}}$. In order to determine the dispersion coefficient, mode field simulations are performed for varying wavelengths in a spectral range of 60 nm (7.5 THz) around 1550 nm. From these simulations, we obtain the effective refractive index, which is then used to determine the group refractive index $n_\mathrm{g} = 4.15$ and the dispersion coefficient $\beta^{(2)} = -0.587\,\mathrm{ps^2\,m^{-1}}$, both at a wavelength of 1550 nm.

C.5 Integration of the Lugiato-Lefever equation and the free-carrier equation

In Chapter 4, Section 4.5, we numerically integrate the normalized Eqs. (4.5) and (4.6) of Chapter 4 using the split-step Fourier method [65]. The normalized

(slow) temporal time step is $\Delta t'$, the dispersion operator is denoted by $\hat{D}$, and the nonlinear operator is $\hat{N}$:

$$\begin{aligned}\underline{a}\left(t'+\Delta t',\tau'\right) =& \sqrt{F}\Delta t' + \mathrm{e}^{\hat{D}\Delta t'/2}\mathrm{e}^{\hat{N}\left(t',\tau'\right)\Delta t'}\mathrm{e}^{\hat{D}\Delta t'/2}\underline{a}\left(t',\tau'\right), \qquad \text{(C.21)}\\ \hat{D} =& -1-\mathrm{i}\zeta-\mathrm{j}\beta'\frac{\partial^2}{\partial\tau'^2},\\ \hat{N}\left(t',\tau'\right) =& \left(\mathrm{j}-r\right)\left|\underline{a}\left(t',\tau'\right)\right|^2 - \sigma'_{\mathrm{car}}\left(1+\mathrm{j}\beta_{\mathrm{car}}\right)N'_{\mathrm{car}}\left(t',\tau'-t'v'\right).\end{aligned}$$

In this approach, the FCA is included in the nonlinear operator $\hat{N}\left(t',\tau'\right)$, where the free-carrier density $N'_{\mathrm{car}}\left(t',\tau'_{\mathrm{S}}\right)$ is computed for each time step via Eq. (C.2). To this end, we use a discretization of $\Delta\tau' = \Delta\tau'_{\mathrm{S}} = 2\pi/1024$ for the normalized fast time τ' by dividing the round-trip time into 1024 parts. We further choose the slow-time increment $\Delta t'$ as an integer multiple of $\Delta\tau'/v'$, i.e., $\Delta t' = N_{\Delta\tau'/v'}\Delta\tau'/v'$ with $N_{\Delta\tau'/v'} = 64$. Over one increment $\Delta t'$ of the slow time, the optical field will thus propagate by $N_{\Delta\tau'/v'} = 64$ positions along the fast time scale, which are indexed by an integer $\kappa = 0, 1, \ldots 63$ in the following. The evolution of the free carriers during one slow-time increment $\Delta t'$ can hence be obtained by integrating Eq. (4.6) in a recursive manner,

$$\begin{aligned}N'_{\mathrm{car}}\left(t'+(\kappa+1)\frac{\Delta\tau'_{\mathrm{S}}}{v'},\tau'_{\mathrm{S}}\right) =& N'_{\mathrm{car}}\left(t'+\kappa\frac{\Delta\tau'_{\mathrm{S}}}{v'},\tau'_{\mathrm{S}}\right)\left(1-\frac{\Delta\tau'_{\mathrm{S}}}{v't'_{\mathrm{eff}}}\right)\\ &+ r\frac{\Delta\tau'_{\mathrm{S}}}{v'}\left|\underline{a}\left(t',\tau'_{\mathrm{S}}+\kappa\Delta\tau'_{\mathrm{S}}+t'v'\right)\right|^4, \qquad \text{(C.22)}\\ \kappa =& 0, 1, \ldots N_{\Delta\tau'/v'}-1.\end{aligned}$$

Note that, during each slow-time increment $\Delta t'$, we neglect the explicit dependence of the optical field $\underline{a}\left(t',\tau'\right)$ on the slow time t' and only consider the implicit dependence via $\tau' = \tau'_{\mathrm{S}} + t'v'$. The delays $t'v'$ and $\kappa\Delta\tau'_{\mathrm{S}}$ of the optical field are implemented as circular rotations of the array associated with $\underline{a}\left(t',\tau'_{\mathrm{S}}+\kappa\Delta\tau'_{\mathrm{S}}+t'v'\right)$. Compared to simplified methods that only consider the evolution of the mean free-carrier density [26, 77]

$$\left\langle N'_{\mathrm{car}}\right\rangle_{\tau'}\left(t'\right) = \frac{1}{2\pi}\int_{-\pi/2}^{+\pi/2} N'_{\mathrm{car}}\left(t',\xi\right)\,\mathrm{d}\xi \qquad \text{(C.23)}$$

the procedure leads to an overall increase of the simulation time by about 10 %. To illustrate the capabilities of our model, we perform simulations of the

dynamics of an optically pumped Si microresonator and compare the results to those obtained by the mean-value approximation of the intra-cavity free-carrier distribution [26, 77].

In Figure C.3, we show the evolution of the intracavity field power and the free-carrier density by integration of Eqs. (4.5) and (4.6) in a regime where free-carrier oscillations occur, see [26] for a discussion of the associated parameter space. Column (a) of Fig. C.3 depicts the simulation results obtained by the algorithm following Eqs. (C.21) and (C.22). The results shown in Column (b) are obtained by approximating the free-carrier density by its mean value $\left\langle N'_{\mathrm{car}} \right\rangle_{\tau'} (t')$ according to Eq. (C.22) and by inserting this value in Eq. (C.21). Row R1 shows the simulation parameters, where we assume a significantly increased forcing $F = 30$ compared to the cases discussed in Chapter 4. Further, we assume a significantly longer free-carrier lifetime $t'_{\mathrm{eff}} = 0.406$ corresponding to 122 ps for our assumed microresonator, see Section 4.5. Note that the group velocity v' is not necessary to compute the mean free-carrier density $\left\langle N'_{\mathrm{car}} \right\rangle_{\tau'} (t')$ and is therefore not considered in Column (b). Rows R2 and R3 show the evolution of the intracavity (IC) field power $\left|\underline{a}\,(t', \tau')\right|^2$ and the free-carrier density (FCD) $N'_{\mathrm{car}}\,(t', \tau' - t'v')$ as a function of slow time t' and as a function of the retarded fast time τ'. Both the field power and the carrier density show oscillations with slow time. Modulation instability is absent, and therefore the optical field remains constant along the fast time τ'. As a consequence, the free carriers do not show any dependence on τ', independent of the underlying algorithm. In Row R4 and R5, the evolution of the mean values of the optical field power $\left\langle \left|\underline{a}\right|^2 \right\rangle_{\tau'} (t')$ and the carrier density $\left\langle N'_{\mathrm{car}} \right\rangle_{\tau'} (t')$ are shown. The vertical grey lines in Row R4 and R5 mark slow-time temporal maxima of the IC power. The maxima of the free-carrier density are delayed relative to the temporal maxima of the optical power, since the free-carrier generation rate $r \left|\underline{a}\,(t', \tau'_{\mathrm{S}} + t'v')\right|^4$ in Eq. (4.6) is larger than the free-carrier decay rate $N'_{\mathrm{car}}\,(t', \tau'_{\mathrm{S}})\,/t'_{\mathrm{eff}}$ for a certain period, even when the optical field is already declining due to increased FCA. These slow-time dynamics are described in the same manner by both algorithms without any significant difference between the simulation results shown Column (a) and (b). We therefore conclude that our algorithm correctly describes the slow-time dynamics of the free-carrier density. For another algorithm describing the slow time dynamics for the fast-time resolved free-carrier density via the boundary condition $N_{\mathrm{car}}\,(t, -t_{\mathrm{R}}/2) = N_{\mathrm{car}}\,(t + \Delta t, +t_{\mathrm{R}}/2)$ [25], expressed as

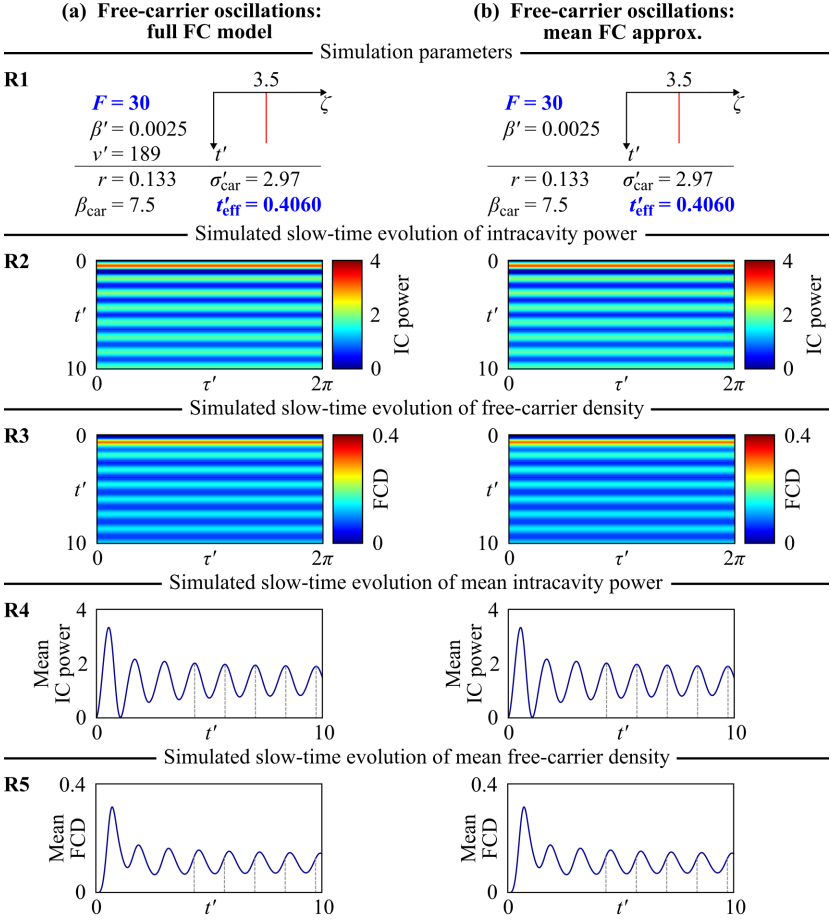

Figure C.3: Results of time integration of the LLE for different integration formalisms. Row R1: Simulation parameters. Row R2: Color-coded intracavity (IC) power $\left|\underline{a}\left(t', \tau'\right)\right|^2$ as a function of fast time τ', evolving over slow time t'. Row R3: Color-coded free-carrier density (FCD) $N'_{\mathrm{car}}\left(t', \tau' - t'\nu'\right)$ as a function of fast time τ', evolving over slow time t'. Row R4: Mean IC power $\left\langle \left|\underline{a}\left(t', \tau'\right)\right|^2 \right\rangle_{\tau'}$ as a function of slow time t'. Vertical dashed lines indicate the temporal positions of maximum IC power. Row R5: Mean FCD $\left\langle N'_{\mathrm{car}}\left(t', \tau' - t'\nu'\right)\right\rangle_{\tau'}$ as a function of slow time t'. Column (a): FC oscillations simulated using the full model for the description of FC dynamics, Eqs. (C.21) and (C.22). Column (b): FC oscillations modeled using a mean FCD.

$N'_{\mathrm{car}}(t', -\pi) = N'_{\mathrm{car}}(t' + \Delta t, +\pi)$ in normalized quantities, the correct accumulation of free carriers is subject to discussion [77].

While the two algorithms give nearly identical results for the IC power and the free-carrier dynamics in the absence of modulation instability, they yield different results when a frequency comb forms. In particular, the dynamics of single-soliton states on both slow and fast time differ significantly. In Figure C.4, we show the results of a time integration of the LLE and the FCE, Eqs. (4.5) and (4.6) for another set of parameters allowing soliton comb formation. Again, Column (a) depicts the simulation results obtained through our algorithm, Eqs. (C.21) and (C.22), while Column (b) approximates the free-carrier density through its mean value $\left\langle N'_{\mathrm{car}} \right\rangle_{\tau'}(t')$ according to Eq. (C.23). Row R1 lists again the simulation parameters. The forcing is kept at $F = 30$ and the detuning swept until $\zeta = 6.65$. The FC lifetime is reduced to $t'_{\mathrm{eff}} = 0.0406$, corresponding to 12.2 ps. The second Row R2 shows the slow-time evolution of the IC power, where we use different initial random optical fields, see also Section 4.5, for Column (a) and (b) respectively. Both algorithms generate a single soliton pulse around $t' = 33$. In Column (a) we observe a drift of the single soliton along the fast time axis τ' when the fast-time free-carrier dynamics are considered. Such a drift was predicted in another study [28]. In Row R4, the evolution of the associated free-carrier density, depicted in the retarded fast time frame τ', is shown. As long as the IC power is high and multiple pulses circulate in the cavity, the FC density is high and nearly constant along τ'. However, once only two pulses or only one pulse circulate in the cavity, the free-carrier density drops significantly and is not constant anymore. The fast-time distribution of the free carriers shows the same temporal drift as the optical field. We attribute this drift to the fact that the sharp rise of the free-carrier density during the pulse leads to an attenuation of the trailing edge and hence to an effectively increased propagation velocity. This effect can only be modelled when including the fast-time free-carrier dynamics. The last Row R5 shows the final FC density $N'_{\mathrm{car}}(t' = 100, \tau' - 100v')$. In Column (a), the soliton pulse, see Row R3, causes a sharp increase of the FC density near $\tau' \approx 1.8\pi$ at $t' = 100$, such that variations of up to 46 % relative to the mean value of the free carriers are observed during one round-trip. These strong variations and the drift of the soliton pulse highlight the importance of the consideration of the fast time dynamics of the FC density for a more precise description of Kerr comb formation in the presence of TPA and FCA. These effects cannot

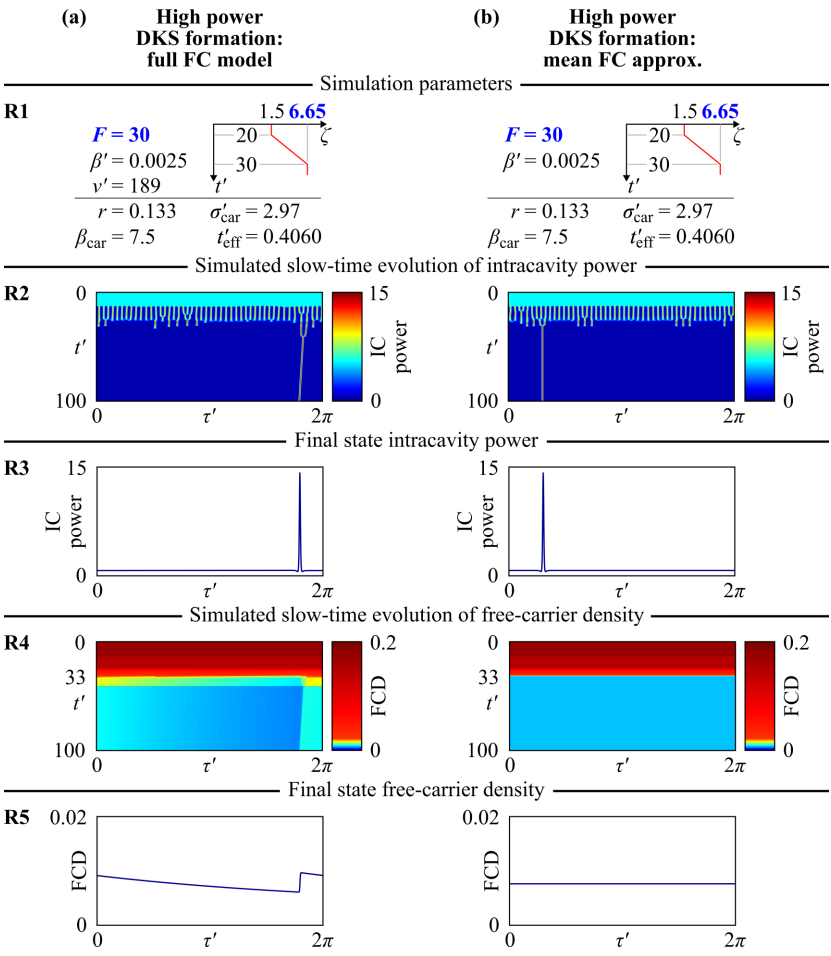

Figure C.4: Results of time integration of the LLE for different integration formalisms. Row R1: Simulation parameters. Row R2: Color-coded intracavity (IC) power $\left|\underline{a}\left(t', \tau'\right)\right|^2$ as a function of fast time τ', evolving over slow time t'. Row R3: IC power at the end of the simulation $\left|\underline{a}\left(t' = 100, \tau'\right)\right|^2$. Row R4: Color-coded free-carrier density (FCD) $N'_{\mathrm{car}}\left(t', \tau' - t'\nu'\right)$ as a function of τ', evolving over t'. Row R5: FCD at the end of the simulation $N'_{\mathrm{car}}\left(t' = 100, \tau' - 100\nu'\right)$. Column (a): Free-carrier (FC) oscillations simulated using the full model for the description of FC dynamics, Eqs. (C.21) and (C.22). Column (b): FC oscillations modeled using a mean FCD. Correct representation of the fast-time FC dynamics results in a drift of the soliton pulse along the fast-time axis τ', which cannot be described by the mean-value approximation of the FCD.

be described by the mean-value approximation of the intra-cavity free-carrier distribution, see Column (b) of Fig. C.4.

Still, despite these inaccuracies, the mean-value approximation of the intra-cavity free-carrier distribution can give reasonably accurate results for certain device parameters. This is, e.g., the case if slow-time dynamics of the optical field in the presence of free-carrier absorption such as the drift along the fast time axis τ' are not of interest and if a certain imprecision in the description of the FC density along the microresonator circumference can be tolerated. An upper limit of the fast-time FC density fluctuations, normalized to the mean value of the FC density, can be estimated by assuming that the optical field is represented by a sharp single pulse without a CW-background. In this case, the square of the optical power density in the microresonator may be denoted as a single, constant delta-pulse, $\left|\underline{a}\left(t',\tau'\right)\right|^4 = A_\delta^2 \delta\left(\tau'\right)$, where $\delta\left(\tau'\right)$ is the Dirac delta distribution. For simplicity, we assume the pulse to be located at $\tau' = 0$. In the stationary fast-time frame, the optical field then reads $\left|\underline{a}\left(t',\tau'_\mathrm{S}+t'v'\right)\right|^4 = A_\delta^2 \delta\left(\tau'_\mathrm{S}+t'v'\right)$. Further assuming that initial FCs do not play a role, $N'_\mathrm{car}\left(0,\tau'_\mathrm{S}\right) \approx 0$, and using Eq. (C.6), the FC density in the retarded fast-time frame reads $N'_\mathrm{car}\left(0,\tau'-t'v'\right) = N'_\mathrm{car,0}\exp\left[-\tau'/\left(v't'_\mathrm{eff}\right)\right]$, where $N'_\mathrm{car,0} = rA_\delta^2\left(1-\exp\left[-2\pi/\left(v't'_\mathrm{eff}\right)\right]\right)^{-1}$. The maximum value of the FC density along the microresonator circumference is $N'_\mathrm{car,0}$, the minimum is given as $N'_\mathrm{car,0}\exp\left[-2\pi/\left(v't'_\mathrm{eff}\right)\right]$, and the mean value amounts to $\left\langle N'_\mathrm{car}\left(t',\tau'-t'v'\right)\right\rangle_{\tau'} = N'_\mathrm{car,0}/(2\pi)\, v't'_\mathrm{eff}\left(1-\exp\left[-2\pi/\left(v't'_\mathrm{eff}\right)\right]\right)$. Thus the local increase of the FC density caused by the optical pulse, normalized to the mean value $\left\langle N'_\mathrm{car}\left(t',\tau'-t'v'\right)\right\rangle_{\tau'}$ at $\tau' = 0$ reads

$$\frac{N'_\mathrm{car,0} - N'_\mathrm{car,0}\exp\left[-2\pi/\left(v't'_\mathrm{eff}\right)\right]}{\left\langle N'_\mathrm{car}\left(t',\tau'-t'v'\right)\right\rangle_{\tau'}} = \frac{2\pi}{v't'_\mathrm{eff}} = \frac{t_\mathrm{R}}{t_\mathrm{eff}}. \tag{C.24}$$

For an FC lifetime equal to the round-trip time, $t_\mathrm{eff} = t_\mathrm{R}$, this difference amounts to 100 %, i.e., the FC density increase is equal to the mean value along the microresonator circumference. In this case, the mean-value approximation of the intra-cavity free-carrier distribution may not give reliable results. When the lifetime is increased to, e.g., $t_\mathrm{eff} = 10t_\mathrm{R}$, the relative FC density increase caused by the optical pulse decreases to 10 % and a mean-FCD approximation becomes increasingly valid. We note that Eq. (C.24) is only an approximation that neglects the CW-background of the optical field that is usually present –

in practice, this aspect will further reduce the fast-time fluctuations of the FC density normalized to its mean value. Thus Eq. (C.24) can thus be used as an upper limit for the normalized fast-time FC density fluctuations.

C.6 Dispersion profile of coupled mode families

In this section we describe the derivation of the dispersion profile used in Chapter 4, Section 4.5 to simulate comb formation in a normal-dispersive microresonator under the influence of an avoided mode crossing, see Fig. 4.6. In a first step, we consider two unperturbed mode families M1 and M2. The comb is generated in the resonances of mode family M1, while mode family M2 may induce a local shift of resonance positions of M1. The mode families are described by the frequency of the central modes $\omega_{0,\mathrm{M1}}$, $\omega_{0,\mathrm{M2}}$ and by the corresponding free spectral ranges $\omega_{\mathrm{r,FSR,M1}}$, $\omega_{\mathrm{r,FSR,M2}}$, such that the respective resonance frequencies read

$$\omega_{\mathrm{r},\mu,\mathrm{M1}} = \omega_{\mathrm{r},0,\mathrm{M1}} + \mu\,\omega_{\mathrm{r,FSR,M1}} - \beta^{(2)} L_{\mathrm{MR}}/(2t_{\mathrm{R}})\left(\mu\,\omega_{\mathrm{r,FSR,M1}}\right)^2, \tag{C.25}$$

$$\omega_{\mathrm{r},\mu,\mathrm{M2}} = \omega_{\mathrm{r},0,\mathrm{M2}} + \mu\,\omega_{\mathrm{r,FSR,M2}}. \tag{C.26}$$

Here, we have omitted dispersive terms of the second mode family for simplicity. The dispersion profiles of the modes describe the deviation of the various resonance frequencies from an equidistant grid defined by the center free spectral range $\omega_{\mathrm{r,FSR,M1}}$ of mode family M1. Using Eq. (C.25), the dispersion profiles can be stated for the two mode families M1 and M2,

$$\omega_{\mathrm{r},\mu,\mathrm{M1}} - \omega_{\mathrm{r},0,\mathrm{M1}} - \mu\,\omega_{\mathrm{r,FSR,M1}} = -\beta^{(2)} L_{\mathrm{MR}}/(2t_{\mathrm{R}})\left(\mu\,\omega_{\mathrm{r,FSR,M1}}\right)^2, \tag{C.27}$$

$$\omega_{\mathrm{r},\mu,\mathrm{M2}} - \omega_{\mathrm{r},0,\mathrm{M1}} - \mu\,\omega_{\mathrm{r,FSR,M1}} = \omega_{\mathrm{r},0,\mathrm{M2}} - \omega_{\mathrm{r},0,\mathrm{M1}} - \mu\left(\omega_{\mathrm{r,FSR,M2}} - \omega_{\mathrm{r,FSR,M1}}\right) \tag{C.28}$$

The dispersion profile of M1 is a set of discrete points located on a parabola, which is defined by the second order dispersion coefficient of mode family M1. It allows to compute the phase deviation $\varphi(\mu)$ accumulated by comb modes μ, see Eq. (4.16) in Chapter 4. In contrast to the parabolic dispersion profile of mode family M1, the points given by the dispersion profile of M2 are located

on a strongly inclined line, which is indicated in red in Chapter 4, Fig. 4.6(a). Unavoidable deviations from the ideal resonator geometry lead to coupling of the mode families and hence to a hybridization, which is accompanied by a local shift of the resonance frequencies from $\omega_{\mathrm{r},\mu,\mathrm{M1/M2}}$ to two hybrid mode resonances $\omega_{\mathrm{r},\mu,\pm}$ for each mode index μ [166]. This shift depends on the coupling strength $\theta_{\mathrm{C,M}}$ between the respective modes, such that the hybrid mode resonance frequencies are given by [166]

$$\omega_{\mathrm{r},\mu,\pm} = \frac{\omega_{\mathrm{r},\mu,\mathrm{M1}} + \omega_{\mathrm{r},\mu,\mathrm{M2}}}{2} \pm \sqrt{\theta_{\mathrm{C,M}}^2 + \frac{\left(\omega_{\mathrm{r},\mu,\mathrm{M1}} - \omega_{\mathrm{r},\mu,\mathrm{M2}}\right)^2}{4}}. \tag{C.29}$$

For these hybrid modes, the dispersion profile is given in the same manner as for $\omega_{\mathrm{r},\mu,\mathrm{M1/M2}}$ by $\omega_{\mathrm{r},\mu,\pm} - \omega_{\mathrm{r},0,\mathrm{M1}} - \mu\,\omega_{\mathrm{r,FSR,M1}}$. Mode family M1 is the relevant mode family for comb formation in our system. For the gain parameter computation and the simulation of comb formation, we need to choose a certain set of resonances that are close to those of mode family M1 and that contain either the up-shifted frequencies $\omega_{\mathrm{r},\mu,+}$ or the down-shifted frequencies $\omega_{\mathrm{r},\mu,-}$ for every mode index μ. For large differences $\omega_{\mathrm{r},\mu,\mathrm{M1}} - \omega_{\mathrm{r},\mu,\mathrm{M2}}$ of resonance frequencies of the native modes M1 and M2, the native resonance $\omega_{\mathrm{r},\mu,\mathrm{M1}}$ corresponds to the hybrid resonance $\omega_{\mathrm{r},\mu,+}$ in the case $\omega_{\mathrm{r},\mu,\mathrm{M1}} - \omega_{\mathrm{r},\mu,\mathrm{M2}} > 0$ and to the hybrid resonance $\omega_{\mathrm{r},\mu,-}$ if $\omega_{\mathrm{r},\mu,\mathrm{M1}} - \omega_{\mathrm{r},\mu,\mathrm{M2}} < 0$. Near the mode coupling, we choose either $\omega_{\mathrm{r},\mu,+}$ or $\omega_{\mathrm{r},\mu,-}$ such that the obtained dispersion profile resembles a typical avoided mode crossing that exhibits approximately symmetric deviations from the native dispersion profile of mode family M1, as observed in experiments, see, e.g., [166]. From the selected hybrid resonances, we determine the resonance shifts by computing $\delta\omega_{\mu,+} = \omega_{\mathrm{r},\mu,\mathrm{M1}} - \omega_{\mathrm{r},\mu,+}$ and $\delta\omega_{\mu,-} = \omega_{\mathrm{r},\mu,\mathrm{M1}} - \omega_{\mathrm{r},\mu,-}$ respectively. These shifts are used for numeric simulations, the computation of the gain parameter according to Eq. (4.10) in Chapter 4 and the determination of phase deviations $\varphi'(\mu)$ according to Eq. (4.16). Generally, the crucial parameter for modulation instability is the maximum resonance frequency shift $\omega_{\mathrm{r},\mu,\mathrm{M1}} - \omega_{\mathrm{r},\mu,\pm}$ which amounts to $-2\pi \times 875\,\mathrm{MHz}$ or $\approx 1\,\%$ of the FSR of the microresonator under investigation. This is in accordance with experimentally observed resonance shifts [166].

C.7 List of physical quantities and parameters for the simulation of frequency comb dynamics

Table C.1 summarizes both the physical and the normalized quantities used for describing the dynamics of the optical field in the Kerr-nonlinear microresonators. In Table C.2, we specify physical and normalized microresonator parameters along with their numerical values and the associated source references.

Table C.1: Physical and normalized quantities.

Physical quantity	**Symbol**	**Value**	**Source**	**Symbol of equivalent normalized quantity**
Angular pump frequency	ω_p	$2\pi \times 193.41\,\mathrm{THz}$	Assumption	–
Pump power	P_in	$12 \ldots 50\,\mathrm{mW}$	Assumption	F
Detuning	$(\omega_{\mathrm{r},0} - \omega_\mathrm{p})t_\mathrm{R}$	$(1.2 \ldots 2)$ GHz $\times 2\pi t_\mathrm{R}$	Assumption	ζ
Slow time (natural time)	t	–	–	t'
Fast time (retarded time frame)	τ	–	–	τ'
Fast time (stationary time frame)	τ_S	–	–	τ'_S
Normalized group velocity	–	–	–	v'
Optical field	$\underline{\mathcal{E}}^*$	–	–	$\underline{a}$
Free-carrier density	N_car	–	–	N'_car
Sideband frequencies	ω_μ	–	–	μ
Gain rate	–	–	–	$\underline{g}$
Phase deviations	$\varphi(\mu)$	–	–	$\varphi'(\mu)$

Table C.2: Microresonator parameters and normalized quantities.

Physical quantity	**Symbol**	**Value**	**Source**	**Symbol of equivalent normalized quantity**	**Further occurrence in normalized quantities**
Power loss per length	α_i	$46\,\mathrm{m}^{-1}$ ($2\,\mathrm{dB\,m}^{-1}$)	[29]	–	β', F, ζ, t', t'_{eff}, ν', $\underline{a}$, N'_{car}, ϕ_μ, φ'
Group refractive index	n_{g}	4.15	Simulation	–	F, ζ, σ'_{car}, t', t'_{eff}, ν', N'_{car}, ϕ_μ, φ'
Second-order dispersion coef.	$\beta^{(2)}$	$-0.587\,\mathrm{ps}^2\,\mathrm{m}^{-1}$	Simulation	β'	–
Nonlinearity parameter	γ	$257\,\mathrm{W}^{-1}\,\mathrm{m}^{-1}$	Simulation	–	F, $\underline{a}$
Kerr coefficient	n_2	$6.5{\times}10^{-18}\,\mathrm{m}^2\,\mathrm{W}^{-1}$	[29]	–	r, σ'_{car}, N'_{car}
TPA parameter	β_{TPA}	$0.7\times10^{-11}\,\mathrm{m\,W}^{-1}$	[29]	r	–
FC dwell time	t_{eff}	12 ... 100 ps	[29]	t'_{eff}	–
FC cross-section	σ_{car}	$1.45\times10^{-21}\,\mathrm{m}^2$	[29]	σ'_{car}	–
FC dispersion parameter	β_{car}	7.5	[25]	–	–
Confinement factor	Γ_{C}	1	Assumption	–	–
Round-trip time	t_{R}	10 ps	Assumption	–	β', F, ζ, τ', τ'_{S}, ν', φ'
Free spectral range	$\omega_{\mathrm{r,FSR}} = 2\pi t_{\mathrm{R}}^{-1}$	100 GHz	Assumption	–	See round-trip time
Local resonance shift	$\delta\omega_\mu$	Max. $2\pi\times875$ MHz	Assumption	ϕ_μ	–

[End of appendix of publication [J2]]

D Dual-comb ranging with multi-heterodyne reception

The text in this chapter has been published as supplementary information of the publication [J3]. It was adapted to fit the layout, structure, notation, and conventions of this dissertation. In Section D.9, Eq. (D.28) as well as in the text before this equation, a mistake was corrected, that occurred in the publication [J3] at this position in the supplementary information. This appendix assumes a positive time dependence of the optical signal of the form $\exp(+\mathrm{j}\omega t)$.

[Start of supplementary information of publication [J3]]

D.1 Mathematical description of the distance metrology scheme

The LiDAR method applied in our experiments is based on a multi-heterodyne phase measurement of the lines of an optical frequency comb that travels to a target and back. In this section, we give a mathematical description of the measurement scheme, see Fig. D.1 for a graphical illustration of an equivalent setup using free-space optical components. Complex analytical signals $\underline{E}(t)$ are used to describe the time-domain electric fields, with the real part of the analytical signal representing the physically relevant field, $E(t) = \Re\left\{\underline{E}(t)\right\}$. A signal comb (index SI, orange) with frequencies $\omega_{\mathrm{SI},\mu} = \omega_{\mathrm{SI},0} + \mu\,\omega_{\mathrm{SI,FSR}}$ is split in two parts at a beam splitter (BS). Here $\omega_{\mathrm{SI},0}$ designates the pump

angular frequency positioned in the center of the comb, $\mu = \pm 1, \pm 2, \ldots$ is the mode index relative to the pump and $\omega_{\mathrm{SI,FSR}}$ is the free spectral range (FSR) of the frequency comb, in publications on soliton Kerr combs often referred to as D_1. The first part of the comb leaves the setup and is reflected by the target, coupled back into the system after traversing a total free-space distance[1] $2n_{\mathrm{air}}d$, and finally routed towards the measurement photoreceiver (PR). The second part of the signal comb is directly guided towards the reference photoreceiver. Both parts of the signal comb are superimposed with two parts of another comb, acting as a multi-wavelength local oscillator (index LO, blue) with frequencies $\omega_{\mathrm{LO},\mu'} = \omega_{\mathrm{LO},0} + \mu'\omega_{\mathrm{LO,FSR}}$ defined in the same manner as those of the signal comb. At a certain optical distance L_{SI} and L_{LO} along the path of the respective comb, the complex electric fields of the signal and the LO comb are given by

$$\begin{aligned}\underline{E}_{\mathrm{SI}}(L_{\mathrm{SI}}, t) &= \sum\nolimits_{\mu} \underline{E}_{\mathrm{SI},\mu}(L_{\mathrm{SI}}, t) \\ &= \sum\nolimits_{\mu} \underline{E}_{\mathrm{SI},\mu,0} \mathrm{e}^{\mathrm{j}\left(\omega_{\mathrm{SI},\mu} t - \left(\omega_{\mathrm{SI},\mu}/c_0\right) L_{\mathrm{SI}}\right)}, \qquad \text{(D.1)} \\ \underline{E}_{\mathrm{LO}}(L_{\mathrm{LO}}, t) &= \sum\nolimits_{\mu'} \underline{E}_{\mathrm{LO},\mu'}(L_{\mathrm{LO}}, t) \\ &= \sum\nolimits_{\mu'} \underline{E}_{\mathrm{LO},\mu',0} \mathrm{e}^{\mathrm{j}\left(\omega_{\mathrm{LO},\mu'} t - \left(\omega_{\mathrm{LO},\mu'}/c_0\right) L_{\mathrm{LO}}\right)}. \qquad \text{(D.2)}\end{aligned}$$

In these definitions, $\underline{E}_{\mathrm{SI},\mu,0}, \underline{E}_{\mathrm{LO},\mu',0}$ denote the complex initial amplitudes at the output of the respective comb source, and c_0 is the vacuum speed of light. Upon reaching the measurement photoreceiver, the optical distance traveled by the signal comb from its source amounts to $L_{\mathrm{SI}} = L_{\mathrm{SI,meas}} + 2n_{\mathrm{air}}d$, comprising the free-space distance $n_{\mathrm{air}}d$, and a total setup-internal optical distance $L_{\mathrm{SI,meas}}$, see Fig. D.1. The distance towards the reference photoreceiver is given in the same manner by $L_{\mathrm{SI}} = L_{\mathrm{SI,ref}}$. Equivalently, the optical path lengths from the LO comb source to the respective photoreceiver are defined as $L_{\mathrm{LO}} = L_{\mathrm{LO,meas}}$ and $L_{\mathrm{LO}} = L_{\mathrm{LO,ref}}$. Note that our experiments relied on a fiber-optic setup rather than the free-space optical arrangement shown in Fig. D.1. In Eqs. (D.1) and (D.2), this is taken into account by using the optical distances to represent L_{SI} and L_{LO} that take into account the physical length of the respective fiber section

[1] Note that in [J3], the variable d defines the *optical* distance, whereat in this dissertation, the variable d is related to the *geometric* distance. Therefore, the refractive index n_{air} of air has been added to the formalism presented in this appendix where applicable.

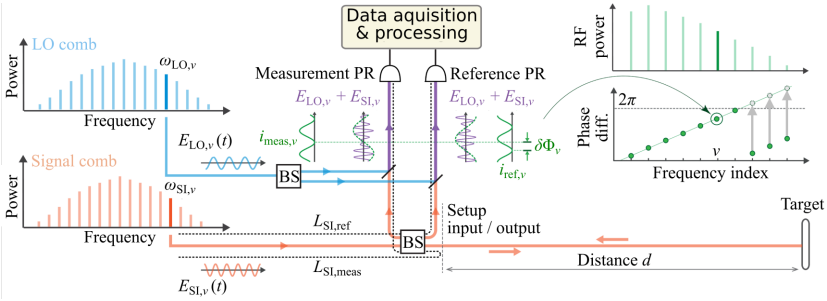

Figure D.1: Multi-heterodyne interferometry based on frequency combs. Measurement principle: The signal comb (orange) and the LO comb (blue) consist of discrete tones at frequencies $\omega_{\mathrm{SI},\mu}$ and $\omega_{\mathrm{LO},\mu}$. Both combs are split at beam splitters (BS). A first part of the signal comb is sent to the target located at a distance d from the setup input/output. The target scatters a part of the incident light back into the setup, where the signal comb is superimposed with a first part of the LO comb on a balanced photoreceiver (Measurement PR), indicated by violet beams and fields for a specific pair of lines with comb line index ν. The other parts of both combs are guided towards another balanced photoreceiver (Reference PR). For the first part of the signal comb, the optical distance to measurement photoreceiver amounts to $L_{\mathrm{SI}} = L_{\mathrm{SI,meas}} + 2n_{\mathrm{air}}d$, comprising the free-space distance $n_{\mathrm{air}}d$ and a total setup-internal optical distance $L_{\mathrm{SI,meas}}$, see Eqs. (D.1) and (D.2). Similarly, $L_{\mathrm{SI}} = L_{\mathrm{SI,ref}}$ denotes the optical distance that the second portion of the signal comb travels from the source to the reference photoreceiver. The quantities $L_{\mathrm{LO}} = L_{\mathrm{LO,meas}}$ and $L_{\mathrm{LO}} = L_{\mathrm{LO,ref}}$ are defined accordingly, but not shown in the figure for better readability. The superposition of the combs on the measurement PR and the reference PR leads to a multitude of beat notes in the RF spectrum of the respective photocurrent (green) at frequencies $\Delta\omega_\nu = \left|\omega_{\mathrm{LO},\nu} - \omega_{\mathrm{SI},\nu}\right|$, which can be separated by a Fourier transform of a recorded time domain signal of the photodetector currents. The phase difference $\delta\Phi_\nu$ between the ν-th frequency component of both currents depends on the distance to the target. The distance is obtained by estimating the slope of the phase differences as a function of the frequency index. Phase differences that would exceed 2π are unwrapped, as indicated by the gray arrows.

as well as its frequency-dependent effective refractive index, see Section D.4 “Analysis and modelling of fiber dispersion”.

In our experiment, we use two balanced receivers with two photodiodes (PD) each. Because a PD is basically a photon counter, it reacts to the incident optical power P impinging on its photosensitive area A_{PD} with a current i, which is in proportion to the PD responsivity $\mathcal{R}$ and the power P. The intensity is expressed by the square of the real part $\Re\{\cdot\}$ of the complex electric field, averaged over a few optical periods $\langle\cdot\rangle$ and divided by the free-space wave

impedance Z_0. The power results from multiplying the intensity with the PD area A_{PD}. This leads to

$$i(t) = \mathcal{R}P(t), \quad P(t) = \frac{A_{\mathrm{PD}}}{Z_0}\left\langle \left(\Re\left\{\underline{E}\,(t)\right\}\right)^2 \right\rangle. \tag{D.3}$$

The balanced detector comprises two PD with individual currents i_1 and i_2,

$$i_1\left(L_{\mathrm{SI}}, L_{\mathrm{LO}}, t\right) = \mathcal{R}\frac{A_{\mathrm{PD}}}{Z_0}\left\langle \left(\Re\left\{\frac{1}{\sqrt{2}}\underline{E}_{\mathrm{SI}}(L_{\mathrm{SI}}, t) - \mathrm{j}\frac{1}{\sqrt{2}}\underline{E}_{\mathrm{LO}}(L_{\mathrm{LO}}, t)\right\}\right)^2 \right\rangle, \tag{D.4}$$

$$i_2\left(L_{\mathrm{SI}}, L_{\mathrm{LO}}, t\right) = \mathcal{R}\frac{A_{\mathrm{PD}}}{Z_0}\left\langle \left(\Re\left\{-\mathrm{j}\frac{1}{\sqrt{2}}\underline{E}_{\mathrm{SI}}(L_{\mathrm{SI}}, t) + \frac{1}{\sqrt{2}}\underline{E}_{\mathrm{LO}}(L_{\mathrm{LO}}, t)\right\}\right)^2 \right\rangle. \tag{D.5}$$

The output current i of the balanced receiver is given by the difference of these photocurrents,

$$\begin{aligned}
i\left(L_{\mathrm{SI}}, L_{\mathrm{LO}}, t\right) &= i_1\left(L_{\mathrm{SI}}, L_{\mathrm{LO}}, t\right) - i_2\left(L_{\mathrm{SI}}, L_{\mathrm{LO}}, t\right) \\
&= \mathcal{R}\frac{A_{\mathrm{PD}}}{Z_0}\frac{1}{2}\left\langle \mathrm{j}\underline{E}_{\mathrm{SI}}\left(L_{\mathrm{SI}}, t\right)\underline{E}^*_{\mathrm{LO}}\left(L_{\mathrm{LO}}, t\right)\right. \\
&\qquad \left. - \mathrm{j}\underline{E}^*_{\mathrm{SI}}\left(L_{\mathrm{SI}}, t\right)\underline{E}_{\mathrm{LO}}\left(L_{\mathrm{LO}}, t\right)\right\rangle \\
&= \mathcal{R}\frac{A_{\mathrm{PD}}}{Z_0}\Im\left\{\underline{E}^*_{\mathrm{SI}}\left(L_{\mathrm{SI}}, t\right)\underline{E}_{\mathrm{LO}}\left(L_{\mathrm{LO}}, t\right)\right\} \\
&= \mathcal{R}\frac{A_{\mathrm{PD}}}{Z_0}\Im\left\{\sum\nolimits_{\mu,\mu'}\underline{E}^*_{\mathrm{SI},\mu,0}\underline{E}_{\mathrm{LO},\mu',0}\right. \\
&\qquad \times \mathrm{e}^{\mathrm{j}\left(\omega_{\mathrm{LO},0}-\omega_{\mathrm{SI},0}+(\mu'-\mu)\omega_{\mathrm{SI,FSR}}+\mu'\left(\omega_{\mathrm{LO,FSR}}-\omega_{\mathrm{SI,FSR}}\right)\right)t} \\
&\qquad \left. \times \mathrm{e}^{\mathrm{j}\left(\omega_{\mathrm{SI},\mu}L_{\mathrm{SI}}/c_0-\omega_{\mathrm{LO},\mu'}L_{\mathrm{LO}}/c_0\right)}\right\},
\end{aligned} \tag{D.6}$$

where $\Im\{\cdot\}$ denotes the imaginary part. For an ideal balanced detector, the current difference $i\left(L_{\mathrm{SI}}, L_{\mathrm{LO}}, t\right)$ is mean-free, as DC terms of the individual PD currents cancel. The quantity $i\left(L_{\mathrm{SI}}, L_{\mathrm{LO}}, t\right)$ comprises discrete sinusoidals, one of which is indicated in green in Fig. D.1. Substituting the optical path lengths

traversed by the signal and the LO comb up to the balanced measurement receiver into Eq. (D.6) yields the photocurrent

$$i_{\mathrm{meas}}\left(2n_{\mathrm{air}}d, t\right) = i_{\mathrm{meas}}\left(L_{\mathrm{SI,meas}} + 2n_{\mathrm{air}}d, L_{\mathrm{LO,meas}}, t\right). \tag{D.7}$$

The distance d of interest can be extracted from the phase of the various beat notes in the photocurrent. However, as can be seen from Eq. (D.6), these phases also depend on the phase of the product of the complex field amplitudes $\underline{E}^{*}_{\mathrm{SI},\mu,0}\underline{E}_{\mathrm{LO},\mu',0}$. Therefore a reference measurement is required, which is obtained by superimposing separate parts of the same frequency combs on a separate reference photoreceiver, see also [20]. The photocurrent i_{ref} of the balanced reference receiver is derived in an analogous way as i_{meas},

$$i_{\mathrm{ref}}\left(t\right) = i_{\mathrm{ref}}\left(L_{\mathrm{SI,ref}}, L_{\mathrm{LO,ref}}, t\right). \tag{D.8}$$

In contrast to Eq. (D.7), the external measurement distance $2n_{\mathrm{air}}d$ does not appear in the reference path length.

The repetition rate detuning $\Delta\omega_{\mathrm{FSR}} = \left|\omega_{\mathrm{LO,FSR}} - \omega_{\mathrm{SI,FSR}}\right|$ between the two frequency combs amounts to $\Delta\omega_{\mathrm{FSR}} = 2\pi \times 100\,\mathrm{MHz}$ and is small compared to the line spacing of $\omega_{\mathrm{SI,FSR}} = 2\pi \times 100\,\mathrm{GHz}$. In theory, the photocurrent spectrum shows beat signals at distinct intermediate frequencies

$$\Delta\omega_{\mu,\mu'} = \left|\omega_{\mathrm{LO},0} - \omega_{\mathrm{SI},0} + \left(\mu' - \mu\right)\omega_{\mathrm{SI,FSR}} + \mu'\Delta\omega_{\mathrm{FSR}}\right|. \tag{D.9}$$

However, only a subset of these lines can actually be acquired by the photodetector and the subsequent analog-to-digital converter (ADC). For the frequency combs deployed in our experiments, the line spacing $\omega_{\mathrm{SI,FSR}}/(2\pi)$ amounts to 100 GHz and is larger than the bandwidth $f_{\mathrm{ADC}} = 33\,\mathrm{GHz}$ of the ADC used to record the signals. Moreover, the number of comb lines in the radio frequency domain satisfies $\mu'\Delta\omega_{\mathrm{FSR}} < \omega_{\mathrm{SI,FSR}}/2 \approx \omega_{\mathrm{LO,FSR}}/2$ for all comb line indices μ', which avoids comb line ambiguity in the intermediate frequency beat notes. As a consequence, for a given LO comb line μ', only the beat note with the corresponding signal comb line having the same index $\mu' = \mu$ shows up in the photocurrent. These beat notes are found at frequencies $\Delta\omega_{\mu} = \left|\Delta\omega_0 + \mu\Delta\omega_{\mathrm{FSR}}\right|$ with $\Delta\omega_0 = \left|\omega_{\mathrm{LO},0} - \omega_{\mathrm{SI},0}\right|$ being the difference of the center frequencies of the two combs. The beat notes, shown in the upper right of Fig. D.1 as a function of frequency index μ, can be identified and extracted by a discrete Fourier transform (DFT) applied to the time-domain

photocurrents recorded by the oscilloscope. The complex Fourier coefficients comprise the amplitude and the phase information of the associated beat notes.

The global phases $\Phi_{\mu,\mathrm{meas}}$ and $\Phi_{\mu,\mathrm{ref}}$ of these beat notes in the photocurrents i_{meas} and i_{ref} depend on the various distances $L_{\mathrm{SI,meas}}$, $2n_{\mathrm{air}}d$, $L_{\mathrm{LO,meas}}$, $L_{\mathrm{SI,ref}}$, and $L_{\mathrm{LO,ref}}$ that the signal comb and the reference comb have traveled from the respective source to the respective detector. Expressions for these global phases of each individual beat note can be derived from Eq. (D.6) – (D.8) by setting $\mu' = \mu$,

$$\begin{aligned}
\Phi_{\mu,\mathrm{meas}}(d) =& \arg\left\{\underline{E}^{*}_{\mathrm{SI},\mu,0}\underline{E}_{\mathrm{LO},\mu,0}\mathrm{e}^{\mathrm{j}\left(\omega_{\mathrm{SI},\mu}\left(L_{\mathrm{SI,meas}}+2n_{\mathrm{air}}d\right)/c_0-\omega_{\mathrm{LO},\mu}L_{\mathrm{LO,meas}}/c_0\right)}\right\}\\
=&\frac{\omega_{\mathrm{SI},0}+\mu\omega_{\mathrm{SI,FSR}}}{c_0}\left(L_{\mathrm{SI,meas}}-L_{\mathrm{LO,meas}}+2n_{\mathrm{air}}d\right)\\
&-\frac{\Delta\omega_0+\mu\Delta\omega_{\mathrm{FSR}}}{c_0}L_{\mathrm{LO,meas}}+\arg\left\{\underline{E}^{*}_{\mathrm{SI},\mu,0}\underline{E}_{\mathrm{LO},\mu,0}\right\}\\
=&2\pi\left(L_{\mathrm{SI,meas}}-L_{\mathrm{LO,meas}}+2n_{\mathrm{air}}d\right)\Lambda^{-1}_{\mathrm{S},\mu}\\
&+2\pi\left(L_{\mathrm{SI,meas}}-L_{\mathrm{LO,meas}}+2n_{\mathrm{air}}d\right)\Lambda^{-1}_{\mathrm{S},0}\\
&-\frac{\Delta\omega_{\mathrm{SI},0}+\mu\Delta\omega_{\mathrm{SI,FSR}}}{c_0}L_{\mathrm{LO,meas}}+\arg\left\{\underline{E}^{*}_{\mathrm{SI},\mu,0}\underline{E}_{\mathrm{LO},\mu,0}\right\},
\end{aligned}\tag{D.10}$$

$$\begin{aligned}
\Phi_{\mu,\mathrm{ref}} =& \arg\left\{\underline{E}^{*}_{\mathrm{SI},\mu,0}\underline{E}_{\mathrm{LO},\mu,0}\mathrm{e}^{\mathrm{j}\left(\omega_{\mathrm{SI},\mu}L_{\mathrm{SI,ref}}/c_0-\omega_{\mathrm{LO},\mu}L_{\mathrm{LO,ref}}/c_0\right)}\right\}\\
=&\frac{\omega_{\mathrm{SI},0}+\mu\omega_{\mathrm{SI,FSR}}}{c_0}\left(L_{\mathrm{SI,ref}}-L_{\mathrm{LO,ref}}\right)\\
&-\frac{\Delta\omega_0+\mu\Delta\omega_{\mathrm{FSR}}}{c_0}L_{\mathrm{LO,ref}}+\arg\left\{\underline{E}^{*}_{\mathrm{SI},\mu,0}\underline{E}_{\mathrm{LO},\mu,0}\right\}\\
=&2\pi\left(L_{\mathrm{SI,ref}}-L_{\mathrm{LO,ref}}\right)\Lambda^{-1}_{\mathrm{S},\mu}\\
&+2\pi\left(L_{\mathrm{SI,ref}}-L_{\mathrm{LO,ref}}\right)\Lambda^{-1}_{\mathrm{S},0}\\
&-\frac{\Delta\omega_{\mathrm{SI},0}+\mu\Delta\omega_{\mathrm{SI,FSR}}}{c_0}L_{\mathrm{LO,ref}}+\arg\left\{\underline{E}^{*}_{\mathrm{SI},\mu,0}\underline{E}_{\mathrm{LO},\mu,0}\right\}.
\end{aligned}\tag{D.11}$$

In these relations, the function $\arg\{\underline{z}\}$ denotes the phase angle of a complex number $\underline{z}$. The last lines of Eq. (D.10) and (D.11) contain the so-called synthetic wavelength $|\Lambda_{\mathrm{S},\mu}| = |c_0/(\mu\,\omega_{\mathrm{SI,FSR}}/(2\pi))|$ and reveal the relation to classical

interferometry with a single optical wavelength λ, where the phase shift φ experienced by an optical signal after propagation over the optical path length L_{path} is determined by $\varphi = 2\pi L_{\text{path}}\lambda^{-1}$. For an increasing mode index μ, the synthetic wavelength progressively reduces.

The global phases of the beat notes in the reference and the measurement photocurrent depend also on the initial global phases $\arg\left\{\underline{E}^{*}_{\text{SI},\mu,0}\underline{E}_{\text{LO},\mu,0}\right\}$ of the associated optical comb tones. These unknown global phases can be eliminated by calculating the phase differences observed after the reference and the measurement detector,

$$\begin{aligned}\delta\Phi_{\mu}(d) =& \Phi_{\mu,\text{meas}}(d) - \Phi_{\mu,\text{ref}} \\ =& \frac{\omega_{\text{SI},0} + \mu\omega_{\text{SI,FSR}}}{c_0}\left(L_{\text{SI,meas}} + 2n_{\text{air}}d - L_{\text{LO,meas}} - L_{\text{SI,ref}} + L_{\text{LO,ref}}\right) \\ &- \frac{\Delta\omega_0 + \mu\Delta\omega_{\text{FSR}}}{c_0}\left(L_{\text{LO,meas}} - L_{\text{LO,ref}}\right). \end{aligned} \tag{D.12}$$

We can further eliminate all expressions that depend on the internal optical path lengths $L_{\text{SI,meas}}$, $L_{\text{LO,meas}}$, $L_{\text{SI,ref}}$, and $L_{\text{LO,ref}}$ by directly subtracting the phase values $\delta\Phi_{\mu}(d_0)$ obtained from a calibration measurement for a specific distance d_0 from the phases $\delta\Phi_{\mu}(d)$ obtained for the target distance d,

$$\begin{aligned}\Delta\Phi_{\mu}(d, d_0) &= \delta\Phi_{\mu}(d) - \delta\Phi_{\mu}(d_0) \\ &= \mu\frac{\omega_{\text{SI,FSR}}}{c_0}2n_{\text{air}}(d - d_0) + \frac{\omega_{\text{SI},0}}{c_0}2n_{\text{air}}(d - d_0) \\ &= D(d, d_0)\,\mu + \Delta\Phi_0(d, d_0). \end{aligned} \tag{D.13}$$

Note that this subtraction also eliminates contributions of fiber dispersion, see Section D.4 “Analysis and modelling of fiber dispersion”.
Equation (D.13) exhibits a linear relation between the phase difference $\Delta\Phi_{\mu}$ and the mode index μ and is used to determine the distance by extracting the slope of $\Delta\Phi_{\mu}$ as a function of μ. We unwrap $\Delta\Phi_{\mu}$ and fit a straight line to the measurement by a least-squares fit

$$\begin{aligned}\min_{D,\Delta\Phi_0}\sum\nolimits_{\mu=-N_{\text{FC}}/2+1}^{N_{\text{FC}}/2}\left(\Delta\Phi_{\mu,\text{meas}} - \Delta\Phi_{\mu,\text{fit}}\right)^2, \\ \Delta\Phi_{\mu,\text{fit}} = D(d, d_0)\,\mu + \Delta\Phi_0(d, d_0). \end{aligned} \tag{D.14}$$

From the fit coefficient $D\,(d, d_0) = \frac{\omega_{\mathrm{SI,FSR}}}{c_0}\, 2n_{\mathrm{air}}\,(d - d_0)$ we extract $d - d_0$. To this end, the FSR $\omega_{\mathrm{SI,FSR}}$ is assumed to be accurately known, while the phase offset $\Delta\Phi_0\,(d, d_0)$ in Eq. (D.13) is a fit parameter.

In some cases, it is not practical to directly subtract the phases $\delta\Phi_\mu\,(d_0)$ obtained from the calibration measurement from the phases $\delta\Phi_\mu\,(d)$ obtained from the measurement to the target. This is, e.g., the case when the calibration measurement is repeated multiple times, followed by averaging to reduce the uncertainty of the distance d_0. In this case, it is necessary to first extract the distance d_0 from the slope of the phase values $\delta\Phi_\mu\,(d_0)$ with respect to μ and then to use this result for averaging and for calibration of all subsequent measurements to the actual target. It must then be taken into account that both the phases $\delta\Phi_\mu\,(d_0)$ and $\delta\Phi_\mu\,(d)$ do not any more depend strictly linearly on the mode index μ due to fiber dispersion. In Eq. (D.12), fiber dispersion enters through a frequency-dependence of the optical path lengths $L_{\mathrm{SI,meas}}$, $L_{\mathrm{LO,meas}}$, $L_{\mathrm{SI,ref}}$, and $L_{\mathrm{LO,ref}}$, which leads to a dependence of $\delta\Phi_\mu$ on higher powers of the mode index μ in addition to the linear dependence which contains the distances of interest d_0 and d. The dependence on higher powers of μ must also be taken into account when unwrapping the phases $\delta\Phi_\mu$ as a function of μ, e.g., by choosing the 2π-complements of the measured phases such that the unwrapped phase sequence describes a parabola or a higher-order polynomial rather than a straight line. Details on the impact of fiber dispersion and its modelling are described in Section D.4 “Analysis and modelling of fiber dispersion”.

It is important to note that the calibration measurement for a specific distance d_0 is only valid as long as the internal optical path lengths $L_{\mathrm{SI,meas}}$, $L_{\mathrm{LO,meas}}$, $L_{\mathrm{SI,ref}}$, and $L_{\mathrm{LO,ref}}$ do not change. In practical systems, however, fibers are subject to environmental influences such as varying temperature or vibration, leading to a change of the optical path lengths of the order of micrometers per second per meter [20], see Fig. D.3(e) and the corresponding explanation. For measurements at highest accuracy over an extended time period, it is hence important to perform the calibration measurements either simultaneously with the actual measurement or to continuously repeat them in a sufficiently quick sequence. This minimizes the associated errors and allows to separate systematic measurement errors from any drift in the optical setup and the fibers. In a technical implementation of a measurement system, the impact of fiber drift can be mitigated by minimizing the fiber lengths, or by introducing

a calibration mirror into the system. The advantage of a calibration mirror is exemplified in Fig. D.3(e).

D.2 Tracking of free spectral ranges of frequency combs

The distance $d - d_0$ as extracted from a linear fit of the phases according to Eq. (D.14) depends on the line spacing $\omega_{\mathrm{SI,FSR}}$ of the signal comb, which may be subject to drift. For a high measurement accuracy, this line spacing must be continuously tracked. To this end, we first determine the line spacing $\omega_{\mathrm{LO,FSR}}$ of the LO comb and then derive $\omega_{\mathrm{SI,FSR}} = \omega_{\mathrm{LO,FSR}} + \Delta\omega_{\mathrm{FSR}}$ from the known spacing $\Delta\omega_{\mathrm{FSR}}$ of the baseband beat notes. To measure the LO line spacing $\omega_{\mathrm{LO,FSR}}$, a part of the LO pump laser light is modulated using a Mach-Zehnder modulator (MZM) at a fixed frequency $f_{\mathrm{mod}} = 30.85\,\mathrm{GHz}$, such that strong third-order sidebands are generated at $\omega_{\mathrm{LO},0} \pm 3 \times 2\pi f_{\mathrm{mod}}$. The modulated LO pump signal and the LO comb are superimposed, and the line spacing $\omega_{\mathrm{LO,FSR}}$ is derived by measuring the frequency $\left|\omega_{\mathrm{LO,FSR}} - 3 \times 2\pi f_{\mathrm{mod}}\right|$ of the RF beat note, which results from the difference frequency of $\omega_{\mathrm{LO},0} \pm 3 \times 2\pi f_{\mathrm{mod}}$ and the nearest comb lines $\omega_{\mathrm{LO},0} \pm \omega_{\mathrm{LO,FSR}}$. The accuracy of this measurement is dictated by the accuracy of the RF frequency references used to generate the modulation signal and to determine the RF beat note. These references typically feature relative accuracies of better than 10^{-7}, which can be improved to better than 10^{-12} by using commercially available GPS-disciplined oscillators.

D.3 Digital signal processing

For each distance evaluation in our experiment, two time traces (measurement and reference) are recorded using a high-speed real-time oscilloscope (Keysight DSO-X 93204A) as for analogue-to-digital conversion at a sample rate of 80 GSa/s and an effective number of bits ENOB ≈ 5. Depending on the target, the length of the recording varies between 100 μs and 12 ms. These recordings are then resampled and subdivided into segments, each corresponding to a single distance measurement. The minimum length of these segments for separating the beat notes at $\Delta\omega_\mu = |\Delta\omega_0 + \mu\Delta\omega_{\mathrm{FSR}}|$ is given by

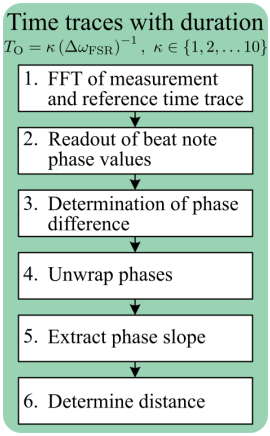

Figure D.2: Scheme of digital signal processing for obtaining distance information for a single distance measurement. First, an FFT of the measurement and the reference time trace is performed. To avoid aliasing, we choose the observation time T_O to be a multiple of the inverse difference of the free spectral ranges of the two combs, $T_O = \kappa\ (\Delta\omega_{FSR})^{-1}$, $\kappa \in \{1, 2, \ldots, 10\}$. Afterwards, the phase values of the beat notes $\Phi_{\mu,\mathrm{meas}}$ and $\Phi_{\mu,\mathrm{ref}}$ are extracted from each spectrum. Then, their pair-wise difference $\delta\Phi_\mu$ is computed according to Eq. (D.12). The slope of the unwrapped phase differences is extracted via a least-squares fit, from which the distance can be determined.

$(2\pi/\Delta\omega_{FSR}) \times 80\,\mathrm{GSa/s} \approx 10.4\,\mathrm{ns} \times 80\,\mathrm{GSa/s} \approx 800\,\mathrm{Sa}$. Further processing of these segments follows the theory described in the previous Section D.1 "Mathematical description of distance metrology scheme", and is illustrated in Fig. D.2. In a first step, we calculate the Fourier transform of each segment and read out the phases at the various beat notes. We then subtract the phases of the reference beat notes from those of the measurement beat notes, see Eq. (D.12), and unwrap the resulting phase differences, considering a potentially nonlinear relationship of $\delta\Phi_\mu\ (d)$ on μ see Section D.4 "Analysis and modelling of fiber dispersion". The distance is then evaluated by determining the slope of the phase differences as a function of the comb line index μ, see Eq. (D.14). The overall scheme is repeated, until the full time trace has been analyzed.

Note that our measurement technique does not only provide distance values but also a parameter that indicates the validity of the respective measurement: For determining the phase slope, a linear function is fitted to the measured phase differences and the residuals $\Delta\Phi_{\mu,\mathrm{meas}} - \Delta\Phi_{\mu,\mathrm{fit}}$ computed. We then calculate

Table D.1: Percentage of reliable data points of distance measurements.

Measurement target	**Figure showing measurement**	**Section of distance measurement**	**Percentage of reliable data points**
Static mirror	Fig. D.6(a)	Overall	99.97 %
Mirror on moveable stage	Fig. D.3(b) (for one position of target mirror)	100 μs segments highlighted in Fig. D.3(b)	68 % . . . 99 %
Rotating disk	Fig. 5.3(b)	Overall	49 % (blue) 43 % (green)
	Fig. 5.3(b), Inset 1	Bottom of groove	61 % (blue) 80 % (green)
Air gun projectile	Fig. 5.3(d)	Thickest section: z = 1.99 mm . . . 2.40 mm	89 %
		After waist: z = 3.45 mm . . . end	67 %
		Inclined surface normal: z = 0.34 mm . . . 1.99 mm z = 2.40 mm . . . 3.32 mm	8 %

the Euclidean norm of this phase residual vector and normalize it to the number of comb lines N_{FC},

$$\varepsilon = \frac{1}{N_{\mathrm{FC}}} \sqrt{\sum_{\mu=-N_{\mathrm{FC}}/2+1}^{N_{\mathrm{FC}}/2} \left(\Delta\Phi_{\mu,\mathrm{meas}} - \Delta\Phi_{\mu,\mathrm{fit}}\right)^2}. \tag{D.15}$$

Large values of ε indicate phase difference values that do not follow a perfect linear trend, e.g., as a consequence of improper unwrapping of the phase differences, which may be caused by a weak back-scattered signal that leads to large phase uncertainties. By defining a threshold value for ε, reliable distance data $D \propto d - d_0$ according to Eq. (D.14) can be distinguished from their unreliable counterparts. The percentage of reliable data points depends on the back-coupled intensity of the respective sample, and is listed in Table D.1 for the various experiments. As expected, the percentage of reliable data points is high for plane surfaces with high levels of back-scattered power, but decreases for weak back-scattering levels that may result from surface tilted with respect to the axis of the illuminating beam.

D.4 Analysis and modelling of fiber dispersion

In Eq. (D.12), the optical path lengths $L_{\mathrm{SI,meas}}$, $L_{\mathrm{LO,meas}}$, $L_{\mathrm{SI,ref}}$, and $L_{\mathrm{LO,ref}}$ depend on the geometric lengths $L^{(\mathrm{g})}_{\mathrm{SI,meas}}$, $L^{(\mathrm{g})}_{\mathrm{LO,meas}}$, $L^{(\mathrm{g})}_{\mathrm{SI,ref}}$, and $L^{(\mathrm{g})}_{\mathrm{LO,ref}}$ and the frequency-dependent effective refractive index $n_{\mathrm{e}}(\omega)$ of the fibers involved, which leads to a frequency-dependent propagation constant $\beta(\omega)$ in the propagator $\exp\left(-\mathrm{j}\,(\omega/c_0)\,n_{\mathrm{e}}(\omega)\,L^{(\mathrm{g})}\right) = \exp\left(-\mathrm{j}\beta(\omega)\,L^{(\mathrm{g})}\right)$. For analysis and modelling of fiber dispersion, the frequency-dependent propagation constant of the optical fibers $\beta(\omega)$ is expanded into a Taylor series around a reference frequency ω_0,

$$\begin{aligned}\beta(\omega) =& \beta_0^{(0)} + \beta_0^{(1)}(\omega-\omega_0) + \frac{1}{2}\beta_0^{(2)}(\omega-\omega_0)^2 + \ldots, \\ \omega_0 =& \frac{\omega_{\mathrm{LO},0}+\omega_{\mathrm{SI},0}}{2}, \quad \beta_0^{(n)} = \frac{\mathrm{d}^n}{\mathrm{d}\omega^n}\beta(\omega)\bigg|_{\omega=\omega_0}.\end{aligned} \tag{D.16}$$

For propagation of the combs in air, we neglect dispersion and assume refractive index n_{air} to be constant, leading to a propagation constant of $(\omega_{\mathrm{SI},\mu}/c_0)\,n_{\mathrm{air}}$. Terminating the Taylor expansion of $\beta(\omega)$ after the second order, we can derive the relation between the phase differences $\delta\Phi(d)$ and the mode index μ by using Eqs. (D.10) and (D.11),

$$\begin{aligned}\delta\Phi(d) =& \Phi_{\mu,\mathrm{meas}} - \Phi_{\mu,\mathrm{ref}} \\ =& \beta(\omega_{\mathrm{SI},\mu})\left(L^{(\mathrm{g})}_{\mathrm{SI,meas}} - L^{(\mathrm{g})}_{\mathrm{SI,ref}}\right) \\ & - \beta(\omega_{\mathrm{LO},\mu})\left(L^{(\mathrm{g})}_{\mathrm{LO,meas}} - L^{(\mathrm{g})}_{\mathrm{LO,ref}}\right) + (\omega_{\mathrm{SI},\mu}/c_0)\,n_{\mathrm{air}}2d \\ =& C_0 + \mu C_1 + \mu^2 C_2 + \mu\,(\omega_{\mathrm{SI,FSR}}/c_0)\,n_{\mathrm{air}}2d,\end{aligned} \tag{D.17}$$

where

$$\begin{aligned} C_0 = &\left(\beta_0^{(0)} + \beta_0^{(1)}\left(\omega_{\mathrm{SI},0} - \omega_0\right)\right)\left(L^{(\mathrm{g})}_{\mathrm{SI,meas}} - L^{(\mathrm{g})}_{\mathrm{SI,ref}}\right) \\ &- \left(\beta_0^{(0)} + \beta_0^{(1)}\left(\omega_{\mathrm{LO},0} - \omega_0\right)\right)\left(L^{(\mathrm{g})}_{\mathrm{LO,meas}} - L^{(\mathrm{g})}_{\mathrm{LO,ref}}\right) \\ &+ \frac{1}{2}\beta_0^{(2)}\left(\omega_{\mathrm{SI},0} - \omega_0\right)^2\left(L^{(\mathrm{g})}_{\mathrm{SI,meas}} - L^{(\mathrm{g})}_{\mathrm{SI,ref}}\right) \\ &- \frac{1}{2}\beta_0^{(2)}\left(\omega_{\mathrm{LO},0} - \omega_0\right)^2\left(L^{(\mathrm{g})}_{\mathrm{LO,meas}} - L^{(\mathrm{g})}_{\mathrm{LO,ref}}\right) \\ &+ \left(\omega_{\mathrm{SI},0}/c_0\right) n_{\mathrm{air}} 2d, \end{aligned} \tag{D.18}$$

$$\begin{aligned} C_1 = &\beta_0^{(1)}\,\omega_{\mathrm{SI,FSR}}\left(L^{(\mathrm{g})}_{\mathrm{SI,meas}} - L^{(\mathrm{g})}_{\mathrm{SI,ref}}\right) \\ &+ \beta_0^{(2)}\left(\omega_{\mathrm{SI},0} - \omega_0\right)\omega_{\mathrm{SI,FSR}}\left(L^{(\mathrm{g})}_{\mathrm{SI,meas}} - L^{(\mathrm{g})}_{\mathrm{SI,ref}}\right) \\ &- \beta_0^{(1)}\omega_{\mathrm{LO,FSR}}\left(L^{(\mathrm{g})}_{\mathrm{LO,meas}} - L^{(\mathrm{g})}_{\mathrm{LO,ref}}\right) \\ &- \beta_0^{(2)}\left(\omega_{\mathrm{LO},0} - \omega_0\right)\omega_{\mathrm{LO,FSR}}\left(L^{(\mathrm{g})}_{\mathrm{LO,meas}} - L^{(\mathrm{g})}_{\mathrm{LO,ref}}\right), \end{aligned} \tag{D.19}$$

$$C_2 = \frac{1}{2}\beta_0^{(2)}\left(\omega^2_{\mathrm{SI,FSR}}\left(L^{(\mathrm{g})}_{\mathrm{SI,meas}} - L^{(\mathrm{g})}_{\mathrm{SI,ref}}\right) - \omega^2_{\mathrm{LO,FSR}}\left(L^{(\mathrm{g})}_{\mathrm{LO,meas}} - L^{(\mathrm{g})}_{\mathrm{LO,ref}}\right)\right). \tag{D.20}$$

According to these equations, the phases $\delta\Phi_\mu\,(d)$ do not only depend linearly on the mode index μ, but also include higher orders such as μ^2. Note that considering the Taylor expansion beyond the second order in Eq. (D.16) would lead to a dependence on μ^3, μ^4 or higher orders in Eq. (D.17). These higher-order contributions must also be taken into account when unwrapping the phases $\delta\Phi_\mu$ as a function of μ, e.g., by choosing the 2π-complements of the measured phases such that the unwrapped phase sequence describes a parabola or a higher-order polynomial rather than a straight line. Importantly, the coefficients $C_1, C_2, \ldots$ depend only on the fixed setup-internal geometrical fiber lengths $L^{(\mathrm{g})}_{\mathrm{SI,meas}}$, $L^{(\mathrm{g})}_{\mathrm{LO,meas}}$, $L^{(\mathrm{g})}_{\mathrm{SI,ref}}$, and $L^{(\mathrm{g})}_{\mathrm{LO,ref}}$. The dependence of $\delta\Phi_\mu\,(d)$ on μ^2 and higher orders of μ can hence be eliminated by performing a calibration measurement over a specific distance d_0, see Section D.1 “Mathematical description of the distance metrology scheme”. The constant phase offset C_0

is currently not taken into account. In future implementations, C_0 could be used to improve the distance measurement accuracy by complementing the multi-heterodyne synthetic wavelength interferometry described here by interferometric measurements at the various optical frequencies $\omega_{\mathrm{SI},\mu}$, provided that these frequencies are known to sufficient accuracy.

D.5 Distance sweep with pointwise calibration measurement

To demonstrate the ability of our system to accurately measure distances over extended ranges without any cyclic error, we measure the distance to a movable mirror mounted on a high-accuracy feedback-stabilized positioning stage (Physik Instrumente, M511.HD), which has an accuracy of better than 50 nm. Signal acquisition for each position takes 45 s so that fiber drift [20] during the measurement must be taken into account, see the last paragraph of Section D.1 "Mathematical description of the distance metrology scheme" and Fig. D.3(e) as well as the associated explanations in Chapter 5 on the target position sweep beyond the unambiguity distance. To separate intrinsic measurement errors of our technique from any drift of the optical setup, the return signal is switched by a rotating chopper wheel (RCW) from a movable target mirror (TM) to a static calibration mirror (CM) and vice versa in intervals of approximately 300 μs, Fig. D.3(a). This is fast enough to eliminate the drift of the 5 m to 10 m long fiber paths in our setup. Figure D.3(b) shows an exemplary measurement: Two distinct levels are visible, indicated by orange (densely spaced) points. The transitions between the levels lead to an unreliable distance information and are discarded from further analysis. In our measurements, the distance close to zero refers to the calibration mirror. The difference between the two levels is computed by evaluating the data at the highest possible acquisition rate of 96 MHz, by performing an average over the shaded 100 μs wide sections, and by subtracting both averaged distances. In a first measurement, we determine the distance difference between target and calibration mirror for the first arbitrary position of the target mirror and use it as a zero-reference for all subsequent measurements. The target mirror is then stepped in increments of 50 μm, and the differences between target and calibration mirror distances are measured. The results are shown in Fig. D.3(c), where the set and measured

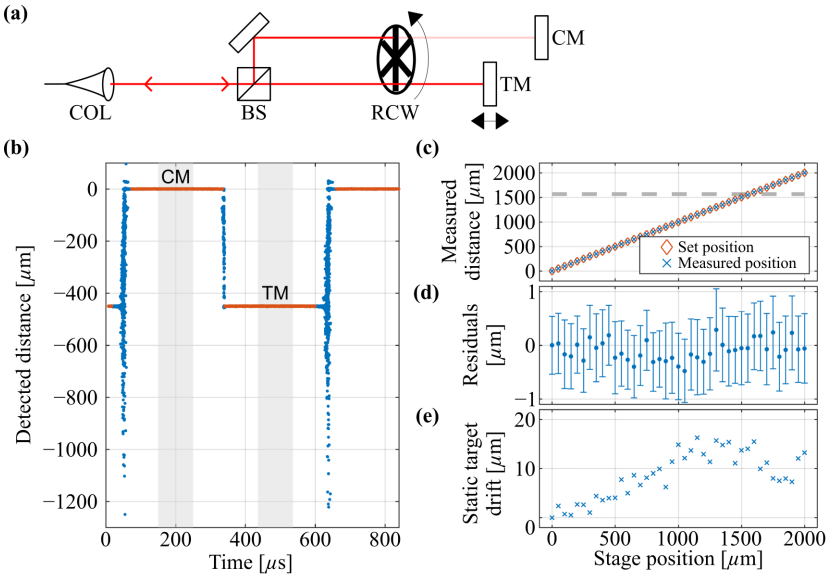

Figure D.3: Distance sweep reaching beyond the unambiguity distance of the system. (a) Experimental setup: The measurement beam leaves the setup via a fiber collimator (COL), is split by a beam splitter (BS) and sent to two mirrors, one fixed and serving as a calibration mirror (CM), and the other one mounted to a feedback-stabilized positioning stage, thus acting as a movable target mirror (TM). A rotating chopper wheel (RCW) ensures that only one signal from either of these mirrors is coupled back into the system at a certain instant in time. This allows independent measurements of the distance to the TM and to the fixed CM. (b) Measurement showing the distance profile as a function of time. The measured distances to CM and TM are indicated in orange, separated by noisy transitions (blue) during which signals were received from both mirrors. These transitions lead to an unreliable distance information and are discarded from further analysis. Gray shaded areas show sections over which the respective distance and standard deviation is evaluated. (c) Distance sweep of the target mirror beyond the unambiguity distance. Blue crosses denote distances measured by our system, whereas orange diamonds indicate the distance set by the stage. The unambiguity distance is marked by the gray dashed horizontal line at $d \approx 1500\,\mu$m; distance values beyond that line have been unwrapped manually. (d) Residual deviations ("residuals") between the measured distance to TM and the set distance. The residuals are of the same order of magnitude as the 50 nm positioning accuracy of the positioning stage. Error bars indicate the standard deviation of the residuals. (e) Drift of the distance to the CM as a function of time. With geometrical fiber lengths between 5 m and 10 m, a typical drift the optical path length in the order of $\mu\mathrm{m}/(\mathrm{s\,m})$ is observed [20].

positions are compared. The unambiguity distance amounts to about 1.5 mm and is marked by the gray dashed line.

Fig. D.3(d) shows the residual differences ("residuals") between the actually measured position and the distance set by the stage. Note that these residuals are of the same order of magnitude as the 50 nm positioning accuracy of the positioning stage, and that no cyclic error can be observed. The error bars in Fig. D.3(d) represent the standard deviation $\sigma_{d,\mathrm{diff}}$ of the measured distance difference between the measurement mirror and the calibration mirror. They are derived from the standard deviation of the measured distances to the target mirror $\sigma_{d,\mathrm{TM}}$ and the calibration mirror $\sigma_{d,\mathrm{CM}}$ within the gray sections,

$$\sigma_{d,\mathrm{diff}} = \sqrt{\sigma_{d,\mathrm{TM}}^2 + \sigma_{d,\mathrm{CM}}^2}. \tag{D.21}$$

Fig. D.3(e) shows the drift of the distance to calibration mirror position during the measurement, which is of the order of 15 μm and which we attribute to thermal drift of he optical path lengths of the fibers [20]. Neighboring data points were taken at intervals of approximately 45 s, dictated by the settling time of the stage and by the data acquisition speed.

D.6 Recording data for projectile measurements

To record a time trace of the signal scattered back from the projectiles, Fig. 5.3(c)-(e) in Chapter 5, the high-speed oscilloscope is configured to continuously acquire data and to record a sequence of defined length upon a trigger event. The stored sequence is defined to start 50 μs before the trigger event and to end 50 μs after the event. The oscilloscope trigger is then set to a level slightly above the signal retrieved from a reference mirror that is positioned behind the flight path of the projectiles. Triggering occurs as soon as the projectile enters the laser beam. Moving at a speed of 150 m/s, it takes around 50 μs for the 7.5 mm-long projectile to pass the beam. We can hence be sure that the entire profile is captured by the 100 μs recording.

D.7 Kerr soliton frequency comb generation in silicon nitride microresonators

Our work relies on integrated silicon-nitride (Si_3N_4) microresonators for the generation of dissipative Kerr soliton (DKS) frequency combs, see [21]. The Si_3N_4 platform is chosen because of its low optical losses and its compatibility with large-scale silicon-based processing [24]. The microresonators have a waveguide height of 800 nm to achieve anomalous group velocity dispersion, and are fabricated using the photonic Damascene process [85]. Neighboring resonances are spaced by approximately 95.8 GHz and have intrinsic quality (Q) factors exceeding 10^6. Dissipative Kerr soliton combs are established by linearly sweeping [21] the external-cavity pump laser through its nearest ring resonance from a blue-detuned wavelength to a predefined red-detuned wavelength [21]. This leads initially to the generation of a modulation-instability Kerr comb followed by DKS states once the resonance is crossed. Importantly, as soon as a multiple-soliton comb state is generated, the transition to a single-soliton state can be accomplished in a reliable and deterministic manner [120] by adjusting the laser frequency using the "backward tuning technique", which enables to selectively extinguish solitons, one by one until the single soliton state has been reached. Figure D.4 shows the experimental setup used for DKS generation. The soliton comb states are remarkably stable for many hours in a laboratory environment – even without employing any active stabilization techniques, such as locking of the laser Kerr shifted cavity detuning [J5]. This property is key to our distance measurements.

D.8 Measurement precision

The measurement precision[2] of our technique depends on the number of comb lines, the optical bandwidth that is covered by these combs, and on the power in the comb lines. In the following, we derive a relationship between the standard deviation σ_d of the measured distance d, the number N_{FC} of comb lines, the

[2] In the supplementary information of [J3], the text refers to the measurement "accuracy", however in the terminology of this thesis, the underlying physical quantity is the measurement "precision" and therefore the text changed where applicable, see also Chapter 5.

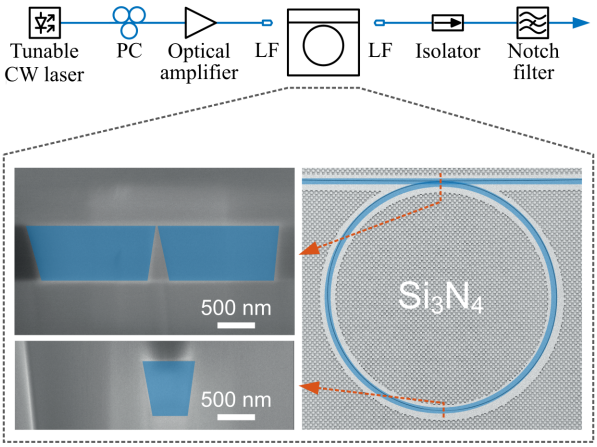

Figure D.4: Principle of soliton frequency comb generation in a high-Q silicon nitride (Si_3N_4) microresonator. The integrated photonic microresonator is pumped by a tunable continuous-wave (CW) laser, which is amplified by an erbium-doped fiber amplifier (Optical amplifier). A fiber polarization controller (PC) is used to optimize the power in the bus waveguide. Lensed fibers (LF) are used to couple light to the chip. After the microresonator, a notch filter suppresses remaining pump light, and an isolator prevents back-propagation of backscattered pump light. The insets show scanning electron microscope images of a Si_3N_4 microresonator with a radius of 240 μm. The checkerboard pattern around the bus and the ring waveguide results from the photonic Damascene fabrication process [85]. The left-hand side insets display cross-sections of the resonator waveguide at positions as indicated by the red arrows. The waveguide dimensions are 0.8 μm × 1.65 μm at the coupling point (top), while the tapered section with a cross-section of 0.8 μm × 0.6 μm acts as a local mode filter and suppresses higher-order modes [224] while preserving a high optical quality factor ($Q \approx 10^6$). (Figure adapted from [J5]).

optical bandwidth $\Omega_{\mathrm{SI,tot}} = N_{\mathrm{FC}}\omega_{\mathrm{SI,FSR}}$ of the signal comb, and the standard deviation σ_ϕ associated with measuring the optical phases of the various comb lines. According to Eq. (D.13), the relation between the ideal phase values $\Delta\Phi_\mu$ and the distance $(d - d_0)$ is given by

$$\Delta\Phi_\mu = \Delta\Phi_0\,(d, d_0) + \mu D\,(d, d_0)\,, \qquad D\,(d, d_0) = \frac{\omega_{\mathrm{SI,FSR}}}{c_0} 2n_{\mathrm{air}}\,(d - d_0)\,. \tag{D.22}$$

In the experiment, the estimation of D relies on actually measured phase values $\Delta\Phi_\mu^{(\mathrm{meas})}$ that contain phase noise $\phi_{\mathrm{n},\mu}$ representing the difference of the random phases of signal and LO line μ, so Eq. (D.22) becomes

$$\Delta\Phi_\mu^{(\mathrm{meas})} = \Delta\Phi_0 + \mu D + \phi_{\mathrm{n},\mu}. \tag{D.23}$$

The phase noise $\phi_{\mathrm{n},\mu}$ will lead to stochastic errors of the extracted slope D. In the following, we assume that the phase noise contributions $\phi_{\mathrm{n},\mu}$ are dominated by the uncertainty of the phases $\delta\Phi_\mu\,(d)$, which are obtained from the measurement of the distance d to the target, and not by the uncertainty of the phases $\delta\Phi_\mu\,(d_0)$ that are related to the calibration measurement to a target at distance d_0. This is justified by the fact that the calibration measurement to a static target can be performed at a much smaller acquisition rate and hence much bigger averaging times than the distance measurement to a rapidly moving target. We further assume that all noise contributions $\phi_{\mathrm{n},\mu}$ of the comb lines feature the same stochastic distribution and that they are statistically independent as well as mean-free. The standard deviation is denoted by $\sigma_{\phi,\mu} = \sigma_\phi \forall \mu$. The confidence interval of a slope D estimated from a linear regression of noisy ordinate data is proportional to the variance σ_D^2 of the slope, which, according to [225] can be expressed as

$$\sigma_D^2 = \frac{\sigma_\phi^2}{\sum_{\mu=1}^{N_{\mathrm{FC}}} (\mu - \overline{\mu})^2}. \tag{D.24}$$

In this relation, $\overline{\mu}$ denotes the mean of all abscissa values used for the regression. In the denominator of Eq. (D.24), the frequency index μ has been chosen to vary between 1 and N_{FC} to simplify the subsequent derivation. This differs from the convention used in the context of Eqs. (D.1) and (D.2), where μ could also assume negative values. Note that, by substituting the index, any other range of integers can be chosen, e.g., between $-\left(N_{\mathrm{FC}} - 1\right)/2$ and $+\left(N_{\mathrm{FC}} - 1\right)/2$ for odd integers N_{FC}, without changing the validity of the final results of this analysis. For the range chosen here, the mean value $\overline{\mu}$ is given by

$$\overline{\mu} = \frac{N_{\mathrm{FC}} + 1}{2}. \tag{D.25}$$

The denominator of Eq. (D.24) can thus be simplified to

$$\sum_{\mu=1}^{N_{\mathrm{FC}}} (\mu - \overline{\mu})^2 = \frac{N_{\mathrm{FC}}\left(N_{\mathrm{FC}}^2 - 1\right)}{12} \approx \frac{N_{\mathrm{FC}}^3}{12} \quad \text{for } N_{\mathrm{FC}} \gg 1. \tag{D.26}$$

With that, we can estimate the standard deviation σ_d of the measured distance d using Eq. (D.22),

$$\sigma_d = \frac{c_0}{2\omega_{\mathrm{SI,FSR}} n_{\mathrm{air}}} \sigma_D = \sqrt{\frac{12}{N_{\mathrm{FC}}^3}} \frac{c_0}{2\omega_{\mathrm{SI,FSR}} n_{\mathrm{air}}} \sigma_\phi = \sqrt{\frac{3}{N_{\mathrm{FC}}}} \frac{c_0}{\Omega_{\mathrm{SI,tot}} n_{\mathrm{air}}} \sigma_\phi. \tag{D.27}$$

For high-speed sampling, the number N_{FC} of optical lines is limited since a minimum observation time $T_{\mathrm{O,min}} = 2\pi/\Delta\omega_{\mathrm{FSR}} \geq N_{\mathrm{FC}}/f_{\mathrm{ADC}}$ is required to spectrally resolve the various baseband beat notes by a Fourier transformation, where f_{ADC} is the maximum analog bandwidth that the analogue-to-digital converter (ADC) of our oscilloscope can acquire. For a fixed total number N_{FC} of optical lines and a given standard deviation σ_ϕ of measured phase differences, the only option that remains for improving the measurement precision is thus to increase the overall optical bandwidth $\Omega_{\mathrm{SI,tot}} = N_{\mathrm{FC}}\omega_{\mathrm{SI,FSR}}$ of the comb, which requires a comb source that provides a large free spectral range $\omega_{\mathrm{SI,FSR}}$. DKS combs generated in microresonators stand out due to a unique combination of large optical bandwidth and large FSR, and are therefore perfectly suited for simultaneously achieving high acquisition rates and high measurement precision. Note that a large FSR is unavoidably linked to a small unambiguity distance $d_{\mathrm{ua}} = (c_0/2n_{\mathrm{air}})\ 2\pi/\omega_{\mathrm{SI,FSR}}$. For covering large measurement ranges, DKS-based distance metrology schemes hence need to be combined with simple, less accurate measurement techniques that allow selecting the correct unambiguity interval.

D.9 Fundamental limits of distance measurement precision

As described in the previous section, the standard deviation σ_d of the measured distance is proportional to the standard deviation σ_ϕ associated with the phase measurements of the individual beat notes. In the following, we estimate the

fundamental limit of the standard deviation of the distance measurement.
For an ideal comb generator without intensity noise or excess phase noise and for an ideal photodetector without thermal noise, this standard deviation is ultimately determined by quantum noise (shot noise). As before, we assume that the noise contributions from different comb lines feature the same stochastic (Poisson) distribution and that they are statistically independent. We further assume that the noise contributions of the recorded phases on the measurement photodetector are statistically independent from the noise contributions of the recorded phases on the reference photodetector, such that the associated variances $\sigma^2_{\phi,\mathrm{meas}}$ and $\sigma^2_{\phi,\mathrm{ref}}$ can be added to obtain the standard deviation associated with the phase difference, $\sigma^2_{\phi} = \sigma^2_{\phi,\mathrm{meas}} + \sigma^2_{\phi,\mathrm{ref}}$. For simplicity, we further assume that the noise of the phase measurements is the same on both photodetectors, $\sigma^2_{\phi,\mathrm{meas}} = \sigma^2_{\phi,\mathrm{ref}}$ that the optical power within each comb is distributed equally among all lines, $P_{\mathrm{SI},\mu} = P_{\mathrm{SI}}/N_{\mathrm{FC}}$, $P_{\mathrm{LO},\mu} = P_{\mathrm{LO}}/N_{\mathrm{FC}}$, and that the total optical power of the two combs is equal, $P_{\mathrm{SI}} = P_{\mathrm{LO}} = P_{\mathrm{FC}}$. As described in [226], the variance of the phase is related to the signal-to-noise ratio (SNR) of the signal according to

$$\sigma^2_{\phi,\mathrm{meas/ref}} = \frac{1}{2\,\mathrm{SNR}}, \qquad \sigma^2_{\phi} = \sigma^2_{\phi,\mathrm{meas}} + \sigma^2_{\phi,\mathrm{ref}} = \frac{1}{\mathrm{SNR}}. \tag{D.28}$$

For the SNR, we find the expression

$$\mathrm{SNR} = 2\frac{\mathcal{R}^2\,(P_{\mathrm{FC}}/N_{\mathrm{FC}})^2}{\sigma^2_{\mathrm{n,shot}}}, \qquad \sigma^2_{\mathrm{n,shot}} = 2q_{\mathrm{e}}\mathcal{R}\,(2P_{\mathrm{FC}})\,B_{\mathrm{eval}}. \tag{D.29}$$

Note that the shot noise contribution $\sigma^2_{\mathrm{n,shot}}$ is dictated by the total power $2P_{\mathrm{FC}}$ that is incident on the detector from both combs, and by the evaluation bandwidth B_{eval} (reciprocal observation time). For the variance of the phase difference we obtain

$$\sigma^2_{\phi} = 2q_{\mathrm{e}}\frac{N^2_{\mathrm{FC}}}{\mathcal{R}P_{\mathrm{FC}}}B_{\mathrm{eval}}. \tag{D.30}$$

Substituting Eq. (D.30) into Eq. (D.27), the variance of the measured distance can be estimated,

$$\sigma_{d,\mathrm{shot}}^2 = \frac{3}{N_{\mathrm{FC}}^3} \frac{c_0^2}{\omega_{\mathrm{SI,FSR}}^2 n_{\mathrm{air}}^2} 2q_{\mathrm{e}} \frac{N_{\mathrm{FC}}^2}{\mathcal{R} P_{\mathrm{FC}}} B_{\mathrm{eval}} = 6 \frac{q_{\mathrm{e}} c_0^2}{N_{\mathrm{FC}} \omega_{\mathrm{SI,FSR}}^2 n_{\mathrm{air}}^2} \frac{B_{\mathrm{eval}}}{\mathcal{R} P_{\mathrm{FC}}}. \quad \text{(D.31)}$$

According to Eq. (D.31), the variance increases in proportion to the evaluation bandwidth B_{eval}, and it decreases with the total power P_{FC} of each comb, with the line spacing $\omega_{\mathrm{SI,FSR}}$, and with the number N_{FC} of comb lines. Assuming a responsivity of $\mathcal{R} = 0.5\,\mathrm{A/W}$, an FFT bin width of $B_{\mathrm{eval}} = 100\,\mathrm{MHz}$, a number of $N_{\mathrm{FC}} = 100$ evaluated comb lines as well as a frequency comb mode spacing of $\omega_{\mathrm{SI,FSR}} = 2\pi \times 100\,\mathrm{GHz}$ (Rounded experimental parameters for the measurement towards a static mirror), Fig. D.5 shows the corresponding shot-noise limited distance uncertainty for comb powers from 1 mW to 100 mW at each photodetector. For a total comb power of each comb of 9 mW, i.e. of 4.5 mW at each of the two detectors, we find a measurement uncertainty of $\sigma_{d,\mathrm{shot}} = 9.9\,\mathrm{nm}$. Relating this value to an unambiguity distance of 1.5 mm, the relative standard deviation amounts to 6.6×10^{-6}. In practice, an optical amplifier is required for achieving a total comb power of 200 mW, and this will contribute additional noise. The red line in Fig. D.5 shows the distance uncertainties, if the noise factor 2 (3 dB) of an ideal optical amplifier is taken into consideration. Its noise reduces the SNR by a factor of 2, and therefore the distance uncertainties increase by a factor of $\sqrt{2}$.

D.10 Experimentally obtained standard deviation of measured distance

In practice, the standard deviation of the measured distance and therefore the measurement precision is impacted by slow thermal drift and by acoustic vibrations of the fiber-optic setup. These influences become relevant for large averaging times only. This is expressed by the Allan deviation depicted in Fig. 5.2(d) in Chapter 5. For a detailed analysis of the precision of the system, we need to eliminate the influence of thermal drift and acoustic vibrations from the noise-related inaccuracy of the optical ranging system itself. This is done by measuring the distance to a static target over an extended period of time, and by applying a high-pass filter to the acquired sequence of computed

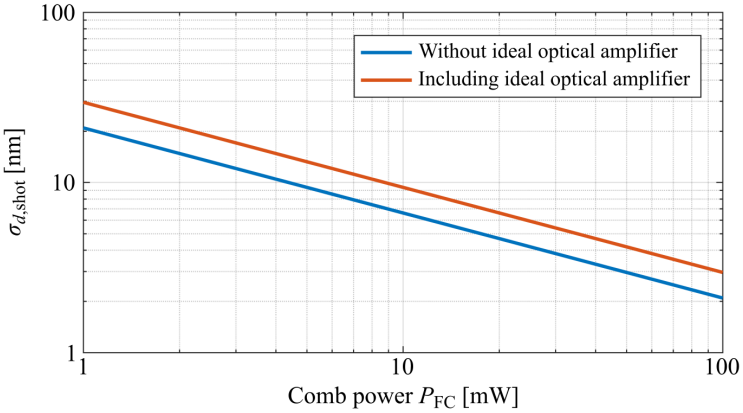

Figure D.5: Standard deviation $\sigma_{d,\mathrm{shot}}$ of the distance measurements for shot-noise-limited reception as a function of the individual comb power P_{FC} that reaches each of the reference and the measurement detector pair. Noise recorded in the photocurrents of both detectors leads to an uncertainty of extracted phase values and therefore to uncertainties of the associated distance. For our calculations, we assumed signal and LO combs, each consisting of 100 lines with identical power. The free spectral range of the signal comb amounts to 100 GHz, the responsivity of the photodetector is 0.5 A/W, and the sampling rate for the distance acquisition amounts to $\Delta f = 100$ MHz. The blue line corresponds to the ideal case, where measurement is only impaired by the shot noise (quantum noise) of the photocurrent. For the orange line, we assumed an ideal optical amplifier with a noise figure of 3 dB that decreases the SNR by a factor of 2 and hence causes an increase of the distance uncertainly by a factor of $\sqrt{2}$.

distances. Figure D.6(a) shows the originally measured distance (top) and its high-pass-filtered counterpart (bottom). The Allan deviation of the original measurement data exhibits a decrease for small averaging times and a drift- and vibration-induced increase for large averaging times, see blue trace in Fig. D.6(b). When applying the high-pass filter, the impact of drift and vibrations can be eliminated, leading to a steady decrease of the Allan deviation with increasing averaging time, see orange trace in Fig. D.6(b). In this case, the Allan deviation behaves similarly as the standard deviation, Fig. D.6(c), assuming values of 284 nm for the highest measurement rate of 96.4 MHz (averaging time of 10.4 ns) and decreasing to 5 nm for an averaging time of 100 μs. This is clearly better than the precision value obtained in the actual experiment for the same averaging time, see Section D.5 “Distance sweep with pointwise calibra-

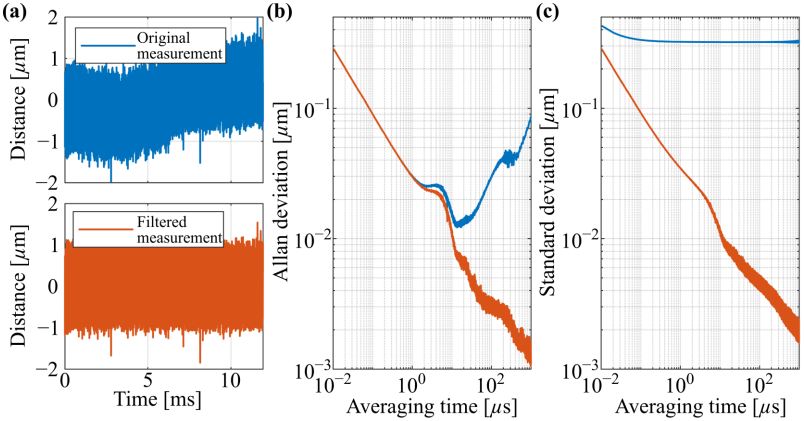

Figure D.6: Standard deviation and Allan deviation as a function of the averaging time for distance measurements towards a static target. (a) Originally measured distance (top) and its high-pass-filtered counterpart (bottom). (b) Allan deviation as a function of averaging time. The Allan deviation of the original measurement decreases going from small to intermediate averaging times, before drift and vibrations induce an increase when the averaging times increase, see blue curve. By applying the high-pass filter, the impact of drift and vibrations is eliminated, leading to a continuous decrease of the Allan deviation for larger averaging times, see orange curve. (c) Standard deviation as a function of averaging time. The standard deviation of the high-pass filtered distance measurement behaves similarly as the respective Allan deviation, assuming a value of 284 nm for the highest measurement rate of 96.4 MHz (averaging time 10.4 ns), and decreasing to 5 nm for an averaging time of 100 μs. In contrast, the standard deviation of the original, unfiltered distance measurement never falls below 300 nm due to drift and vibrations.

tion measurement". We may hence conclude that the experimentally observed precision is limited by fiber drift and vibrations rather than by noise in the detected signal. For the experimental parameters listed above and comb powers of 11 mW at each balanced detector, a minimum measurement uncertainty of 0.09 nm could be obtained, including the consideration of an ideal EDFA. This is significantly better than the 5 nm obtained in the experiment, indicating that there is further room for improving the precision.

[End of supplementary information of publication [J3]]

E Dual-comb ranging under the influence of high optical round-trip losses

The Sections E.1 to E.7 in this chapter have been published as supplementary information of the publication [J4]. They are adapted to fit the layout, structure and notation of this dissertation. Sections E.8 and E.9 contain an additional analysis investigating the trade-off of a dual-comb LiDAR system between its sampling rate, precision, free-space loss tolerance, and maximum target distance.

[Start of supplementary information of manuscript [J4]]

E.1 Free-space optical setup for compensation of fiber drift

For the ranging experiments described in Section 6.4 of Chapter 6, we compensate thermally and mechanically induced drift of the fiber lengths by periodically measuring the length of a fixed reference path and by comparing it to the measured path length to the target mirror. The corresponding setup is shown in Fig. E.1. Light from the transmitter is guided to an optical output collimator ($\mathrm{COL_O}$) and emitted as a free-space beam. Neutral-density filters (ATT) are used to adjust the power of the free-space beam. The beam is split into two parts at a beam splitter (BS), and both parts are guided towards the optical input collimator ($\mathrm{COL_I}$) and from there to the receiver (Rx). The gray path serves as a fixed reference, whereas the red beam is guided towards the target mirror, reflected, and sent to the input collimator. A chopper wheel (CPW) alternatingly blocks the red and the gray beam with a frequency of 2 kHz. Comparing the path length d_{tar} to the fixed reference length d_{fix} on a timescale of less than a

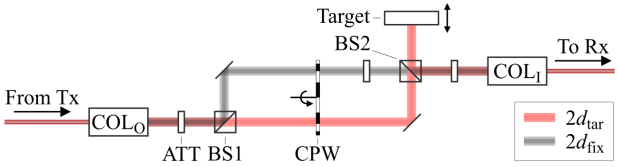

Figure E.1: Free-space optical setup used for compensating thermally and mechanically induced drift of the fiber lengths during the ranging experiments. Light is emitted from the transmitter (Tx, left) and guided to an output collimator (COL_O) by optical fibers. The emitted light is guided to the receiver (Rx, right) via two different paths. One path serves as static reference with a fixed length $2d_{fix}$ (gray), while the beam following the other path (red) is guided towards the target, traveling a distance of $2d_{tar}$ before reaching the input collimator COL_I. A combination of beam splitters (BS) and a rotating chopper wheel (CPW) allows to alternate between the two paths with a frequency of 2 kHz. Comparing the distance d_{tar} to the fixed reference distance d_{fix} on a timescale of less than a millisecond allows to greatly reduce the drift of the fiber lengths. Optical power levels can be adjusted via variable neutral density filters (ATT). Details on the components that were used in the setup can be found in Section E.7.

millisecond allows to eliminate drift of the fiber lengths, which can amount to several micrometers on a time-scale of minutes [J3]. Note that we introduced a factor of 2 into the definition of the beam path lengths to account for the back- and forth-propagation to the target mirror. As a consequence, the overall length of the red beam path is denoted as $2d_{tar}$, whereas the overall length of the gray path is $2d_{fix}$. A movement of the target mirror by a small increment Δz hence leads to an equivalent change of the difference $d_{tar} - d_{fix}$. Further details regarding the components used in our experiments can be found in Section E.7.

E.2 Selection of reliable distance data by fit error

As described in Section 6.3 of Chapter 6, every distance data point d is the result of a linear fit to a set of unwrapped phases $\delta\Phi_\mu$ of μ beat signals. The quality of the fit is given by the fit error ε defined in Eq. (6.5) of Chapter 6. For low received optical powers, the associated beat signals are weak and the extracted phases are distorted by shot noise of the LO comb, by thermal noise of the receiver electronics, and by noise of the analog-to-digital-converters, see Sections E.3 and E.4 for details. As a result, the unwrapped phase values cannot be fitted by a straight line and therefore the error ε of the linear fit will

be high. To identify unreliable data points in a sequence of measured distances d_i, $i = 1, 2, 3 \ldots$, we introduce an adaptive local threshold $\varepsilon_{\text{th,loc}}(d_i)$ that distinguishes between reliable ($\varepsilon(d_i) < \varepsilon_{\text{th,loc}}(d_i)$) and unreliable ($\varepsilon(d_i) > \varepsilon_{\text{th,loc}}(d_i)$) data points. The adaptive threshold $\varepsilon_{\text{th,loc}}(d_i)$ is defined by a moving average of the fit error over an interval of N_d measurements that is centered at the data point of interest d_i and by a constant offset $\varepsilon_{\text{th,o}}$,

$$\varepsilon_{\text{th,loc}}(d_i) = \overline{\varepsilon(d_i)} + \varepsilon_{\text{th,o}}, \quad \overline{\varepsilon(d_i)} = \frac{1}{N_d} \sum_{m=i+\lfloor -N_d/2 \rfloor +1}^{i+\lfloor N_d/2 \rfloor} \varepsilon(d_m), \tag{E.1}$$

where the floor operator $\lfloor \bullet \rfloor$ denotes the nearest smaller integer. The threshold offset accounts for the fact that the fit errors $\varepsilon(d_i)$ are approximately symmetrically distributed above and below the local moving average $\overline{\varepsilon(d_i)}$, and that data points with an error slightly above the local moving average can still be regarded reliable. Note that, when used in real-time systems, this procedure leads to a latency of $N_d/2$ data points. This can be avoided by averaging over N_d values of the fit errors $\varepsilon(d_i)$ that precede the actual data point of interest instead of averaging around this data point, as described in Eq. (E.1). In addition to the adaptive local threshold $\varepsilon_{\text{th,loc}}(d_i)$, we introduce a global upper threshold $\varepsilon_{\text{th,up}}$ that is used in case the fit errors become too large. The upper threshold accounts for the fact that, in case of very noisy data, the local moving average $\overline{\varepsilon(d_i)}$ may become too large and cannot be used as a base for determining the threshold for the acceptable fit error. Conversely, in case of high received power levels, the mean error can become very small, and there is no reason to reject any data points. This is taken into account by global lower threshold $\varepsilon_{\text{th,lo}}$. The overall threshold ε_{th} for the fit error of a data point d_i can hence be defined by

$$\varepsilon_{\text{th}}(d_i) = \begin{cases} \varepsilon_{\text{th,up}} & \text{for} \quad \varepsilon_{\text{th,loc}}(d_i) \geq \varepsilon_{\text{th,up}} \\ \varepsilon_{\text{th,lo}} & \text{for} \quad \varepsilon_{\text{th,loc}}(d_i) \leq \varepsilon_{\text{th,lo}} \\ \varepsilon_{\text{th,loc}}(d_i) & \text{else} \end{cases} . \tag{E.2}$$

According to Eq. (6.5) in Chapter 6, all measurements with an error $\varepsilon(d_i) \geq \varepsilon_{\text{th}}$ are discarded. In our evaluation, we chose $N_d = 101$, $\varepsilon_{\text{th,o}} = 0.01 \times 2\pi$, $\varepsilon_{\text{th,up}} = 0.16 \times 2\pi$ and $\varepsilon_{\text{th,lo}} = 0.02 \times 2\pi$, which were found to lead to a good trade-off between rejection of reliable and acceptance of unreliable data points

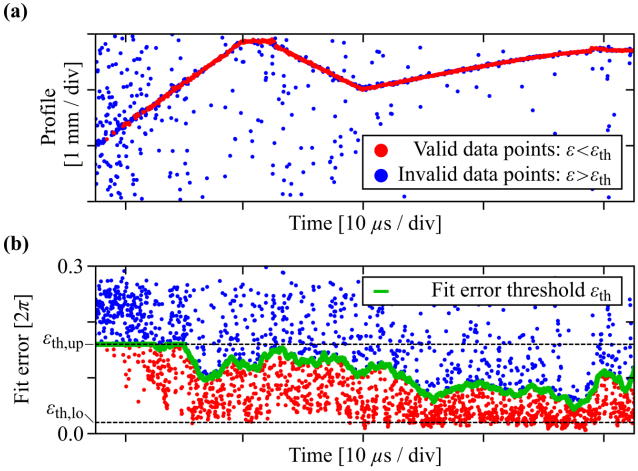

Figure E.2: Distance data points and fit error for cross-sectional characterization of flying projectile, see Section 6.5 in Chapter 6. (a) Distance data points as a function of measurement time. Red dots indicate accepted distance values and blue dots represent discarded data points. (b) Fit error associated with the various distance data points. Red points below the fit-error threshold $\varepsilon_{\mathrm{th}}(d_i)$ according to Eq. (E.2) (green curve) are considered accepted, whereas blue dots above the green line are discarded. The horizontal dashed lines indicate the global upper and lower thresholds $\varepsilon_{\mathrm{th,up}} = 0.16 \times 2\pi$ and $\varepsilon_{\mathrm{th,lo}} = 0.02 \times 2\pi$ for the fit error.

over a large range of received power levels. The values for the global limits $\varepsilon_{\mathrm{th,up}}$ and $\varepsilon_{\mathrm{th,lo}}$ as well as the offset γ and the number N_d of samples in the moving average are fixed parameters of our measurement system, which may be adapted to the respective application, finding a favorable trade-off between the number of accepted data points, the ability of the system to quickly adapt to new overall levels of the fit error, and the quality of the obtained distance data points.

In Fig. E.2 we show how this selection of distance data points affects the final result. Figure E.2(a) shows the distance profile obtained from a flying projectile moving at a speed of $150\,\mathrm{m\,s^{-1}}$ as a function of measurement time, see Section 6.5 in Chapter 6 for more details. The red dots indicate accepted distance values where $\varepsilon(d_i) < \varepsilon_{\mathrm{th}}(d_i)$, and the blue dots represent discarded data points where $\varepsilon(d_i) \geq \varepsilon_{\mathrm{th}}(d_i)$. The most unreliable distance data points d_i are found at the beginning of the measurement, i. e., at the tip of the

projectile, where the scattering surface is strongly inclined with respect to the measurement beam axis and thus only a small fraction of the incident power re-enters the system. Figure E.2(b) depicts the associated fit errors – the green curve indicates the fit-error thresholds $\varepsilon_{\mathrm{th}}(d_i)$, whereas blue dots correspond to discarded and red dots to accepted distance data points.

E.3 Noise impairments of recorded signals

In the following we investigate the impact of noise on our recorded signals and on the extracted distance values described in Sections 6.4 and 6.5 of Chapter 6 and we identify the most relevant noise sources. To this end, we assume that the receiver of each optical signal consists of a balanced photodetector (BD), an electrical amplifier (EA) as well as an analogue-to-digital converter (ADC), see Fig. E.3. We assume that the gain of the electrical amplifier is automatically controlled such that the full voltage range of the ADC is used during the recording of the signals. The photodetector is characterized by its responsivity $\mathcal{R}$, and the electrical amplifier by its gain G and its noise figure F_{n}.

In our distance measurements, we determine the phase of beat notes in RF signals generated by the measurement and reference photodetectors. For simplicity, we assume that the power of the signal and the LO optical comb P_{SI} and P_{LO} is evenly distributed across all N_{FC} comb lines, such that the power per line amounts to $P_{\mathrm{SI}}/N_{\mathrm{FC}}$ and $P_{\mathrm{LO}}/N_{\mathrm{FC}}$, respectively. For a given photodetector responsivity $\mathcal{R}$ and a system impedance of $Z = 50\,\Omega$, the RF power P_{RF} of the beat signals on the reference (subscript "ref") and the measurement (subscript "meas") photodetector can be written as [J3]

$$P_{\mathrm{RF,meas}} = \frac{Z}{2}\frac{2\mathcal{R}P_{\mathrm{SI,meas}}}{N_{\mathrm{FC}}}\frac{2\mathcal{R}P_{\mathrm{LO,meas}}}{N_{\mathrm{FC}}}, \tag{E.3}$$

$$P_{\mathrm{RF,ref}} = \frac{Z}{2}\frac{2\mathcal{R}P_{\mathrm{SI,ref}}}{N_{\mathrm{FC}}}\frac{2\mathcal{R}P_{\mathrm{LO,ref}}}{N_{\mathrm{FC}}}. \tag{E.4}$$

Clearly, the power of the RF beat signals strongly depends on the power of the signal and the LO comb lines received at the respective detector. In the following, we estimate the ranging accuracy that can be achieved for low levels of received optical power on the measurement detector. In this case, the associated beat signal on the measurement detector is weak and heavily

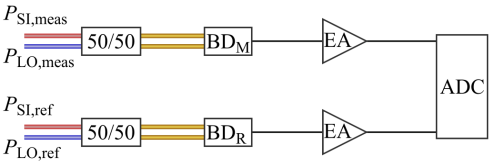

Figure E.3: Model of the receiver system. The optical signal powers of the signal (SI) and the local oscillator (LO) comb on the balanced measurement and reference photodetectors BD_M and BD_R are denoted as $P_{SI,meas}$, $P_{LO,meas}$, $P_{SI,ref}$ and $P_{LO,ref}$, respectively. The photodetector output signals are fed to electrical amplifiers (EA) and recorded by a pair of analogue-to-digital converters (ADC). Noise may arise from the inherent shot noise of the photodetection process, from thermal noise of the electric amplifier, and from quantization noise of the ADC.

impaired by noise. We may hence restrict our analysis to the measurement detector, while assuming a 'perfect' beat signal on the reference detector. We further assume that the recorded RF signals are only impaired by shot noise with RF power $P_{n,shot}$ and thermal noise with power $P_{n,ther}$. The associated signal-to-noise ratio (SNR) of the photocurrent from the measurement detector then reads

$$\mathrm{SNR} = \mathrm{SNR}_{\mathrm{RF,meas}} = \frac{P_{\mathrm{RF,meas}}}{P_{\mathrm{n,shot}} + P_{\mathrm{n,ther}}}. \tag{E.5}$$

The shot noise is dominated by the contribution of the LO comb, which has usually contributes a much higher optical power on the photodetector than the SI comb, $P_{SI} \ll P_{LO}$. Given a $Z = 50\,\Omega$ termination and a noise bandwidth Δf_n which is approximately equal to the evaluation bandwidth B_{eval}, $\Delta f_n \approx B_{eval}$, the shot-noise power after amplification can be written as

$$P_{\mathrm{n,shot}} = Z\, 2 q_e \mathcal{R} P_{\mathrm{LO}} \Delta f_n\, G. \tag{E.6}$$

where q_e is the elementary charge. Thermal noise is generated in the internal $50\,\Omega$ impedance of the photodetector circuit and in the subsequent electrical amplifier. For a given system temperature T and an amplifier noise figure F_n, the total thermal noise power at the amplifier output can be written as

$$P_{\mathrm{n,ther}} = k_B T\, \Delta f_n\, G\, F_n. \tag{E.7}$$

where k_B denotes the Boltzmann constant.

Comparing Eqs. (E.6) and (E.7) shows that the system can always be operated in its shot-noise limited regime, $P_{\mathrm{n,shot}} > P_{\mathrm{n,ther}}$, provided that the LO power is sufficiently high. Specifically, for a photodiode responsivity of $\mathcal{R} = 0.5\,\mathrm{A\,W^{-1}}$, an amplifier noise figure of $F_{\mathrm{n}} = 3$ (5 dB), and a system operated at room temperature ($k_{\mathrm{B}}T = 25\,\mathrm{meV}$), we find that shot-noise limited reception is already achieved for comparatively low LO comb powers of $P_{\mathrm{LO}} > 1.5\,\mathrm{mW}$. This holds independently of the amplifier gain G and the noise bandwidth Δf_{n}. For shot-noise limited reception, the SNR of the RF signal at the output of the electrical amplifier amounts to

$$\mathrm{SNR} = \frac{P_{\mathrm{RF}}}{P_{\mathrm{n,shot}}} \approx \frac{\mathcal{R} P_{\mathrm{SI}}}{N_{\mathrm{FC}}^2 q_{\mathrm{e}} \Delta f_{\mathrm{n}}}. \tag{E.8}$$

For low received optical signal power P_{SI}, the SNR according to Eq. (E.8) can be directly translated into the precision of the distance measurement, see Section E.4, provided that quantization noise and other impairments of the ADC can be neglected. In most cases of practical interest, this is a valid assumption: State-of-the-art ADC with bandwidths of a few GHz offer effective numbers of bits (ENOB) of approximately 10. This translates into an SNR of $(6.02\,\mathrm{ENOB} + 1.76)\,\mathrm{dB} = 62\,\mathrm{dB}$ that can ultimately be achieved for the digitized signal, provided that the received signal power is high enough and that the only relevant signal impairments are those coming from the ADC. However, this case is not of too much practical interest. Assuming am ENOB of 10, a responsivity of $\mathcal{R} = 0.5\,\mathrm{A\,W^{-1}}$, a comb line number of $N_{\mathrm{FC}} = 25$ and a measurement rate[1] of $\Delta f_{\mathrm{n}} = 5\,\mathrm{MHz}$, ADC impairments would only become visible for relatively high received signal comb powers of more than 1 mW. For typically received power levels in the microwatt or nanowatt regime, the ranging performance of properly designed system will thus be limited by shot noise.

We also analyze the different noise contributions found in our measurements. To this end, we extract the power spectral density of the spectrally white background noise that is found in the recorded RF beat signals for different received signal comb powers $P_{\mathrm{SI,meas}}$, see orange dots in Fig. E.4(a). To quantify the background noise level, we calculate the mean power spectral density in a frequency range of 24 to 26 GHz, where no beat signals are found, see orange

[1] In [J4], the measurement rate is equivalent to the noise bandwidth.

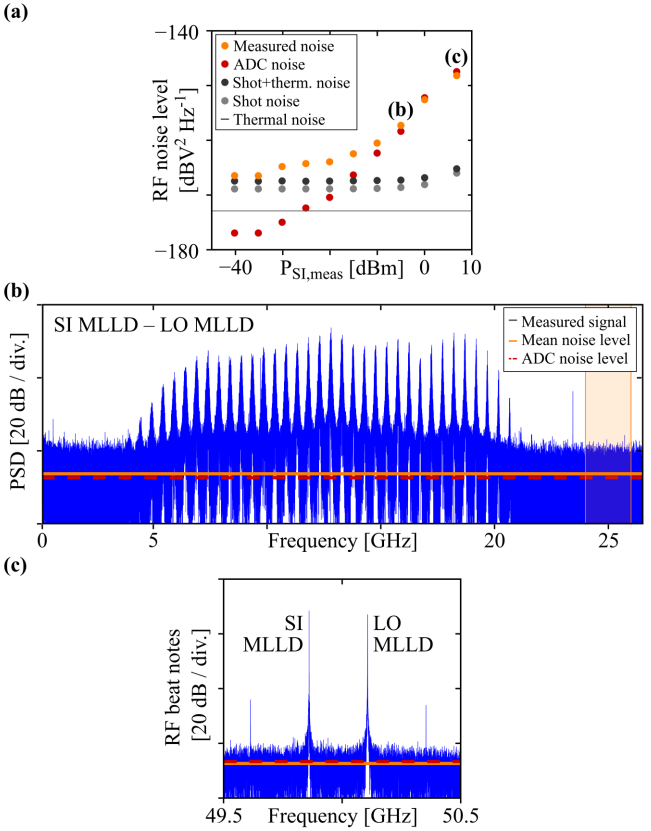

Figure E.4: Analysis of the different noise contributions found in our measurements. (a) Power spectral density levels of the measured noise (orange dots), ADC noise (red dots), thermal noise (grey line), shot noise (light grey dots) and the sum of thermal noise and shot noise (dark grey dots) for different received signal powers incident on the measurement detector. The labels (b) and (c) refer to the measurements depicted in the respective subfigure. (b) Power spectral density (PSD) of an electric signal obtained from the measurement photodetector BD_M as shown in Fig. 6.4(a) in Chapter 6. The orange line indicates the mean noise level extracted in the frequency range 24 – 26 GHz (orange box), and the red dashed lines represents the expected ADC noise floor. For the incident signal comb power of −5 dBm, the noise floor is clearly limited by ADC noise. (c) RF beat notes of both MLLDs (blue), shown in Fig. 6.4(b) in Chapter 6. The mean noise floor (orange line) and the expected ADC noise floor (red dashed line) are again indicated by an orange and a red dashed line, respectively. The measured spectrum was corrected by a constant offset which compensates the decay of the frequency response of the oscilloscope towards higher frequencies.

box in Fig. E.4(b). For comparison, we also extract the expected ADC noise level (red dots) as well as the expected shot noise level (light grey dots). The ADC noise level is extracted from the ENOB of 5.0 that is specified by the manufacturer of the high-speed oscilloscopes (Keysight UXR0804A). The ADC acquisition range is adapted to the amplitude of the RF beat signals, and the ADC noise level thus decreases for lower signal comb powers until the smallest acquisition range is reached at a signal power of approximately −35 dBm. The shot noise is dominated by the contribution of the LO comb $P_{\mathrm{LO,meas}}$ of 7 dBm and does hence not vary significantly with the signal comb power. Note that in this set of measurements, no optical amplifier is used. The estimated shot-noise levels consider an effective gain figure G_{eff} of the RF amplifier, which also contains signal losses occurring in our electronic receiver components and which was obtained by comparing the expected beat signal power levels on the measurement detector, see Eq. (E.3), with the recorded signals in our oscilloscopes. In addition, we consider an additional increase of the measured shot-noise level by approximately 3 dB due to fact that the high-speed oscilloscopes were operated at a sampling rate of only 128 GSa/s with an analogue antialiasing filter having a bandwidth of approximately 100 GHz. We find that for high received signal powers of −10 dBm or more, the observed noise in our experiments can be fully explained with the expected ADC noise, see Fig. E.4(a). For signal comb powers below −10 dBm, the measured noise reaches a plateau at a power spectral density of approximately $-166.5\,\mathrm{dBV^2Hz^{-1}}$. We attribute this noise floor to a combination of shot noise and thermal noise of our RF amplifier. To confirm this notion, we also extract the power spectral density of approximately $-173\,\mathrm{dBV^2Hz^{-1}}$ that is to be expected for the thermal noise of the RF amplifier (SHF 807), see grey line in Fig. E.4(a), and we add it to the shot-noise level (grey dots) to obtain the overall noise floor of approximately $-167.5\,\mathrm{dBV^2Hz^{-1}}$ (dark grey dots). The thermal noise level was estimated from the noise figure of the amplifier ($F_{\mathrm{n}} = 6\,\mathrm{dB}$)[2], using again the effective gain G_{eff} of our electronic signal chain and taking again into account an additional increase of the measured noise by approximately 3 dB due to fact that the anti-aliasing filter was too broadband for the given sampling rate. We find that the noise level extracted from our measurements approaches the overall expected noise limit comprising both thermal and shot noise (dark grey

[2] For more details, see datasheet of the linear broadband amplifier SHF 807-C, *https://www.shf-communication.com/wpcontent/uploads/datasheets/datasheet_shf_s807_c.pdf* (17.10.2021).

dots) for low received power signal power levels, and we thus conclude that a combination of shot noise and thermal noise of the RF amplifier represents the main limitation of our system for low received signal power levels. Based on our analysis, we believe that the performance presented in our main manuscript can be further improved by using ADC with higher ENOB and RF amplifiers with lower noise figure, rendering thermal noise fully negligible compared to shot noise. In the following section, we estimate the achievable measurement precision for this scenario.

E.4 Impact of shot noise on the measurement precision

In [J3], we derived in detail how shot noise is related to the precision of a dual-comb ranging system, and we only summarize the main findings here. To extract a distance value d_i from the measured signals, a straight line fitted is to a set of $\mu = 1, 2, \ldots, N_\mathrm{b}$ unwrapped phase differences $\delta\Phi_\mu(d_i) = \Phi_{\mu,\mathrm{meas}}(d_i) - \Phi_{\mu,\mathrm{ref},i}$. These phase differences are impaired by random fluctuations, which we assume to be uncorrelated and to have the same distribution with zero mean and with a standard deviation σ_ϕ. The standard deviation σ_d of the extracted distance, as obtained from a linear regression of N_b phase difference values, is then given by

$$\sigma_d = \sqrt{\frac{12}{N_\mathrm{b}^3}} \frac{c_0}{2\omega_{\mathrm{SI,FSR}} n_\mathrm{air}} \sigma_\phi, \tag{E.9}$$

see Eq. (S26) in [J3]. Note that it may be advantageous to use only a subset of N_b comb lines of the overall N_FC available lines for extracting the distance information and to discard some lines that are strongly impaired by noise. The standard deviation σ_ϕ of the phase differences is estimated from the standard deviation $\sigma_{\phi,\mathrm{meas}}$ of the phases obtained from the signal of the measurement photodetector and from the standard deviation $\sigma_{\phi,\mathrm{ref}}$ of the phases obtained

from the reference photodetector. The quantities $\sigma_{\phi,\mathrm{meas}}$ and $\sigma_{\phi,\mathrm{ref}}$ depend on the respective signal-to-noise ratio (SNR) [226],

$$\sigma_\phi^2 = \sigma_{\phi,\mathrm{meas}}^2 + \sigma_{\phi,\mathrm{ref}}^2 = \frac{1}{2\mathrm{SNR}_{\mathrm{meas}}} + \frac{1}{2\mathrm{SNR}_{\mathrm{ref}}}. \tag{E.10}$$

Note that the relation between the phase variance and the SNR on the respective detector is only valid for high SNR > 10 and needs to be replaced with a more precise expression for lower SNR, see Eq. (17) in [226]. Note also that Eq. (E.10) accounts for the finite SNR of both the reference and the measurement detector. For low received optical power, the standard deviation σ_ϕ of the phase differences will be dominated by the shot noise on the measurement detector, see Section E.3 for details.

To estimate $\mathrm{SNR}_{\mathrm{meas}}$, we rely on Eqs. (E.5) and (E.6), and equivalent relations can be used for estimating $\mathrm{SNR}_{\mathrm{ref}}$. In both cases, we assume that the LO power is high enough such that thermal noise of the respective receiver circuit, Eq. (E.7) can be neglected. If, in addition, an optical amplifier is used to boost the SI comb power, additional amplified spontaneous emission (ASE) noise will further degrade the SNR performance. This can be taken into account by replacing the relation for the shot-noise power at the measurement detector, Eq. (E.5), by an equivalent relation that accounts for the noise figure F_{EDFA} of the EDFA,

$$\mathrm{SNR}_{\mathrm{meas}} = \frac{P_{\mathrm{RF}}}{P_{\mathrm{n,shot}}\, F_{\mathrm{EDFA}}}. \tag{E.11}$$

For the EDFA used in our experiments, a noise figure of 5.4 dB ($F_{\mathrm{EDFA}} = 3.5$) is specified by the manufacturer.

Inserting the SNR for the measurement and the reference detector in Eq. (E.10), we can use Eq. (E.9) to determine the achievable precision for given comb parameters $P_{\mathrm{SI,meas}}$, $P_{\mathrm{LO,meas}}$, $P_{\mathrm{SI,ref}}$, $P_{\mathrm{LO,ref}}$, $\omega_{\mathrm{SI,FSR}}$, N_{b}, N_{FC}, a given responsivity $\mathcal{R}$ of the photodetectors, and a given electrical bandwidth Δf_{n}. The results are summarized in Table E.1, specifying the achievable shot-noise limited precision σ_d for the different setup configurations that are described in Figs. 6.5 and 6.6 of Chapter 6. Note that, for the sake of simplicity, we have rounded some of the parameters listed in Table E.1 such as the optical powers $P_{\mathrm{SI,meas}}$, $P_{\mathrm{LO,meas}}$, $P_{\mathrm{SI,ref}}$, $P_{\mathrm{LO,ref}}$, and the FSR $\omega_{\mathrm{SI,FSR}}$ – the precise values can be found in Chap-

Table E.1: Achievable measurement precision limited by shot noise. Experimental parameters are rounded for simplicity.

Measurement No.	**1**	**2**	**3**	**4**	**5**	**6**
EDFA included	No	No	No	Yes	Yes	Yes
$P_{\mathrm{LO,meas}}$ [dBm]			7			
$P_{\mathrm{LO,ref}}$ [dBm]			7			
$P_{\mathrm{SI,meas}}$ [dBm]	7	−20	−40	5	−20	−40
$P_{\mathrm{SI,ref}}$ [dBm]			0			
N_{FC}			40			
N_{b}			25			
$\Delta f_{\mathrm{n}} = B_{\mathrm{eval}}$ [MHz]	500	500	50	500	500	50
$\omega_{\mathrm{SI,FSR}}/(2\pi)$ [GHz]			50			
$\mathcal{R}$ [A W^{-1}]			0.5			
σ_d [μm]	0.19	1.51	4.74	0.26	2.80	8.82
σ_{exp} [μm]	1.85	4.03	16.2	3.52	4.22	14.5

ter 6. For data evaluation, we choose $N_{\mathrm{b}} = 26$ comb lines which proved to work best at low optical return powers of the signal comb, whereas the entire comb consisted of approximately $N_{\mathrm{FC}} = 40$ lines, see also Fig. 6.2 in Chapter 6. The electrical bandwidth Δf_{n} was equal to the evaluation bandwidth B_{eval}.

In addition to the theoretically achievable precision σ_d, Table E.1 also specifies the experimentally demonstrated counterpart $\sigma_{d,\mathrm{exp}}$. For high optical return powers, we observe a difference between the achievable and the experimentally observed standard deviation of about one order of magnitude, which reduces to a factor of 1.5 – 3.5 at low powers. At high signal powers, we attribute this to our ADC, which have a rather small ENOB $\approx$ 5.0 in the frequency range between 10 GHz and 20 GHz, see Section E.3. As a consequence, the signal impairments are dominated by ADC noise rather than by shot noise, as assumed for the theoretical analysis of Table E.1. The observed degradation of the measurement accuracy of approximately a factor of 10 is consistent with the fact that, for a received signal power level of 7 dBm, the ADC noise is approximately 20 dB stronger than the shot noise, see Fig. E.4(a). At lower received signal powers, this effect becomes less pronounced and thus the difference between the observed and the estimated distance precision decreases.

E.5 Evaluation of unambiguity-distance sweep with fiber drift compensation

The unambiguity-distance sweep considered in Section 6.4 of Chapter 6 contains 16 distances that were consecutively measured over several minutes, where the time needed for each position was dictated by the data transfer from the temporal memory of our oscilloscope (ADC) to a storage network drive. During this time, the fiber lengths within our setup drift due to temperature fluctuations and mechanical vibrations, which leads to altered path lengths towards the target mirror extracted from each data set. To eliminate the effects of fiber drift, we rely on the referencing scheme described in Fig. E.1, where a chopper wheel (CPW) is used to continuously switch between measuring the path length to the target mirror (red beam path) and the length of static reference beam path (gray). We set the CPW to a chopping frequency of 2 kHz, which allows to retrieve the distance to the target and the length of the reference beam path with a temporal separation of approximately 250 μs. A subtraction of the two distance values eliminates the impact of slow fiber drifts, which typically become relevant only over a time scale of several milliseconds.

In Figures E.5 and E.6, we show two distance profiles obtained for two positions $m = 15$ and $m = 16$ of the target mirror, which are separated by 200 μm. Figure E.5(a) shows the distance profile of the first measurement ($m = 15$) for an evaluation period of $B_{\text{eval}} = 1/(10T_{\text{r}})$. Accepted data points are indicated in red, whereas discarded data points are shown in blue, for details of the selection procedure see Section E.2 as well as Chapter 6, Eq. (6.5) and the text following Eq. (6.5). Two alternating levels are visible, with short transition times during which the chopper wheel partially blocks both beams such that the measurement becomes unreliable. The level at $\overline{d}_{\text{fix}} = 2.1536$ mm corresponds to the static reference beam path, whereas the level at $\overline{d}_{\text{tar},15} = 1.1229$ mm represents the beam path to the target mirror. Figure E.5(b) shows the fit error $\varepsilon(d_i)$ as well as the fit-error threshold $\varepsilon_{\text{th}}(d_i)$ for the various measurements, which exhibit a peak during the transition periods between the levels. Note that the evaluation of the fit errors allows for selection of reliable measurements even for partially blocked beams, emphasizing once more the robustness of the technique.

For further evaluation, we consider an equal number N_{accept} of accepted distance data points on each level in a temporal range of approximately 100 μs,

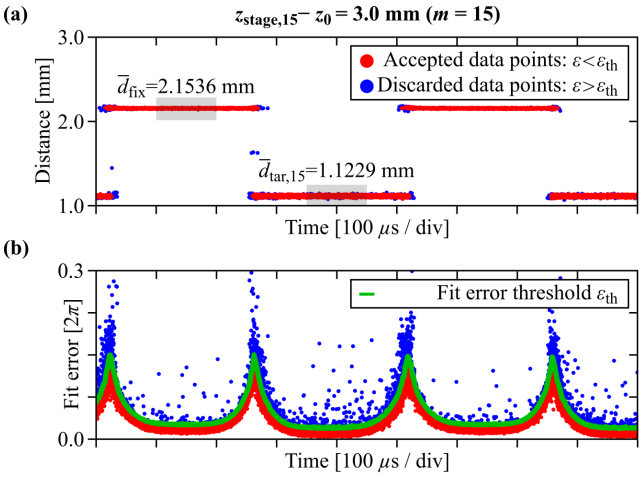

Figure E.5: Evaluation of distance sweep with fiber drift compensation for the position $z_{stage,15} - z_0 = 3.0$ mm ($m = 15$) of the target mirror. Fiber drift is eliminated by periodically comparing the variable distance d_{tar} to the target with the length d_{fix} of a fixed free-space reference beam, see Figure E.1 for details of the setup. The measurement rate amounts to 49.7 MHz. Data points are accepted (•, red) or discarded (•, blue) based on the respective fit error, see Section E.2 as well as Chapter 6, Eq. (6.5) and the text following Eq. (6.5). (a) Measured distances for target mirror in position $z_{stage,15} - z_0 = 3.0$ mm. Gray boxes mark the data points from which the average distances $\overline{d}_{tar,15}$ and $\overline{d}_{fix}$ are calculated. (b) Fit error $\varepsilon(d_i)$ (red and blue) and fit error threshold $\varepsilon_{th}(d_i)$ (green) of measurement shown in Fig. E.5(a). Fit errors are calculated according to Eq. (6.5) of Chapter 6 and fit-error thresholds are calculated according to Eqs. (E.1) and (E.2) of this chapter. The fit error increases in the transition regions where the chopper wheel partially blocks both beams.

indicated by gray boxes. We compute the point-wise difference of these data points the upper and the lower level. The mean value of these differences then gives the path-length difference between the gray and the red beam, reduced by an integer multiple of the unambiguity distance. For the unambiguity-distance sweep, we move the target mirror by increments of 200 μm away from the beam splitter BS2 in Fig. E.1 and thereby increase the length of the associated free-space beam path. The resulting distance profile for mirror position $m = 16$ is shown in Fig. E.6(a). In this measurement, the measured beam path length to the target mirror has increased to $\overline{d}_{tar,16} = 1.3251$ mm, whereas the measured length of the static beam path has changed only slightly by approximately 0.8 μm due to fiber drift. Computing and averaging again the point-wise

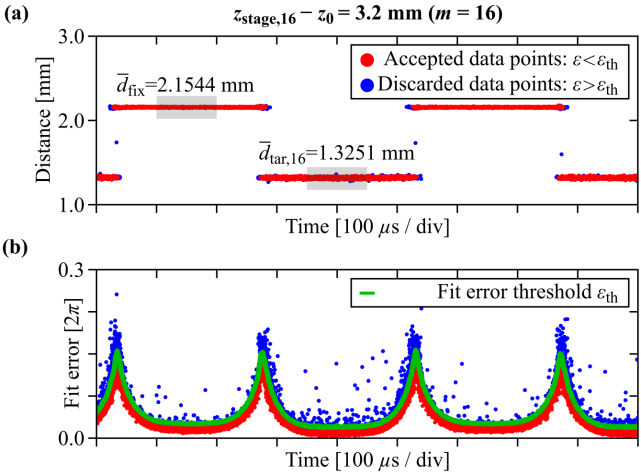

Figure E.6: Evaluation of distance sweep with fiber drift compensation for the position $z_{stage,16} - z_0 = 3.2$ mm ($m = 16$) of the target mirror. Fiber drift is eliminated by periodically comparing the variable distance d_{tar} to the target with the length d_{fix} of a fixed free-space reference beam, see Figure E.1 for details of the setup. The measurement rate amounts to 49.7 MHz. Data points are accepted (•, red) or discarded (•, blue) based on the respective fit error, see Section E.2 as well as Chapter 6, Eq. (6.5) and the text following Eq. (6.5). (a) Measured distances for target mirror in position $z_{stage,16} - z_0 = 3.2$ mm. Gray boxes mark the data points from which the average distances $\overline{d}_{tar,16}$ and $\overline{d}_{fix}$ are calculated. (b) Fit error $\varepsilon(d_i)$ (red and blue) and fit error threshold $\varepsilon_{th}(d_i)$ (green) of measurement shown in Fig. E.6(a). Fit errors are calculated according to Eq. (6.5) of Chapter 6 and fit-error thresholds are calculated according to Eqs. (E.1) and (E.2) of this chapter. The fit error increases in the transition regions where the chopper wheel partially blocks both beams. Between the two measurements for the target positions $m = 15$, see Fig. E.5, and $m = 16$ shown here, the target mirror is moved by 200 μm. This is well reproduced by the measured increment of 201.4 μm, obtained after accounting for a fiber drift of approximately 0.8 μm.

differences between the measured distances shown in Fig. E.6(a) leads to an increase of the path-length difference of 201.4 μm, which is in good agreement with the set increment of the mirror position.

E.6 One-port ranging system and triggering data acquisition of projectile measurements

For the high-speed ranging experiments described in Section 6.5 of Chapter 6, we relied on the system depicted in Fig. E.7. In this system, the optical in- and output are combined in a single output/input collimator (COL), and a fiber-optic circulator (CIRC) is used to separate the incoming receive signal from the outgoing transmit signal. Note that scheme is only useful if spurious back-reflections of the transmit signal along the path from the circulator to the target can be neglected – otherwise cyclic errors will occur and a two-port systems as shown in Fig. 6.3 of Chapter 6 should be used. The SI comb is split at a 90/10 coupler, and the major part is fed to the circulator and is then guided to the collimator. After scattering at the target, a small portion of the SI comb enters the system through the collimator and is then guided towards the balanced photodetector by the circulator. All other components in this system are the same as for the two-port ranging system, see Fig. 6.3 in Chapter 6 and Section E.7 for details. The collimator (Thorlabs F280APC-1550, focal length $f = 18.75\,\mathrm{mm}$) is coated with an anti-reflective layer designed for the wavelength range of the SI comb such that the spurious back-coupling into the attached single-mode fiber can be neglected with respect to the signal returning from the target.

We use the one-port ranging system to measure surface profiles of flying air-gun projectiles, see Section 6.5 in Chapter 6. In this experiment, we set our oscilloscope to continuously record data and to temporarily store the acquired waveforms in the internal memory. When a projectile passes the measurement beam, a part of the light is reflected and re-enters the ranging system. This is visible in the recorded data as a sharp increase of the amplitude of the recorded signal, which we use as a trigger event. Once triggered, the oscilloscope will keep the last $50\,\mu\mathrm{s}$ of data in its memory and acquire an additional $50\,\mu\mathrm{s}$ of data after the trigger event. Given the length of the projectile of approximately 7 mm and its speed of $150\,\mathrm{m/s}$, the projectile will be sampled over a period of $50\,\mu\mathrm{s}$. We can hence be sure that the whole projectile has been captured, independent of the temporal position of the trigger event within the acquired back-reflection signal of the projectile.

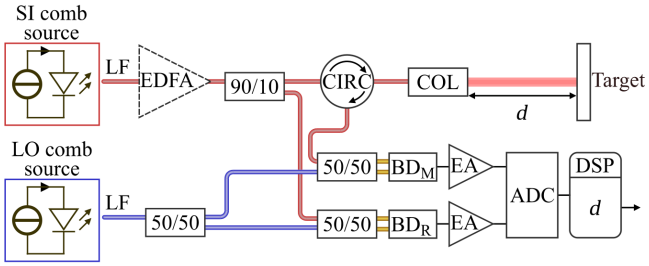

Figure E.7: One-port ranging system for low-loss measurements. CIRC: Circulator; COL: output/input collimator. All other components are the same as the ones used in the two-port ranging system shown in Fig. 6.3 in Chapter 6.

E.7 Detailed description of experimental setups

In the following, we provide a full representation of our experimental setups, see Fig. E.8. Commercial model numbers of specific components are given in the caption of Fig. E.8.

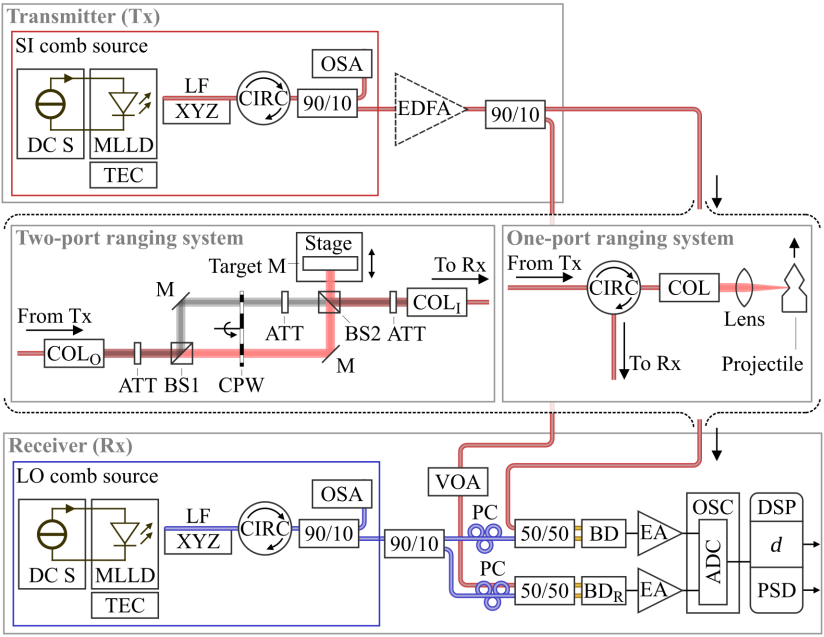

Figure E.8: Full representation of the experimental setups used in our work. Optical fibers, indicated as thick red and blue lines, are standard single-mode fibers, unless specified otherwise. Components used in multiple instances with the same model number are mentioned once. **Transmitter (Tx)**: DC Power supply (DC S): *ILX Lightwave LDC-3742*, *Newport Laser Diode Controller 6000*. Quantum-dash mode-locked laser diode (MLLD): *Custom device provided by Centre de Nanosciences et de Nanotechnologies, Centre national de la recherche scientifique, Université Paris-Saclay, Palaiseau, France*. Temperature controller (TEC): *Newport ILX Lightwave LTD-5910 / LTD-5910B*. Lensed fiber (LF): *OZ Optics TSMJ-3A-1550-9/125-1-7-2-12-0.9-AR*. XYZ stage (XYZ): *Thorlabs MAX313D*. Fiber-optic circulator (CIRC): *Thorlabs 6015-3-APC*. Fiber-optic 90/10 coupler (90/10): Thorlabs *TN1550R2A2*. Optical spectrum analyzer (OSA): *Ando AQ6317B*. Erbium-doped fiber amplifier (EDFA): *Manlight ML-YEDFA-B-FG-33C33*.**Two-port ranging system**: Collimator (COL): *Thorlabs F280APC-1550*. Variable attenuator wheels (ATT): *Thorlabs NDC-50C-2*, *NDC-50C-2M*, partially in combination with neutral density filters. Beam splitters (BS): E.g., *Thorlabs BS018*. Silver mirror (M): E.g., *Thorlabs PF10-03-P01*. Chopper wheel (CPW): *SRS SR540*. Nano-precision heavy-duty stage (Stage): *Physik Instrumente M511.HD*. **One-port ranging system**: High-NA lens with focal length of 20 mm (Lens): E.g., *Thorlabs LB4854-C*. **Receiver (Rx)**: Polarization controller (PC): E.g., *Thorlabs FPC032*. Variable optical attenuator (VOA): E.g., *Thorlabs VOA50-APC*. 50/50: Fiber-optic 50/50 coupler (50/50): Thorlabs *TN1550R5A2*. Balanced photodetector (BD): *Finisar BPDV2150R*. Electrical amplifier (EA): *SHF 807*. Oscilloscope (OSC): *Keysight UXR0804A*.

[End of supplementary information of manuscript [J4]]

E.8 Optical scattering losses for target with Lambertian surface and atmospheric attenuation

This section discusses the free-space scattering loss occurring for a Lambertian target [227]. The target is illuminated by a collimated laser beam with beam area A_{beam} and power P_{beam}. The beam reaches the target under an angle θ with respect to the target normal, and the illuminated area A_{illum} is given by $A_{\text{illum}} = A_{\text{beam}} / \cos\theta$. At the target surface, a fraction of the light is absorbed and the other fraction reflected. The total reflected power $P_{\text{beam,R}}$ is determined by the reflectivity $\rho \leq 1$, such that $P_{\text{beam,R}} = \rho P_{\text{beam}}$. Assuming a spatially constant intensity of the incoming light across the beam area, and a spatially constant reflectivity of the illuminated surface, the intensity of the reflected light I_{R} at the target surface is constant over the illuminated area and given by

$$I_{\text{R}} = \frac{P_{\text{beam,R}}}{A_{\text{illum}}} = \frac{\rho P_{\text{beam}}}{A_{\text{beam}}/\cos\theta}. \tag{E.12}$$

In the following we assume that the target surface is diffusely reflecting, i.e., it is a Lambertian surface [227]. The observer views the reflecting target under the same angle θ under which the illuminating beam hits the target. For a Lambertian surface, the radiance L of the reflected light, given as reflected differential power $\mathrm{d}^2 P_{\text{R}}$ per apparent differential area $\mathrm{d}A_{\text{illum}} \cos\theta$ and per differential solid angle $\mathrm{d}\Omega$, is a constant,

$$L = \frac{\mathrm{d}^2 P_{\text{R}}}{\mathrm{d}A_{\text{illum}} \cos\theta \mathrm{d}\Omega} = \frac{\rho P}{A_{\text{beam}}/\cos\theta}. \tag{E.13}$$

The (near-field) intensity (unit W/m^2) of the reflected light at the target is equal to the radiance integrated over the solid angle Ω of the half space,

$$I_\mathrm{R} = L \int_\Omega \cos\theta \,\mathrm{d}\Omega = L \int_{\varphi=0}^{2\pi} \int_{\theta=0}^{\pi/2} \cos\theta \,\sin\theta \,\mathrm{d}\theta \,\mathrm{d}\varphi = L\pi. \tag{E.14}$$

As a consequence, the radiance of the reflected light can be expressed as $L = I_\mathrm{R}/\pi = P_\mathrm{beam,R}/(A_\mathrm{illum}\pi)$. With this result, we can compute the far-field intensity P_F (unit W/sr) of the reflected light by integrating the radiance over the illuminated target area,

$$P_\mathrm{F} = \cos\theta \int_{A_\mathrm{illum}} L \,\mathrm{d}A_\mathrm{illum} = A_\mathrm{illum}\, P_\mathrm{beam,R}/(A_\mathrm{illum}\pi)\, \cos\theta. \tag{E.15}$$

In Figure E.9, the cosine dependence of the far-field intensity is depicted as a function of θ. Only a small part of the totally reflected light re-enters the ranging system through its input aperture, which we assume as circular with a radius r_A. The (small) solid angle seen by the aperture is then given by $\Omega_\mathrm{A} = \pi r_\mathrm{A}^2/d^2$. The received part $P_{\mathrm{R},r}$ of the reflected power is

$$P_{\mathrm{R},r} = P_\mathrm{F}\Omega_r = \frac{P_\mathrm{beam,R}}{\pi} \cos\theta \frac{\pi r_\mathrm{A}^2}{d^2} = \rho P \frac{r_\mathrm{A}^2}{d^2} \cos\theta. \tag{E.16}$$

The ratio of the received reflected power and the transmitted power is the optical round-trip "gain", $\alpha_\mathrm{RT} < 1$,

$$\alpha_\mathrm{RT} = \frac{P_{\mathrm{R},r}}{P} = \rho \frac{r_\mathrm{A}^2}{d^2} \cos\theta. \tag{E.17}$$

This expression serves as a lower boundary of the losses to be expected. Specular reflection [228] can be neglected because of the small receiving numerical aperture of the ranging system.

Using Eq. (E.17), we can estimate the maximum operating range of a LiDAR system depending on its power budget, aperture size and target reflectivity. Assuming a target reflectivity of $\rho = 0.1$, an aperture radius of $r_\mathrm{A} = (2.54\,\mathrm{cm})/2$, and a target surface normal oriented perpendicularly to the ranging system input aperture, i.e., $\theta = 0$, diffuse scattering losses amount to 48 dB for a target distance of $d = 1\,\mathrm{m}$. We therefore estimate the working range of our

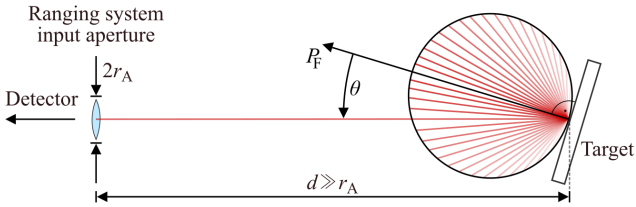

Figure E.9: Light scattered from a Lambertian surface. The ranging system aperture radius and the illuminated area are small compared to the distance d. Only a part of the scattered light enters the LiDAR system through its input aperture.

QD-MLLD-based LiDAR system without any optical amplifiers to 1 m for a sample rate of 50 MHz. In automotive applications, target distances in the order of $d = 200$ m are of interest [229]. For the same reflectivity as before, a LiDAR system would need to operate at 94 dB free-space losses. This can be achieved by, e.g., reducing the sample rate, or by accepting a decreased precision, see Section E.9 for a more detailed discussion.

E.9 Estimation of lower limit of optical return power required for distance determination

In a practical scenario, a certain measurement precision of, e.g., at least 1 % relative to the unambiguity distance should be achieved. In the following we derive how this is related to a certain optical power that needs to be received from the target. We define the relative precision σ_r as a ratio of the standard deviation $\sigma_{d,\text{shot}}$ of for distance measurements caused by fundamental shot noise, and the unambiguity range d_{ua},

$$\frac{\sigma_{d,\text{shot}}}{d_{ua}} = \sigma_r = \frac{\sqrt{12/N_b^3}\, c_0/\left(2n_{air}\omega_{SI,FSR}\right)\ \sigma_\phi}{2\pi c_0/\left(2n_{air}\omega_{SI,FSR}\right)} = \sqrt{12/N_b^3}\, \sigma_\phi/(2\pi)\,. \tag{E.18}$$

For a derivation of Eq. (E.18), see Section D.8. In the following it is assumed that phase noise σ_ϕ is dominated by noise on the measurement detector, since the reference phases can be measured over an extended period of time at high SNR, which results in high phase certainty, see also Appendix D, Section D.8. As described in Eq. (D.28), the phase uncertainty σ_ϕ is then related to the SNR on the measurement detector. At high SNR $>$ 10, the phase uncertainty and the SNR are related via $\sigma_\phi = 1/(2\,\mathrm{SNR})$ [226]. At low SNR $\leq$ 10 however, an explicit formula between the SNR and the phase variance is not given anymore [226]. For a given required precision σ_r and a given number of comb lines N_b for phase evaluation, we determine the required phase variance σ_ϕ and then implicitly the required SNR (σ_r) based on Eq. (17) in [226]. At low optical return powers, shot noise on the measurement detector will be dominated by the LO comb power, such that the expression for the SNR reads:

$$\begin{aligned} \sigma^2_{\mathrm{n,shot}} &\approx 2q_\mathrm{e}\mathcal{R}P_\mathrm{LO}\Delta f, \\ \mathrm{SNR}\,(\sigma_\mathrm{r}) &\overset{!}{=} \frac{\frac{1}{2}\,(2\mathcal{R}P_\mathrm{SI}/N_\mathrm{c})\,(2\mathcal{R}P_\mathrm{LO}/N_\mathrm{c})}{2q_\mathrm{e}\mathcal{R}P_\mathrm{LO}\Delta f} = \frac{\mathcal{R}P_\mathrm{SI}}{N_\mathrm{c}^2 q_\mathrm{e}\Delta f}. \end{aligned} \tag{E.19}$$

The last equation allows to determine the required optical power $P_\mathrm{SI}\,(\sigma_\mathrm{r})$ to achieve the SNR (σ_r):

$$P_\mathrm{SI}\,(\sigma_\mathrm{r}) = \mathrm{SNR}\,(\sigma_\mathrm{r})\,eN_\mathrm{c}^2\Delta f/\mathcal{R}. \tag{E.20}$$

For a relative precision of $\sigma_\mathrm{r} = 1\,\%$, $N_\mathrm{b} = 25$ evaluation comb lines and an assumed total comb line count $N_\mathrm{c} = N_\mathrm{b} = 25$, the required phase variance amounts to $\sigma_\phi = 2\pi \times 0.24$. This is achieved for an SNR (1 %) = 0.1 (−10 dB). At a sampling rate of $\Delta f = 500\,\mathrm{MHz}$, this translates into a minimum required optical return power of the signal comb of $P_\mathrm{SI}\,(1\,\%) = 10\,\mathrm{nW}$ (−50 dBm). For $\Delta f = 50\,\mathrm{MHz}$, the 1 % precision return power decreases to 1 nW (−60 dBm) and at $\Delta f = 1\,\mathrm{MHz}$ to 20 pW (−77 dBm). This indicates that very low optical return powers can be tolerated with reasonable remaining precision as long as the sample rate is decreased. If a QD-MLLD is operated at high pump currents to achieve an optical output power of 50 mW (17 dBm), an overall loss tolerance of 94 dB may be possible for a QD-MLLD-based ranging system and allow for the detection of targets at a distance of 200 m or more, see Section E.8.

Acknowledgements (German)

Die vorliegende Arbeit entstand während meiner Tätigkeit am Institut für Photonik und Quantenelektronik (IPQ) am Karlsruher Institut für Technologie (KIT) und wurde durch den Sonderforschungsbereich 1173 "Wave Phenomena" der Deutschen Forschungsgemeinschaft gefördert. An dieser Stelle möchte ich allen danken, die zum Gelingen dieser Arbeit beigetragen haben.

Zuerst möchte ich hierbei meinen Doktorvater Prof. Christian Koos nennen, der mir die Chance gab, an seinem Institut eine Promotion anzutreten. Sein Ideenreichtum und sein Drang, Dinge bis ins kleinste Detail zu verstehen, aber auch in einen größeren Zusammenhang zu setzen, haben im Laufe der Zeit auf mich abgefärbt und bilden somit Teile des Fundaments, auf dem diese Dissertation steht. Die von ihm bereitgestellten Rahmenbedingungen, wie etwa eine hervorragende Laborausstattung und ein weitverzweigtes Kooperationsnetzwerk, waren ebenfalls unerlässlich für den Erfolg dieser Arbeit. Ich möchte ihm hierfür, aber auch für die langen Diskussionen zu physikalischen und technischen Zusammenhängen sowie für die im Laufe der Zeit übertragene Verantwortung danken.

Professor Freude danke ich herzlich für die ausgiebigen Gespräche zu meinen wissenschaftlichen Publikationen und zu dieser Dissertation. Er hat maßgeblich zum Gelingen dieser Arbeiten beigetragen, indem er nicht nur wissenschaftliche Missstände aufgedeckt, sondern auch allzu hitzige Debatten stets erkannt und diese mit Kaffee und Schokolade wieder in geregelte Bahnen gelenkt hat. Ein Dankeschön gilt ebenfalls Professor Sebastian Randel, der mich der optischen Telekommunikationstechnik durch Einsatz als Tutor zu seinen Vorlesungen nähergebracht hat und darüber hinaus zu einem Treffen der ITG-Fachgruppe Kommunikationstechnik einlud.

Sehr herzlich möchte ich mich zudem bei meinen Projektpartnern Professor Wolfgang Reichel, Professor Tobias Jahnke, Janina Gärtner, Rainer Mandel und Elias Gasmi aus dem Fachbereich Mathematik bedanken. Die gemein-

samen Publikationen sowie die erfolgreiche Projektverlängerung bezeugen die produktive und sehr angenehme Zusammenarbeit über die letzten Jahre. Besonders möchte ich dabei Professor Reichel und Janina Gärtner danken, die die mathematische Sinnhaftigkeit meiner Arbeit überprüft und an den notwendigen Stellen korrigiert haben. Professor Jahnke danke ich für Diskussionen zu den verwendeten numerischen Methoden, auf welchen wesentliche Teile meiner Arbeit beruhen. Darüber hinaus gilt auch Laurette Lauffer und Christian Knieling ein Dankeschön für die reibungslose organisatorische Zusammenarbeit mit dem Sonderforschungsbereich Wave Phenomena.
Weiterhin möchte ich mich bei Professor Tobias Kippenberg und dessen Gruppe von der École Polytechnique Fédérale de Lausanne für die Herstellung der verwendeten Siliziumnitrid-Kerr-Mikroresonatoren bedanken, sowie für die gute und intensive Zusammenarbeit an den gemeinsamen Publikationen. Im gleichen Sinne gilt auch Abderrahim Ramdane vom Centre de Nanosciences et de Nanotechnologies und dessen Kollegen Dank für die Bereitstellung der modengekoppelten Quanten-Strich-Laserdioden und den inhaltlichen Austausch zu diesen Lichtquellen.

Daneben gilt ein großer Dank meinen wissenschaftlichen Kollegen. Hier sind vor allem Denis Ganin, Pablo Marin, Juned Kemal und Jörg Pfeifle zu nennen, mit denen ich Experimente gemeinsam durchgeführt habe und welche mich insbesondere zu Beginn der Promotion unterstützt haben. Weiterhin gilt ein Dankeschön Jonas Krockenberger, Daniel Bauer und Sebastian Gassel, die mit ihren Studienabschlussarbeiten ebenfalls zu dieser Dissertation beigetragen haben. Aber auch meinen weiteren wissenschaftlichen Kollegen möchte ich einerseits für die gute unmittelbare Zusammenarbeit, andererseits aber auch für eine schöne Zeit am Institut danken. Fachliche Diskussionen, gemeinsame Mittags- und Kaffeepausen haben meinen Arbeitsalltag stets bereichert. Darüber hinaus waren die gemeinsamen Besuche von Konferenzen sowie einer Sommerschule in St. Andrews schöne Erlebnisse, an die ich mich sehr gerne zurückerinnere – hier möchte ich mich insbesondere bei Clemens Kieninger und Heiner Zwickel für die gute Zeit bedanken.

Den Kolleginnen aus dem Sekretariat gilt ebenfalls mein Dank. Zunächst möchte ich dabei bei Andrea Riemensperger und Tatiana Gassmann nennen – die gute Zusammenarbeit bei organisatorischen und administrativen Themen ließ mir stets Mindestmaß an Zeit für meine wissenschaftlichen Tätigkeiten. Aber auch Maria-Luise Koch und Bernadette Lehmann gilt mein Dank für

die Hilfe bei vielen alltäglichen Anfragen. Den Kolleginnen und Kollegen aus der Optik-, Elektronik- und Mechanikwerkstatt danke ich für die Beratung und die Unterstützung bei der Umsetzung experimenteller Versuchsaufbauten. In einem Optiklabor Objekte kontrolliert auf nahezu halbe Schallgeschwindigkeit zu beschleunigen war keine triviale Aufgabe – hier haben Martin Winkeler und Marco Hummel maßgeblich zum Erfolg der zugehörigen Experimente beigetragen. David Guder und Volker Bös danke ich für den IT-Support, ohne den ein Großteil meiner Arbeit nicht möglich gewesen wäre.

Außerhalb meines beruflichen Umfelds möchte ich mit herzlich bei meinen Freunden und meiner Wohngemeinschaft für die Unterstützung während der letzten Jahre bedanken. In herausfordernden Phasen konnte ich auf offene Ohren, Zerstreuung, Nachsicht und an so manchen Wochenenden auch auf Verpflegung zählen.

Zu guter Letzt gilt meinen Eltern, Birgit und Rico Trocha, noch besonderer Dank. Vor der Einschulung habe ich wohl Ambitionen einer wissenschaftlichen Karriere laut werden lassen (”Werde mal Professor“) und gute 25 Jahre später ist viel in dieser Richtung passiert. Danke, dass ihr mir diesen Weg ermöglicht und jede meiner Entscheidungen mitgetragen habt.